

**INFLUENCE OF BORON DISTRIBUTION ON  
PRECIPITATION AND RECRYSTALLIZATION  
IN HOT WORKED AUSTENITE**

by

**Mohammad Djahazi**

**A Thesis Submitted to the Faculty of Graduate Studies and  
Research in Partial Fulfillment of the Requirements  
for the Degree of Doctor of Philosophy**

**Department of Mining and Metallurgical Engineering  
McGill University  
Montreal, Canada**

**August 1989**

## ABSTRACT

The influence of boron distribution on the precipitation of Nb(C,N) and on austenite recrystallization was studied by means of a stress relaxation technique. A plain carbon steel containing 0.026% C, used as the reference material, and three other steels alloyed with 0.003% B, 0.055% Nb and 0.003% B + 0.055% Nb were employed. The microstructural evolution during relaxation was interpreted in terms of the pinning effect of precipitates on mobile dislocations.

C-shaped precipitation-time-temperature diagrams were determined for both the Nb + B and Nb steels. The presence of boron accelerates precipitation so that it begins at higher temperatures and after shorter times. Also, the combined addition of Nb and boron delays the recrystallization start time at 1000°C and suppresses the partial recrystallization of austenite observed at 950°C.

Samples were quenched or control cooled at different stages of the tests and the evolution of precipitation and the location of boron and boron compounds were studied by various microanalytical techniques. The occurrence of the non-equilibrium segregation of boron after deformation and during recrystallization at austenite grain boundaries was revealed in this way. The observations are interpreted in terms of the interaction between vacancies and boron atoms.

The strong retardation of recrystallization and the acceleration of precipitation observed when both Nb and boron are present is explained in terms of the formation of Nb-B complexes and the increase in the effective concentration of precipitate forming interstitials. At deformation temperatures of 950°C and above, boron appears to increase the solute drag effect of Nb, leading to greater delays in recrystallization. At lower temperatures, boron plays its role in accelerating the nucleation stage of precipitation.

Finally, changes in the size distribution of the precipitates as a function of composition, temperature and time were measured. These data are employed in the framework of the diffusion controlled nucleation and particle growth theory. Expressions for the Nb(C,N) precipitation start times and for the diffusion of Nb in austenite were obtained which are in accord with the values reported in the literature.

## RESUME

Les influences du bore sur la précipitation du Nb(C,N) et sur la recristallisation de l'austénite ont été étudiées par une technique de relaxation des contraintes. Un acier au carbone contenant 0.026% C, utilisé comme matériau de référence, et trois autres aciers microalliés avec 0.003% B, 0.055% Nb et 0.003% B + 0.055% Nb ont été employés. L'évolution de la microstructure au cours de la relaxation a été interprétée par l'effet d'une précipitation dynamique sur les dislocations en mouvement.

Les diagrammes précipitation-temps-température ont été déterminés pour les aciers Nb + B et Nb. Les résultats indiquent qu'en présence du bore, le processus de précipitation est accéléré et débute à plus hautes températures et après de plus courtes périodes d'incubation. De plus, l'addition simultanée du Nb et du bore retarde le début de la recristallisation à 1000°C et la supprime à 950°C.

Des échantillons ont été trempés ou refroidis à vitesse contrôlée à différents stades des tests. Les évolutions de la précipitation et de la localisation du bore et des composés borés ont été étudiées par plusieurs méthodes microanalytiques. La ségrégation hors-équilibre du bore aux joints de grains de l'austénite après déformation et durant la recristallisation a pu être ainsi révélée. Les interprétations sont basées sur les interactions qui existent entre les lacunes et les atomes du bore.

Le retard de la recristallisation et l'accélération de la précipitation observées quand le bore et le Nb sont présents simultanément sont expliqués par la formation de complexes Nb-B ainsi que par un accroissement de la concentration effective des interstitiels formant les précipités. Pour des températures de déformation de 950°C et plus, le bore semble accroître l'effet du dragage du Nb aboutissant à des importants délais de recristallisation tandis qu'à des températures inférieures, cet élément joue un rôle dans l'étape de la nucléation des précipités.

Finalement, l'évolution de la taille des précipités en fonction de la composition, de la température et du temps a été mesurée et analysée dans le cadre de la théorie de la germination et croissance par diffusion. Les expressions donnant le temps du début de la précipitation et celle de la diffusion du Nb dans l'austénite ont été déterminées et sont en accord avec celles de la littérature.

## ACKNOWLEDGMENTS

I would like to express my sincere appreciation to my thesis supervisor, Professor John J. Jonas, who communicated to me his enthusiasm for the field of physical and mechanical metallurgy throughout the course of this study. His devotion to scientific inquiry together with his personal generosity have been inspiring, not only during my Ph. D. studies but will set an example for my life.

I am sincerely grateful to Professor Xinlai He (Beijing University of Iron and Steel Technology), who introduced me to the non-equilibrium segregation of boron and for all his help and invaluable discussions. His scientific rigor along with his fatherly kindness have been greatly appreciated.

Much gratitude is due to my friend and former colleague Dr. W.J. Liu for all our fruitful discussions and for his help with the stress relaxation testing. I am similarly indebted to Dr S. Yue for his assistance with the electron microscopy.

Special thanks go to Drs. J.J. Jackman, L.E. Collins, T.Malis and G.E. Ruddle, all of MTL CANMET, for helping me during the SIMS, deformation dilatometer, and EELS experiments and for the preparation of the experimental materials. I am also thankful to Dr. M.D. Watson and to Mr M. Smith from Atomic Energy of Canada Ltd. for carrying out the irradiation of the specimens.

The sympathy and useful encouragement I received from my fellow graduate students are deeply appreciated. I would also like to express my gratitude to M. Knoepfel and B. Grondin for their assistance in the preparation of test specimens and to L. Mello and C. Rousseau for their continuous help.

This study could not have been carried out without the financial support received from the Canadian Steel Industry Research Association (CSIRA), the Natural Sciences and Engineering Research Council of Canada and MTL,

**CANMET.** I am much indebted to these organizations for sponsoring this investigation

Last, but not least, my wife, with her permanent kindness and assistance in typing this thesis, and all my family and friends in Iran, France and Canada never doubted that I would succeed in this project and always supported me during the busy years that it consumed. I am deeply grateful to them for their valuable friendship, without which the achievement of this work would not have been possible.

## TABLE OF CONTENTS

	<u>Page</u>
ABSTRACT . . . . .	i
RESUME . . . . .	ii
ACKNOWLEDGMENTS . . . . .	iii
TABLE OF CONTENTS . . . . .	v
LIST OF FIGURES . . . . .	xi
LIST OF TABLES . . . . .	xvii
<b>CHAPTER I</b>	
INTRODUCTION . . . . .	1
<b>CHAPTER II</b>	
LITERATURE REVIEW. . . . .	4
II.1. Boron in Steel . . . . .	4
II.1.1. Boron in HSLA Steels . . . . .	7
II.2. Location of Boron in the Iron Lattice . . . . .	9
II.2.1. Solubility of Boron in Iron . . . . .	9
II.2.2. Nature of Boron in Iron . . . . .	9
II.3. Non-equilibrium Grain Boundary Segregation of Boron	
II.3.1. Description of the Phenomenon . . . . .	12
II.3.2. Mechanism and Kinetics of Non-equilibrium. Segregation . . . . .	13
II.4. Influence of Boron on the Precipitation Process . . . . .	15
II.4.1. Types of Boron Compounds . . . . .	15
II.4.2. Influence of Boron on Precipitation Kinetics and on Particle Size and Distribution. . . . .	20
II.5. Influence of Boron on Mechanical Properties . . . . .	21
II.5.1. Hardenability . . . . .	22
II.5.2. Hot Workability . . . . .	23
II.5.3. Creep Rupture Life . . . . .	24
II.5.4. Temper Embrittlement . . . . .	24
II.6. Experimental Techniques for Boron Detection . . . . .	25
II.6.1. Wet Chemical Analysis . . . . .	25
II.6.2. Atom Probe Field Ion Microscopy (FIM) and Imaging Atom Probe (IAP). . . . .	27

	<u>Page</u>
II.6.3. Auger Electron Spectroscopy (AES) . . . . .	28
II.6.4. Electron Microprobe Analysis (EMA) . . . . .	28
II.6.5. Transmission Electron Microscopy (TEM) . . . . .	29
II.6.6. Secondary Ion Mass Spectroscopy (SIMS) . . . . .	29
II.6.7. Particle Tracking Autoradiography (PTA). . . . .	30
<b>II.7. Precipitation Behaviour in Hot Worked HSLA Steels . . . . .</b>	<b>32</b>
II.7.1. Types and Kinds of Precipitates . . . . .	32
II.7.2. Crystallographic Structure . . . . .	34
II.7.3. Simple and Complex Precipitates . . . . .	34
II.7.4. Precipitate Solubility . . . . .	39
II.7.5. Influence of Non-stoichiometry and of Alloying Element Interaction . . . . .	40
<b>II.8. Precipitation in Hot Worked Austenite. . . . .</b>	<b>43</b>
II.8.1. Precipitation at Dislocations and on Dislocation Substructures . . . . .	44
II.8.2. Precipitation on Stacking Faults . . . . .	45
II.8.3. Precipitation at Grain Boundaries . . . . .	46
II.8.3.1. Precipitation of $M_{23}I_6$ Compounds . . . . .	46
II.8.3.2. Precipitation of FCC Carbides and Nitrides . . . . .	46
II.8.4. Precipitation in the Matrix . . . . .	47
<b>II.9. The Kinetics of Precipitation from Supersaturated     Austenite . . . . .</b>	<b>47</b>
II.9.1. Influence of Time and Temperature . . . . .	48
II.9.2. Influence of Strain and Strain rate . . . . .	50
II.9.3. Influence of Alloying Elements . . . . .	50
II.9.4. Interaction Between Recrystallization and Precipitation . . . . .	51
II.9.5. Modelling Precipitation Kinetics . . . . .	51

### CHAPTER III

<b>EXPERIMENTAL MATERIALS AND PROCEDURES . . . . .</b>	<b>54</b>
<b>III.1. Materials . . . . .</b>	<b>54</b>
<b>III.2. Mechanical Testing Equipment . . . . .</b>	<b>54</b>
III.2.1. MTS Testing System . . . . .	54
III.2.2. The High Temperature Vacuum Furnace . . . . .	56

	<u>Page</u>
III.2.3. Hot Deformation Dilatometer . . . . .	58
<b>III.3. Specimen Preparation and Heat Treatment . . . . .</b>	<b>60</b>
III.3.1. Specimen Preparation . . . . .	60
III.3.1.1. MTS Tests . . . . .	60
III.3.1.2. Deformation Dilatometer . . . . .	60
III.3.2. Heat Treatment . . . . .	60
III.3.2.1. Solutionizing Heat Treatment . . . . .	62
<b>III.4. Experimental Procedure . . . . .</b>	<b>63</b>
III.4.1. Stress Relaxation Testing . . . . .	63
<b>III.5. Metallography . . . . .</b>	<b>67</b>
III.5.1. Particle Tracking Autoradiography . . . . .	67
III.5.2. Electron Microscopy of Carbon Extraction Replicas . . . . .	68
III.5.3. SIMS Analysis . . . . .	69
III.5.4. EELS . . . . .	69
III.5.5. Particle Size Measurements . . . . .	69

## CHAPTER IV

<b>MECHANICAL TESTING RESULTS . . . . .</b>	<b>70</b>
IV.1. Determination of the Prior Austenite Grain Size . . . . .	70
IV.2. Stress Relaxation Test Results . . . . .	73
IV.2.1. Case of the Plain Carbon Steel . . . . .	73
IV.2.2. Stress Relaxation Results after 5% Prestrain . . . . .	75
IV.2.3. Stress Relaxation Results After 25% Prestrain . . . . .	87
IV.2.4. Precipitation-Time-Temperature Diagrams . . . . .	87
IV.3. No-deformation Tests . . . . .	98

## CHAPTER V

<b>METALLOGRAPHIC RESULTS . . . . .</b>	<b>99</b>
<b>PART 1: TRANSMISSION ELECTRON MICROSCOPY . . . . .</b>	<b>99</b>
V.1.1. State of Precipitation After Austenitization . . . . .	99
V.1.2. State of Precipitation After Testing . . . . .	101
V.1.2.1. Nature and Distribution of the Large Precipitates . . . . .	101
V.1.2.2. Nature and Distribution of the Small Precipitates . . . . .	102
V.1.3. Identification of the Interstitial Elements by EELS . . . . .	105
V.1.3.1. Introduction . . . . .	105

	<u>Page</u>
V.1.3.2. The Analysis . . . . .	107
<b>V.1.4. Evolution of the Precipitation Process During Stress</b>	
<b>Relaxation . . . . .</b>	<b>112</b>
V.1.4.1. After 25% Deformation at 850°C . . . . .	112
V.1.4.2. After 5% Deformation at 850°C . . . . .	112
V.1.4.3. In the Absence of Deformation at 850°C . . . . .	116
V.1.4.4. After 25% Deformation at 900 and 950°C . . . . .	116
<b>V.1.5. Composition and Morphology Changes in the</b>	
<b>Precipitates . . . . .</b>	<b>116</b>
V.1.5.1. Composition Changes . . . . .	116
V.1.5.2. Morphology of the Precipitates. . . . .	120
<b>V.1.6. Particle Size Distribution . . . . .</b>	<b>121</b>
<b>PART 2: PTA AND SIMS RESULTS</b>	
<b>V.2.1. The Segregation of Boron During Quenching . . . . .</b>	<b>132</b>
V 2.1.1. Case of the Nb + B Steel. . . . .	132
V.2.1.2. Case of the Boron Steel . . . . .	138
<b>V.2.2. Boron Segregation After High Temperature</b>	
<b>Deformation . . . . .</b>	<b>141</b>
V.2.2.1. Results Pertaining to the Nb + B Steel . . . . .	141
V.2.2.2. Results Pertaining to the Boron Steel . . . . .	146
<b>V.2.3. The Characteristics of Grain Boundary Segregation . . . . .</b>	<b>149</b>
<b>V.2.4. Influence of Cooling Rate on Boron Distribution . . . . .</b>	<b>151</b>
<b>V.2.5. State of the Boron Distribution in the Samples</b>	
<b>Examined by TEM . . . . .</b>	<b>155</b>
<b>V.2.6. Evolution From Segregation to Precipitation . . . . .</b>	<b>157</b>
<b>V.2.7. Presence of Boron in Inclusions and Precipitates . . . . .</b>	<b>159</b>
V.2.7.1. Inclusions . . . . .	159
V.2.7.2. Precipitates . . . . .	159
<b>V.2.8. Influence of Boron on Recrystallization at 950°C . . . . .</b>	<b>161</b>
<b>CHAPTER VI</b>	
<b>DISCUSSION . . . . .</b>	<b>165</b>
<b>PART 1: MICROSTRUCTURAL EVOLUTION DURING</b>	
<b>STRESS RELAXATION . . . . .</b>	<b>165</b>

	<u>Page</u>
<b>VI.1.1. Stress Relaxation After Deformation . . . . .</b>	<b>165</b>
VI.1.1.1. Formulation of the Problem . . . . .	165
VI.1.1.2. Dislocation Dynamics During Stress Relaxation .	166
VI.1.1.3. Application of the Model . . . . .	170
a) The Activation Area, $A^*$ . . . . .	170
b) The Internal Stress, $\tau_i$ . . . . .	170
c) Calculation of $A^*$ . . . . .	171
<b>VI.1.2. Effect of Precipitation on Stress Relaxation. . . . .</b>	<b>174</b>
VI.1.2.1. Dislocation-Particle Interactions at High Temperatures . . . . .	174
a) Cutting or Bowing? . . . . .	174
b) Elastic Dislocation-Particle Interactions . . . . .	179
VI.1.2.2. A Possible Explanation . . . . .	182
a) Nucleation of Precipitates on Mobile Dislocations . . . . .	183
b) The Unpinning Stress. . . . .	186
<b>VI.1.3. Stress Relaxation During Particle Coarsening . . . . .</b>	<b>188</b>
<b>VI.1.4. Influence of Composition and Testing Conditions on     Dislocation Density. . . . .</b>	<b>193</b>
 <b>PART 2: NUCLEATION, GROWTH AND     COARSENING OF THE PRECIPITATES . . . . .</b>	
<b>VI.2.1. Nucleation . . . . .</b>	<b>195</b>
VI.2.1.1. Critical Free Energy for Nucleation, $\Delta G^*$ . . . . .	195
VI.2.1.2. Precipitation Start Time, $P_s$ . . . . .	196
<b>VI.2.2. Growth . . . . .</b>	<b>198</b>
VI.2.2.1. Determination of the Diffusion Coefficients . . . . .	202
<b>VI.2.3. Coarsening . . . . .</b>	<b>206</b>
 <b>CHAPTER VII</b> <b>THE MECHANISMS ASSOCIATED WITH THE EFFECT OF BORON . . . . .</b>	
<b>VII.1. The Influence of Boron on the Precipitation Kinetics .</b>	<b>210</b>
VII.1.1. Influence of Boron Segregation on Precipitate Nucleation . . . . .	212

	<u>Page</u>
VII.1.2. Effect of Boron on Particle Growth . . . . .	214
<b>VII.2. Influence of Boron on the Recrystallization Process . . . . .</b>	<b>215</b>
VII.2.1. Influence of Boron on the Solute Drag Effect of Nb . . . . .	220
VII.2.2. The Synergistic Effect of Nb and Boron . . . . .	221
<b>VII.3 Origins of the Non-equilibrium Segregation of Boron . . . . .</b>	<b>223</b>
VII.3.1. Cooling Induced Segregation of Boron . . . . .	223
VII.3.2. Boron Segregation after High Temperature Deformation . . . . .	228
VII.3.3. The Non-equilibrium Segregation of Boron during Recrystallization. . . . .	228
VII.3.3.1. The Mechanism of Segregation . . . . .	229
<b>VII.4. Semi-Quantitative Analysis of Segregation . . . . .</b>	<b>231</b>
VII.4.1. Assumptions and Analysis . . . . .	233
VII.4.2. Comparison of the Results . . . . .	236
<b>VII.5. Comparison with the Precipitation Results of Other     Workers. . . . .</b>	<b>240</b>

## CHAPTER VIII

<b>CONCLUSIONS. . . . .</b>	<b>243</b>
<b>STATEMENT OF ORIGINALITY AND CONTRIBUTION TO KNOWLEDGE. . . . .</b>	<b>248</b>
<b>REFERENCES . . . . .</b>	<b>251</b>
<b>APPENDIX 1. LISTING OF THE TESTING PROGRAM . . . . .</b>	<b>261</b>
<b>APPENDIX 2. DETERMINATION OF THE DISLOCATION     DENSITY . . . . .</b>	<b>269</b>
<b>APPENDIX 3. CALCULATION OF THE STRAIN RATE USING     A CREEP MODEL . . . . .</b>	<b>271</b>
<b>APPENDIX 4. DETERMINATION OF THE CRITICAL STRESS     FOR DISLOCATION UNPINNING. . . . .</b>	<b>273</b>
<b>APPENDIX 5. DETERMINATION OF THE INTERFACIAL,     STRAIN AND CHEMICAL FREE ENERGY     FOR NUCLEATION . . . . .</b>	<b>275</b>

**LIST OF FIGURES**

<u>Figure</u>	<u>Page</u>
II.1. Influence of effective boron content on the hardenability of a low carbon, low alloy steel.	6
II.2. Effect of alloy addition on the mechanical properties of steel plates.	8
II.3. Phase diagrams of the Fe-B system.	10
II.4. Effect of cooling rate on calculated segregation profiles.	16
II.5. Crystallographic structures of the different types of precipitates in microalloyed steels.	36
II.6. Schematic histogram showing the size, shape and chemical composition of a typical precipitate sequence.	38
II.7. The solubility products of microalloy carbides and nitrides.	42
II.8. Schematic recrystallization-precipitation-temperature-time (RPTT) diagram.	52
III.1. An external view of the high temperature compression testing system : 1) MTS load frame; 2) Centorr vacuum furnace; 3) temperature and vacuum control console; 4) PDP 11/04 computer; and 5) Tektronix terminal.	57
III.2. An interior view of the Centorr high temperature, high vacuum furnace. 1) vacuum chamber; 2) tungsten mesh heating elements; 3) shields; 4) TZM anvils; 5) thermocouples; 6) specimen; 7) specimen pusher.	59
III.3. Sample geometry and groove design.	61
III.4. Heat treatment schedules (type I).	65
III.5. Heat treatment schedules (type II).	66
IV.1. Prior austenite grain size as a function of reheat temperature.	72
IV.2. Stress relaxation data for the base steel, solutionized at 1100°C and deformed 5%.	74
IV.3. Comparison of stress relaxation data for the Nb + B and the base steel, deformed 5% at 850°C.	76

<u>Figure</u>	<u>Page</u>
IV.4. Stress relaxation data for the Nb + B steel, solutionized at 1100°C and deformed 5%. a)800, 830 and 850°C b)870 and 900°C	78 79
IV.5. Stress relaxation data for the Nb + B steel, solutionized at 1200°C and deformed 5%. a)800, 830 and 850°C b)870, 900 and 950°C	80 81
IV.6. Stress relaxation data for the Nb steel, solutionized at 1100°C and deformed 5%. a)800, 830 and 850°C b)870 and 900°C	82 83
IV.7. Stress relaxation data for the Nb steel, solutionized at 1200°C and deformed 5%. a)800, 830 and 850°C b)870, 900 and 950°C	84 85
IV.8. Microstructures of the Nb and Nb + B steels, quenched after 1800 s of stress relaxation at 800°C.	86
IV.9. Stress relaxation data for the Nb + B steel, solutionized at 1100°C and deformed 25%.	88
IV.10. Stress relaxation data for the Nb + B steel, solutionized at 1200°C and deformed 25%.	89
IV.11. Stress relaxation data for the Nb steel, solutionized at 1100°C and deformed 25%.	90
IV.12. Stress relaxation data for the Nb steel, solutionized at 1200°C and deformed 25%.	91
IV.13. PTT curves for the Nb + B and Nb steels, solutionized at 1100°C and deformed 5%.	94
IV.14. PTT curves for the Nb + B and Nb steels, solutionized at 1200°C and deformed 5%.	95
IV.15. PTT curves for the Nb + B and Nb steels, solutionized at 1100°C and deformed 25%.	96
IV.16. PTT curves for the Nb + B and Nb steels, solutionized at 1200°C and deformed 25%.	97

<u>Figure</u>	<u>Page</u>
V.1. Carbon extraction replicas showing iron containing precipitates along with their EDX spectra, observed in the B steel after 1800 s of holding at 850°C.	103
V.2. Carbon extraction replicas and the EDX spectra of : a) a Nb rich precipitate, and b) a complex (Ti, Nb) precipitate.	104
V.3. EDX spectra showing the evolution in precipitate composition during stress relaxation in both Nb + B and Nb steels.	106
V.4. Cluster of B-containing precipitates.	108
V.5. EELS spectra showing area 1 in Fig.V.4.	109
V.6. EELS spectra showing area 2 in Fig.V.4.	110
V.7. EELS spectra showing area 3 in Fig.V.4.	111
V.8. Carbon extraction replicas showing the progress of precipitation in the Nb + B steel after 25% deformation at 850°C and different relaxation times.	113
V.9. Carbon extraction replicas showing the progress of precipitation in the Nb steel after 25% deformation at 850°C and different relaxation times.	114
V.10. Carbon extraction replicas showing the progress of precipitation in the Nb + B steel after 5% deformation at 850°C and different relaxation times.	115
V.11. Carbon extraction replicas showing the progress of precipitation in an undeformed Nb + B steel sample at 850°C and different holding times.	117
V.12. Carbon extraction replicas showing the progress of precipitation in the Nb + B steel after 25% deformation at 900°C and different relaxation times.	118
V.13. Carbon extraction replicas showing the progress of precipitation in the Nb + B steel after 25% deformation at 950°C and different relaxation times.	119
V.14. Effect of temperature and relaxation time on the particle size distribution in the Nb + B steel after 25% deformation.	122
V.15. Effect of deformation and relaxation time on the particle size distribution in the Nb + B steel at 850°C.	123
V.16. Effect of composition and relaxation time on the particle size distribution after 25% deformation at 850°C.	124

<u>Figure</u>	<u>Page</u>
V.17. Effect of test temperature on the mean particle size ( $d_v$ ) in the Nb + B steel after 25% deformation.	129
V.18. Effect of deformation and relaxation time on the mean particle size ( $d_v$ ) in the Nb + B steel at 850°C.	130
V.19. Effect of composition on the mean particle size ( $d_v$ ) during stress relaxation at 850 °C.	131
V.20. The boron distributions revealed by PTA in the Nb + B steel as a function of quench temperature. Oil quenched after 600 s of isothermal holding.	135
V.21. Comparison between PTA and optical micrographs of a Nb + B steel specimen held isothermally for 30 min at 850°C.	137
V.22. Ion micrographs showing the distribution of boron in the Nb + B steel after quenching from different temperatures. $O_2^+$ was used as the primary ion and $BO_2^-$ as the secondary ion.	139
V.23. The boron distribution revealed by PTA in the B steel as a function of quench temperature. Oil quenched after 600 s of isothermal holding.	140
V.24. The boron distribution revealed by PTA in the Nb + B steel after 25% deformation at 1000°C and different holding times (ice brine quenching).	142
V.25. The boron distributions revealed by SIMS in the Nb + B steel after 25% deformation at 1000°C and different holding times (ice brine quenching).	144
V.26. The boron distribution revealed by PTA in the Nb + B steel after 25% deformation at 950°C and different holding times (helium quenching).	145
V.27. The boron distribution revealed by PTA in the Nb + B steel after 25% deformation at 850°C and different holding times (helium quenching).	147
V.28. The boron distribution revealed by PTA in the B steel after 25% deformation at 1000°C and different holding times (ice brine quenching).	148
V.29. The boron distribution revealed by PTA in the B steel after 25% deformation at 900°C and different holding times (helium quenching).	150
V.30. Evolution of the amplitude of segregation with isothermal holding time after 25% deformation at 1000°C.	152

<u>Figure</u>	<u>Page</u>
V.31. The boron distribution revealed by PTA in the Nb + B steel after 25% deformation at 1000°C and different holding times (oil quenching).	153
V.32. The boron distribution revealed by PTA in the Nb + B steel after 25% deformation at 900°C after different holding times (cooling rate 13 to 17 °C/sec).	156
V.33. Evolution from segregation to precipitation in the B steel after deformation at 850°C.	158
V.34. Ion micrographs showing the distribution of boron and other alloying elements in undissolved inclusions in the Nb + B steel. O <sub>2</sub> <sup>+</sup> was used as the primary ion and BO <sub>2</sub> <sup>-</sup> as the secondary ion. a) Fe <sup>+</sup> , b) Mn <sup>+</sup> , c) Al <sup>+</sup> , d) Ti <sup>+</sup> , e) Nb <sup>+</sup> , f) B <sup>+</sup> .	160
V.35. PTA micrograph of carbon extraction replicas showing the presence of boron in the precipitates, Nb + B steel deformed 5% at 850°C.	162
V.36. State of the microstructure in the Nb + B and Nb steels after 25% deformation at 950°C. a) PTA micrograph of the Nb + B steel hold for 100 s, and b) optical micrograph of the Nb steel after etching with hot picric acid after 65 s of holding.	164
VI.1. Dislocation held up at a random array of particles.	175
VI.2. Interaction between coherency hardening, shear modulus hardening and Orowan stress showing the transition from cutting to bowing.	178
VI.3. Evolution of the plastic strain rate with time for the Nb steel deformed 5% at 850°C. (×) experimental, (●) Hausselt and Nix model.	181
VI.4. Influence of particle coarsening on relaxation behaviour for the Nb + B steel deformed 5% at 850 °C.	184
VI.5. Variation of the Orowan stress during stress relaxation of the Nb steel after 5% deformation at 850°C .	185
VI.6. Influence of particle coarsening on relaxation behaviour for the Nb + B steel deformed 5% at 850°C.	187
VI.7. Influence of temperature and composition on dislocation density.	191
VI.8. Influence of temperature and deformation on dislocation density for the Nb steel.	192
VI.9. Comparison between the observed (●) and calculated (×) P <sub>s</sub> values for the Nb + B steel.	200

<u>Figure</u>	<u>Page</u>
VI.10. Comparison between the observed (●) and calculated (×) $P_s$ values for the Nb steel.	201
VI.11. Dependence of $d^2/a^2$ on relaxation time in the Nb steel after 5% deformation.	203
VI.12. Dependence of $d^2/a^2$ on relaxation time in the Nb+B steel after 5% deformation.	204
VI.13. Dependence of $d^2/a^2$ on time during the early stages of stress relaxation for the Nb+B steel after 5% deformation at 850°C.	205
VI.14. Influence of boron on the diffusion coefficient of Nb.	207
VII.1. Comparison between the stress relaxation curves for the Nb+B and Nb steels after 25% deformation at 850°C.	211
VII.2. Comparison between the stress relaxation curves for the Nb+B and Nb steels after 25% deformation at 950°C.	216
VII.3. Comparison between the stress relaxation curves for the Nb+B and Nb steels after 25% deformation at 1000°C.	217
VII.4. Influence of the simultaneous presence of Nb and boron on the recrystallization process. PTA micrographs of the Nb+B and B steels deformed 25% at 1000°C and quenched after 10 s.	218
VII.5. The softening behaviours of the four steels deformed 25% at 1000°C.	219
VII.6. Comparison between the diffusivities of B-V complexes, vacancies and boron atoms according to the Williams (a) and Karlsson (b) models.	227
VII.7. Grain boundary enrichment by boron atoms when the boundary moves from $x$ to $x + \delta x$ .	230
VII.8. Dependence of $L/L_{\max}$ and $L_S/L_{S\max}$ on isothermal holding time in the Nb+B steel after 25% deformation at 1000°C.	232
VII.9. Schematic illustration of the formation of new boundaries and the annihilation of old ones.	234
VII.10 Dependences of $L_T/L_{\max}$ , $L_N/L_{\max}$ , $L_o/L_{\max}$ and $L/L_{\max}$ on holding time for the Nb+B steel deformed 25% at 1000°C.	237
VII.11 Distinction between the segregation produced at original and newly formed boundaries.	238
VII.12 Comparison between the PTT curves determined in this investigation and those of some other workers.	242

## LIST OF TABLES

<u>Table</u>	<u>Page</u>
II.1. Atomic Radii of Alloying Elements in Steels .	11
II.2. Binding Energies Between Boron Atoms and Lattice Defects.	13
II.3. Characterization of Each Kind of Segregation.	13
II.4. Data Used in Theoretical Calculations.	17
II.5. Classification of Borides and Boro-Carbides.	19
II.6. Comparison Between Different Boron Detection Techniques.	26
II.7. Advantages and Disadvantages of Each Technique.	33
II.8. Types of Precipitates in Microalloyed Steels.	35
II.9. Solubility Products of the Ti, Nb, and V Carbides, Nitrides and Carbonitrides in Austenite.	41
II.10. Variation of Avrami Exponent With Experimental Conditions.	49
III.1. Chemical Compositions of the Steels Tested.	55
III.2. Summary of the Experimental Conditions Employed.	64
IV.1. Prior Austenite Grain Size, $\mu\text{m}$ , as a Function of Reheat Temperature.	71
IV.2. $P_s$ and $P_f$ Times for the Nb + B Steel.	92
IV.3. $P_s$ and $P_f$ Times for the Nb Steel.	93
V.1. Identification of the Samples Used for the TEM Study.	100
V.2. Influence of Composition, Deformation and Time on the Particle Density at 850°C.	125
V.3. Influence of Composition, Deformation and Time on the Mean Particle Size for the Nb + B Steel.	127
V.4. Influence of Composition, Deformation and Time on the Mean Particle Size for the Nb Steel.	128
V.5. Quenching Schedule Used for PTA and SIMS analysis in the Nb + B Steel.	133

<u>Table</u>	<u>Page</u>
V.6. Quenching Schedule Used for PTA and SIMS analysis in the B Steel.	134
VI.1. Values of $\alpha$ , $\beta$ and $A^*$ Determined from the Stress Relaxation Data for the Nb Steel.	172
VI.2. Values of $\alpha$ , $\beta$ and $A^*$ Determined from the Stress Relaxation Data for the Nb + B Steel.	173
VI.3. Effects of Composition, Deformation and Temperature on Dislocation Density.	190
VI.4. Dependence of the Surface and Volume Free Energies on Temperature.	196
VI.5. Effect of Testing Conditions on the Values of $K$ and $\eta$ .	197
VI.6. Comparison Between the Observed and Calculated $P_s$ Values.	199
VI.7. Comparison of observed Activation Energies for the Diffusion of Nb.	208
VII.1. Specific Volumes of Selected Precipitates and Austenite.	214
VII.2. Times for the Beginning ( $t_0$ ) and the Half Completion of Recrystallization ( $t_{0.5}$ ).	220
VII.3. Influence of the Solutionizing Temperature on the Vacancy ( $C_V$ ), Complex ( $C_C$ ) and Boron ( $C_B$ ) Concentrations.	224
VII.4. Diffusivity Equations for Vacancies, Complexes and Boron Atoms.	225
VII.5. Comparison Between the PTT Curves Obtained by Different Investigators.	241

## CHAPTER I

### INTRODUCTION

Boron containing low carbon bainitic steels have been known to have high strengths and reasonable toughnesses since the early days of the development of HSLA steels. The incentive for the use of boron is derived from the fact that minute additions (5 to 30 ppm) are sufficient to delay substantially the formation of pro-eutectoid ferrite, thereby retarding the  $\gamma$ -to- $\alpha$  transformation. In order to play its role, boron has to be protected from nitrogen and other compound formers. This was not possible in the past due to the lack of sufficient control in steelmaking, and led to negative opinions about these grades.

In recent years with the advent of modern steelmaking technology, ultra low carbon bainitic (ULCB) HSLA steels have been produced. They contain Nb and Ti in addition to boron and possesses high strength, toughness and excellent weldability, making them suitable for energy conversion and transportation systems.

During the hot rolling of these steels, recrystallization takes place, both during and after high temperature deformation. The presence of Nb and Ti in solid solution or as precipitate modifies the rate of structural change because of complex interactions with the mechanisms of recovery and recrystallization. These softening processes can be further affected by the non-equilibrium segregation of boron to austenite grain boundaries. In fact, the influence of the boron distribution in the material and of the interactions between boron and the other alloying elements on recrystallization and precipitation remain largely unknown. An understanding of these effects is of considerable interest to metallurgists because of the commercial significance of ULCB HSLA steels. It is also useful for the rational design of controlled rolling schedules and for its fundamental importance in physical metallurgy.

One of the important factors hindering a clear understanding of the influence of boron is the absence of a sufficiently sensitive technique for determining its location. Because of its low atomic weight, classical x-ray

analysis is unable to reveal its presence. Alternative techniques must therefore be employed for the detection of boron. However, each technique has its limitations from a resolution or sensitivity point of view and several methods are required to provide information regarding the different aspects of the problem. Only limited attempts have been made in this area in the past, and few comparative results have been published.

The present research program was undertaken in this context, the main objectives of which were the following:

I) To determine how the presence of boron in a Nb steel affects the precipitation kinetics of Nb(C,N) and the recrystallization of austenite; to study in this way the interaction between recrystallization and precipitation in B-modified steels.

II) To study the influence of the rolling temperature, reduction, cooling rate and interpass time on the state of the boron distribution and to determine the effect of the latter on the softening and strengthening mechanisms.

III) If the above rolling parameters modify the boron distribution, to try to explain the origin of the changes and to isolate the key factors controlling the effectiveness of the boron effect.

IV) To employ the techniques for boron detection in order to establish the presence or absence of boron in strain induced Nb precipitates, in undissolved inclusions and in the matrix.

The present thesis is divided into the following chapters:

In Chapter II, a summary of the literature is presented. The different effects of boron addition are first described and then the precipitation of the transition metal carbides and nitrides in austenite is considered.

In Chapter III, the experimental materials and equipment are described. The methods employed for stress relaxation testing are also discussed.

The mechanical testing results are presented in Chapter IV, together with the influence of composition, deformation and temperature on precipitation-time-temperature (PTT) diagrams and on austenite recrystallization.

Chapter V contains two parts: the first illustrates the dependence of particle size and morphology on the testing conditions. In the second part, the PTA and SIMS results regarding the state of the boron distribution are presented and experimental evidence for the existence of two new sources of non-equilibrium segregation of boron is displayed. In this chapter, EELS spectra and PTA micrographs illustrating the presence of boron in strain induced precipitates are also reproduced.

In Chapter VI, the microstructural evolution during stress relaxation and the kinetics of precipitation are studied. The theory of the thermally activated motion of dislocations is employed for the interpretation of the relaxation results. The precipitation data are analyzed in terms of the classical theory of nucleation and that of diffusion controlled particle growth. Based on this analysis, the coefficients for the diffusion of Nb in austenite in the presence or absence of boron are evaluated.

Chapter VII concerns a clarification of the mechanisms of the boron effect. The accelerating influence of boron on carbonitride precipitation is interpreted in terms of a mechanism proposed in this investigation. A model is suggested to explain the synergistic effect of Nb and boron on the recrystallization and precipitation processes. A mechanism describing how boron segregation can be produced on moving austenite grain boundaries during recrystallization is suggested. Furthermore, an original semi-quantitative analysis is carried out to separate the segregation at original and newly formed boundaries.

Finally, the general conclusions of the study are summarized in Chapter VIII.

## CHAPTER II

### LITERATURE REVIEW

#### II.1. Boron in Steel

An overview of the literature of the last 80 years on the use of boron in steels shows that there is, in many ways, a parallel between the use of boron in steels and technical progress in the steel industry [1]. It was at the beginning of this century, 1907, that boron was first considered as a potential alloying agent in steels. Since then, boron has played a significant role as an alloying element in the development of heat treatable steels.

During the years that followed, various investigations took place and steels were produced with boron contents which would now be regarded as extremely high. However, in 1921, it was recognized that even such minute amounts as 10 ppm of boron were enough to produce significant effects on steel properties [2].

During the next decade and in the early 1940's, a considerable amount of work was done on the effect of alloying elements, including boron, on the hardenability of steel [3-5]. From these investigations it was concluded that boron was by far the most potent hardenability agent, a use which remains its predominant function in carbon and alloyed steels to this day. The occurrence of the second world war and the shortage of many "classical" hardenability promoters such as nickel and chromium created an incentive for the use of boron as an alternative for these strategic materials. The true commercial development of boron steels began in this way.

Although boron seemed to be a very promising alternative addition, producers were slow to make full use of these steels because of the difficulty of obtaining consistent mechanical properties, both from heat to heat and after processing into the finished product. These early problems originated from the steelmaking techniques employed. Because of its high affinity for oxygen and

nitrogen, boron combines readily with these elements to form  $B_2O_3$  and BN, respectively. It also combines with carbon to form iron borocarbide  $[Fe_{23}(C,B)_6]$  and iron borocementite  $[Fe_3(C,B)]$ , thereby losing its effectiveness unless "protected" by suitable additives [6]. Thus, the necessity was recognized of assuring full deoxidation by the addition of silicon, aluminum, and other deoxidizers prior to the addition of boron. The use as well as the addition of elements such as Ti and/or Zr, which are stronger nitride formers than boron, was also generally accepted as necessary before 1960.

The effects of interactions between boron, nitrogen, aluminum and titanium or zirconium on hardenability in low carbon low alloy steels were studied in 1968 by Kapadia and coworkers [7]. They introduced the parameter  $\beta$  which represents the "effective" ( i.e. not combined with oxygen or nitrogen) boron content.  $\beta$  is related to the nitrogen, Ti and Zr contents by the following empirical formula:

$$\beta = \{B - [(N - 0.002) - Ti/5 - Zr/15] \}$$

Their results show (see Fig. II.1) that there is a maximum in hardenability at about 10 ppm effective boron, which decreases slightly as the boron level is further increased. Other factors which influence the effective level of boron in the steel are the austenitizing times and temperatures (i.e. the grain size) and how these heat treatment variables influence the dissolution and precipitation of boron carbides and nitrides within the grains or at the grain boundaries [8].

Today, with the advent of sophisticated analytical instruments and microprocessor-based controls, there is a far better understanding of the way boron produces its beneficial effects, so that steelmakers produce consistent products on a routine basis. Reproducible properties can now be obtained with boron steels [9] so that their previous bad reputation has almost disappeared and new perspectives have been opened on the use of boron for the production of quality steels.

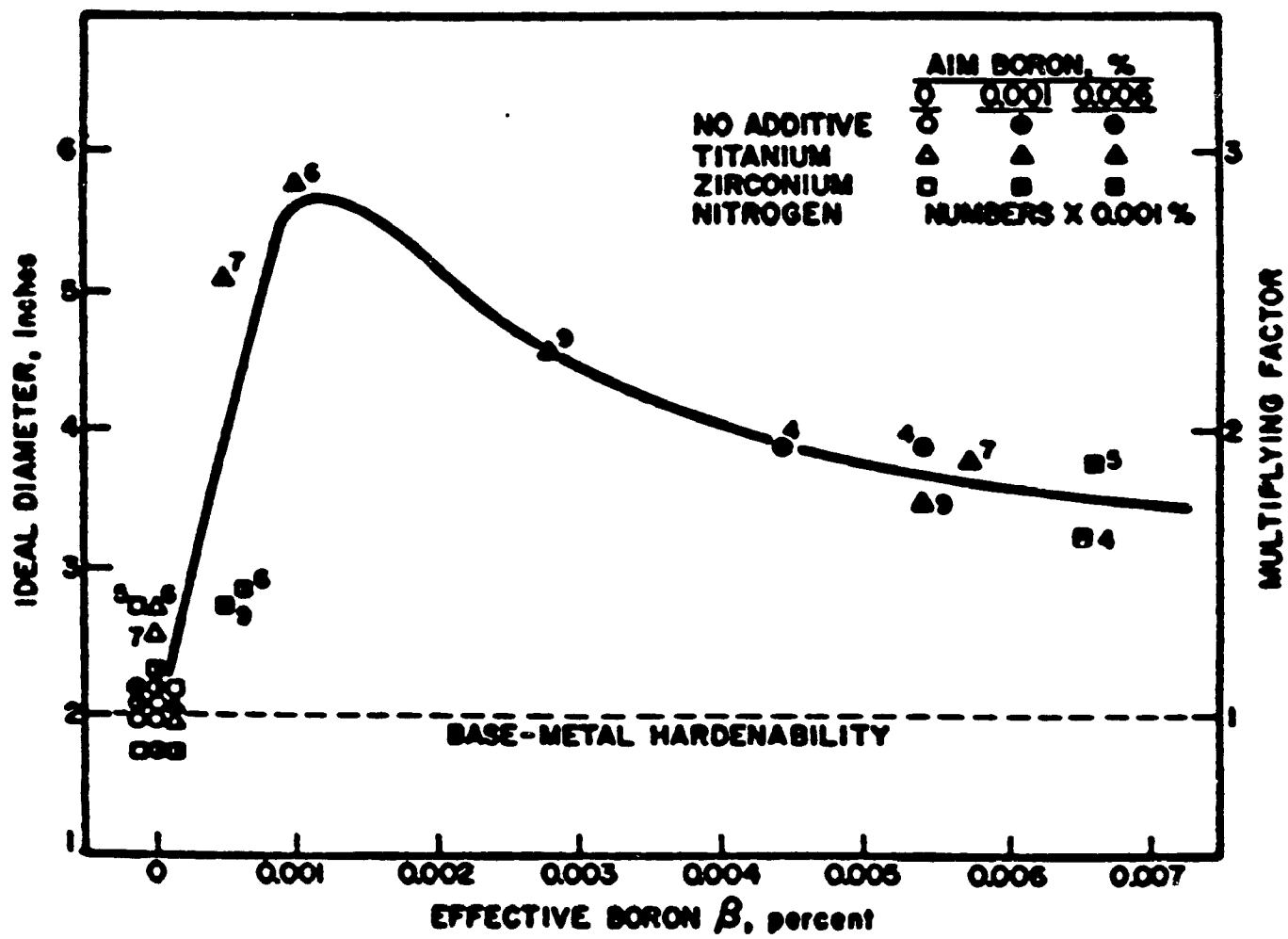


Fig.II.1 Influence of effective boron content on the hardenability of a low carbon, low alloy steel.

### II.1.1. Boron in HSLA Steels

The demand for steels with high strength, toughness and excellent welding properties for energy conversion and transportation systems has led in recent years to the development of new classes of HSLA steels. In this context, boron occupies an important place because it can replace expensive alloying elements. Control rolled boron-containing bainitic steels with a good combination of strength and toughness have recently been produced [10]. It is now established that boron has a synergistic effect with Nb and Mo in retarding the formation of polygonal ferrite [11]. It has also been reported that the excess Ti not combined with nitrogen can have a synergistic effect on hardenability with boron [12], although there is still some controversy over the existence of synergism between vanadium and boron. In order to improve notch toughness and, more importantly, to counteract the large increase in carbon equivalent derived from boron, a carbon level of less than 0.03% is recommended in boron treated bainitic steels.

During the last ten years, several ultra low carbon bainitic (ULCB) HSLA steels were developed for large diameter line pipe and put into practical use [10, 11, 13]. These steels are characterized by their excellent combination of strength, toughness and weldability, which is attained by the combined addition of niobium and boron.

In a recent work, Tamehiro et al. [14] studied the influence of the combined addition of boron and of a grain refining element such as niobium, titanium or vanadium on the mechanical properties and microstructures of ULCB steels. Fig.II.2 shows the effect of alloy addition (Nb, Ti, and V) on tensile strength (TS), Charpy impact energy ( $vE_{40}$ ) and Charpy impact transition temperature ( $vTrs$ ). It was concluded from this study that the best combination of strength and toughness is obtained from the addition of Nb, while vanadium does not have a synergistic effect with boron. Although Ti in combination with boron is very effective in improving the strength, it affects the low temperature toughness adversely.

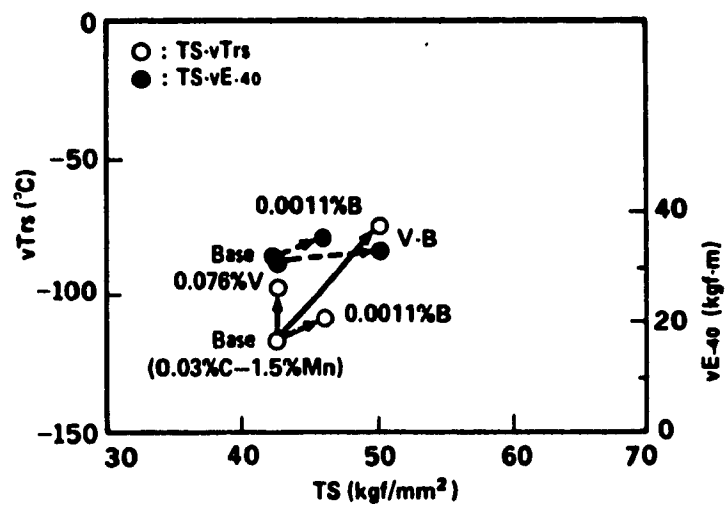
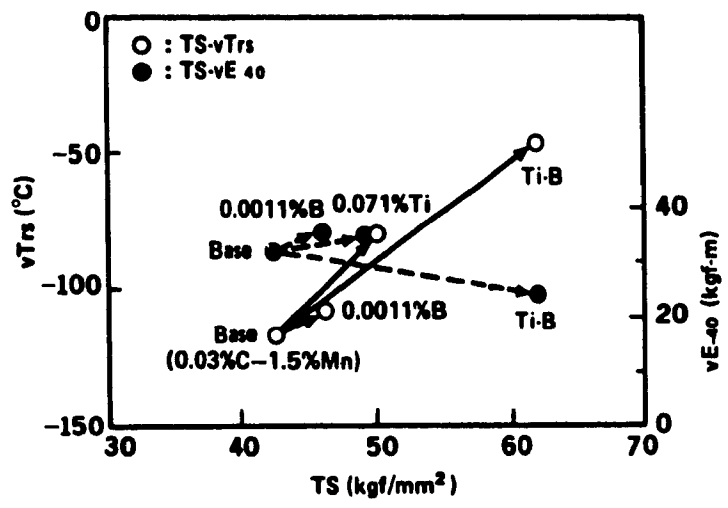
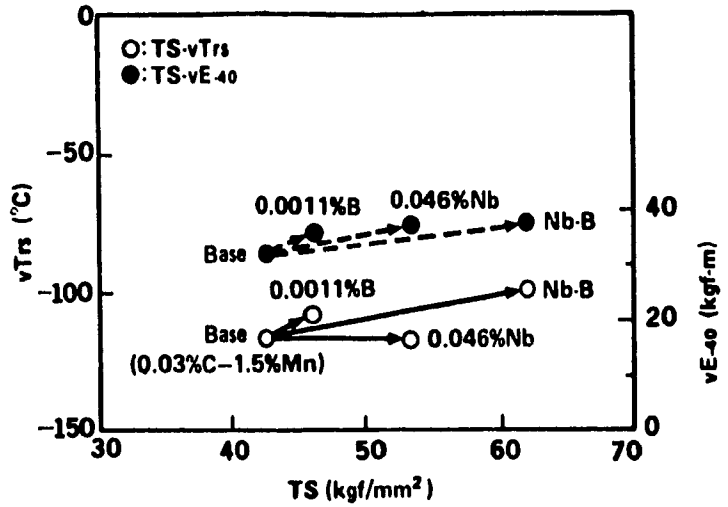


Fig.II.2 Effect of alloy addition on the mechanical properties of steel plates.

## II.2. Location of Boron in the Iron Lattice

### II.2.1. Solubility of Boron in Iron

The solubility of boron in iron has been investigated since the early days of boron steels and different values have been published for the limit in alpha and gamma iron [15]. Because of the very small quantities of boron added to the steel, the purity of the materials used to determine the solubility becomes extremely important. The solubilities reported by various workers have tended to lower levels as the purity of the materials has increased, showing that there is a strong interaction between boron and other elements, particularly interstitials, which may be present in the iron. Fig.II.3 shows the phase diagrams for the low-boron end of the iron system reported by Brown et al. [16]. It is worth noting that little information is available concerning the effect of boron on the solubility of carbon, although several authors [17, 18] have reported that, in the case of austenitic steels, the addition of boron has no effect on the solubility of carbon.

### II.2.2. Nature of Boron in Iron

As in the case of solubility determination, there is also controversy regarding whether boron forms an interstitial or a substitutional solid solution in iron. The atomic radius of boron is indeed intermediate between those associated with each mode of solution (Table II.1) and much conflicting data have been presented supporting one or the other idea.

On the nature of boron in alpha iron, x-ray measurements of the lattice parameter of alpha iron [19], diffusion experiments [20], and internal friction measurements [21] all indicate *substitutional* solid solution. On the other hand, internal friction measurements by other authors suggest an *interstitial* solid solution in alpha iron [16,22]. Some authors have also suggested on the basis of internal friction measurements that boron could be in both interstitial and substitutional positions [23].

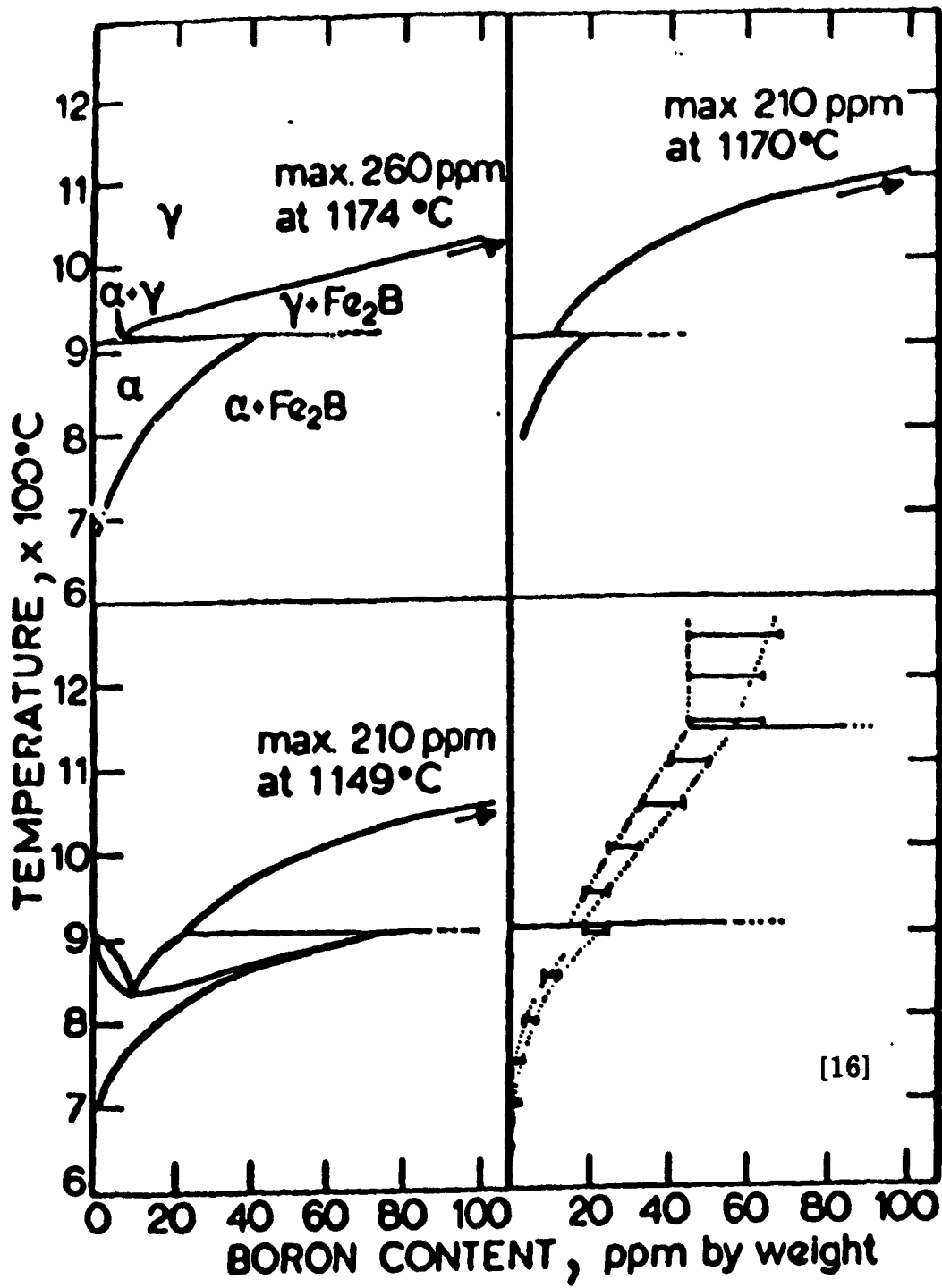


Fig.II.3 Phase diagrams of the Fe-B system.

Table II.1.

Atomic Radii of Alloying Elements in Steels

Element	N	C	B	Fe	Mn	Mo	Ti	Nb
Atomic radius Å	0.71	0.77	0.97	1.274	1.312	1.40	1.462	1.468

The location of boron atoms in the austenite lattice has also been the subject of some controversy. Diffusion data obtained by Nicholson [24] give diffusion rates and an activation energy appropriate to interstitial solubility; likewise, a pronounced discontinuity was observed by Goldhoff and Spretnak [25] in thermal expansion experiments within the austenite region, suggesting that there is a transition in the lattice position of boron atoms away from the substitutional sites with increasing temperature. In opposition to the above results, lattice spacing studies [26] have shown lattice contraction when boron is added to austenite, suggesting a substitutional location for the boron atoms.

One of the most important factors which can be responsible for such uncertainty about the location of boron atoms in the iron lattice is the lack of purity of the materials investigated, as reported by Goldschmidt [27]. The simultaneous presence of carbon as a competitive-interstitial, or of silicon as a competitive-substitutional, atom may have a profound influence on the position of the boron.

In order to explain these apparently contradictory observations, a detailed understanding of the interaction between boron atoms and other lattice defects such as vacancies, substitutional and interstitial solute atoms, dislocations and grain boundaries is absolutely necessary. Minor changes in heat treatment conditions and specimen deformation histories which can modify the defect concentrations can then influence the experimental measurement of physical parameters related to the siting of the boron atoms. As a matter of fact, this seems to be the case, indicating that there is a significant interaction between boron atoms and lattice defects such as dislocations, vacancies and grain boundaries.

### II.3. Non-equilibrium Grain Boundary Segregation of Boron

A large body of evidence (for example, the case of boron in steel, S in Ni, phosphorus in the intergranular embrittlement of steels, etc.) has gradually been built up to show that the effects caused by these very small amounts of impurities are often associated with the segregation of the impurity atoms to free surfaces, grain boundaries and other interfaces or regions of structural discontinuity, such as particle / matrix interfaces and dislocations. As a result of this segregation, much higher local concentrations of solute atoms are found at these sites.

#### II.3.1. Description of the Phenomenon

Two types of segregation will now be discussed: equilibrium and non-equilibrium segregation. The phenomenon of the equilibrium segregation of dilute solutes to interfaces in solids has been described by McLean [28]. Since then, several authors have periodically reviewed the latest developments regarding the understanding of the phenomenon and the techniques used to study such segregation [11, 29]. Because of large size differences between boron and the matrix atoms (Fe, Ti, Ni, Mo, Mn), the elastic binding energy to dislocations and grain boundaries is quite strong, as shown by Table II.2. The driving force for this kind of segregation is then the minimization of the surface free energy which is produced by the segregation of solute atoms to these sites.

The non-equilibrium segregation of boron to interfaces was first noted by Westbrook [29], who detected a hardness increase at grain boundaries in a number of quenched, dilute non-ferrous alloys. He associated this increase with atomic segregation at grain boundaries produced during cooling. Non-equilibrium segregation was also observed in boron steels using boron particle tracking autoradiography (PTA) [30-33], secondary ion mass spectroscopy (SIMS) [34, 35] and a combination of transmission electron microscopy (TEM), field ion microscopy (FIM), atom probe microanalysis (AP) and imaging atom probe microanalysis (IAP) techniques. Karlsson and Nordén [36] have used these methods to study this phenomenon in some austenitic stainless steels. Table II.3 summarizes the two main characteristics which can in principle be used to distinguish non-equilibrium segregation from the equilibrium one.

**Table II.2.**  
**Binding Energies Between Boron Atoms and**  
**Lattice Defects**

Nature of the defect	Binding Energy	
	KJ/mol	eV
Grain boundaries	40.2	0.42
	55.3	0.57
Dislocations	≈58	≈0.6
Vacancies	48.3	0.5

It should also be mentioned that equilibrium segregation occurs when a material is held at temperatures sufficiently high to permit the appreciable diffusion of impurities. Non-equilibrium segregation, on the other hand, is produced during cooling and generally during any physical process which can produce an excess vacancy concentration (like irradiation [37], sintering [38], etc.).

**Table II.3.**  
**Characterization of Each Kind of Segregation**

Equilibrium Segregation	Non-equilibrium Segregation
Segregation decreases when the temperature increases	Segregation increases when the temperature increases
The lowest energy state corresponds to the equilibrium segregation one	The lowest energy state corresponds to uniform solute distribution (at high temperatures)

### II.3.2. Mechanism and Kinetics of Non-equilibrium Segregation

The theoretical bases of non-equilibrium segregation were first established by Aust et al. [39] and by Anthony [40]. The mechanisms proposed

for non-equilibrium segregation originate from the postulate that mobile vacancies and impurities can form complexes, as reported by Bercovici et al. [41]. The equilibrium which should exist between the three species (vacancies, isolated impurities and complexes) during cooling and the fact that vacancies are annihilated at dislocations, grain boundaries and interfaces will lead to the segregation of solute atoms to these sites. After holding at a given temperature (say the solution treatment temperature), the bulk concentrations of the vacancies [V], boron atoms [B] and complexes [C] are uniform, and the thermodynamic equilibrium can be written as

$$[V] + [B] = [C] \quad (\text{II.1})$$

During cooling, a supersaturation of vacancies and boron atoms is produced, but near the grain boundaries, the supersaturation with respect to vacancies is rapidly reduced by their migration to the boundaries. In order to maintain the equilibrium given by relation (II.1), the complex concentration should decrease; complexes also migrate to the grain boundaries and consequently the boron concentration should increase at these places. Simultaneously, far from the grain boundary zone, where vacancies cannot be annihilated, the cooling induced supersaturation of vacancies should move reaction (II.1) to the right, leading to an increase in the concentration of the complexes. The concentration gradient then induces diffusion of the vacancy-boron complexes to the grain boundary zone and thus maintains a high concentration of boron atoms in these regions which would otherwise tend to be reduced by back diffusion.

Williams et al. [42] applied this concept to the case of the non-equilibrium segregation of boron to austenite grain boundaries in solution treated 316 steels. In their analysis, they assume that for the above mechanism to be operative during cooling, the mobility of complexes must be higher than that of individual vacancies and boron atoms. In keeping with this view, they assumed that the diffusivity of the boron-vacancy complexes is about 70 times faster than that of the boron atoms and also much higher than that of the vacancies on their own. Based on experimental findings such those reported by Williams et al. [42], it has also been suggested [43] that boron is brought to the boundaries in the form

of boron-divacancies or monovacancies at temperatures higher or lower than 1000°C, respectively.

The kinetics of the non-equilibrium segregation process have been studied by several authors, and both experimental and theoretical approaches have been used. For the case of boron segregation, the experimental studies have been focused mainly on stainless steels [42, 44] and on low alloy steels [32, 45]. The differences in composition, heat treatment and cooling rate render it difficult to make comparisons between the different results. Nevertheless, relations have been proposed to predict the developing rate of non-equilibrium segregation [42, 46]. Computer modeling and numerical analysis methods have also been employed by several authors [47-49]. Figure II.4 illustrates the calculated segregation profiles, in austenite with 206 at. ppm boron after cooling at 1000, 100, 10 and 1°C, obtained by Karlsson [49].

Each of the above methods has its advantages and disadvantages. For example, the model developed by Chapman and Faulkner [48] is better suited for locations within a few nm of the boundary, while the approach used by Karlsson [49] is most suitable for the simulation of long range segregation profiles, with a resolution of a few hundred nm.

Two major difficulties arise when trying to make quantitative predictions of the segregation. The most important one involves obtaining a realistic estimate of the binding energy of the complexes. The other difficult parameters are the diffusivities of the boron and vacancy complexes. Table II.4 shows some of the values for these constants used in the literature to obtain the segregation profiles.

## **II.4. Influence of Boron on the Precipitation Process**

### **II.4.1. Types of Boron Compounds**

The existence and presence of many transition metal borides and borocarbides have been reported [50], and Goldschmidt [51] has surveyed their crystallographic and thermodynamic characteristics extensively. It has also

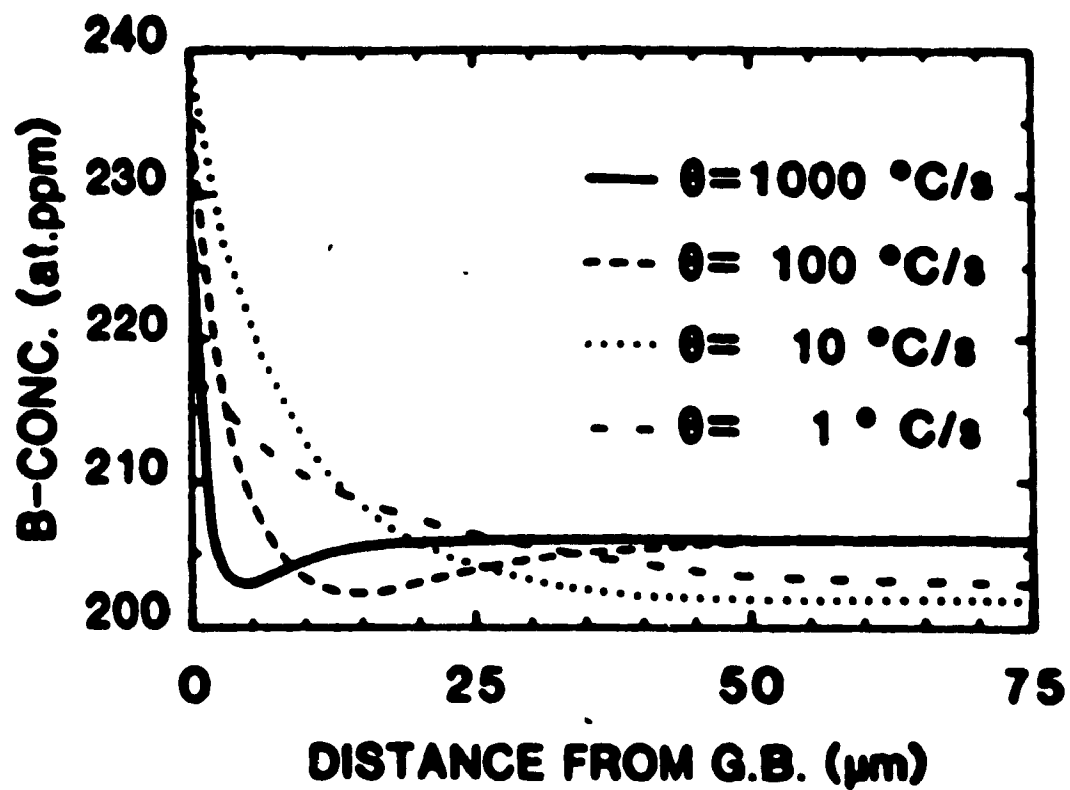


Fig.V. Effect of cooling rate on calculated segregation profiles.

Table II.4.

Data Used in Theoretical Calculations

$E_f^V$ eV	$E_f^{V-B}$ eV	$D^B = D_0^B \exp(-Q_B/kT)$		$D^V = D_0^V \exp(-Q_V/kT)$		$D^C = D_0^C \exp(-Q_C/kT)$		Reference
		$D_0^B$ m <sup>2</sup> /sec	$Q_B$ eV	$D_0^V$ m <sup>2</sup> /sec	$Q_V$ eV	$D_0^C$ m <sup>2</sup> /sec	$Q_C$ eV	
1.4	0.5	2 10 <sup>-5</sup>	0.91	0.5	2.7	0.5	0.91	[42]
1.4	0.5	2 10 <sup>-7</sup>	0.91	5 10 <sup>-5</sup>	0.91	0.5	-	[47]
1.4	0.5	-	1.4	-	1.6	-	-	[48]
1.4	0.5	1.9 10 <sup>-5</sup>	1.7	1.4 10 <sup>-5</sup>	1.4	1.9 10 <sup>-4</sup>	1.7	[49]
1.4	0.5	1.9 10 <sup>-5</sup>	1.61	1.4 10 <sup>-5</sup>	1.4	1.9 10 <sup>-4</sup>	1.61	[49]
1.4	0.5	2 10 <sup>-6</sup>	1.15	1.4 10 <sup>-5</sup>	1.4	2 10 <sup>-7</sup>	1.15	[49]
1.4	0.5	2 10 <sup>-7</sup>	0.91	1.4 10 <sup>-5</sup>	1.4	1.4 10 <sup>-5</sup>	0.91	[49]
1.4	0.5	2 10 <sup>-7</sup>	1.15	1.4 10 <sup>-5</sup>	1.4	2 10 <sup>-6</sup>	1.15	[49]

been shown [51] that boride structure and stoichiometry are principally controlled by the size of boron atoms, which is the largest among the most common interstitials (see Table II.1), rather than by valency considerations. The small size of boron atoms makes possible the formation of B-B bonds, which control the crystal structure of the boride phase. In Table II.5, the metallic borides occurring in steels are classified according to their types and structures. This table also includes some of the borocarbides.

Although, as shown by Table II.5, a large number of borides have been identified, only a few of them ( $\text{Fe}_2\text{B}$ ,  $\text{M}_{23}(\text{C},\text{B})_6$ ,  $\text{M}_3\text{B}_2$  and  $\text{Fe}_3(\text{B},\text{C})$ ) have been reliably detected and reported in alloy steels. Among these borides and borocarbides,  $\text{M}_{23}(\text{C},\text{B})_6$  (also known as the "boron constituent") has been investigated the most. It was first identified by Carol et al. [52] by x-ray diffraction and since then, many investigations have been carried out to determine the influence of these precipitates on the effect of boron on hardenability, phase transformations, creep properties, etc. [34, 53, 54]. It has also been reported [55] that the metallic element in  $\text{M}_{23}(\text{C},\text{B})_6$  can be iron, with extensive replacement by chromium, molybdenum and manganese, and that carbon and boron can replace each other to a considerable extent.

Both  $\text{M}_2\text{B}$  and  $\text{M}_3\text{B}_2$  precipitates have been identified in 12% Cr-Mo-V steels and austenitic steels; these alloys contained large amounts of boron (about 400 ppm) in the case of the  $\text{M}_2\text{B}$  precipitates and more than 40 ppm in the case of the  $\text{M}_3\text{B}_2$  compounds [56]. Although it is accepted [51] that boron can replace carbon or nitrogen in the carbides or carbonitrides commonly occurring in steels (i.e. in the  $\text{M}(\text{C},\text{N})$  compounds, where M can be Ti, Nb, V, Mo... ) there are few detailed reports available in the literature. The only evidence reported is that of Keown and Pickering [56], in which case the material was a 5000 kg ingot of a complex stainless steel cooled very slowly and having an as-cast structure of austenite dendrites with an inter-dendritic eutectic of austenite-NbC. Henry et al. [57] reported that the presence of boron has little or no effect on the solubility of titanium carbide in an 18Cr-10Ni stainless steel containing titanium. A similar conclusion was reached by Deighton [17] concerning the effect of boron on the solubility of NbC in a 20Cr-25Ni stainless steel. However, it has been found [58] that the soluble boron content  $B_s$  [acid soluble

**Table II.5.**  
**Classification of Borides and Boro-Carbides**

Boride Type and Structure	Boride Composition					
	Fe	Mn	Ti	Mo	Nb	V
M <sub>4</sub> B orthorhombic	Fe <sub>23</sub> (C,B) <sub>6</sub> *	Mn <sub>4</sub> B				
M <sub>3</sub> B orthorhombic	Fe <sub>3</sub> (C,B)					
M <sub>2</sub> B tetragonal	Fe <sub>2</sub> B	Mn <sub>2</sub> B	Ti <sub>2</sub> B	Mo <sub>2</sub> B		
M <sub>3</sub> B <sub>2</sub> tetragonal	Fe <sub>3</sub> B <sub>2</sub>			Mo <sub>3</sub> B <sub>2</sub>	Nb <sub>3</sub> B <sub>2</sub>	V <sub>3</sub> B <sub>2</sub>
MB orthorhombic	FeB	MnB	TiB	MoB	NbB	VB
M <sub>3</sub> B <sub>4</sub> orthorhombic	FeMo <sub>2</sub> B <sub>4</sub>	Mn <sub>3</sub> B <sub>4</sub>		FeMo <sub>2</sub> B <sub>4</sub>	Nb <sub>3</sub> B <sub>4</sub>	V <sub>3</sub> B <sub>4</sub>
MB <sub>2</sub> hexagonal		MnB <sub>2</sub>	TiB <sub>2</sub>	MoB <sub>2</sub>	NbB <sub>2</sub>	VB <sub>2</sub>
M <sub>2</sub> B <sub>5</sub> hexagonal			Ti <sub>2</sub> B <sub>5</sub>	Mo <sub>2</sub> B <sub>5</sub>		

\* Cubic

concentration of boron] of the steel controls the temperature of complete redissolution in austenite. This temperature increases as a function of  $B_s$ .

#### II.4.2. Influence of Boron on Precipitation Kinetics and on Particle Size and Distribution

A survey of the literature regarding the effect of boron on precipitate morphology, size distribution and spatial arrangement indicates that evidence for the effect of boron is based on qualitative observations by optical or electron microscopy and that there is a general lack of systematic studies in this field. Such a need can be illustrated by the work of Henry et al. [59] in which it is shown that the spatial density, morphology and size distribution of the  $M_{23}(C,B)_6$  grain boundary precipitates vary markedly from one grain boundary to another because of the changes in their structure as a function of the misorientation between adjacent grains.

The presence of boron affects the precipitation behaviour of  $M_{23}C_6$  compounds in several ways. An enhancement of intracrystalline  $M_{23}C_6$  precipitation has been observed in the presence of boron both in austenitic stainless steels [44, 60] and in molybdenum steels [61]. The amount of  $M_{23}(C,B)_6$  precipitation has also been found to increase with the boron content of the steel [61]. Other authors [62, 63] have also reported a precipitate refining effect of boron addition in quenched and aged samples. Henry and Philibert [62] reported that in boron-doped 316 grade stainless steel, the grain boundary and matrix  $M_{23}(C,B)_6$  precipitates are finer than in boron-free steel. This effect is more marked in quenched and aged samples than in step-quenched specimens and cold working prior to aging or annealing after quenching enhances markedly the density of the intracrystalline precipitates. The nucleation sites of these precipitates were identified by transmission electron microscopy as the dislocations introduced by quenching stresses or by cold working prior to aging. However, Davidson et al. [60] observed that these precipitates nucleated not only on dislocations but also on unidentified sites in the matrix away from dislocations and that precipitate-free zones occurred near the grain boundaries. Some authors [58, 64] have also reported that boron postpones the appearance of the sigma phase, which has a deleterious effect on the creep rupture properties

of austenitic stainless steels, by promoting the formation of  $M_{23}(C,B)_6$  precipitates.

The effect of boron on precipitation in stabilized stainless steels and in low alloy steels containing Ti and/or Nb has been studied by several authors [14, 16, 57, 64, 65]. Also, it was found [57, 64] that both  $M_{23}C_6$  and TiC are present at the grain boundaries in quenched and aged stainless steels and that the surface density of precipitates is much higher in the boron containing steels. Only limited data are available regarding the effect of boron on the formation of other kinds of precipitates. According to Burgeot et al. [64], the principal effect of boron in stabilized stainless steels is to provoke matrix precipitation more or less simultaneously with the heterogeneous nucleation of precipitates on dislocations. Harris and Robert [66] report that boron promotes  $M_{23}C_6$  precipitation at the expense of NbC in 18-10 niobium-stabilized stainless steel, while in a recent paper, Tamehiro et al. [14] indicate that the presence of boron suppresses the formation of  $Fe_{23}(C,B)_6$  precipitates in a very low carbon HSLA steel containing Nb and Ti or only Ti. This inhibition is associated with the presence of strain-induced NbC or TiC, which could limit the supply of carbon required for the precipitation of  $Fe_{23}(C,B)_6$ .

On the basis of the published literature and of the review which has been carried out here, it can be said that the effect of boron addition on transformation and hardenability has been reasonably well clarified. Nevertheless, its influence on the precipitation process remains obscure. The boron-vacancy interaction seems to be one of the cornerstone mechanisms associated with the effect of boron. This is probably why the influence of boron on the precipitation process depends so much on the parameters of the heat treatment and on the nature of the dislocation configurations induced by quenching or deformation.

## II.5. Influence of Boron on Mechanical Properties

As mentioned at the beginning of this chapter, the effects of boron addition have long been recognized as very important, mainly with respect to hardenability of the heat treatable steels. In addition, the use of boron presents other advantages, such as better hot workability and improved creep resistance

and formability. It can also induce some deleterious consequences, such as temper embrittlement. In what follows, we will describe some of these by-products of boron addition.

### II.5.1. Hardenability

This is the most striking and well known effect of boron; it has been studied extensively and the way in which it plays its role has been clarified. The influence of parameters such as the boron concentration, austenitizing conditions, carbon content, alloying elements present and the method of boron protection on the action of boron on the hardenability have been studied by several workers [5-7, 11, 12]. However, because of the erratic behaviour of boron steels, much conflicting data exist, as shown by [67, 68]. Similarly the hardenability mechanisms which have been proposed to explain these observations are only capable of accounting for part of the evidence reported. Among the mechanisms proposed, only four have been retained; their common point is that they all assume that boron influences hardenability by retarding ferrite nucleation and that because of its low concentration, it does not influence the thermodynamic properties of the bulk austenite or ferrite phase [69]. It is well known that ferrite generally nucleates at gamma grain boundaries; as a result, all the mechanisms are concerned with the changes which can occur in these regions. The four most likely mechanisms are described briefly below.

#### a) Reduction in austenite grain boundary energy

In this case, it is assumed that boron reduces the energy of austenite grain boundaries by diffusing there and then retards ferrite nucleation. However, Sharma and Purdy [70] have reported that the reduction in energy is less than 1% and is therefore insignificant. Morral and Cameron [71] have concluded that the magnitude of the effect depends on the *shape* of the ferrite nucleus and that, under proper conditions, the grain boundary energy can be considerably reduced. As it has not yet been possible to determine the shape of the ferrite nucleus, this mechanism, which is one of the earliest proposed, remains a possible one.

#### b) Reduction in diffusivity

It was reported [72] that boron decreases the self diffusivity of iron at austenite grain boundaries, and possibly the carbon diffusivity, by blocking interstitial sites or by increasing the modulus of the boundary. However, these possibilities have not yet been verified experimentally.

#### c) Reduction in the number of sites

In high angle grain boundaries, there are always regions of low atom density which are favored sites for the nucleation of ferrite. If boron fills up these sites partially or totally (by segregation or through precipitation as borocarbides) the nucleation rate of ferrite will be reduced.

#### d) Nucleation of ferrite on borocarbides

It is now well known that borocarbides stop ferrite formation when they are very small and encourage ferrite nucleation on their incoherent faces when they are sufficiently large [69]. Although the defenders of the three previous theories can interpret these results on the bases of their favored mechanisms, it should be mentioned that the observation of early borocarbide formation does not distinguish between the mechanisms already proposed. This means that what finally determines boron hardenability is not the reduction in ferrite nucleation rate but rather the rate of nucleation and growth of the borocarbides which control ferrite nucleation.

### II.5.2. Hot Workability

Grange [5] has reported that most common alloying elements strengthen the austenite phase at hot working temperatures and thereby decrease the workability. Conversely, if they are replaced by boron, the hot workability is improved. This beneficial effect of boron was observed in a wide range of stainless steels [44], but is only important over a limited range of temperatures (from 1050°C to 1200°C). The mechanism of this effect has not yet been elucidated, but metallographic examination [44] indicates:

- 1) a marked decrease in intergranular cavitation associated with the temperatures at which boron is in solution and is no longer trapped in the form of borocarbides;
- 2) a fully recrystallized material in the highly deformable zones.

The decrease in the beneficial effect of boron above some critical temperature is associated with the formation of a low melting point eutectic  $M_2(B,C)$  at the grain boundaries and the incipient melting of the adjacent boron-saturated metal [5]. This clearly indicates that, as the boron content increases, the melting point of the steel decreases. These facts suggest that the following precautions should be taken to avoid hot shortness: i) the boron concentration should be maintained within the optimum range; and ii) high temperatures and excessively long soaking times should be avoided.

### II.5.3. Creep Rupture Life

It is well known that boron improves the creep rupture life of stainless steels [44, 73]. The addition of 50 ppm boron leads to an increase in the mean stress rupture life by a factor of about 3 or an increase in stress to failure in 10,000 hours of up to 25% [44]. These effects appear to be strongly composition dependent because the effect is clearly present in the stabilized grades, while it is virtually absent in grades containing no Mo, Ti or Nb [74]. As reported by Williams [75], the beneficial effects of boron on creep behaviour have to be explained in terms of its effect on the precipitates which form during testing or prior aging, and also in terms of the influence of precipitation on grain boundary sliding and cavitation.

### II.5.4. Temper Embrittlement

It is generally believed that boron increases the susceptibility to temper embrittlement, which is the loss of as-tempered ductility in a specific tempering range or after slow cooling through it. However, close examination shows that this is only true in some cases and that the opposite applies under other conditions.

For example, it is known that molybdenum has a beneficial effect on temper embrittlement while chromium has the opposite effect. If molybdenum is replaced by boron as the hardenability agent in a given steel, there will be a higher sensitivity to temper embrittlement. If boron replaces chromium, the opposite will be observed. It has also been reported [5, 76] that if a steel is already susceptible without any boron and there is no change in composition other than that boron has been added, there will be an increase in susceptibility.

Finally, it should be mentioned that boron is also used in and influences the mechanical properties of non-aging steels [77], castings [78], superalloys [79] and amorphous materials [80]. This is very interesting, but will not be described here due to space limitations.

## **II.6. Experimental Techniques for Boron Detection**

As mentioned in the earlier sections, the absence of a sufficiently sensitive technique which can provide the chemistry and structure of precipitated second phases or identify segregated boron atoms at interfaces is responsible for the existing uncertainties about the mechanisms responsible for the different effects of boron. Each of the techniques available presents some advantages and disadvantages, not only from the detection and resolution point of view, but also with respect to the cost and complexity of the equipment and the level of technical assistance required.

In what follows, we will describe briefly the most common techniques used to detect boron. The comparison will be based on the following parameters: detection limit, lateral resolution, depth resolution and whether it is destructive or not. These techniques are compared in Table II.6 as a function of the four parameters cited above.

### **II.6.1. Wet Chemical Analysis**

The total boron content of a steel can be found by emission spectroscopy, mass spectrography and wet chemical techniques. Wet chemical analysis has the advantage of being able to measure boron levels in solid solution and in the

Table II.6.

Comparison Between Different Boron Detection Techniques

	Destructive	Detection Limit ppm	Lateral Resolution $\mu\text{m}$	Depth Resolution $\mu\text{m}$
Wet Chemical Analysis	Yes	<1	>1000	>1000
Particle Tracking Autoradiography	No	<1	1-2	1
Secondary Ion Mass Spectroscopy	Yes	$\approx 10$	$\approx 1$	$5 \cdot 10^{-3}$
Imaging Atom Probe	Yes	$\approx 50$	$10^{-4}$	$10^{-4}$
Auger Electron Spectroscopy	No	$\approx 75$	1	$10^{-3}$
Electron Energy Loss Spectroscopy	No	$\approx 200$	$10^{-2}$	$10^{-2}$
Electron Microprobe Analysis	No	200-300	1	1
Atom Probe	Yes	$\approx 500$	$10^{-4}$	$10^{-4}$

form of insoluble precipitates. However, precise determination of the insoluble precipitate level is difficult due to the fact that some very fine insoluble particles can pass through the filters during the filtration operation. Conversely, some boronitrides may partially dissolve in acid solutions. These two unfavorable effects lead to the misleadingly high results observed in wet chemical analysis. Kawamura et al. [81] reviewed several wet chemical techniques and concluded that the best approach for finding the soluble boron content is to find the total and insoluble boron levels and then take the difference. They also proposed an electrolytic dissolution process in order to overcome the problems encountered in analyzing the insoluble portion.

### II.6.2. Atom Probe Field Ion Microscopy (FIM) and Imaging Atom Probe (IAP)

The field ion microscope was first developed by Müller [82] and involves the application of a high voltage (more than  $10^8$  V/cm) to a surface held in an atmosphere of inert gas. The ionized gas travels in linear radial paths to form an image which can have a resolution of approximately  $2.5 \text{ \AA}$ , making it possible to identify individual atoms, lattice imperfections such as vacancies and interstitials, voids caused by irradiation damage and dislocations. The unique capability of FIM to evaporate surface atoms in succession makes this technique suitable for study of the fine scale segregation of boron. It has recently been employed for this purpose by Karlsson and Nordén in austenitic stainless steels [36].

Although the atom probe FIM is unique in providing the ultimate in spatial resolution combined with elemental and sometimes molecular analysis, its instrumental complexity has made it rather unpopular. For example, spurious signals from the imaging gas required to monitor the location of the probe hole in the microstructure can decrease the detection limit by a factor of 100 [83] and field curvature effects may deflect atoms emitted from grain boundaries away from the probe hole. The difficult preparation of specimens of practical materials for surface analysis and the insurmountable difficulties often encountered in preparing tips that contain grain boundary precipitates add to the complexity of this technique. However, as mentioned earlier, FIM is the only method available for the study of defects at grain boundaries.

Some of the difficulties encountered in the FIM technique can be eliminated by using the imaging atom probe (IAP). Here the small probe hole and the mass spectrometer of the FIM are replaced by a time gated channel such that only desorbed atoms with a pre-selected mass/charge ratio are imaged.

### II.6.3. Auger Electron Spectroscopy (AES)

Although the energy of the emitted auger electron is a characteristic of the target material, some predictable shifts in this energy for the signal transition  $(k,l,l)$  produced in boron atoms occur due to valence or chemical effects [84]. The detection limit of the AES technique for boron in iron does not seem to be available, but it has been reported [85] that the bulk detectability limit for boron in silicon is about 75 ppm, although typical detection limits for AES are much higher.

The most common technique used to study boron in iron is the in situ fracturing of embrittled samples along grain boundaries. In this way, the relation between grain growth and segregation level and the distinction between soluble boron and precipitated boron [84] has been obtained. However, the in situ fracturing technique is limited to the family of brittle materials and this constitutes an important limitation. It prevents the study of materials of great interest, which are often ductile and undergo the austenite transformation.

### II.6.4. Electron Microprobe Analysis (EMA)

EMA is similar to AES in that a beam of high voltage is used which ionizes the inner shell, but in this case an x-ray spectrometer is employed. The x-rays generated in this way are referred to as the fluorescent yield and are highly sensitive to the atomic number and the inner shell  $(k,l,m)$  where the ionization occurs. However, it has been reported [86] that this technique gives poor results for elements with an atomic number less than 12. Hence, B, N, and O are not easily detected by the electron microprobe. On the other hand the minimum detectable diameter of precipitates is of the order of 0.5-1  $\mu\text{m}$ , although the effective analysis depth for boron is no more than 0.1 to 0.5  $\mu\text{m}$  because of the high absorption of iron. Because of all the above factors, the

minimum detectable amount of boron is about 200-300 ppm, which is of course too high for the usual levels of boron present in steels. Although EMA has many limitations, it can be very useful in a multi-faceted approach such as the study of inclusions, in which a combination of boron autoradiography and x-ray mapping can be used.

#### II.6.5. Transmission Electron Microscopy (TEM)

The TEM technique is very well known and provides morphological and crystallographic information with a spatial resolution of less than 5 nm. This high spatial resolution, which can be used to obtain quantitative data, is obtained by using the scanning transmission electron microscope (STEM); however, as in the case of EMA, the limitation with regard to light element analysis exists. In order to overcome this problem, thin foils which produce a higher signal to noise ratio over the EMA method have been used. But even with this modification, it is not possible to detect boron at its conventional levels.

The high boron concentrations which exist at grain boundaries or precipitates can be detected by using electron energy loss spectroscopy (EELS). In this technique, the most useful spectra result from elements of *low* atomic number which undergo k or l shell excitations, making possible the detection of boron. However, relatively high background noise levels and thickness limitations lower the detection limit to more than 200 ppm.

#### II.6.6. Secondary Ion Mass Spectroscopy (SIMS)

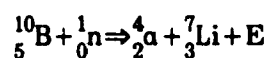
When an energetic beam of ions (generally oxygen, cesium, argon or nitrogen) hits the flat surface of a polished sample, atoms and molecules in neutral or charged states are produced. SIMS involves the measurement of the mass/charge ratio, by a mass spectrometer, of the ejected secondary positive and negative ions. Because of the high detection sensitivity of mass spectrometers for ions, the technique is a sensitive tool for surface analysis and its detection capabilities are generally several orders of magnitude higher than that of AES. The depth of analysis depends primarily upon the sputtered depth during the time of analysis. It typically varies between 5 to 50 Å, depending upon the beam

size and the raster gating parameters, energy of primary ions and ion detection sensitivities [82]. Detection sensitivities of 5 ppm and even 47 ppb in Si have been reported by some authors [71, 87], but values between less than 10 and 20 ppm have been quoted as detection limits for boron in steels [88].

SIMS has proven to be an excellent technique for detecting of isotopes and light elements (including hydrogen) and for providing molecular information. But the destructive nature inherent in the technique is a considerable disadvantage in many applications. As a result of the complexities encountered in secondary ion production, quantification of the data is difficult unless sufficient standardization procedures and precautions are exercised [82].

### II.6.7. Particle Tracking Autoradiography (PTA)

The PTA technique, based on the reaction of a fissionable isotope, is commonly applied to study segregation or diffusion. The first application of this technique to boron identification and location in metals was reported by M.Hillert in 1951 [89]. The method can be described briefly as follows: when a sample containing boron undergoes neutron irradiation, the isotope  $^{10}\text{B}$ , which is always present in natural boron, takes part in a fission reaction. Neutrons are captured and alpha particles are emitted from boron nuclei according to the following reaction:



The energy is dissipated as kinetic energy of the products. By irradiating a boron-containing sample in contact with a photographic emulsion and subsequently developing this emulsion, alpha particle tracks are revealed, whose locations correspond to the locations of boron rich areas in the sample. Over the past 20 years, several attempts have been made to improve different aspects of this technique. Thompson improved the detection limit from 100 ppm to 50 ppm [90] and later on, Hughes and Rogers [91], by using a cellulose acetobutyrate film, were able to improve the detection limit to as low as 1 ppm and obtain a lateral resolution of 2  $\mu\text{m}$ . As it will be shown in the forthcoming

chapters, further improvements in resolution can be obtained by using a double gluing method.

Although the PTA technique is very useful in detecting very low concentrations of boron, its prime limitation is that small boron precipitates cannot be detected. According to Cameron [92], the smallest detectable precipitate at the surface of a sample has a diameter of at least 0.4  $\mu\text{m}$ . In fact, the fundamental question is not the size of the precipitate but rather the adjustment of the neutron dose used (i.e. the track density produced on the autoradiograph) and the boron content of the sample. For a given track density, the proportion of boron atoms undergoing fission is inversely proportional to the boron content, so that the critical volume of an "undetectable" precipitate increases with the apparent "soluble" boron content. Brown et al. [16] reported that for a track density of  $10^7/\text{cm}^2$  employed on a specimen with a uniformly distributed boron content of 70 ppm, the smallest detectable  $\text{Fe}_2\text{B}$  precipitate in a pure iron sample had a diameter of about 2500  $\text{\AA}$ . It seems then that the best chance of detecting precipitates is in samples with high supersaturations of boron, which tend to produce large precipitates. It is also clear that with the PTA technique, it is not possible to distinguish between "soluble" boron atoms and boron atoms segregated to dislocations. Such autoradiography is most often employed qualitatively to illustrate the presence or absence of boron. Some authors have also attempted to carry out quantitative analysis [46, 93], measuring the boron concentration at and in the neighbourhood of the grain boundary, by adjusting the neutron irradiation flux. Brown et al. [16] have even been able to deduce the Fe-B phase diagram by measuring soluble boron levels in the interior of the grains.

The simplicity and capabilities of this technique are striking when compared to the complexities of techniques such as SIMS or AES. However, with this technique, it is only possible to detect boron and so it must be combined with other methods if further information is required on the effect of boron in multicomponent systems.

It seems clear from this review that, although many techniques exist for studying the effects of boron, none of them is able to answer all questions alone. Each of them possesses some advantages and is suitable for the study of one or a

few aspects of the problem. Table II.7 summarizes the advantages and disadvantages of each technique. Finally, it is worth noting that in this review we voluntarily limited ourselves to the application of these techniques to the presence of boron, with little attention paid to a description of the methods themselves. Excellent reviews which provide such details can be found in the papers by Joshi [94], Hondros and Seah [95] and Cameron and Morral [92].

## **II.7. Precipitation Behaviour in Hot Worked HSLA Steels**

The development of new HSLA steels with high strength and toughness and having excellent weldability properties was made possible by searching for optimum microalloying combinations and introducing techniques such as accelerated cooling, and controlled rolling. In this context, it is important to understand the strengthening and softening processes occurring during and after high temperature deformation, such as recovery, recrystallization and precipitation. The influence of the various microalloying elements on these phenomena is also relevant, as is their mutual interaction. In what follows, some aspects of the precipitation behaviour in austenite of carbides and nitrides of the most commonly used microalloying elements (i.e Ti, Nb, and V) will be examined.

### **II.7.1. Type and Kinds of Precipitates**

Nb and V belong to transition element group V and Ti to group IV; this leads to closely related electronic structure, size and electronegativity properties. The carbides and nitrides of the microalloying elements appear in a wide range of sizes that depend on the chemical composition of the steel, the nature of the compound (carbide, nitride or sulfide), and the formation temperature. This range extends from the coarse inclusions which precipitate in liquid steel or in the early stages of solidification (the titanium carbosulfides and nitrides), to the extremely fine semi-coherent clusters formed in the ferrite. Among the commonly employed microalloying elements, Ti has the widest range of uses. For example, when dissolved in austenite, it substantially retards austenite transformation. Because of its high affinity for nitrogen, it removes it from solution and improves the aging properties of the steel. When added in stoichiometric quantities, the fine TiN precipitates that form act to refine the

**Table II.7.**

**Advantages and Disadvantages of Each Technique**

<b>Method</b>	<b>Advantage</b>	<b>Disadvantage</b>
<b>Wet chemical analysis</b>	-Separates soluble and insoluble boron	-Filtration technique -Dissolution of precipitates in the acid
<b>FIM and IAP</b>	-Excellent for the study of individual atoms, vacancies and grain boundary structure	-High instrumental complexity -Very difficult sample preparation -Poor depth resolution (FIM) -Poor sharp concentration gradient analysis (FIM)
<b>AES</b>	-High surface sensitivity -Rapid data acquisition -High sensitivity for light and heavy elements	-In situ fracturing limits the type of materials that can be studied
<b>EMA</b>	-X-ray mapping of elements with $Z > 12$ and combination with boron autoradiography	-Low detectability -Poor results for elements with $Z < 12$
<b>EELS and STEM</b>	-Spatial resolution $< 50$ nm -Detectability of light elements -Qualitative and semi-quantitative analysis	-High noise level -Thin foil thickness -Low detectability
<b>SIMS</b>	-Able to analyse isotopes and light elements -Very high depth resolution	-Destructive analysis -Technical complexity
<b>PTA</b>	-Very low detectability limit ( $< 1$ ppm) -Can make quantitative analyses -Very simple technique compared to the others	-Cannot distinguish between small precipitates and segregated boron atoms -Can only detect boron

austenite grain size. In the lower austenite temperature range, the precipitation of TiC is observed, which retards recrystallization substantially.

The effect of niobium addition is manifested in the precipitation of very fine Nb(C,N) in austenite or ferrite. When precipitated in austenite, this retards or prevents recrystallization and the effect is amplified as the amount of deformation is increased. When precipitation occurs in the upper ferrite temperature range, substantial precipitation hardening occurs because of the formation of very fine, semi-coherent particles or clusters.

In contrast to Nb and Ti, vanadium is much more soluble in steel. As a result, it has little effect on retarding austenite recrystallization, but causes ferrite hardening by the formation of very fine vanadium nitrides. Table II.8 lists the different types of precipitates in steels microalloyed with Ti, Nb and V.

### II.7.2. Crystallographic Structure

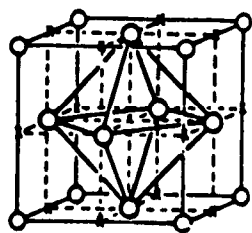
Almost all the carbides and nitrides of Ti, Nb and V have the NaCl (B1) crystal structure, with metallic atoms in the fcc positions and C and/or N in the interstitial sites. The only exception is NbN, which exists in four different forms: a)  $\delta$ -NbN-B1 structure, b) hexagonal NbN, c)  $\delta$ -NbN anti NiAs structure, and d)  $\epsilon$ -NbN-TiP structure. The phase structure of each of these carbides and nitrides is illustrated in Fig. II.5 [96]. The ideal composition of these compounds is MI, where M is the metallic atom and I the interstitial. However, as we will see later, phases of the form M(I,J) and (M,M') (I,J) with the B1 structure, can also exist.

### II.7.3. Simple and Complex Precipitates

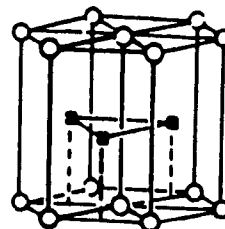
It is well known that interstitial atoms can replace each other and that they have great mutual solubility [51]. The presence of ternary compounds such as Nb carbonitride Nb(C,N) and iron borocarbide is well established [51]. Sharma et al. [97] also reported that in the Fe-Nb-C-N system within the concentration range of microalloyed steels, only Nb(C,N) precipitates are observed and that they form according to the B1 structure. Thus in what is nominally NbC, nitrogen appears to be able to replace carbon randomly. The

**Table II.8.**  
**Types of Precipitates in Microalloyed Steels**

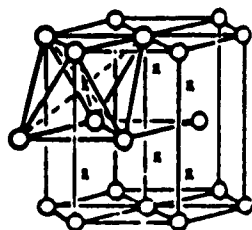
Size Category	Site of Precipitation	Typical Size nm	Example
large inclusions	precipitation in liquid steel or during solidification	$\approx 10^4$	TiN Ti <sub>4</sub> C <sub>2</sub> S <sub>2</sub>
small precipitates	precipitation in the austenite phase	10	TiN
medium to large precipitates	precipitation at austenite grain boundaries and in the substructure	10-100	TiC NbC BN
medium to large precipitates	strain -induced precipitation	10-100	TiC NbC
fine precipitates	precipitation at $\gamma/\alpha$ interphase boundary	10	TiC NbC V(C,N)
very fine precipitates	precipitation in ferrite	< 10	NbC V(C,N)



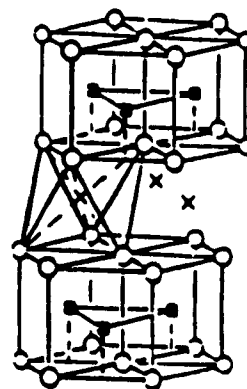
a) B1



b) hex



c) anti-NiAs



d) TiP

**Fig.II.5** Crystallographic structures of the different types of precipitates in microalloyed steels.

C/N ratio seems to depend on the basic composition, precipitation temperature, and heating and cooling history during processing of the steel [98]. Although the structure of V carbonitride has not yet been discussed in detail in the literature, it is logical to expect an NaCl type of structure for this compound, as both VN and VC have the same B1 structure. It seems that there is some controversy regarding the nature of Ti carbonitride; Shiraiwa et al. [99] have suggested that Ti(C,N) is not a ternary compound like Nb(C,N) but is composed of two distinct phases, with a core of almost pure TiN and a shell of almost pure TiC. However, thermodynamic analysis by several authors [100, 101] indicates that the formation of Ti(C,N) in HSLA steels is indeed possible.

As mentioned earlier, Ti, Nb and V have closely related electronic structure, size and electronegativity properties. On the other hand, the simple carbonitrides of these elements are isomorphous; consequently, it is logical to expect that when two or more microalloying elements are present concurrently, complex carbonitrides will form in which some of the metallic atoms replace each other. The existence of these complex carbonitrides has indeed been shown in V-Ti HSLA steels [102], in V-Nb steels [103] and Nb-Ti microalloyed steels [100, 104]. Using scanning transmission electron microscopy with energy dispersive x-ray spectroscopy (STEM-EDX), Güth et al. [104] were even able to show the existence of complex carbonitrides containing Al, Nb, Ti and V as metallic elements. As in the case of the simple carbonitrides, the base composition of the steel and the heat treatment influence the size, morphology and composition of these complex precipitates.

The formation mechanism and sequence of precipitation are not well established yet. Houghton et al. [100] studied a family of controlled rolled HSLA steels containing Ti and Nb that were soaked at 1200°C, a temperature at which most of the carbon and niobium are taken into solution. An array of precipitates formed with the composition  $Ti_xNb_{(1-x)}N$  and covered the size range 50 to 200 nm. These pre-existing high temperature precipitates are expected to play the role of nucleation sites for the  $Nb_x(C_y, N_{1-y})$  precipitates that form during rolling and subsequent cooling. As a result, the latter particles have a shell which is more Nb rich around them. In Fig.II.6 the schematic histogram of a typical precipitate sequence given by these authors is shown.

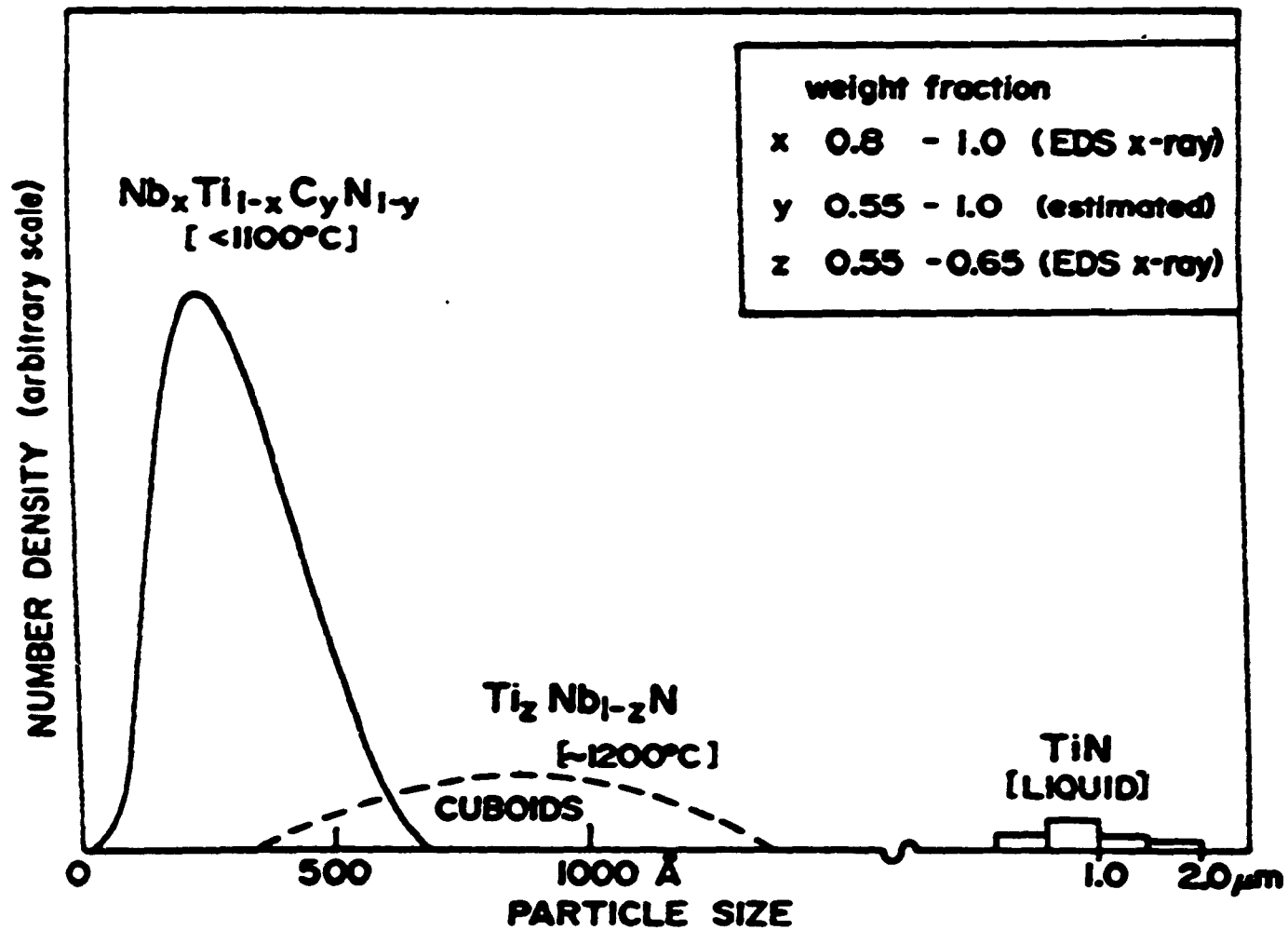


Fig.II.6 Schematic histogram showing the size, shape and chemical composition of a typical precipitate sequence.

#### II.7.4. Precipitate Solubility

A considerable amount of work has been done to establish the solubility products of the carbides and nitrides of Ti, Nb and vanadium. The chemical extraction technique has ordinarily been used [105] to determine these products. However, a problem arises due to the fact that it is difficult to extract these very fine precipitates without any loss or contamination. Moreover, it has often been observed that the C atoms in austenite are not perfectly dissolved in acid solutions; instead, some remain as amorphous graphite.

Advanced experimental methods, such as the sealed capsule technique and the diffusion couple method [106], have been employed to overcome some of these difficulties. Such experimental problems and the lack of information regarding the number of regions in the phase fields of interest have led to the development of thermodynamic modelling. One of the earliest thermodynamic analyses concerned with the solubility of carbides and nitrides is that of Narita [107]. Since then, other authors have carried out similar work [108, 109]. The methodology employed by the different investigators is nearly identical and the following basic assumptions are used:

- 1) that the carbide or nitride is stoichiometric; and
- 2) that the solutes in austenite obey ideal Henrian behaviour.

With these assumptions, the following solubility products have been obtained

$$RT \ln a_M a_I = \Delta G_{MI}$$

$$RT \ln [M][I] = \Delta G_{MI}$$

$$\log [M][I] = A + B/T$$

Here [M] and [I] are the weight percentages of the metal and interstitial (C,N or an equivalent combination such as C + (12/14)N) elements,  $\Delta G_{MI}$  is the free energy of formation of the stoichiometric precipitate, and A and B are constants related to the entropy and enthalpy of formation of the compound. Summaries

of the solubility products for Ti, Nb and V found in the literature are presented in Table II.9 and Fig. II.7.

Although there is some disagreement about published values, several major conclusions can be drawn, irrespective of the data source:

- 1) The solubility of TiN is far lower than that of the other common microalloying precipitates.
- 2) The solubility of a microalloy carbide is generally higher than that of the corresponding microalloy nitride.
- 3) The solubility of VC is dramatically higher than that of any other common microalloy precipitate.

Few data have been published regarding the solubility products of the complex carbides, nitrides and carbonitrides. Only the solubility product for Nb(C,N) is known; it is presented in Table II.9 and Fig. II.7.

#### II.7.5. Influence of Non-stoichiometry and of Alloying Element Interaction

The assumptions employed to date fail to take into account two major factors. The first is that Ti and Nb are strong carbide and nitride formers and can therefore be expected to interact very strongly in austenite. This effect can indeed influence the solubility [110]. The second point is that the ideal composition of the compound is generally not observed; this non-stoichiometry implies that the free energy of formation of the precipitate depends on both temperature and composition. In order to predict austenite-precipitate equilibria more accurately, more rigorous thermodynamics has been employed. The Wagner formalism and a sublattice regular solution model has recently been used by Balasubramanian and Kirkaldy [110] to describe austenite non-stoichiometric precipitate equilibria in Fe-Ti-C and Fe-Nb-C systems.

Their results indicate that non-stoichiometry leads to a reduction in solubility of the precipitate, while solute interactions result in increased solubility. Furthermore, Balasubramanian and Kirkaldy's calculations reveal

Table II.9.

Solubility Products of the Ti, Nb, and V Carbides, Nitrides and Carbonitrides in Austenite

Compound	Temperature Interval °C	log [M] [I] = A + B/T		Reference
		A	B	
TiN	1000-1300	4.94	-14400	[110]
	1200-1300	3.82	-15020	[110]
	1250-1450	0.32	-8000	[110]
NbN	900-1300	2.86*	-7929	[97]
	1100-1300	2.89	-8500	[103]
	1190-1330	2.80	-8500	[110]
VN	900-1100	3.46	-8330	[147]
TiC	900-1300	5.33	-10475	[107]
	950-1350	2.75	-7000	[147]
NbC	900-1200	3.11*	-7520	[103]
	900-1300	2.81*	-7019	[97]
	950-1050	4.37	-9290	[110]
	1000-1250	3.40*	-7920	[107]
	1000-1300	3.70	-9100	[108]
VC	-	6.72	-9500	[110]
Nb(C + 12/14 N)	900-1300	2.26	-6770	[147]

\* NbN<sub>.87</sub> or NbC<sub>.87</sub>

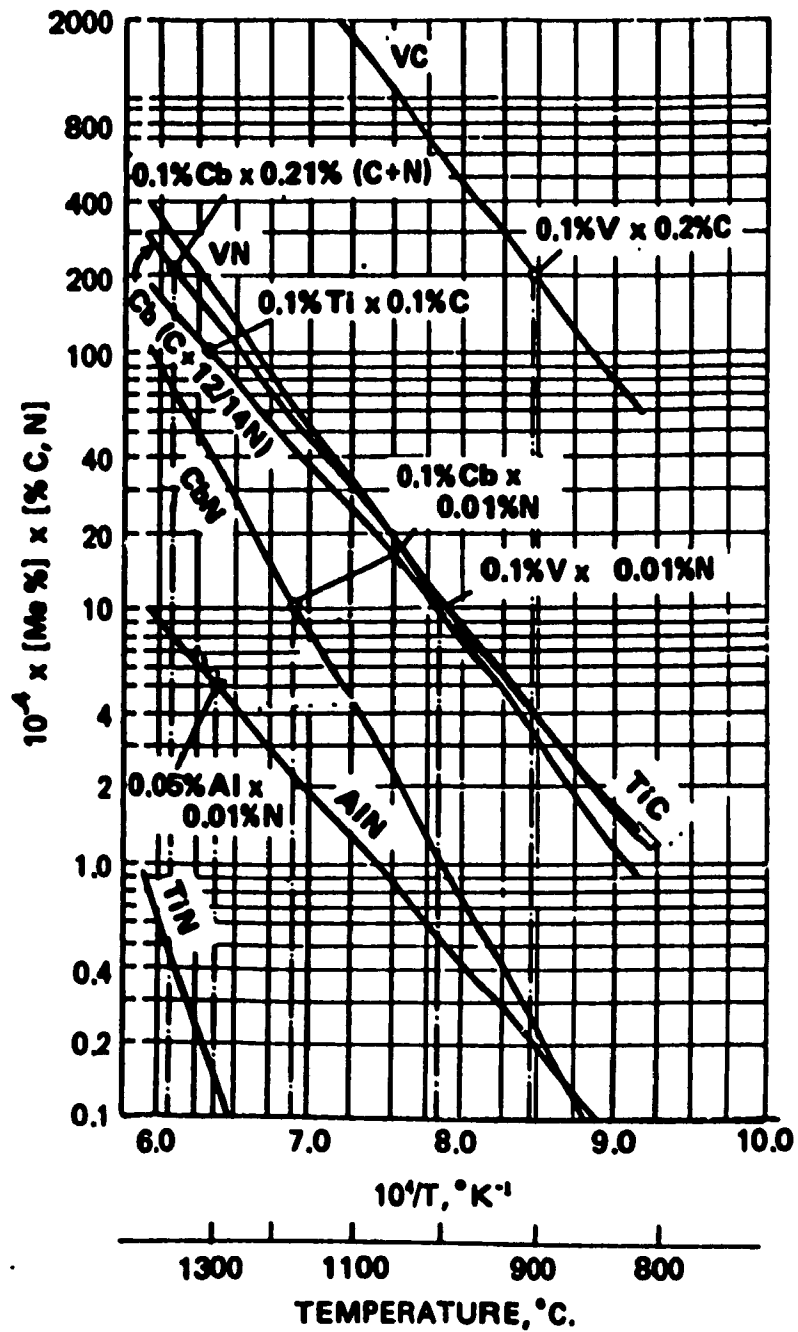


Fig.II.7 The solubility products of microalloy carbides and nitrides.

that, in the solute concentration range associated with microalloyed steels, conventional investigations of interstitial phase solubility, as reported in Table II.9, can be considered to be valid.

## II.8. Precipitation in Hot Worked Austenite

The most common precipitates found in microalloyed steels are TiC, Ti(C,N), NbC, Nb(C,N), and VN, as well as still more complex carbonitrides such as (Ti,Nb)(C,N). It is clear that, depending on the composition of the steel, the complex precipitate can contain more than two metal solutes. TiN and VC precipitates were omitted from this list because the first is almost insoluble in austenite and the latter is too soluble. Thus, VC only precipitates in ferrite or during the austenite-to-ferrite transformation.

Considerable evidence in the literature [111, 112] supports the view that there is a unique orientation relation between certain lattice planes and directions in the precipitate and in the parent austenite. This relation can be presented as

$$\begin{aligned} \{111\}_{\text{ppt}} // \{111\}_{\gamma} \\ \langle 110 \rangle_{\text{ppt}} // \langle 110 \rangle_{\gamma} \end{aligned}$$

Because of this precise relationship, it is assumed that the precipitates are coherent with the austenite during the early stages of growth. However, lattice parameters of the NaCl type precipitates are 16 to 30% greater than that of the austenite. This implies that the interface between the precipitate and the matrix is likely to become semi-coherent rather than totally coherent once the particle has attained a certain size.

For studying precipitation in austenite, it is apparent that the basic phenomena are most easily investigated in steels which remain austenitic at room temperature. The preservation of the gamma phase at room temperature also enables the structure to be observed by transmission electron microscopy (TEM). As mentioned above, the carbides and nitrides of Ti, Nb and V display large misfits with respect to the parent austenite. This introduces a strain

energy which can be best relieved by nucleation of the precipitates at lattice defects such as dislocations and grain boundaries. The precipitation of the transition metal carbides and nitrides in austenite has been observed to occur at four principal sites: i) on dislocations, ii) on stacking faults, iii) in the matrix, iv) at grain boundaries.

### II.8.1. Precipitation at Dislocations and on Dislocation Substructures

The presence of precipitates on dislocations and on substructures is widely observed. Haddad et al. [113] described the continuous precipitation of NbC along dislocation lines, while other authors reported chain-like precipitation [114, 115] or repeated precipitation on climbing dislocations, which should produce planar particle arrays [116]. The dislocation substructure formed in austenite during or after high temperature rolling has also been mentioned by several authors to be an important nucleation site for precipitates. Davenport et al. [112] and Fitzsimons et al. [117] employed dark field microscopy techniques to reveal a cell like distribution of Nb(C,N) precipitates in hot rolled microalloyed steels. Weiss and Jonas [118] and Liu [101] have also found this kind of precipitate distribution by using carbon extraction replicas.

Two models have been suggested for the mechanism of precipitation on dislocations: these are the dislocation climb model and the moving dislocation model. The first was originally developed by Silcock and Tunstall [119] for the precipitation of NbC on partial dislocations and stacking faults. It was later improved by Nes [120], who extended it to the case of nucleation on edge dislocations. This model is based on the observation that there is a large volume increase when a precipitate is formed; thus, a vacancy flux to the precipitates is needed to reduce the local internal stresses resulting from carbide growth. This supply of vacancies can be provided by climbing dislocations. However, Kesternich [121] reviewed the dislocation climb model critically and concluded that there are always sufficient vacancies to reduce the strain energy between precipitates and the matrix, so that the vacancy concentration is not likely to be the limiting factor controlling precipitation.

Kesternich [121] proposed a different model, which has the following characteristics:

- a) There is an interfacial reaction barrier which prevents nucleus growth unless another mechanism intervenes which can either reduce the interfacial barrier or increase the driving force.
- b) Such a mechanism can be the collection of solute atoms by moving dislocations. At locations where two dislocations react or even annihilate each other, their Cottrell atmospheres unite and a locally enhanced supersaturation of precipitating elements is created.
- c) Significant growth occurs only as long as it is assisted by mobile dislocations. The dislocation annealing process stops automatically as soon as the precipitates are large enough to effectively pin the dislocations.

However, further experimental and theoretical work is certainly required for the verification or modification of these models.

### II.8.2. Precipitation on Stacking Faults

Silcock and Tunstall [119] established that the basic dislocation reaction leading to the formation of stacking faults is:



Precipitates can nucleate on the  $a/3 \langle 111 \rangle$  dislocation and accept vacancies from the stacking fault to lower local internal stresses. As a result, the stacking fault grows, eventually escapes from the particles, and is again free to provide fresh nucleation sites for more precipitates. However, compared with undissociated dislocations, stacking faults are less favored sites for the nucleation of precipitates. This is perhaps due to the higher energy required for the creation of a stacking fault by the climb of a partial dislocation [121]. Stacking fault precipitation has nevertheless been observed with most of the MC carbides [122]. The influence of solute concentration [123], vacancy concentration [124], type of nucleation site [124] and the role of dislocations [122] on this kind of precipitation have been investigated extensively and clarified in many ways.

### II.8.3. Precipitation at Grain Boundaries

#### II.8.3.1. Precipitation of $M_{23}I_6$ Compounds

The best known  $M_{23}I_6$  precipitate is  $Cr_{23}C_6$ , which forms in high chromium and chromium-austenitic steels; however, as mentioned in previous sections, the presence of  $Fe_{23}(C,B)_6$  has also been observed in boron containing steels. It has a complex cubic structure containing 92 atoms per unit cell, with a lattice parameter of about 10.6 Å. In the earliest stages of precipitation,  $M_{23}I_6$  nucleates at grain boundaries; it does not normally form on coherent twin boundaries, but will nucleate on higher energy incoherent twin boundaries [125]. If the steel is quenched or deformed, dislocations will move to the coherent twin boundaries, providing nucleation sites for the precipitation to occur [126]. It has also been shown that each particle has a parallel orientation relationship with one of the two austenite grains and the facets which develop on one side of the particle correspond with {111} planes [126].

$M_{23}I_6$  also nucleates *within* austenite grains in two different ways: i) on dislocations as a result of quenching strains or deformation [127]; and ii) within grains in the absence of dislocations as fine dot-like precipitates. As this kind of precipitation tends to be absent near boundaries, Singhal and Martin [128] concluded that nucleation takes place on vacancy/solute clusters. In both cases, there is a cube-cube orientation relationship between the precipitates and the austenite phase.

#### II.8.3.2. Precipitation of FCC Carbides and Nitrides

Such precipitation occurs on two main types of defect: on grain boundary topographical defects such as steps, ledges and discontinuities, and on the extrinsic grain boundary dislocations introduced by the interaction between dislocations and boundaries during deformation. Kesternich has recently reported that TiC precipitates are rarely observed on grain boundaries which have few topographical defects, while they are present at extrinsic grain boundary dislocations [121]. Jones et al. [129] also showed that NbC particles nucleate on the dislocations in grain boundaries and the precipitates form a

"linear chain" during growth. The orientation relationship between such precipitates and the parent austenite is again a cube-cube one.

#### II.8.4. Precipitation in the Matrix

Random matrix precipitation where a cube-cube orientation relationship exists but the particles are not nucleated on dislocations has been observed by a number of authors [111, 124, 130]. However, compared with the other modes of precipitation, matrix precipitation is the most difficult to identify. Various experimental observations [111, 124] suggest that matrix precipitation is sensitive to vacancy concentration. The nucleation of such precipitates has been related to the formation of metal-carbon-vacancy complexes by Froes and Warrington [111]. The matrix precipitates are probably semi-coherent in the early stages of growth, but because of the 20% mismatch between the lattices of the matrix and precipitate, a substantial strain field is present. Evaluation of these strain fields indicates a mismatch of only 5%, suggesting that much of the strain field has been eliminated by the absorption of vacancies in the early stages and also by the generation of interfacial dislocations during growth.

#### II.9. The Kinetics of Precipitation from Supersaturated Austenite

The precipitation kinetics of the transition metal carbides and carbonitrides have been studied by numerous investigators [131, 132]. Isothermal precipitation from supersaturated austenite has been interpreted in terms of the Avrami equation:

$$X = 1 - \exp(-Kt^n)$$

Here X is the normalized fraction of precipitation, K is a constant dependent on the degree of supersaturation and the temperature, t is the elapsed time and n is an experimental constant.

Several values have been reported for the Avrami exponent n, and experimental evidence seems to indicate that n depends on a series of factors such as the type of nucleation site, the size and shape of the precipitate, and the precipitation mechanism. For example, Bradford [133] used dilatometry

experiments to follow NbC precipitation in austenite and found that  $n$  varies from 0.7 to 1 as the precipitate fraction increases from 5% to more than this value. Harris and Nag [134] found that, as the rolling deformation of a low carbon austenite increases from 5 to 10%, the Avrami exponent decreases from 2.1 to 1.8. Table II.10 summarizes the values of the Avrami exponent  $n$  observed under different experimental conditions for the case of precipitation from supersaturated solid solution with diffusion growth control.

The kinetics of precipitation depend on several factors which involve chemistry, thermodynamics and mechanics. In what follows, we will describe each of these factors.

### II.9.1. Influence of Time and Temperature

From a practical point of view, it is important to determine precipitation start ( $P_s$ ) and precipitation finish ( $P_f$ ) times over the temperature range used in controlled rolling. A variety of techniques have been used [131, 132, 135] and precipitation-time-temperature (PTT) diagrams have been obtained. In the context of HSLA steels, most of the PTT curves are of "C" shape, indicating a diffusion controlled mechanism for precipitation. The "C" shape of the PTT diagram is in fact the result of competition between two phenomena:

- i) supersaturation of the precipitating elements,
- ii) the diffusivity of the precipitating elements.

At low temperatures, the supersaturation is high, but diffusion of the atoms involved is difficult. At temperatures just below the complete dissolution temperature, the supersaturation is very low, but because of the high temperature the diffusivity is high. In these two extreme cases, the precipitation kinetics are slow, and it becomes clear that under certain time and temperature conditions, the precipitation rate is maximum (the "nose" in the PTT

Table II.10.

Variation of Avrami Exponent  $n$  With Experimental Conditions

Conditions	$n$
All shapes growing from small dimensions, increasing nucleation rate	$> 2\frac{1}{2}$
All shapes growing from small dimensions, constant nucleation rate	$2\frac{1}{2}$
All shapes growing from small dimensions, decreasing nucleation rate	$1\frac{1}{2} - 2\frac{1}{2}$
All shapes growing from small dimensions, zero nucleation rate	$1\frac{1}{2}$
Growth of particles of appreciable initial volume	$1 - 1\frac{1}{2}$
Needles and plates of finite long dimensions, small in comparison with their separation	1
Thickening of long cylinders (needles), e.g. after complete end impingement	1
Thickening of very large plates (e.g. after complete edge impingement)	$\frac{1}{2}$
Precipitation on dislocations (very early stages)	$-\frac{2}{3}$

curve). Nose temperatures between 875 and 1000°C have been reported for typical microalloyed steels in the literature.

### II.9.2. Influence of Strain and Strain rate

Weiss and Jonas [135] reported that a 5% prestrain accelerates the rate of static precipitation of Nb(C, N) by about one order of magnitude. Similarly, the results of Hoogendorn et al. [131] indicate that the volume fraction of Nb-containing precipitates is doubled as the amount of deformation is increased from 33% to 50%. Jonas and Weiss [136] have reported also that prestraining the austenite at different strain rates will affect the precipitation kinetics of Nb(C,N). The acceleration of the kinetics by strain and strain rate has been associated with the increase in dislocation density by deformation as well as the deformation enhanced diffusivity of the precipitate forming elements.

### II.9.3. Influence of Alloying Elements

Although Ti, Nb and V are the principal microalloying elements in HSLA steels, the presence and amount of other alloying elements, such as Mn, Si, Cr and Ni, can have significant effects on the precipitation kinetics of their carbonitrides. Koyama et al. [137] have reported that Mn, Cr and Ni increase the solubility of carbides and nitrides and decrease the diffusivities of the precipitate forming elements. Conversely, they showed that the addition of silicon has the opposite effect. Akben et al. [138] have mentioned that the presence of Mo in a Nb microalloyed steel decreased the precipitation rate of Nb(C, N) by an order of magnitude. They obtained similar results when the amount of Mn was increased from 0.4 to 1.9 %.

From the above experimental results, it becomes evident that ternary alloying elements have a significant effect on the activities of precipitate forming species and that this effect is illustrated by changes in their diffusivities and solubilities.

#### II.9.4. Interaction Between Recrystallization and Precipitation

Numerous investigations have been undertaken to study the interaction between recrystallization and precipitation. The schematic recrystallization-precipitation-temperature-time (RPTT) diagram proposed by Hansen et al. [139] is illustrated in Fig. II.8. It is clear from this diagram that recrystallization can have a major effect on precipitation. These results are in good agreement with the findings of LeBon et al. [140]. They are interpreted in terms of the effects of temperature and deformation on the condition of the austenite. Indeed, high temperature deformation may induce austenite recrystallization, which will drastically decrease the dislocation density created during deformation, slowing down the precipitation rate. Other authors have either reported that recrystallization has a very small effect on precipitation kinetics [131] or even that it accelerates precipitation [141] as recrystallization brings about grain refinement and will thus accelerate the precipitate nucleation rate in dislocation-free austenite.

#### II.9.5. Modelling Precipitation Kinetics

Numerous experimental investigations of precipitation kinetics have been performed, both in deformed and undeformed austenite. These studies have clarified the effects of chemistry, temperature, strain, strain rate, etc. on the precipitation kinetics. However, because of the use of different conditions of deformation, steel composition and methods of detection of the precipitates, the quantification of the influence of each of these variables is not easy. Also, it is not always possible to study the whole spectrum of parameters by means of experimental work.

In order to overcome this problem, theoretical models have been developed which are based on the thermodynamics of the system. The fact that the precipitation process is diffusion controlled and that the dislocations present in the deformed austenite are the main nucleation sites for the precipitates are also used. The first kinetic model for the precipitation of the transition metal carbides and nitrides in microalloyed austenite is, to our knowledge, attributable to Dutta and Sellars [142]. This theory predicts the PTT curves for Nb(C,N) precipitation in austenite, the lower temperature limit for complete

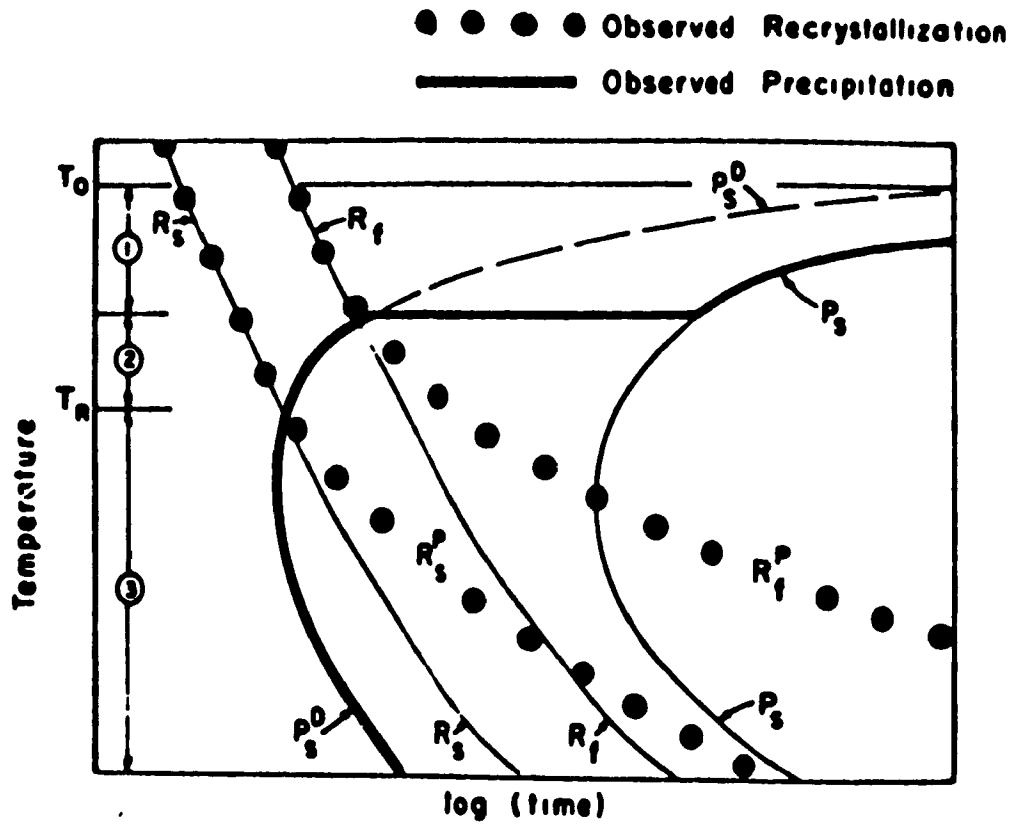


Fig.II.8 Schematic recrystallization-precipitation-temperature-time (RPTT) diagram.

recrystallization, and the upper temperature limit for the effective prevention of recrystallization. Their model is based on classical nucleation theory and on the solubility product for NbC and NbN in austenite; it leads to good agreement with the experimental results of several authors.

Another model has recently been proposed for the case of Ti(C,N) precipitation [101]. The only difference between this model and that of Dutta and Sellars is that, as the solubility product for Ti(C,N) was unknown at the time of the work, the chemical driving force for precipitate nucleation was evaluated from a thermodynamic analysis of the system.

## CHAPTER III

### EXPERIMENTAL MATERIALS AND PROCEDURES

#### III.1 Materials

For the purpose of investigating the effect of boron addition on the recrystallization and precipitation behaviour of ultra low carbon steels, a series of four steels was prepared in the Metals Technology Laboratories of the Department of Energy, Mines and Resources, Ottawa. The chemical compositions of these steels are shown in Table III.1. The plain carbon steel was used for reference purposes, while the boron and niobium steels were employed to illustrate the individual effects of each of these elements. Finally, the niobium plus boron steel was used to study the effect of the combined addition of these two elements on the high temperature softening and strengthening of the materials.

The low carbon content was selected as being representative of the ULCB (ultra low carbon bainitic) steels being made for pipeline applications. Titanium was added, not only for grain size control, but also to tie up the free nitrogen which would otherwise have combined with the boron to form insoluble boronitrides and in this way would have eliminated the boron in solution. Finally, the niobium addition was designed to provide precipitation strengthening and to improve the hardenability by acting in conjunction with the boron.

#### III.2 Mechanical Testing Equipment

##### III.2.1 MTS Testing System

The apparatus consists of a load frame rated at 100 KN under static loading, a hydraulic power supply, a closed loop servohydraulic system and a computerized outer loop system. A hydraulic actuator controlled by a servovalve generates the force and the linear displacement, which are measured by the load cell and LVDT (linear variable differential

**Table III.1**

**Chemical Compositions of the Steels Tested**

	<u>C</u>	<u>Mn</u>	<u>Si</u>	<u>P</u>	<u>S</u>	<u>Ti</u>	<u>Nb</u>	<u>B</u>	<u>Al</u>	<u>N</u>
<b>Base</b>	.03	1.54	.19	.008	.005	.02	----	----	.02	.0048
<b>Boron</b>	.03	1.55	.18	.007	.006	.02	----	.0033	.02	.0043
<b>Nb</b>	.026	1.42	.156	.007	.007	.02	.055	----	.02	.0063
<b>Nb + B</b>	.026	1.56	.150	.006	.007	.02	.055	.0030	.025	.0064

transformer), respectively. The operating range most suitable for a given test is chosen by adjusting selector switches associated with the transducer conditioners. The computerized outer loop system mainly performs the functions of command generation, data acquisition and real time decision making. It consists of an MTS 433 unit which interfaces the MTS testing machine to a PDP-11/04 minicomputer. A system software known as MTS-BASIC/RT-11 and a Tektronix 4010 graphics terminal and Tektronix 4613 hard copy device complete the installation.

### III.2.2 The High Temperature Vacuum Furnace

The high temperature experiments were made possible by the addition of an elevated temperature, high vacuum furnace to the MTS system. It consists of a 17 kVA CENTORR model M60 front loading furnace, and a 0.1 m high speed diffusion pump backed by an  $8.6 \times 10^{-3}$  m<sup>3</sup>/s mechanical pump. A vacuum of  $5 \times 10^{-6}$  to  $10^{-5}$  torr is generally provided for the testing chamber. An exterior view of the high temperature MTS automated testing system can be seen in Fig.III.1.

The heating elements are made of tungsten; these are cylindrically shaped and are placed one each in the four quadrants. The hot zone of the chamber (d=76 mm, h=200 mm) is surrounded by concentric multi-layered tungsten and molybdenum radiation shields. The anvils (lower and upper) are made of a molybdenum alloy called TZM and are fixed to the load cell and the ram of the MTS machine, respectively, through internally water cooled stainless steel extension rods.

The temperature of the test chamber was continuously controlled by means of a J-type Pt/Pt-10 Rh thermocouple placed close to the center of the chamber. The thermocouple is linked to a current adjusting type (CAT) temperature controller made by Leeds & Northrup. The CAT controller provides an output current which is proportional to the difference in temperature from that of the set point. This current is then translated into a power input by means of a silicon controlled rectifier (SCR) power package.

The sample temperature was measured using a K-type chromel-alumel thermocouple which was placed in contact with the specimen. A second

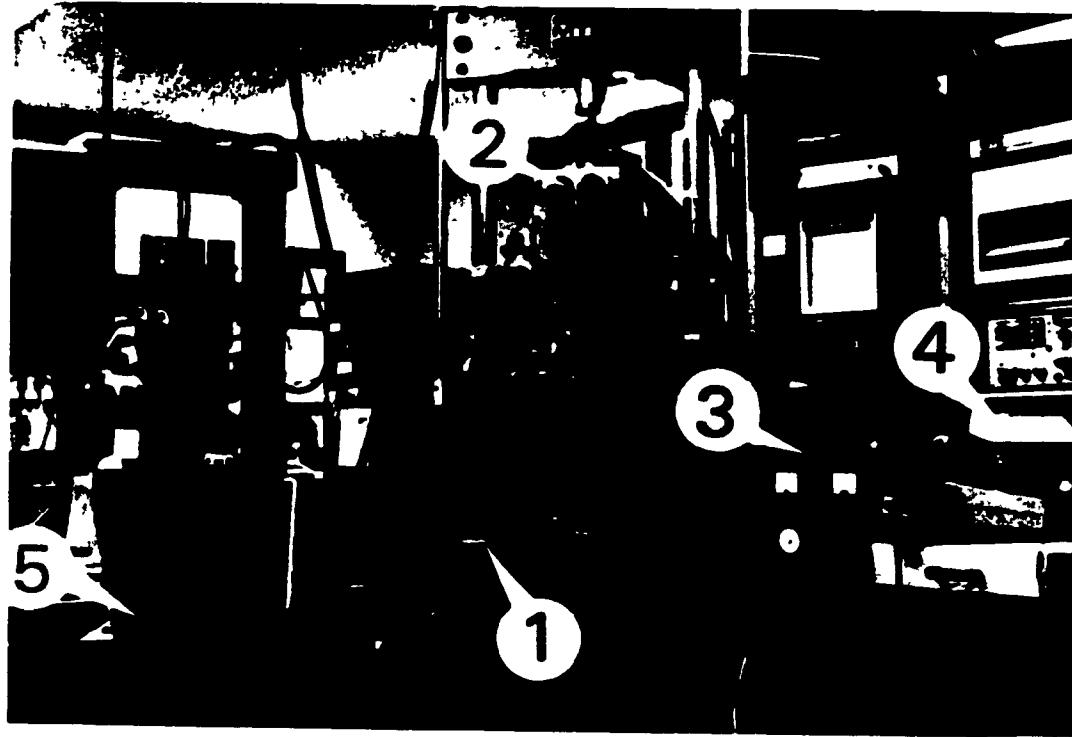


**Fig.III.1** An external view of the high temperature compression testing system: 1) MTS load frame; 2) Centorr vacuum furnace; 3) temperature and vacuum control console; 4) PDP 11/04 computer; and 5) Tektronix terminal.

thermocouple not in contact with the sample was used for reference and for verification when the sample thermocouple was broken or lost contact with the sample; it therefore served to check whether the indicated temperature was correct or not. The checking was done as follows: If during cooling from the solutionizing to the test temperature, the two cooling rates are similar, this indicates a contact failure. In fact, the reference thermocouple has a lower heat capacity than the specimen or the piston; thus the cooling rate indicated by the thermocouple should be higher than that of either of the two elements when heat input to the furnace is shut off.

Samples were quenched at different stages of a test by means of an existing helium quenching device on the MTS machine. However, in order to improve the efficiency of the existing device, several modifications to the initial design were carried out in the present investigation. These consisted of an improved specimen pusher and the addition of a funnel which guides the sample into the quenching cup. With these modifications, the rate of successful quenching increased significantly (from 50% to almost 100%). An interior view of the high temperature, high vacuum furnace is presented in Fig.III.2.

### III.2.3 Hot Deformation Dilatometer

The cooling rate which is produced when the specimen is quenched in the MTS machine is about 60 °C/sec. Although this cooling rate is sufficient for investigating the precipitation process, it may not be fast enough to study boron segregation. The MMC quench and deformation dilatometer which was used in this investigation\* has the advantage of being programmable (i.e. heat treatment conditions the same as that used in the MTS could be reproduced). It also has the capability of controlling the cooling rate of the specimen and quenching it at rates of up to 400 °C/sec.

\* Made available at MTL, CANMET, through the kind assistance and cooperation of Dr. L.E. Collins.

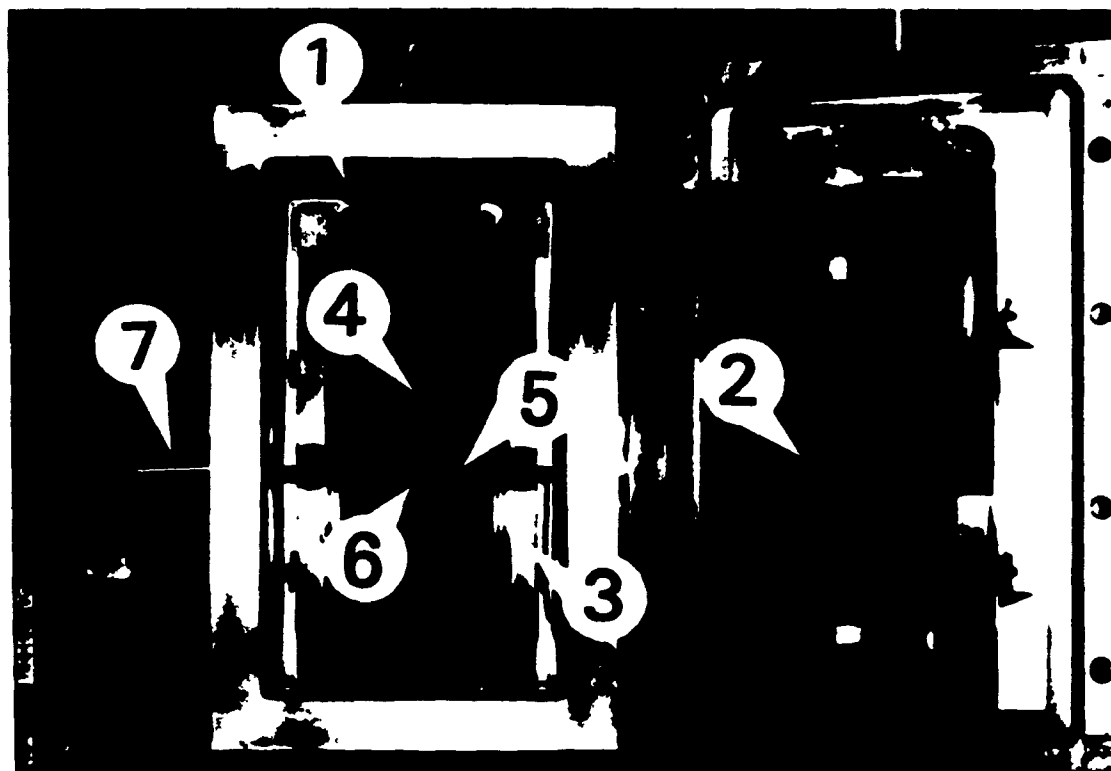


**Fig.III.2** An interior view of the Centorr high temperature, high vacuum furnace. 1) vacuum chamber; 2) tungsten mesh heating elements; 3) shields; 4) TZM anvils; 5) thermocouples; 6) specimen; 7) specimen pusher.

### **III.3 Specimen Preparation and Heat Treatment**

#### **III.3.1 Specimen Preparation**

The steels were received in the form of 13 mm thick plates and, depending on the testing machine to be used, their preparation and heat treatment were different.

##### **III.3.1.1 MTS Tests**

The plates were cut into square bars, with their longitudinal axes parallel to the rolling direction. Subsequently, cylindrical samples 11.9 mm in height and 7.9 mm in diameter were machined; this height-to-diameter ratio was selected for the present specimen dimensions to promote homogeneous deformation [143].

The end surfaces of the samples were grooved [144] to allow the retention of the glass powder lubricant. Fig.III.3 illustrates the specimen dimensions and details of the groove geometry. The glass lubricant was used in order to minimize the friction between the end faces of the specimen and the anvils. Previous investigations [144] showed that adequate lubrication is obtained with glasses having a viscosity of  $10^4$  poises at the testing temperature. The glasses used in this study were manufactured by the Corning Glass Co. Ltd.

##### **III.3.1.2 Deformation Dilatometer**

The sample preparation followed the same pattern as for the MTS tests. However, the cylindrical specimens in this instance were 8 mm long and 4 mm in diameter. The samples did not have grooves; instead, molybdenum foils were used to avoid the sticking of the specimen ends to the deformation platens.

#### **III.3.2 Heat Treatment**

All the samples were given a prior heat treatment at 1000°C for two hours under vacuum, and then air cooled. This was done in order to eliminate the rolling textures present in the steel after hot rolling. It has been reported [144]

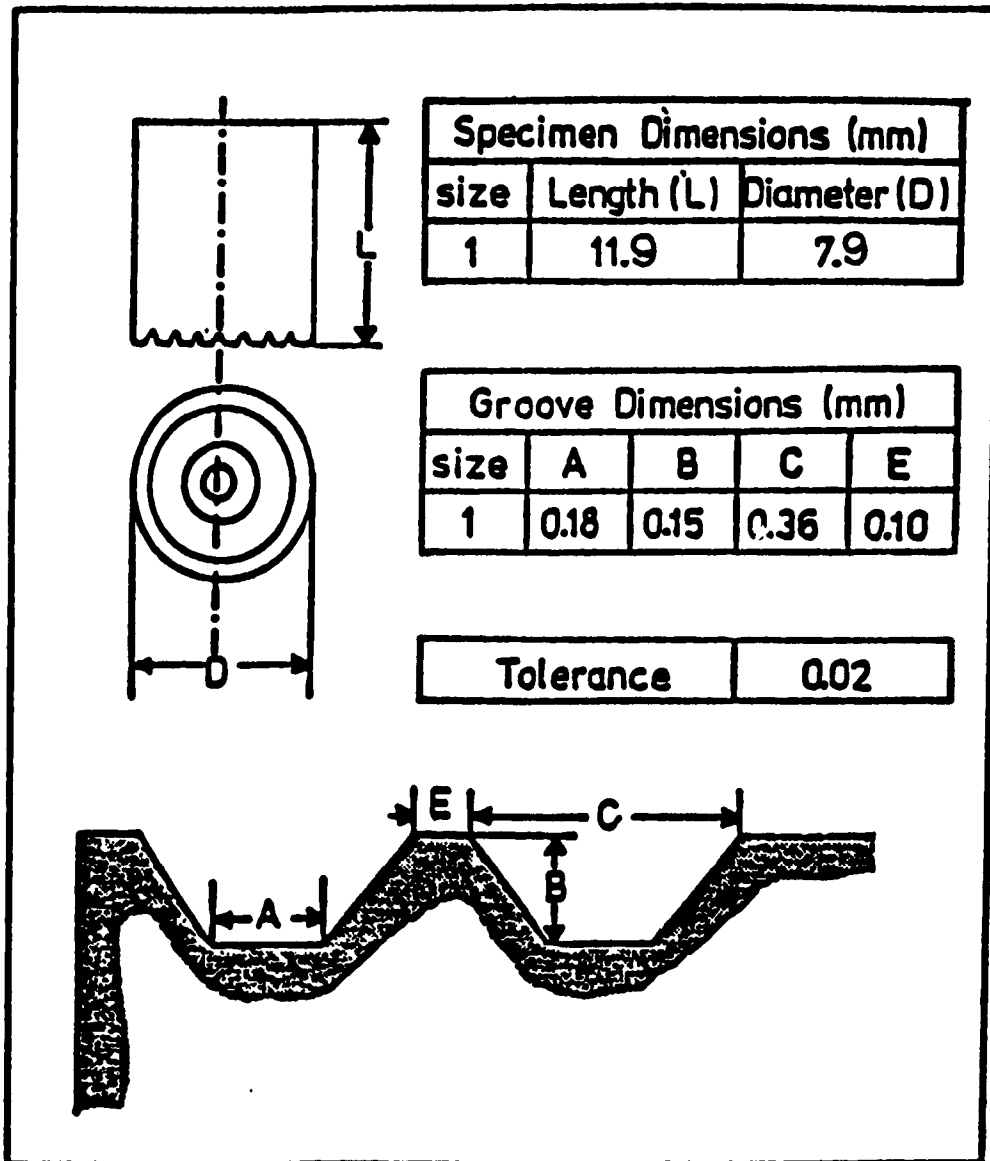


Figure III.3 Sample geometry and groove design.

that such textures frequently lead to the production of elliptical cross-sections in deformed specimens.

### III.3.2.1 Solutionizing Heat Treatment

For any interpretation of the effect of boron, it is essential to know whether this element is trapped in coarse undissolved particles or is in solid solution at the austenitizing temperature. The total boron content of the steel controls the temperature of complete dissolution of the borocarbides. This temperature has been found to vary from slightly over 1000°C for B = 25 ppm to approximately 1150°C for B = 100 ppm [145, 146]. On the other hand, all the Nb(C,N) particles present in the steel must also be dissolved before testing.

The equilibrium solution temperature of Nb(C,N) in austenite was evaluated from the following equation given by Irvine et al. [147].

$$\log[\text{Nb}][\text{C} + (12/14) \text{N}] = 2.26 - 6770/T$$

In the above equation, [Nb], [C] and [N] are the concentrations in weight percent of Nb, C and N, respectively, and T is the absolute temperature. The present solution temperature was estimated to be approximately 1070°C. Austenitization temperatures of 1100°C and 1200°C were therefore selected, either of which was high enough to dissolve, not only the  $\text{Fe}_{23}(\text{C},\text{B})_6$  precipitates, but also the Nb(C,N) ones.

For the tests done in the MTS machine, a solutionizing time of 30 minutes was selected, while the time was only 15 minutes in the case of the tests executed in the deformation dilatometer. This is due to the fact that the samples used in the MTS testing system were larger than those employed in the dilatometer. However, in both cases, the initial austenite grain size was the same.

After austenitization, the specimens were cooled to the test temperature by shutting off the furnace of the MTS machine. The time taken to go from the solutionizing to the test temperature was measured repeatedly. A mean cooling rate of 2 °C/s was achieved in all cases and was used in the experiments carried

out on the dilatometer, where the cooling rate of the sample can be controlled automatically.

In order to study the effect of deformation on boron segregation as well as on the precipitation process, two principal types of experiments were carried out during this investigation. In the first type, two prestrains were used: 5% and 25% true strain, with strain rates of 0.1 and 1 sec<sup>-1</sup>, respectively. Test temperatures between 800 and 1000°C were employed and, depending on the experimental conditions, samples were quenched after different holding times. Also, in order to investigate the effect of cooling rate on boron distribution, two different cooling rates were employed. In the first case, the specimens were cooled at 17 to 20 °C/sec, while they were helium quenched at 400 °C/sec in the second case. In the second type of experiment, no deformation was used. After solutionizing at 1200°C for 30 minutes, the samples were cooled to the test temperature. At this stage, they were either water quenched after different holding times, or isothermally held for 10 minutes and then water or oil quenched. The experiments were carried out in an annealing furnace under a vacuum of 10<sup>-3</sup> torr and test temperatures between 800 and 1200°C were employed. The different experimental conditions used in this investigation are summarized in Table III.2. Figs.III.4 and III.5 illustrate the heat treatments which were applied to the samples for the two types of experiments.

### III.4 Experimental Procedure

The experimental technique employed in this study was based on the effect of carbonitride precipitation on the stress relaxation of prestrained samples. This method was first developed by Liu [101] for the case of Ti(C,N) precipitation in austenite. However, it was modified and improved in this investigation and was also employed to follow the recrystallization process and to study the interaction between recrystallization and precipitation. The computer program used to carry out the tests is listed in Appendix 1.

#### III.4.1 Stress Relaxation Testing

The procedure for the non-isothermal stress relaxation tests was the same as that employed previously. The most important steps are:

**Table III.2.**  
**Summary of the Experimental Conditions Employed**

Solution Temp. °C	$\epsilon$ %	$\epsilon$ s <sup>-1</sup>	Test Temp. °C	Nb + B Steel	Nb Steel†	B Steel	Cooling Method	
							Q.	C.C.
1100	5	0.1	800, 830, 850, 870, 900	×	×	×	×	
1100	25	1	800, 850, 900, 950, 1000	×	×	×	×	×
1200	5	0.1	800, 830, 850, 870, 900, 950	×	×	×	×	
1200	25	0.1	800, 850, 900, 950, 1000	×	×	×	×	×
1200	0		800, 850, 900, 950, 1000, 1100, 1200	×		×	×	×

Q. = quenched, C.C. = control cooled

†: quenched only

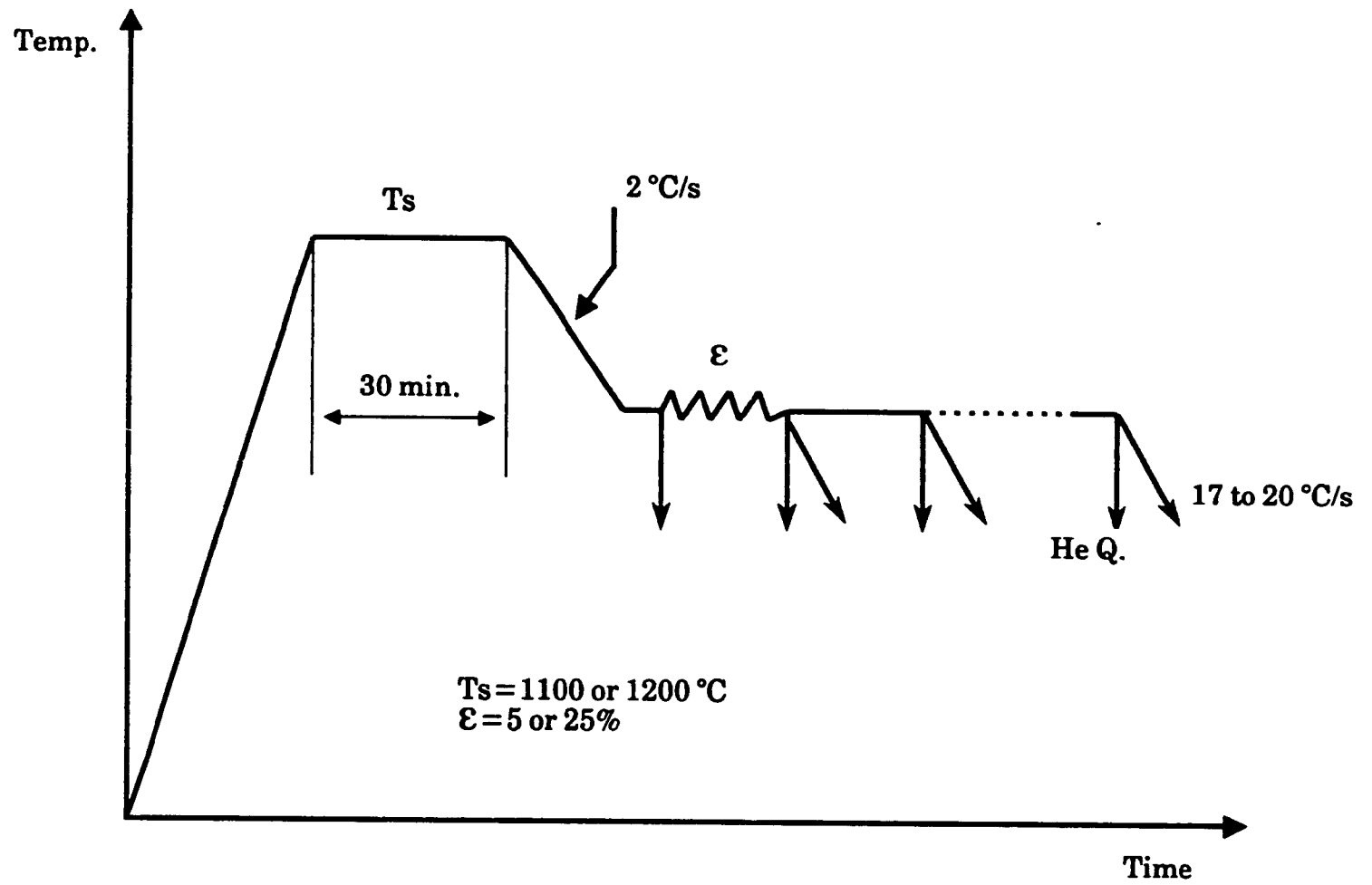


Fig. III.4 Heat treatment schedules (type I).

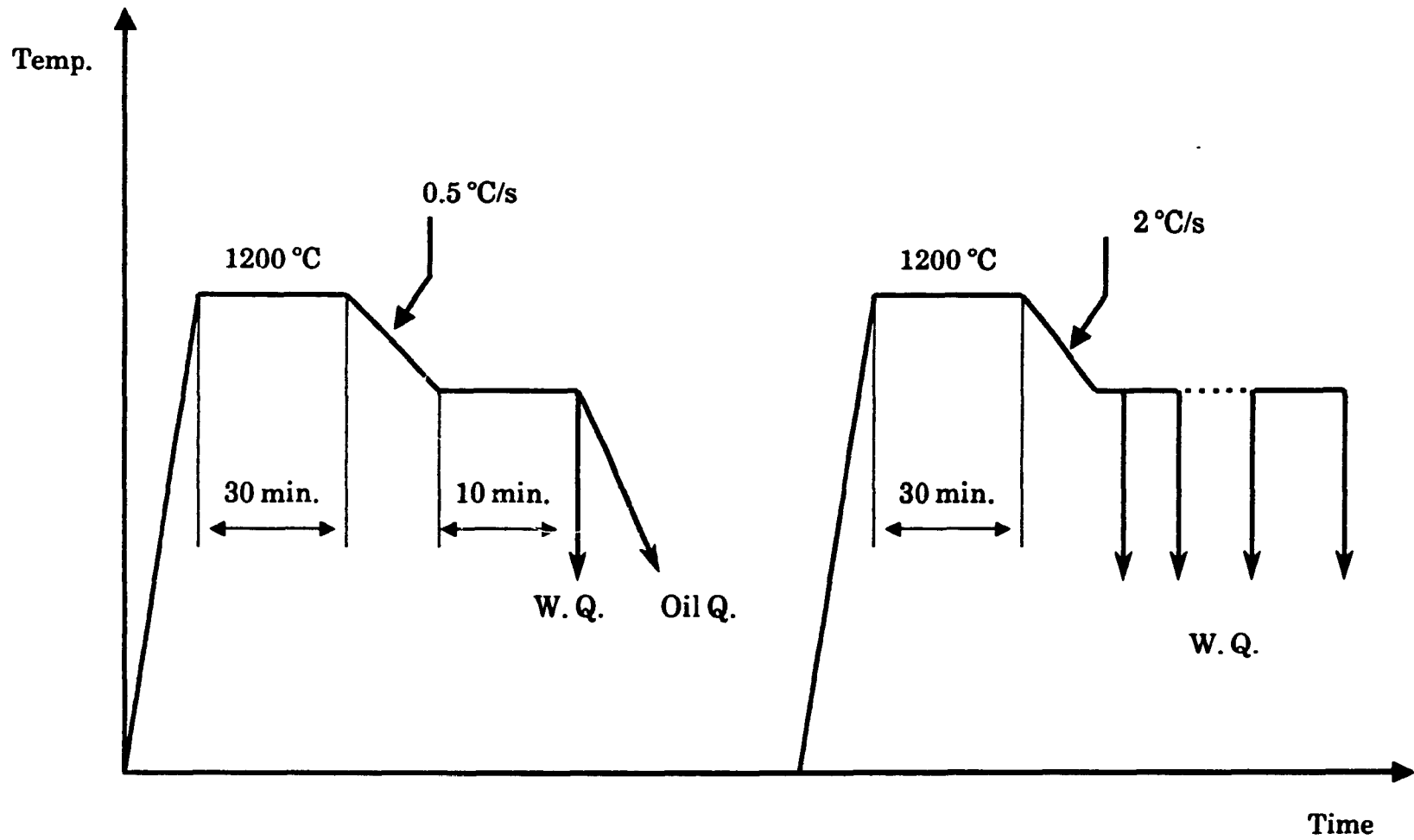


Fig. III.5 Heat treatment schedules (type II).

- 1) determination of compression tool length changes when cooling from the austenitizing to the test temperature,
- 2) automatic positioning of the anvil on top of the specimen,
- 3) prestraining,
- 4) data acquisition and treatment.

The improvement introduced by the author consists of a modification of the software monitoring the process of stress relaxation. The changes reduce the significant scatter previously present in the stress versus log(time) curves obtained.

### **III.5 Metallography**

Five different metallographic techniques were employed in the present study. The initial stages of sample preparation are almost identical for all five. This consisted of cutting the tested specimens along the compression axis with a diamond saw. After mounting in bakelite, they were polished using different grades of silicon carbide paper and finally fine polishing was performed with the aid of 6, 1 and 0.1  $\mu$  diamond paste.

The prior austenite grain size of the Nb steel was determined by using a saturated aqueous solution of hot picric acid at 60 to 90°C to which some Teepol 601 and a few drops of Palmolive detergent had been added. In the case of the Nb + B and B steels, the PTA micrographs, which show the boron distribution at the prior austenite grain boundaries, were employed.

#### **III.5.1 Particle Tracking Autoradiography**

The principles of this technique were described in the previous chapter. Sample preparation consisted of the following steps :

- 1) Attach the cellulose acetate film to the polished face of the specimen.

- 2) Heat treat the sample at 140°C for at least 18 hours. This is done in order to remove the air bubbles which may be present between the surface and the film. Defective samples found in this way have their films replaced.
- 3) Place the samples in aluminum capsules (four per capsule) and then seal. Insert into the J-rod trays of the NRX reactor at the Chalk River Nuclear Laboratories. The integrated neutron flux of thermal neutrons that was applied ranged from  $4 \times 10^{14}$  to  $2.8 \times 10^{15}$  neutrons/cm<sup>2</sup>.
- 4) Remove the film and etch it in a strong alkaline solution (7N KMnO<sub>4</sub>). This treatment converts the alpha tracks into etch pits.
- 5) Coat the films with chromium in order to increase the contrast when they are observed under the optical microscope. Finally, take the photographs with a type 55 polaroid film.

### III.5.2 Electron Microscopy of Carbon Extraction Replicas

The polished samples were carbon coated under a vacuum of better than  $5 \times 10^{-4}$  torr. Squares of 3x3 mm were scribed on the coated surfaces and removed by electropolishing using a solution of 10% perchloric acid, 70% ethanol, 10% butanol and 10% distilled water. After this stage, the carbon replicas were washed gently in ethanol and then in a 50-50 mixture of ethanol and distilled water. They were finally placed on TEM copper grids (Cu, 3mm, 200 mesh) and dried.

The extraction replicas were observed in a JEOL-100CX scanning transmission electron microscope operated at 100 kV. The composition profiles of the observed particles were obtained with the aid of a PGT system IV energy dispersive x-ray spectrometer. Both the scanning and transmission modes were used in analyzing the particle compositions.

### III.5.3 SIMS Analysis

The bakelite supports of the polished samples were removed in order to improve electrical contact between the specimen and the SIMS sample holder and also to avoid charging effects originating from the bakelite. The samples were carefully cleaned before being put into the machine. SIMS analysis was performed in a CAMECA IMSF4F instrument. Both oxygen and cesium were employed as primary ions.

The energy of  $O_2^+$  ions is 12.5 keV and that of cesium is 10 keV. The ion probe (approximately 100  $\mu\text{m}$  in diameter, current 2  $\mu\text{A}$ ) was rastered over an area 250 by 250  $\mu\text{m}$  under normal operating conditions and 62 by 62  $\mu\text{m}$  for high mass resolution (i.e.  $m/\Delta m \geq 2000$ ). In this way it was assumed that there was no interference between the secondary ions being analyzed and other undesirable elements. Finally, an image field of 150  $\mu\text{m}$  was used during the SIMS investigation.

### III.5.4 EELS

Carbon extraction replicas were examined at 120 keV in a Philips EM400T equipped with an EDAX x-ray detector, a Gatan 607 energy loss spectrometer and the necessary processing software. It is worth noting that the latter included the latest, relativistically-corrected elemental partial cross-sections for EELS quantification. The most common EELS collection condition was the focussed-beam TEM mode with a collection semi-angle  $\beta = 14.5$  mrad and a convergence angle  $\alpha = 12$  mrad.

### III.5.5 Particle Size Measurements

The particle size distribution was determined using micrographs taken of the carbon extraction replicas. To do the measurement, each micrograph was enlarged such that the final magnification was 100,000. A monocular was then employed to determine the size of the individual particles; it magnifies 7 times and has a precision of  $\pm 0.1$   $\mu\text{m}$ . From 200 to 400 particle diameters were measured for each specimen.

## CHAPTER IV

### MECHANICAL TESTING RESULTS

#### IV.1. Determination of the Prior Austenite Grain Size

When studying precipitation and recrystallization, it is important that the initial conditions (i.e. the prior austenite grain size) of all the tested materials be the same. To achieve this aim, individual samples were reheated to different austenitization temperatures and held for half an hour before quenching. For these tests, Nb + B, Nb and B steels were used and the reheating temperatures were 1100, 1200, 1250 and 1350°C.

The prior austenite grain boundaries were revealed either by etching the samples in a saturated solution of hot picric acid or by using the technique of particle tracking autoradiography, which reveals the segregation of boron to prior austenite grain boundaries during quenching. The grain sizes were measured using the mean linear intercept method. Five micrographs of each sample were used and a total of at least 280 to 300 intersections were counted in each case; the grain size was estimated from this number. The results are presented in Table IV.1 and Fig. IV.1.

It can be seen from the data that the boron steel has a higher grain size at all reheat temperatures. As shown in Table IV.1, the values for the boron steel are 6 to 10  $\mu\text{m}$  greater than those obtained for the Nb and Nb + B steels. The Nb steel has a consistently finer grain size than the Nb + B steel. However, the difference is not large and falls into the error interval. These results are in good agreement with those of Ohmori and Yamanaka [88], who observed that the austenite grain size was coarsened by the addition of boron. By contrast, Maitrepierre et al. [58] reported that boron had little effect on the  $\gamma$  grain size in AISI type 4025 and 4010 steels.

It seems then that the composition of the steel influences the role which may be played by boron regarding the austenite grain size. The interactions between boron and the other elements present in the material, such as N, Al, Ti

**Table IV.1.**  
**Prior Austenite Grain Size,  $\mu\text{m}$ , as a Function of Reheat Temperature**

Steel	Reheat Temperature °C			
	1100	1200	1250	1350
Nb + B	$39 \pm 2.9$	$44 \pm 2.3$	$49 \pm 2.8$	$89 \pm 3.1$
Nb	$38 \pm 3.1$	$42 \pm 2.9$	$47 \pm 2.2$	$86 \pm 2.7$
B	$44 \pm 1.7$	$48 \pm 2.7$	$55 \pm 3.2$	$96 \pm 2.9$

and Nb, have in fact to be considered for a better understanding of the boron effect.

The results show a two-stage grain growth process. When reheat temperatures of 1100, 1200 and 1250°C are used, there is not much grain growth in the steels. However, when the specimens are reheated to 1350°C, marked grain growth occurs, taking the size from about 50  $\mu\text{m}$  when reheated at 1250°C to about 90  $\mu\text{m}$  at 1350°C. This behaviour can be interpreted in terms of the role played by the second phase particles on the growth process. In fact, Ti was added to these steels in order to prevent the formation of boron nitride particles. The small TiN precipitates formed at the higher temperatures then hinder austenite grain growth. However, as the reheat temperature is increased, the grain growth inhibitors (i.e. fine TiN particles) become more and more ineffective as a result of dissolution and coalescence. When the precipitates are no longer effective in pinning the boundaries, grain coarsening suddenly occurs.

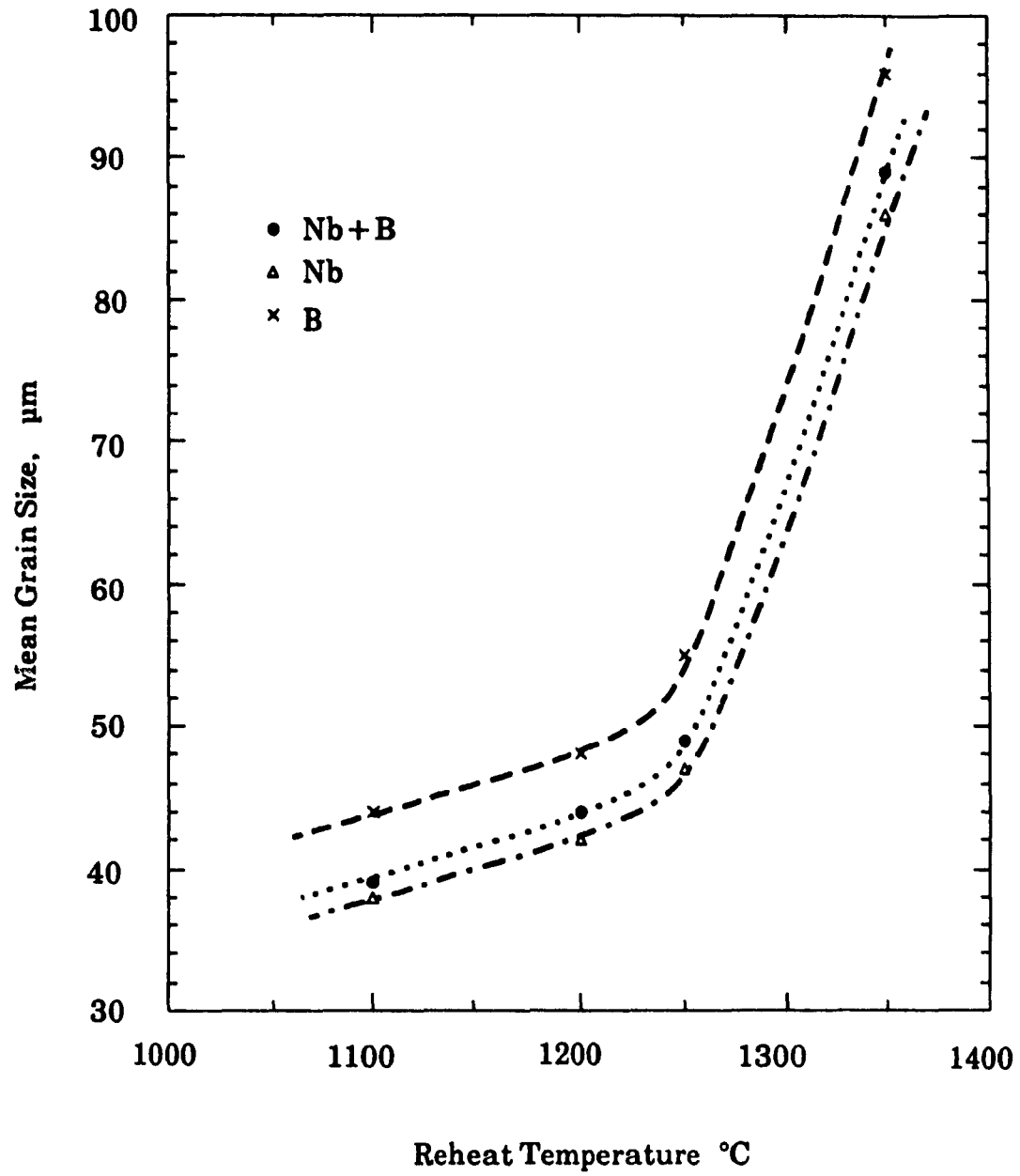


Fig. IV.1 Prior austenite grain size as a function of reheat temperature.

## IV.2. Stress Relaxation Test Results

As described in the previous chapter, prestrains of 5 and 25% were applied to each sample. Although four steels were used in this investigation, the stress relaxation results which will be presented in the following sections will be mainly those obtained on the plain carbon, Nb + B and Nb steels. Results pertaining to the boron steel are absent because the nature and type of precipitation taking place in this steel are different from those occurring in both Nb + B and Nb steels, making comparison difficult between them.

It has been extensively reported that  $M_{23}(C,B)_6$  is the most common precipitate observed in this kind of steel (i.e. boron steel) [14, 58, 146] and that, such precipitation takes place mainly at austenite grain boundaries. But the stress relaxation technique is only able to detect the precipitation occurring at dislocations, as will be seen later. As a result, it is not possible to follow iron borocarbide precipitation in austenite by this technique. Consequently, only the results pertaining to the Nb + B and Nb steels will be presented here. It should be mentioned, however, that different heat treatment conditions of temperature and deformation were applied to the boron steel specimens. Several samples were quenched at different stages of testing and various microscopic techniques were employed to study them, the results of which will be presented in the sections that follow.

### IV.2.1. Case of the Plain Carbon Steel

The stress relaxation behaviour of the base steel tested at 850 and 900°C is shown in Fig. IV.2. The samples were austenitized at 1100°C for 30 minutes and deformed 5%. The results indicate that, after a transition period ranging from 10 to 100 ms, the stress versus log (time) curves are linear. However, for the sample tested at 850°C, after about 300 seconds, there is a sudden drop in stress leading rapidly to very low levels of stress. This unexpected behaviour is associated with the occurrence of the austenite-to-ferrite transformation, which is responsible for the marked decrease in stress. On the other hand, in the sample tested at 900°C, the relaxation behaviour is unaffected, and in this case the stress versus log (time) curve is a straight line.

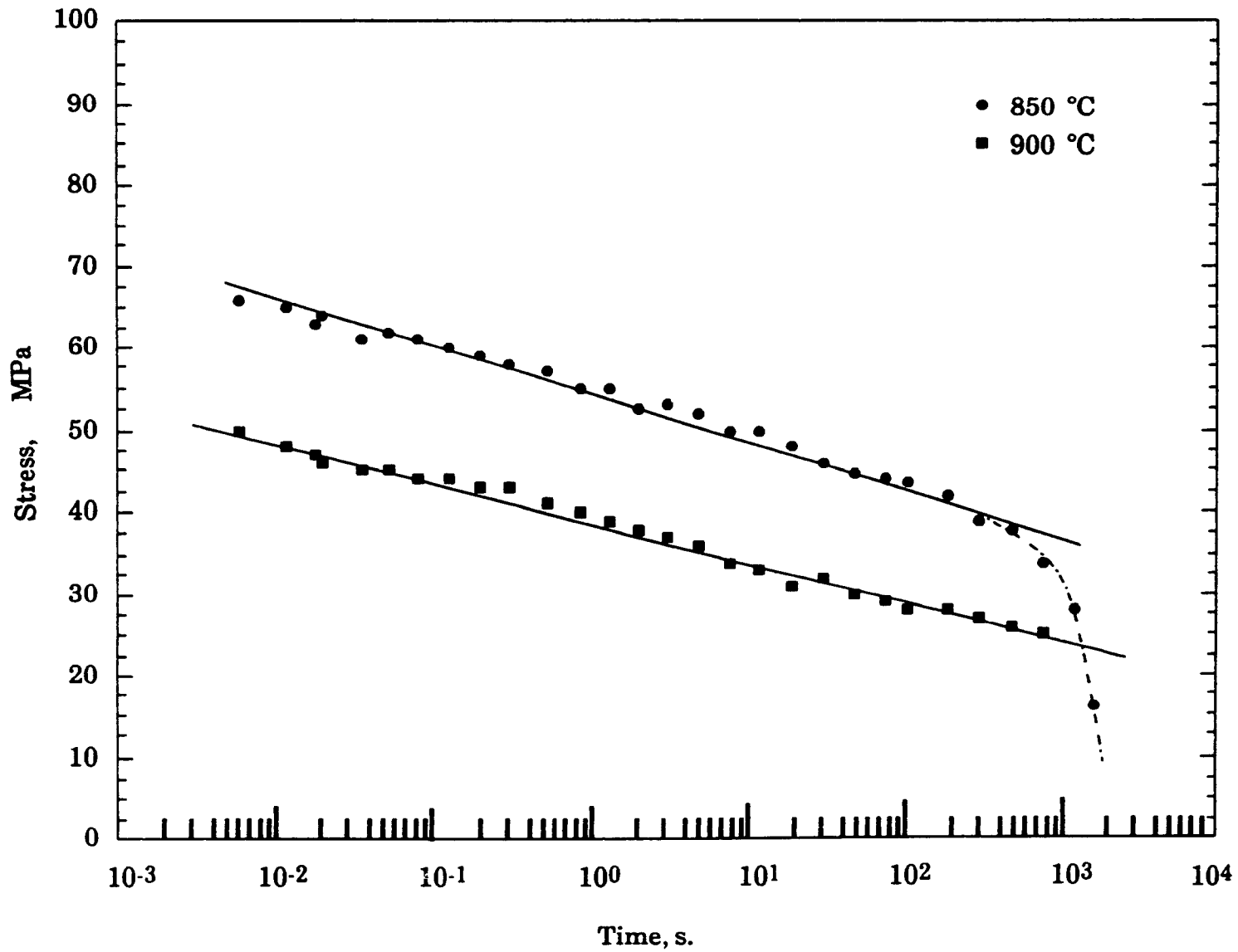


Fig.IV.2 Stress relaxation data for the base steel, solutionized at 1100°C and deformed 5%.

To check whether the specimen tested at 850°C undergoes the  $\gamma$ -to- $\alpha$  phase transformation, samples of the three steels were submitted to identical test conditions and then helium quenched. Metallographic examination indicated that, while no transformation is observed in the Nb + B and Nb steels, the plain carbon steel is almost fully transformed.

Dilatometric experiments simulating the stress relaxation testing conditions were carried out on the Nb + B, Nb and B steels. The results indicate that the  $\gamma$ -to- $\alpha$  transformation occurs in the B steel after approximately 40 minutes at 770°C, while no transformation takes place in the Nb + B steel. However, it was found that when the Nb steel is tested at 800°C, a considerable quantity of ferrite is formed and the transformation occurs after a shorter period of time compared to the Nb + B steel, as will be shown later (Fig.IV.8). It seems then that the combined addition of Nb and B affects strongly the transformation temperature of the steel.

#### IV.2.2. Stress Relaxation Results after 5% Prestrain

As illustrated in Fig.IV.2, the stress versus log (time) curve is generally straight and obeys the following empirical equation:

$$\sigma = \sigma_0 - \alpha \ln(1 + \beta t) \quad (\text{IV.1})$$

This kind of behaviour has been observed in a variety of materials, such as stainless steel [148], copper [149], high purity iron [150] and plain carbon steel [148]. In Eq. IV.1,  $\alpha$  and  $\beta$  are constants for a given material under isothermal test conditions. In Fig.IV.3, a comparison is presented between the relaxation behaviours of the base and Nb + B steels tested under the same conditions at 850°C. According to these results, the stress relaxation behaviours of the two steels seem identical for the first 12 seconds. After this time, the stress versus log (time) curve of the Nb + B steel starts to deviate from the straight line and the process of relaxation is almost stopped. This suggests that a phenomenon (such as precipitation) which can arrest the relaxation is occurring. After a certain time, the plateau disappears and the relaxation curve again approaches the initial straight line.

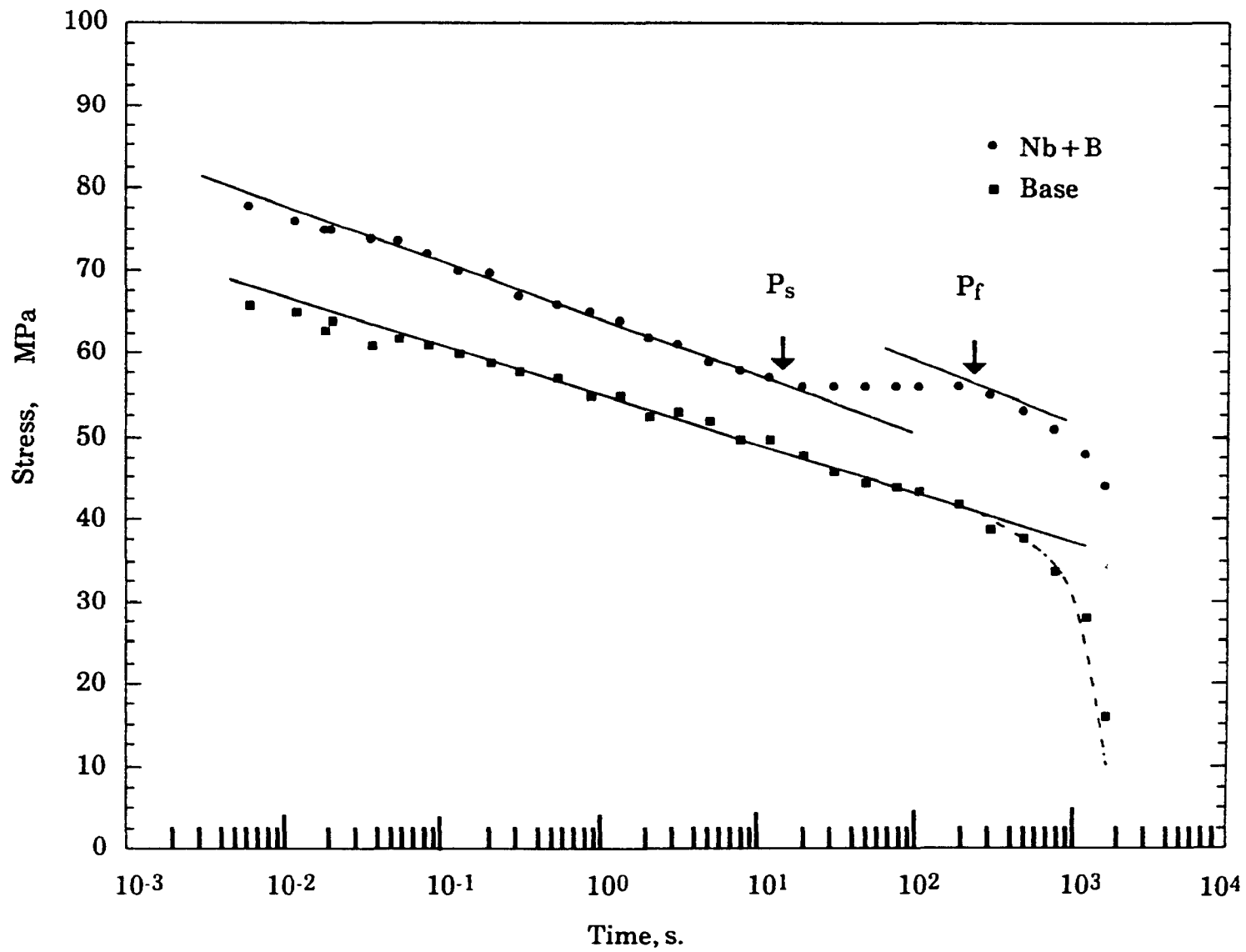


Fig.IV. 3 Comparison of stress relaxation data for the Nb + B and the base steel, deformed 5% at 350°C.

The stress versus log (time) relationship of the Nb + B steel can be described as a combination of the basic logarithmic curve and a stress increment,  $\Delta\sigma$ , corresponding to the deviation. Equation IV.1 then becomes

$$\sigma = \sigma_0 - \alpha \ln(1 + \beta t) + \Delta\sigma \quad (\text{IV.2})$$

The first point at which  $\Delta\sigma$  is no longer zero ( $\Delta\sigma$  minimum) and the point where  $\Delta\sigma$  is a maximum (end of the plateau) are identified as the precipitation start and finish times, respectively. It should also be mentioned that if another process (such as recrystallization) occurs, the same type of relationship can be applied.

Figures IV.4 and IV.5 show stress relaxation curves for the Nb + B steel solutionized at 1100 and 1200°C, respectively. Data for the Nb steel are presented in Figs. IV.6 and IV.7, respectively, for these two soak temperatures. Comparison of the results obtained at 1100 and 1200°C shows that, although the precipitation start times are similar for both steels, longer times are required for the precipitation to finish when the specimens are solutionized at 1200°C. It should also be noted that, for the tests done at 800°C, the stress decreases markedly after the end of the precipitation process. This behaviour is associated with the occurrence of the  $\gamma$ -to- $\alpha$  transformation. To check this point, samples of the Nb+B and Nb steels were solutionized at 1100°C, deformed 5% at 850°C and quenched 30 min later. The microstructure was revealed by etching the polished samples in a 3% nital solution and the micrographs are presented in Fig. IV.8. It is clear that in the Nb steel more than 70% of the austenite phase has transformed into ferrite at the end of the test, while no transformation occurred in the Nb+B grade.

It can be seen from these results that all the curves can be represented by Equation IV.2, the values of  $\Delta\sigma$  being dependent upon the testing or solutionizing temperature. Finally, it should be noted that as the test temperature is increased, the stress plateau is less marked; this is due to the fact that the volume fraction of precipitate formed during the relaxation decreases as the test temperature is increased.

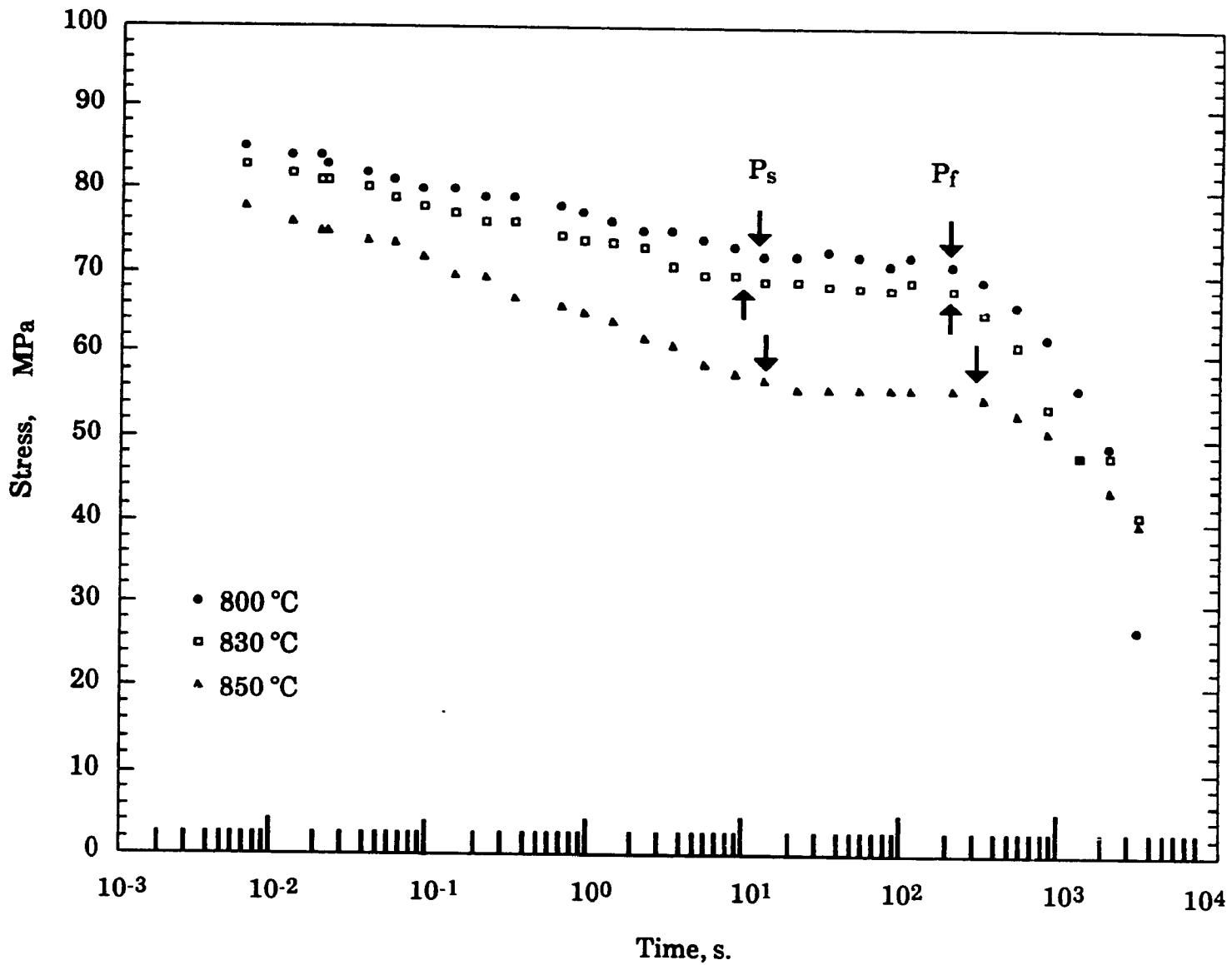


Fig.IV.4 a) Stress relaxation data for the Nb + B steel, solutionized at 1100 °C and deformed 5%.  
 a) 800, 830 and 850 °C; b) 870 and 900 °C

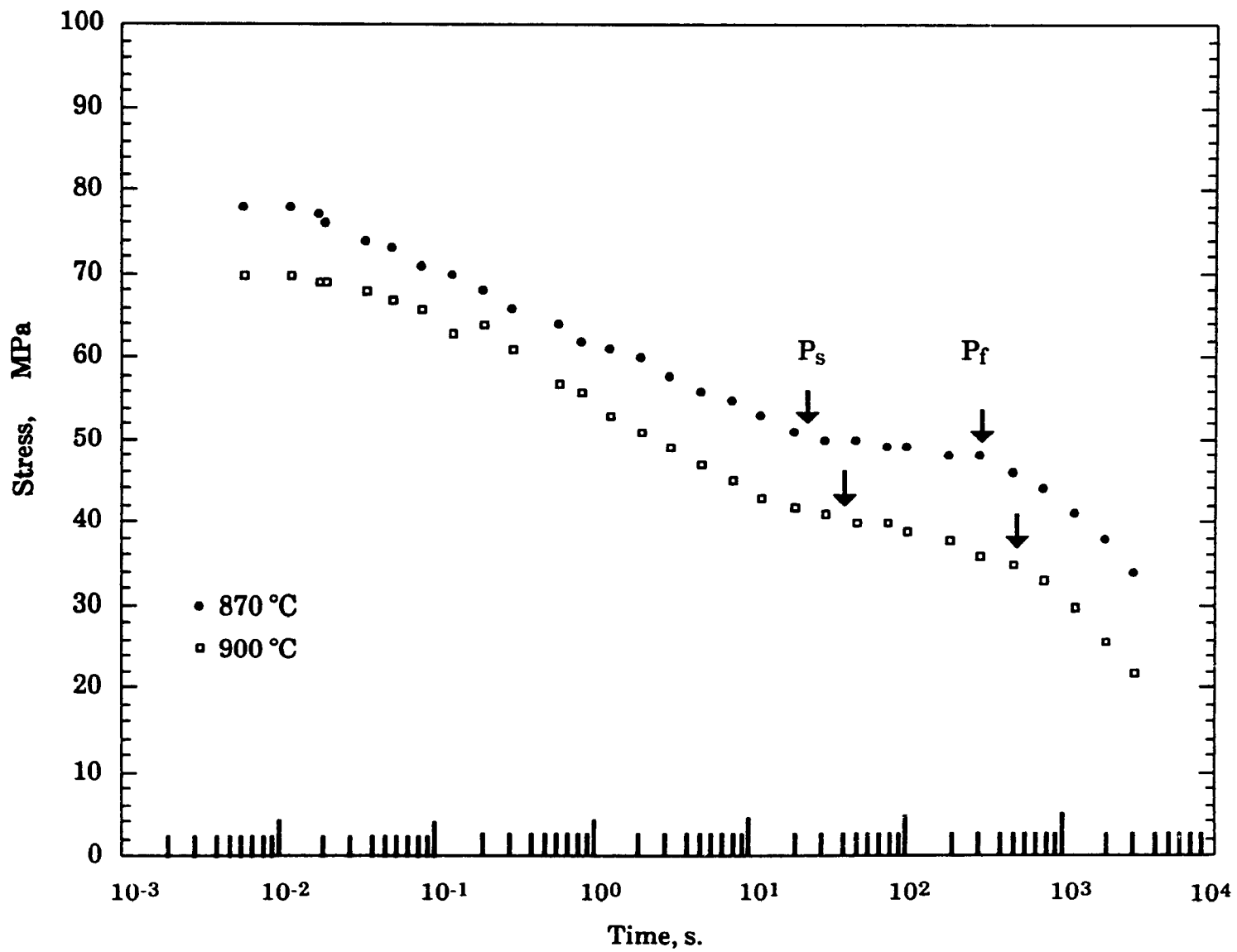


Fig.IV.4 b) Stress relaxation data for the Nb + B Steel, solutionized at 1100 °C and deformed 5%.

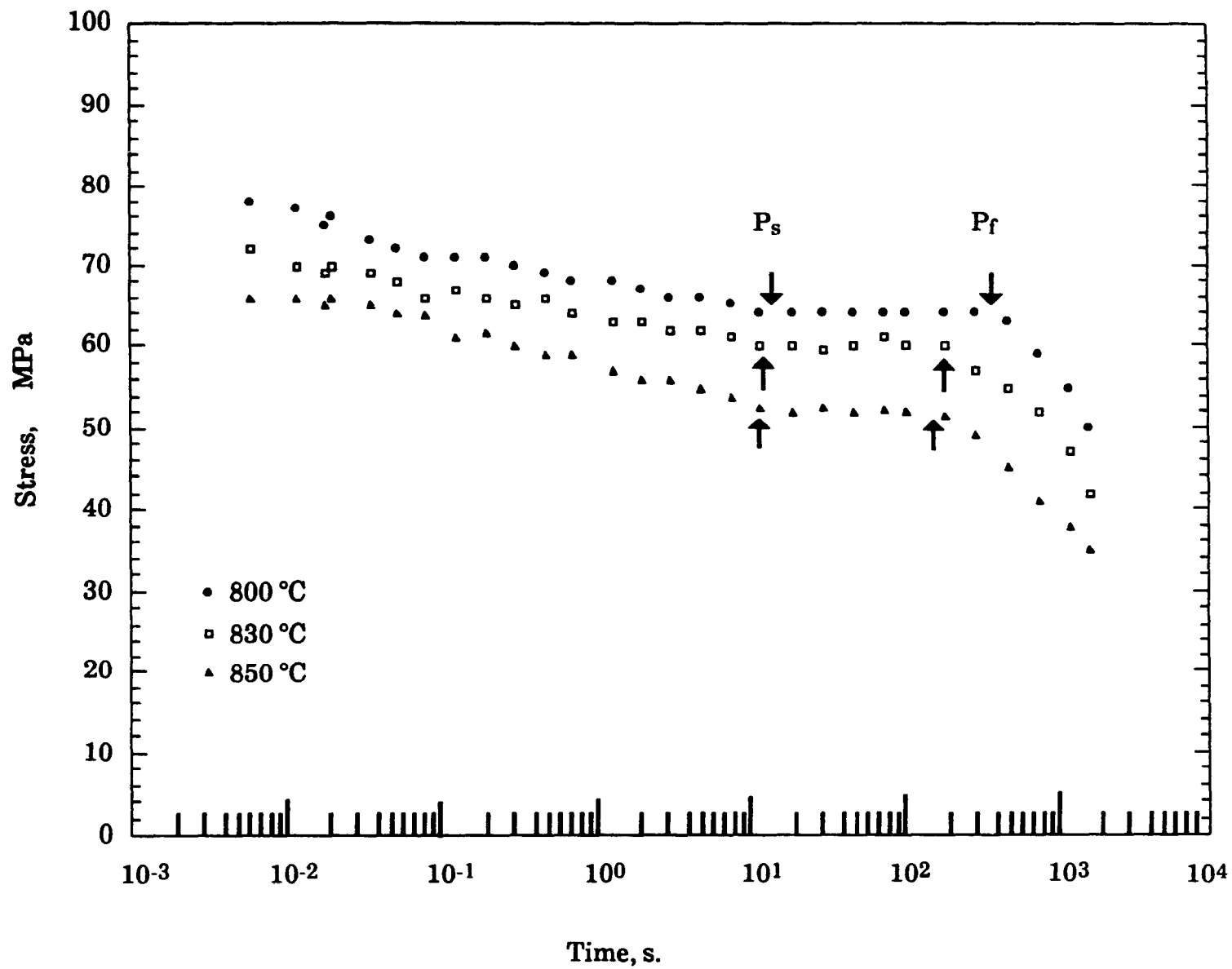


Fig.IV.5 a) Stress relaxation data for the Nb+B steel, solutionized at 1200 °C and deformed 5%.  
 a)800, 830 and 850 °C; b)870, 900 and 950 °C

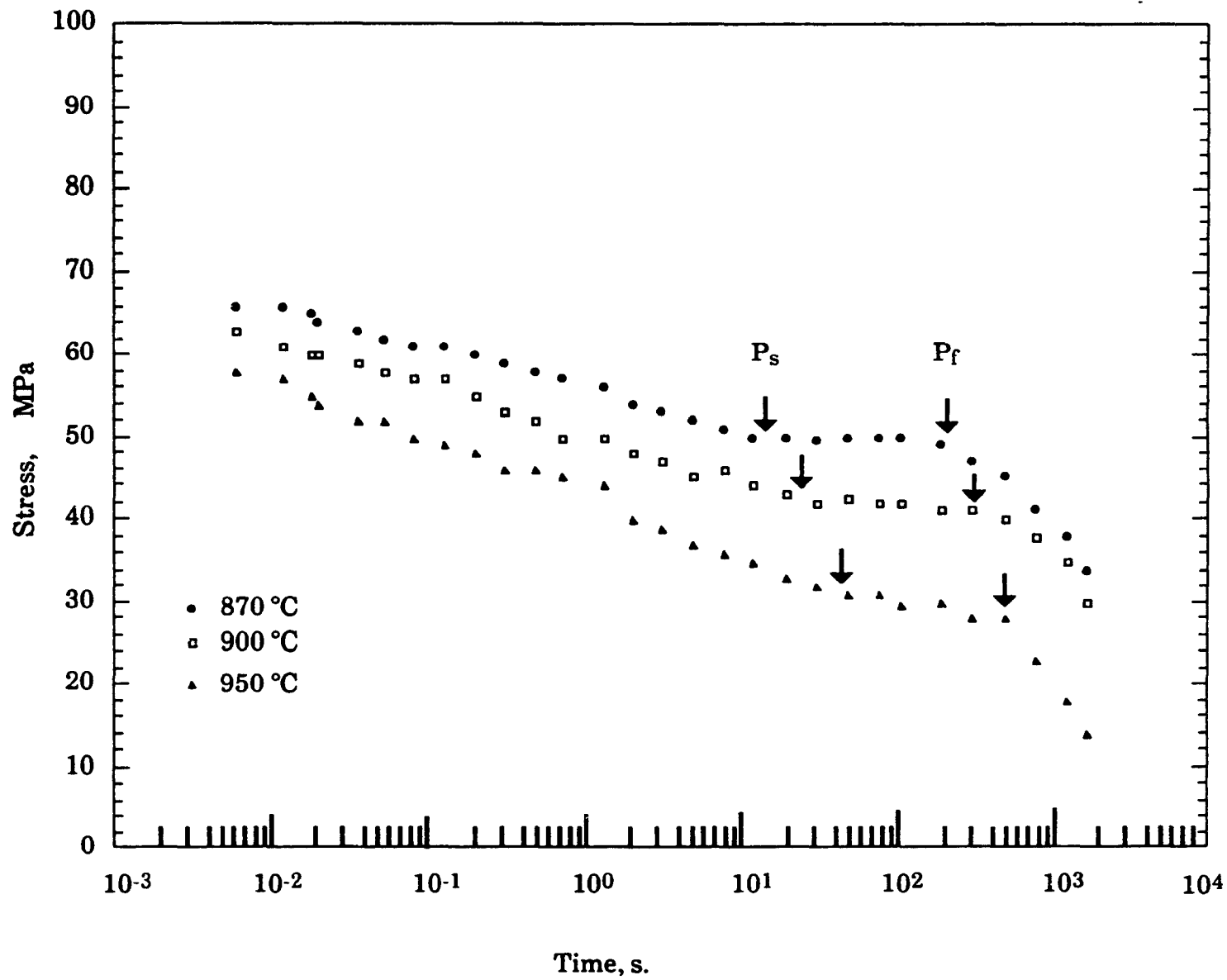


Fig.IV.5 b) Stress relaxation data for the Nb + B steel, solutionized at 1200 °C and deformed 5%.

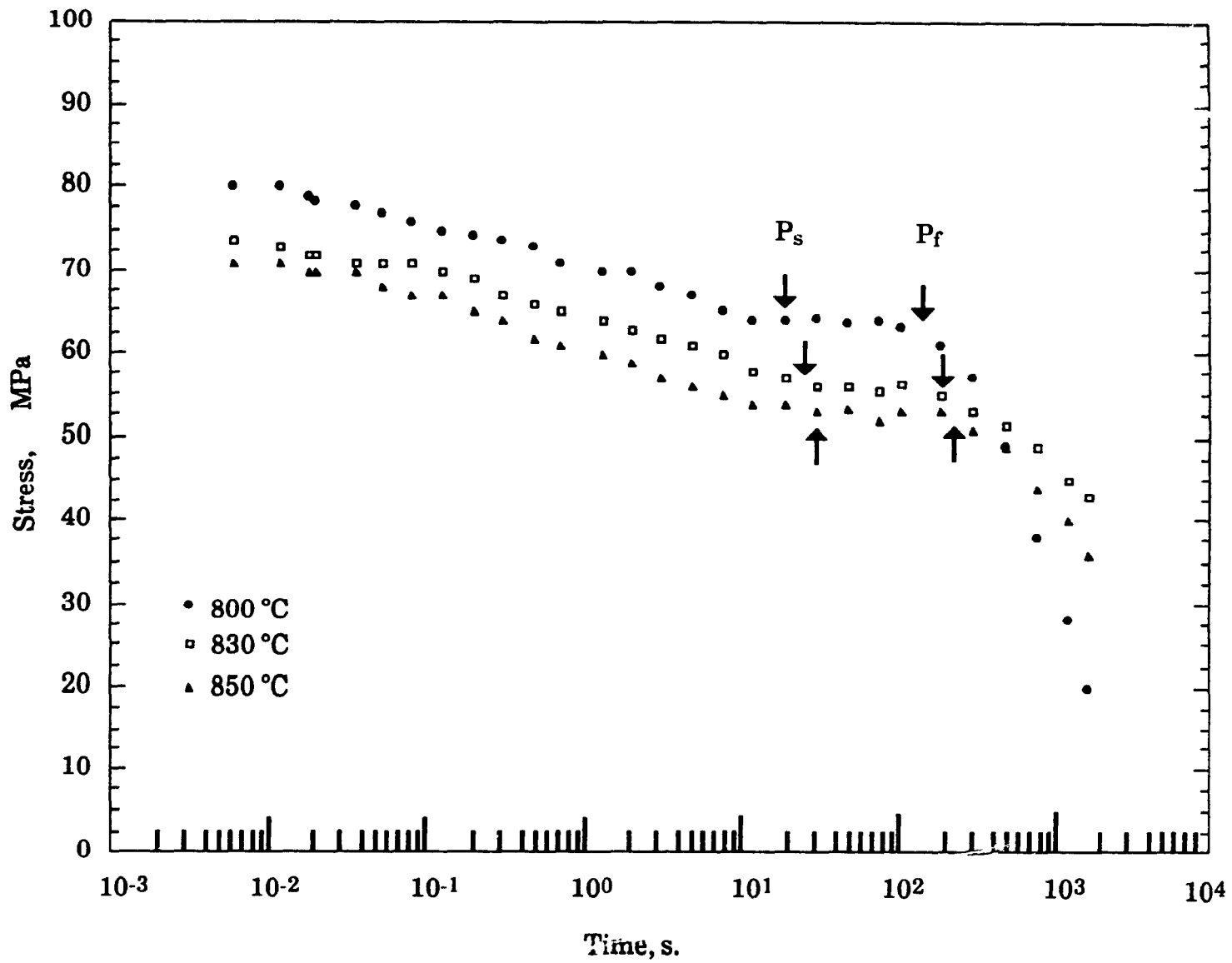


Fig.IV.6 a) Stress relaxation data for the Nb steel, solutionized at 1100 °C and deformed 5%.  
 a)800, 830 and 850 °C;      b)870 and 900 °C

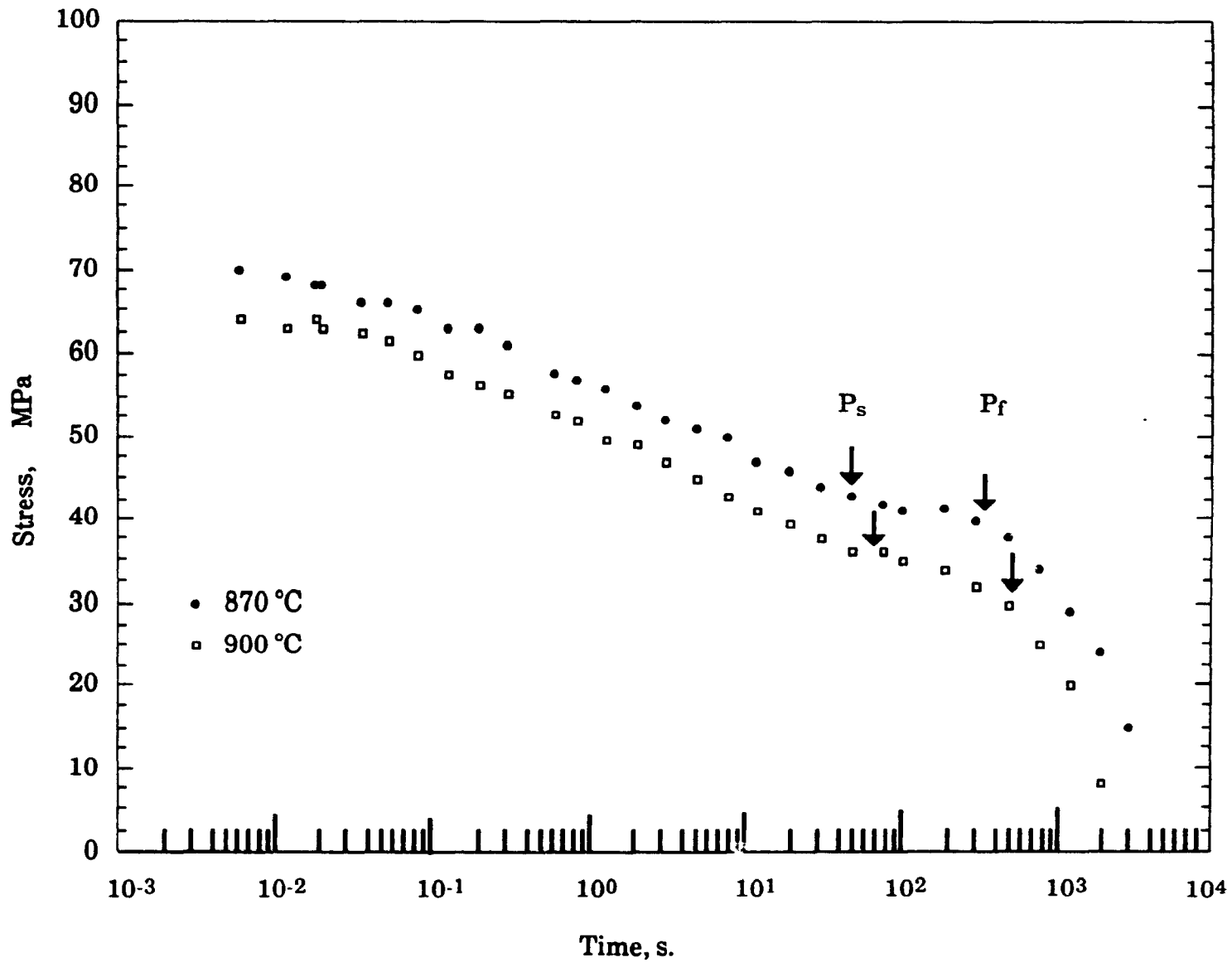


Fig.IV.6 b) Stress relaxation data for the Nb steel, solutionized at 1100 °C and deformed 5%.

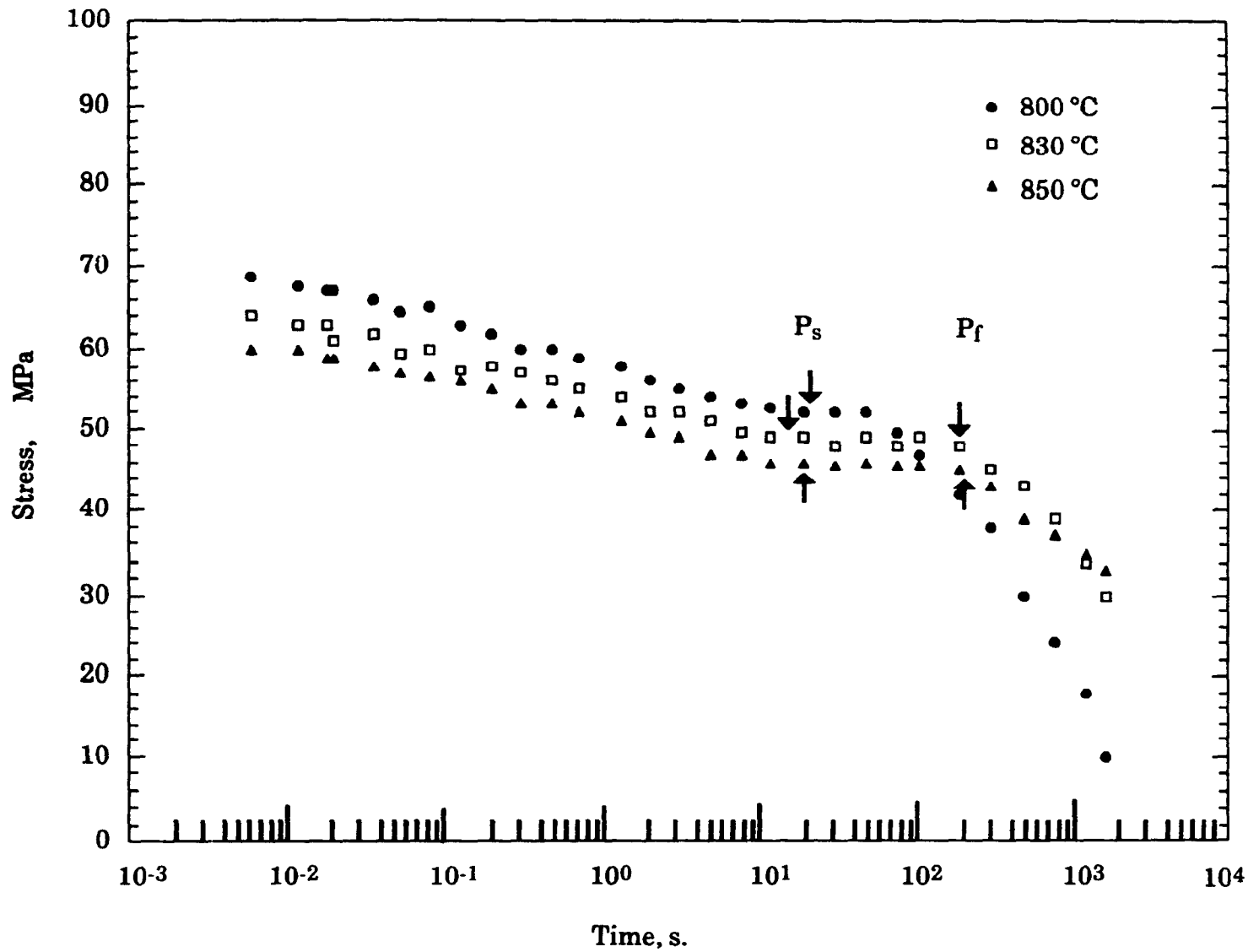


Fig.IV.7 a) Stress relaxation Data for the Nb Steel , solutionized at 1200 °C and deformed 5%.  
 a)800, 830 and 850 °C; b)870, 900 and 950 °C

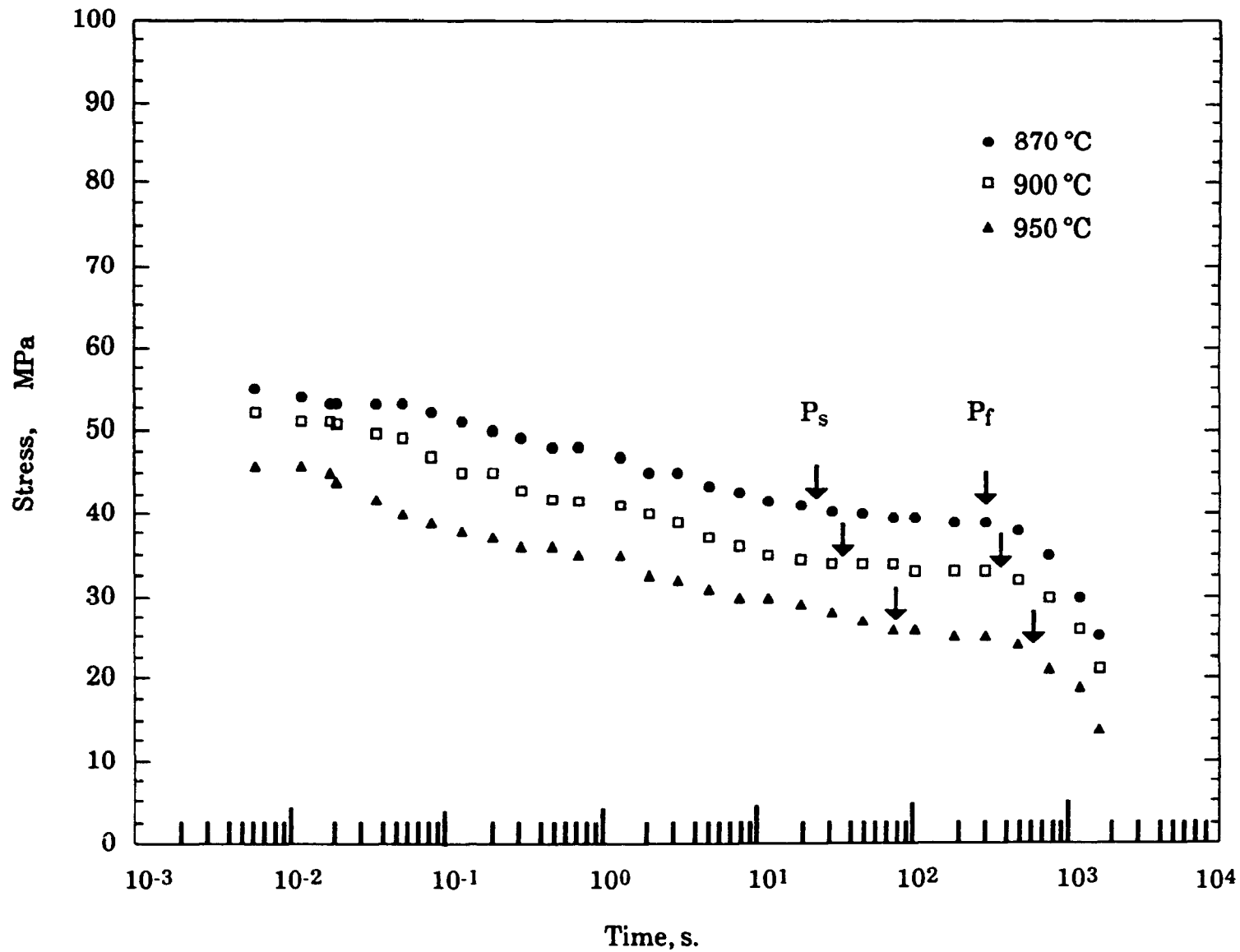
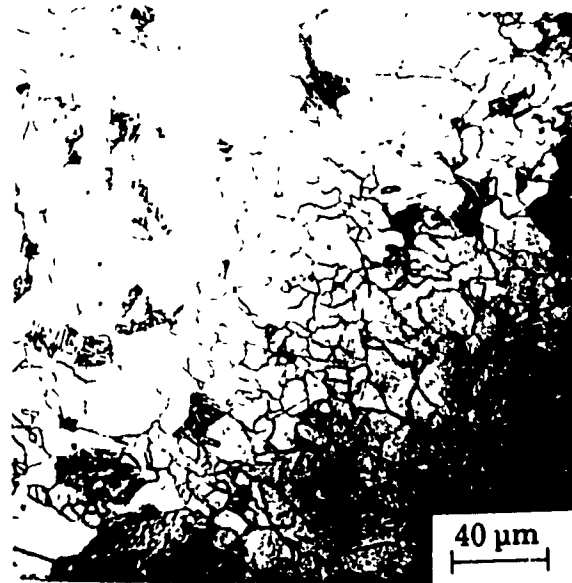
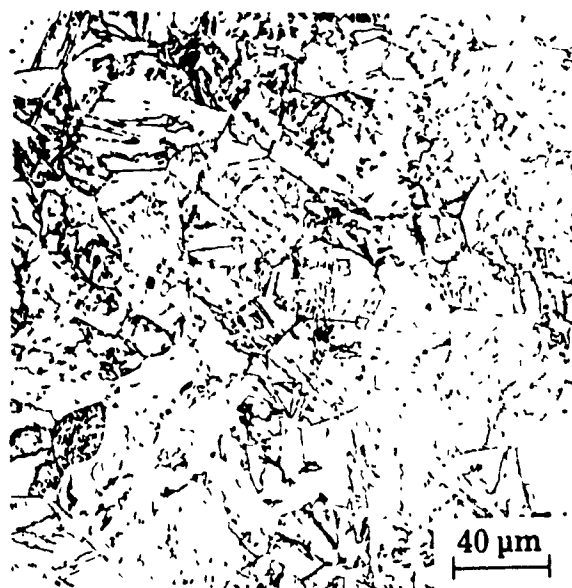


Fig.IV.7 b) Stress relaxation data for the Nb steel, solutionized at 1200 °C and deformed 5%.



Nb



Nb + B

**Fig.IV.8** Microstructures of the Nb and Nb + B steels, quenched after 1800 s of stress relaxation at 800°C.

### IV.2.3. Stress Relaxation Results After 25% Prestrain

Figs. IV.9 and IV.10 illustrate the stress relaxation behaviour of the Nb + B steel preheated to 1100 and 1200°C, respectively, deformed 25% and tested between 800 and 1000°C. The equivalent curves for the Nb steel are presented in Figs. IV.11 and 12, respectively. Generally, three types of relaxation are observed. In the first case, only a plateau appears, indicating that the relaxation process is arrested by precipitation. These curves are similar to those observed after 5% deformation, although the precipitation start times are shorter. In the second case, no plateau appears (tests done at 1000°C), but the slope of the stress versus log (time) curve changes after a certain time and the stress drops much more quickly until the material is almost fully relaxed. Finally, the third type of curve corresponds to the mixed situation where there is first a sudden fall in stress which is later arrested by the appearance of a plateau.

The observed changes in the slope of the stress versus log (time) curve are associated with the occurrence of recrystallization. This claim will be confirmed below when the results of the microstructural examinations will be shown. It should also be mentioned that the general observations made in the previous section about the effect of solutionizing temperature on precipitation start time and the effect of test temperature on the width of the stress plateau are also valid in this case.

### IV.2.4. Precipitation-Time-Temperature Diagrams

Tables IV.2 and IV.3 list the precipitation start ( $P_s$ ) and precipitation finish ( $P_f$ ) times determined from the stress relaxation curves for the Nb + B and Nb steels, respectively. These results are also presented in the form of precipitation-time-temperature (PTT) diagrams in Figs. IV.13 to IV.16. All the PTT curves are of classical C-shape. The driving force for this kind of precipitation is controlled by the degree of supersaturation of the precipitating element (Nb). Above the nose (i.e. at higher temperatures), there is less supersaturation, which reduces the nucleation rate; longer times are then required to start precipitation. Below the nose, on the other hand, the low

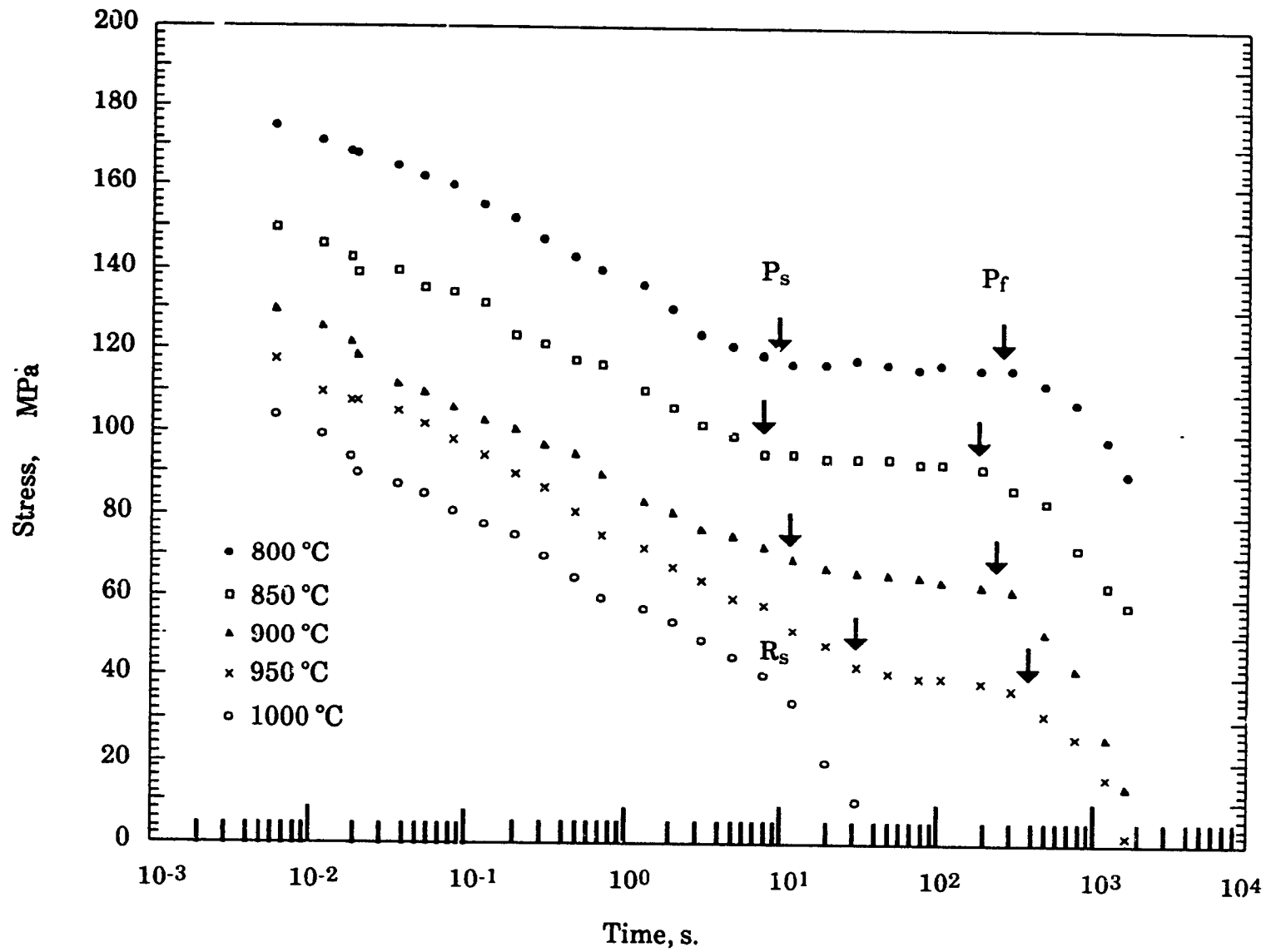


Fig.IV.9 Stress relaxation data for the Nb + B steel, solutionized at 1100 °C and deformed 25%.

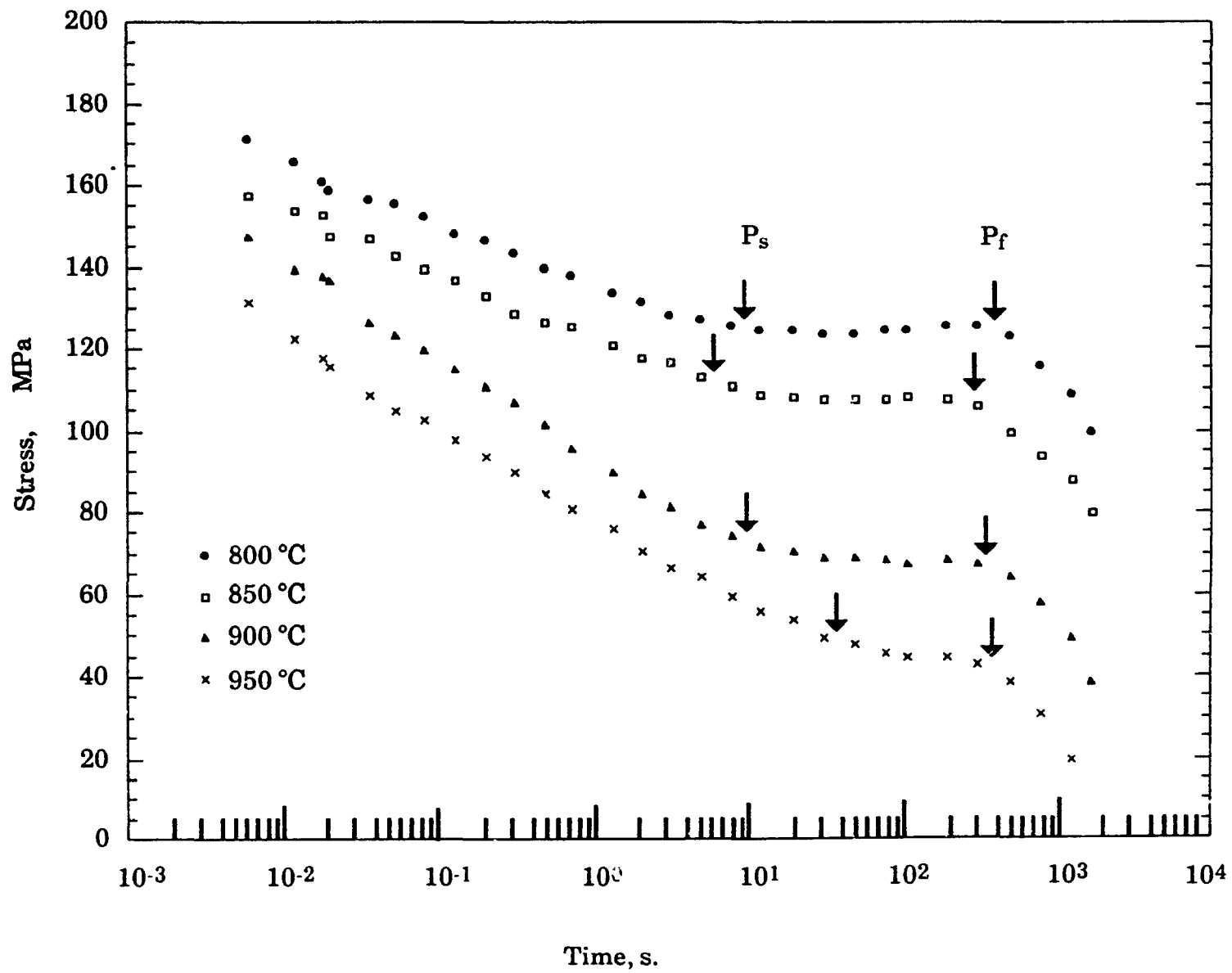


Fig.IV.10 Stress relaxation data for the Nb + B steel, solutionized at 1200 °C and deformed 25%.

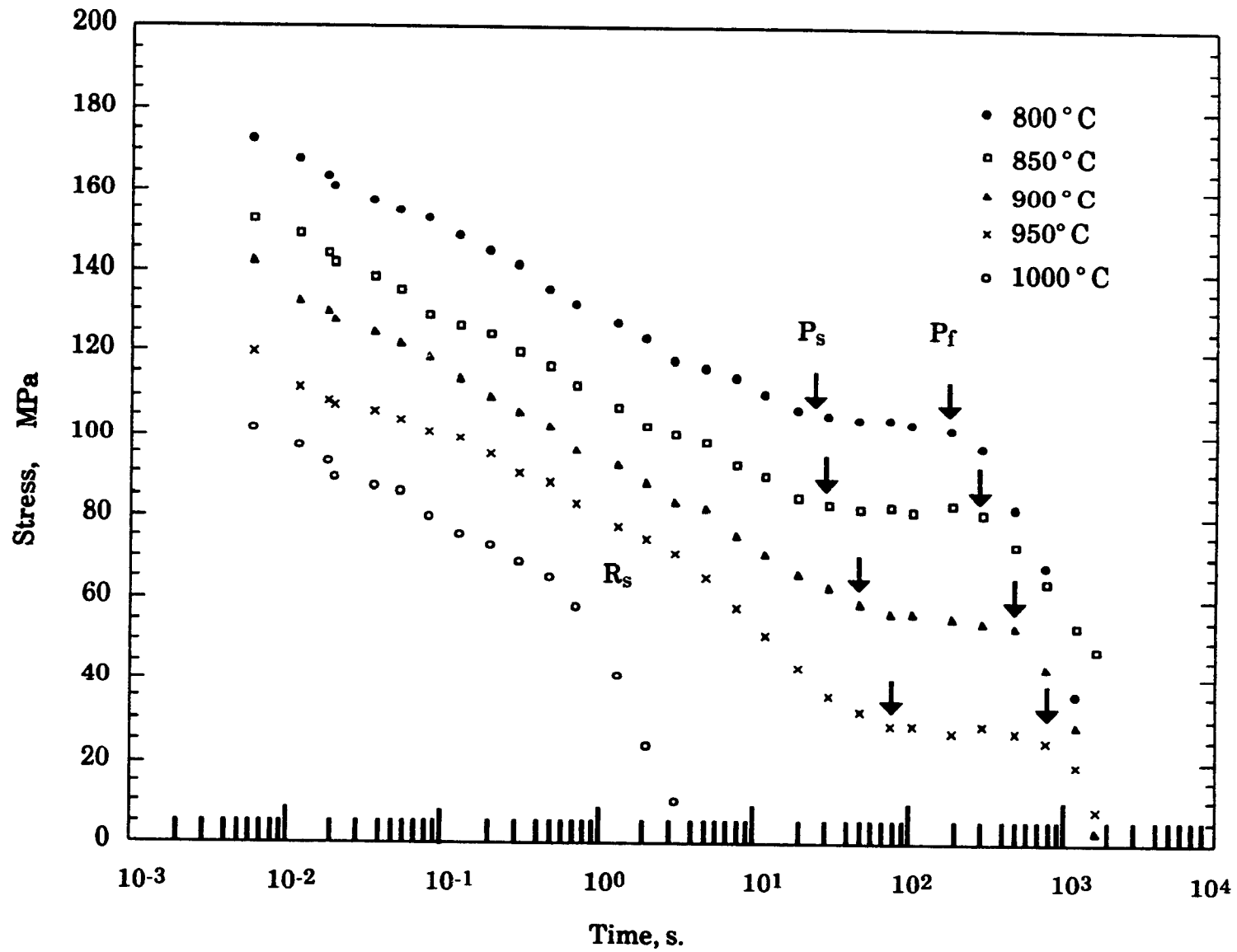


Fig.IV.11 Stress relaxation data for the Nb steel, solutionized at 1100 °C and deformed 25%.

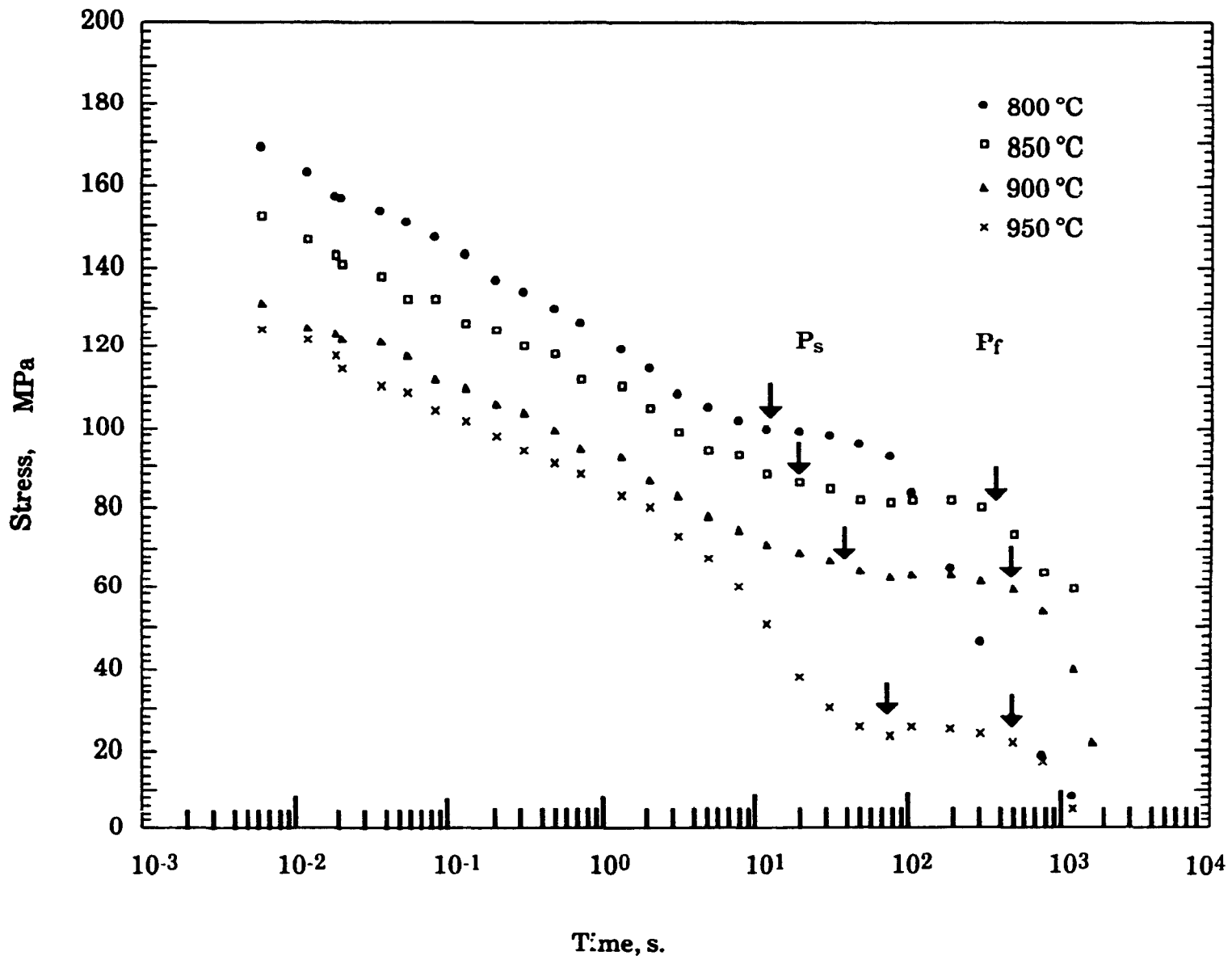


Fig.IV.12 Stress relaxation data for the Nb steel, solutionized at 1200 °C and deformed 25%.

**Table IV.2.**  
**P<sub>s</sub> and P<sub>f</sub> Times for the Nb + B Steel**

Solutionizing Temperature °C	Prestrain %	Test Temperature °C	Time (s.)	
			P <sub>s</sub>	P <sub>f</sub>
1100	5	800	12	200
		830	10	240
		850	12	280
		870	19	330
		900	33	550
1100	25	800	9	290
		850	7	250
		900	11	275
		950	30	450
		1000	-	-
1200	5	800	17	450
		830	14	280
		850	13	250
		870	15	270
		900	22	340
		950	47	510
1200	25	800	9	400
		850	6	300
		900	10	350
		950	35	480
		1000	-	-

**Table IV.3.**  
**P<sub>s</sub> and P<sub>f</sub> Times for the Nb Steel**

Solutionizing Temperature °C	Prestrain %	Test Temperature °C	Time (s.)	
			P <sub>s</sub>	P <sub>f</sub>
1100	5	800	20	180
		830	25	210
		850	33	250
		870	48	360
		900	75	610
1100	25	800	24	250
		850	27	270
		900	46	430
		950	90	710
		1000	-	-
1200	5	800	22	-
		830	18	260
		850	20	270
		870	27	310
		900	35	380
		950	79	600
1200	25	800	15	-
		850	19	420
		900	33	440
		950	80	650
		1000	-	-

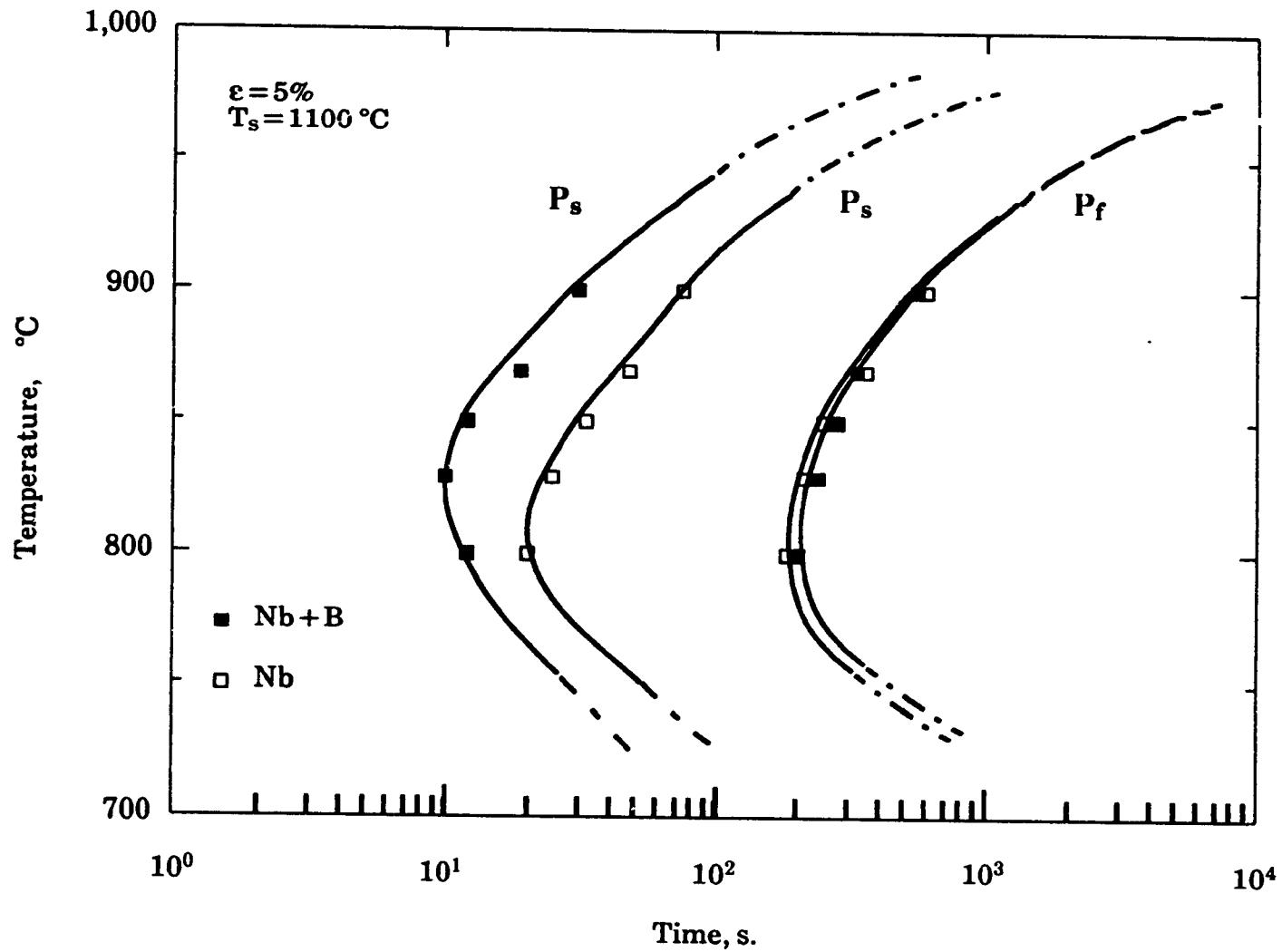


Fig. IV. 13 PTT curves for the Nb + B and Nb steels, solutionized at 1100  $^\circ\text{C}$  and deformed 5%.

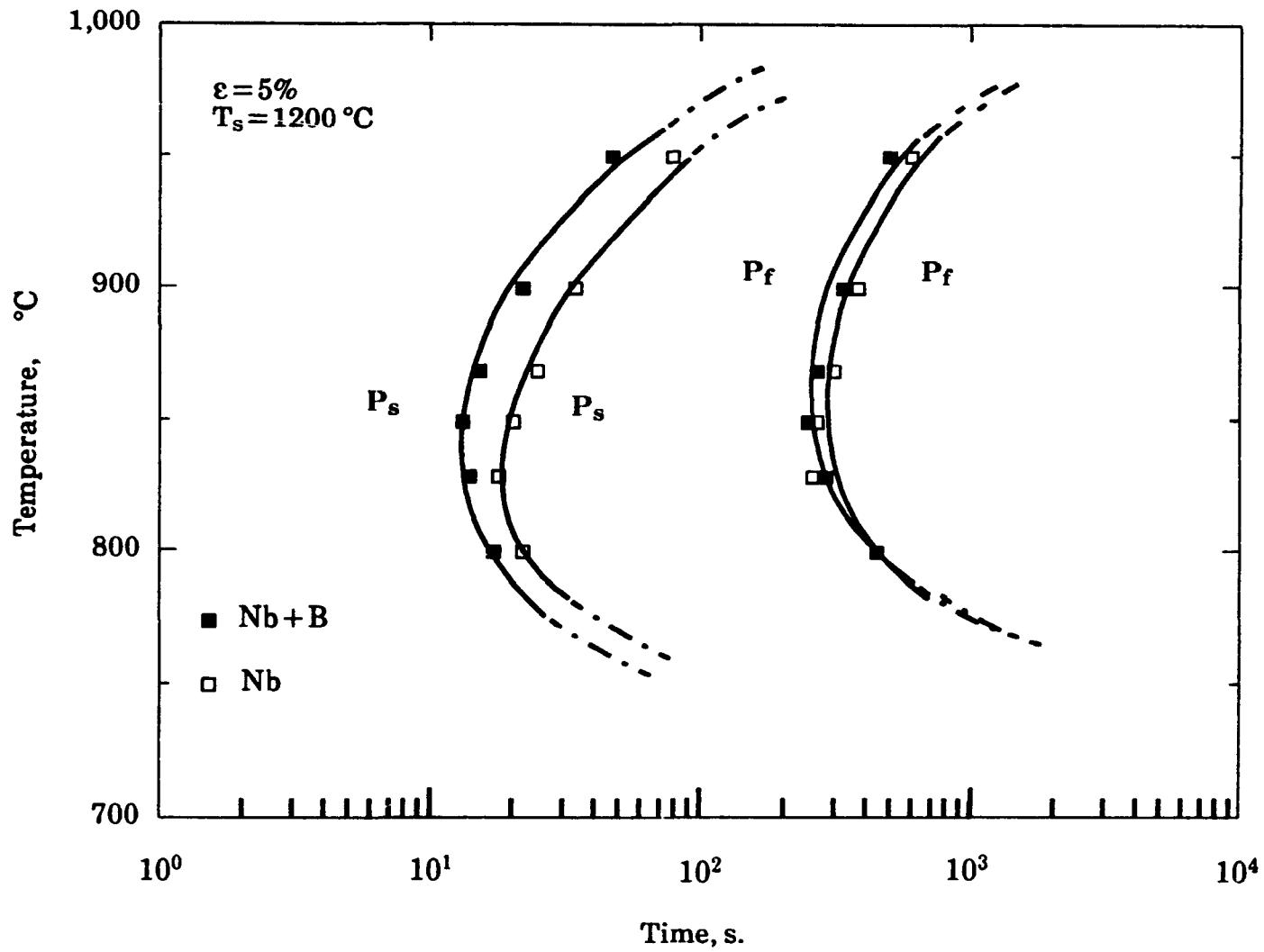


Fig. IV. 14 PTT curves for the Nb + B and Nb steels, solutionized at 1200 °C and deformed 5%.

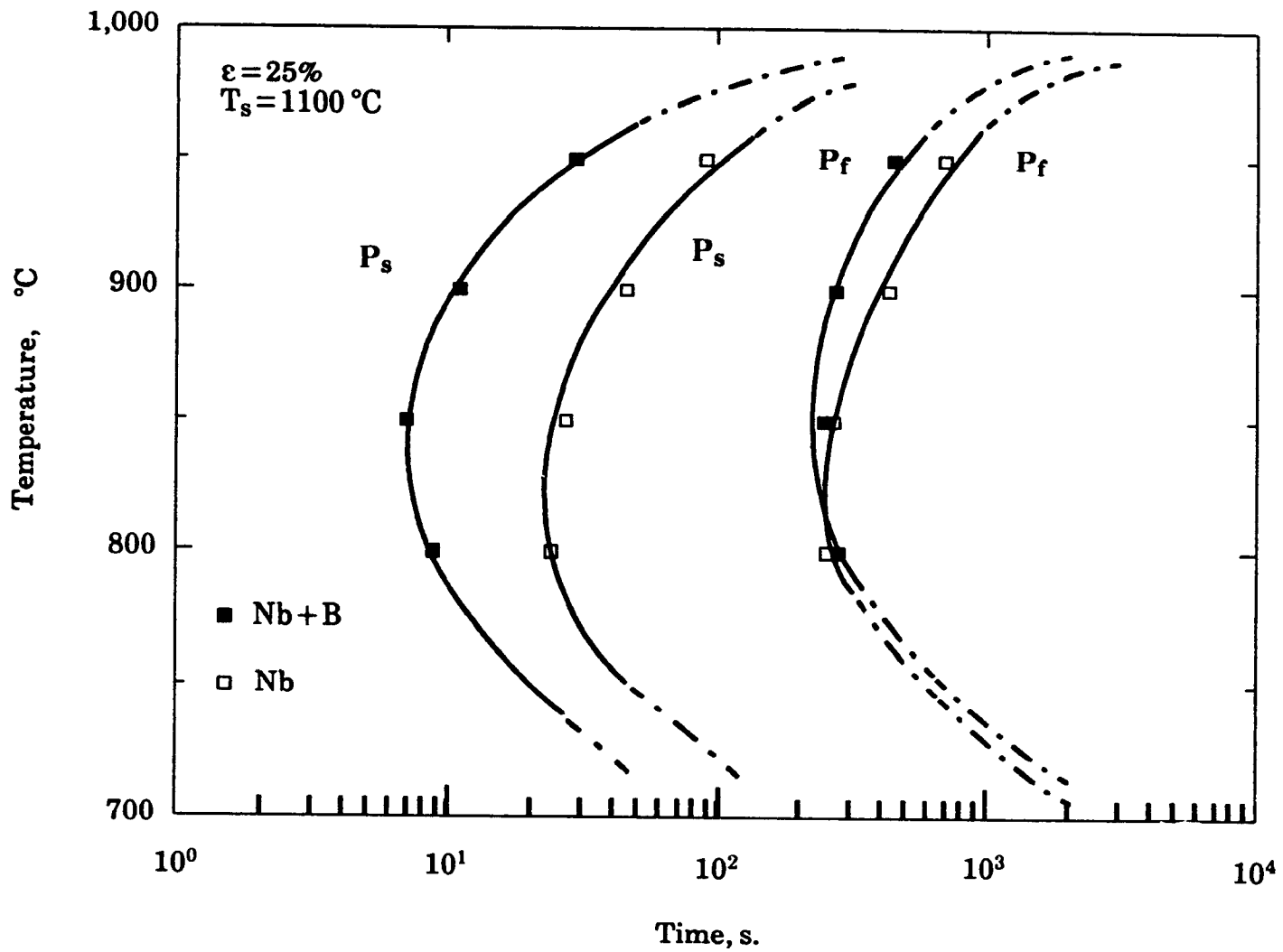


Fig. IV. 15 PTT curves for the Nb + B and Nb steels, solutionized at 1100 °C and deformed 25%.

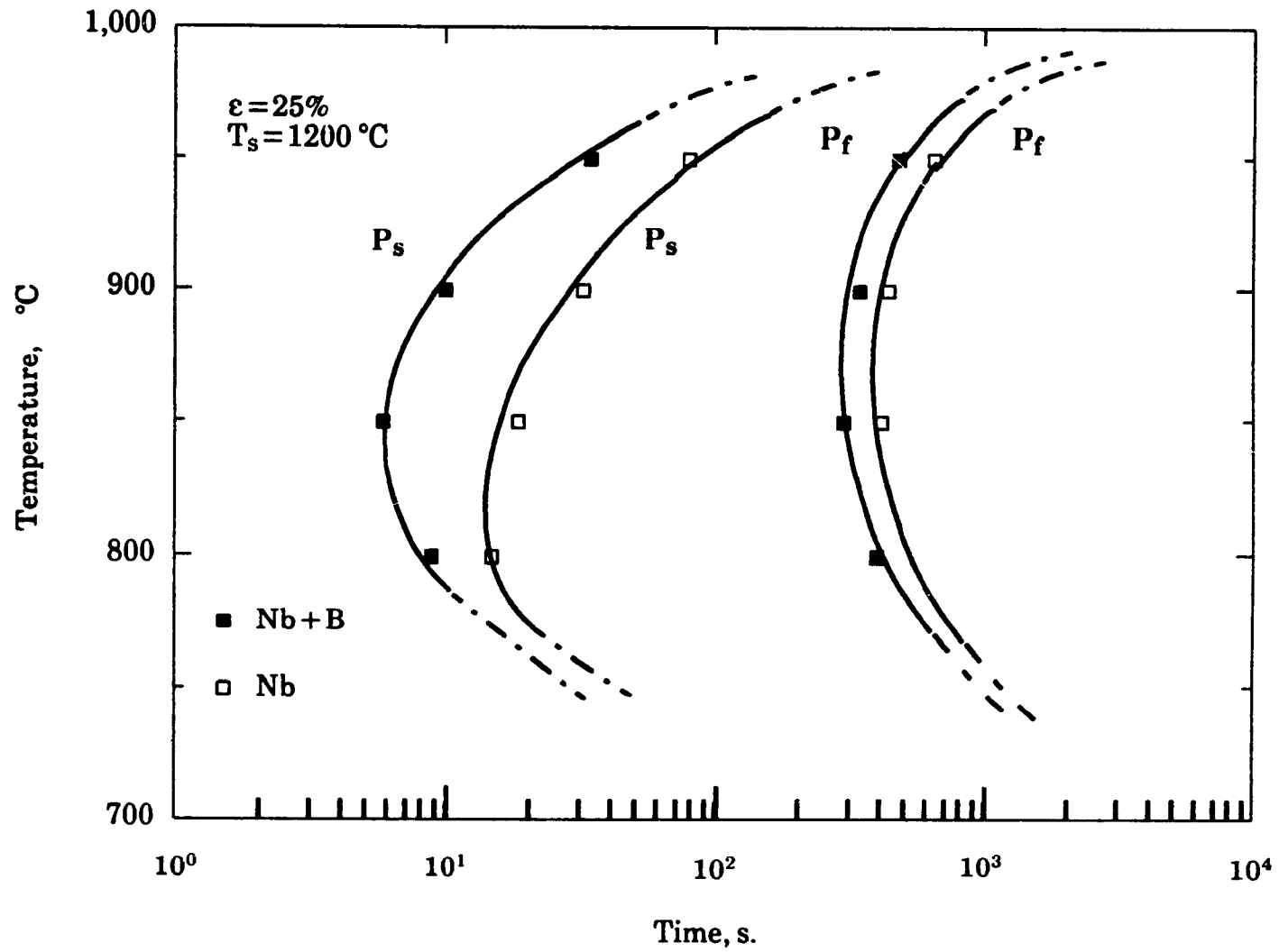


Fig. IV. 16 PTT curves for the Nb + B and Nb steels, solutionized at 1200 °C and deformed 25%.

diffusivity of the precipitating element is the cause of the increase in the start time.

### IV.3. No-deformation Tests

In this series of tests, the influence was investigated of several parameters such as composition, cooling rate, hold time at the test temperature, and quenching rate on the boron distribution and precipitation kinetics. To study the effect of composition on the precipitation behaviour, the Nb + B and Nb steels were used. The comparison between the Nb + B and B steel specimens provides information on the influence of composition on the boron distribution and also on the precipitation kinetics.

Two types of heat treatment were employed in the no-deformation tests (see Fig. III.5). The first used to study the effect of composition and quench rate on boron distribution consisted of cooling the samples very slowly ( $0.5^{\circ}\text{C}/\text{sec}$ ) from the solutionizing to the test temperature and holding for ten minutes. After this constant hold time, the specimens were water or oil quenched. On the other hand, in order to study the effects of deformation and hold time on carbonitride precipitation, samples of the Nb + B and Nb steels were quenched after different hold times. The specimens were cooled in this case to the test temperature at a speed of about  $2^{\circ}\text{C}/\text{sec}$  and water quenched after the appropriate interval of time.

As mentioned in Chapter III, all the no-deformation tests were carried out in an annealing furnace and heat treatment conditions similar to those employed on the MTS machine were produced. Because of the absence of deformation, no mechanical test results are available for these conditions. However, the nature, morphology and size distribution of the precipitates were studied by means of TEM/STEM, while the boron distribution was obtained using the SIMS and PTA techniques. The metallographic examination results will be presented in the chapters that follow.

## CHAPTER V

### METALLOGRAPHIC RESULTS

#### PART 1: TRANSMISSION ELECTRON MICROSCOPY

The influence of composition, deformation and test temperature on the nature of the precipitates and on the progress of carbonitride precipitation were studied by means of electron microscopy. For this purpose, both carbon extraction replicas and thin foils were employed. The carbon replicas were also used to establish the state of the microstructure, and particularly that of the precipitate distribution corresponding to each stage of the stress relaxation process.

After solutionizing at 1200°C, the samples were cooled to the test temperature and were subsequently submitted to a prestrain of 25, 5 or 0%. They were then quenched after different hold times. Table V.1 summarizes the quenching schedules used for the TEM study. The shortest time to quench a sample in the MTS machine was calculated to be between 12 to 16 seconds. In order to quench specimens after shorter delays, the deformation dilatometer at MTL, CANMET was employed. In this machine, the shortest quench time was about three seconds.

##### V.1.1. State of Precipitation After Austenitization

In order to have clear ideas about the precipitation process, it is necessary to know the nature, size and distribution of the precipitates present in the material prior to prestraining. Samples of the three steels were therefore water quenched after solutionizing and carbon extraction replicas were prepared.

Large TiN and MnS particles were found in the four steels. Because of their large sizes, they are believed to have formed at relatively high temperatures. The MnS inclusions all have circular shapes and are not generally found alone, but rather have a TiN particle attached to them. Their mean diameters lay in the range 330 to 370 nm. The large TiN particles on the

**Table V.1.**  
**Identification of the Samples Used for the TEM Study**

Steel	Test Temp. °C	$\epsilon$ %	Time Before Quenching (s.)
Nb + B	1000	25	10, 100
	950	25	20, 100, 1800
	900	25	50, 500, 3600
	850	25	5, 50, 300, 1800
	900	5	10, 200, 500, 3600
	850	5	15, 60, 200, 900, 1800, 3600
	830	5	20, 200, 900
	850	0	30, 150, 600, 3600
Nb	950	25	70, 300, 1000
	900	25	20, 80, 300, 1000
	850	25	10, 50, 300, 1000, 1800
	900	5	30, 100, 300, 1800
	850	5	20, 100, 300, 600, 1800, 3600
	830	5	10, 100, 600, 1800
B	900	25	10, 50, 600
	850	5	25, 40, 100, 200, 300, 600, 1800, 2400

\* C.C. : Control cooled, cooling rate = 13 to 17 °C/sec.

other hand, have cubic shapes and their mean diameter was  $85 \pm 28$  nm (as measured on 60 individual particles). The scatter in size distribution was almost the same for all four steels. This indicates that the presence of boron does not influence the morphology and distribution of the large undissolved TiN and MnS inclusions. Finally, it should be mentioned that because of their large sizes, these particles are not likely to play significant roles during the recrystallization or precipitation processes that will take place later in the hot worked austenite.

Apart from the above-mentioned precipitates, a second group of much smaller particles was also found after the solutionizing treatment. These were

complex (Ti,Nb) precipitates ranging from 25 to 30 nm in diameter and present throughout the matrix. They all had cubic shapes and their EDX spectra showed that they are rich in Ti. In the case of the boron steel, the small precipitates contained only Ti, indicating in this way that they are TiN particles.

### V.1.2. State of Precipitation After Testing

Regardless of the testing conditions, the observed precipitates could be divided into two groups from the point of view their size. The first consists of very large particles ( $\geq 1 \mu\text{m}$ ) produced during cooling or isothermal holding. The second group is composed of much smaller precipitates (5 to 30 nm) which precipitate after deformation. In the sections that follow, the characteristics of each group will be described.

#### V.1.2.1. Nature and Distribution of the Large Precipitates

This kind of precipitation is observed both in the Nb+B and B steels independently of the experimental conditions. The large particles are present at prior austenite grain boundaries, although some intragranular ones were also found in the samples quenched from low testing temperatures (800 or 850°C) or after long holding times.

The size of these precipitates increases as the testing temperature decreases and/or long holding times are employed. All the particles were found to be rich in iron; however, in some cases, the presence of Ti or Ti and Nb was also detected.

As mentioned in chapter II, there is considerable evidence in the literature that the iron-rich phase in boron-containing microalloyed steels is  $M_{23}(C,B)_6$  precipitate, with  $M = \text{Fe, Cr and Mo}$  [14, 65, 146]. Consequently, no structure determination was carried out and it was assumed that the precipitates at the austenite grain boundaries are also  $M_{23}(C,B)_6$  borocarbides.

Several authors [34, 151] have already reported that extraction replicas of these precipitates are difficult to prepare because of the easy dissolution of the borides in the usual etching and polishing solutions. The same problem was

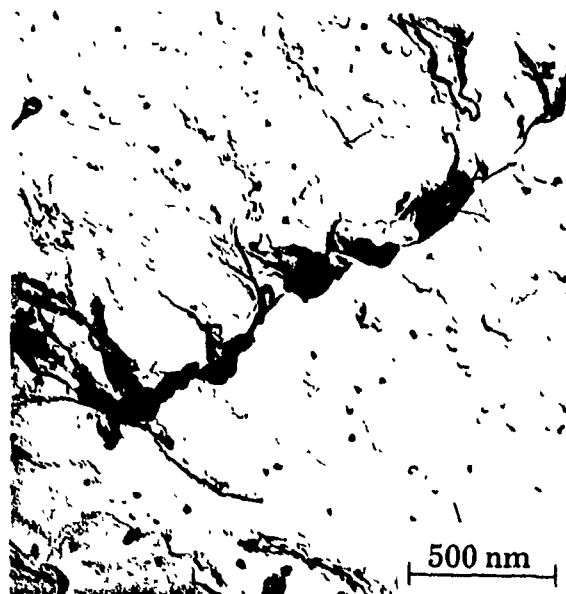
encountered in this study; nevertheless, we were successful in some cases. In fact, in order to avoid the dissolution of iron borocarbides, the samples must be etched very lightly before and after coating. Figs.V.1a and b illustrate electron micrographs and the corresponding EDX spectra of the  $M_{23}(C,B)_6$  borocarbides found in a B steel specimen held 30 min at 850°C. It should also be mentioned that, although the etching was light, there is always some dissolution of the precipitate. Consequently, the observed size in the microscope is not representative of the true size of the particle.

Finally, it should be mentioned that the PTA and SIMS results also indicated the presence of large boron-rich precipitates at the austenite grain boundaries. On the other hand, because of their large sizes, these precipitates were also seen by optical microscopy. The PTA and SIMS results will be presented in the second part of this chapter.

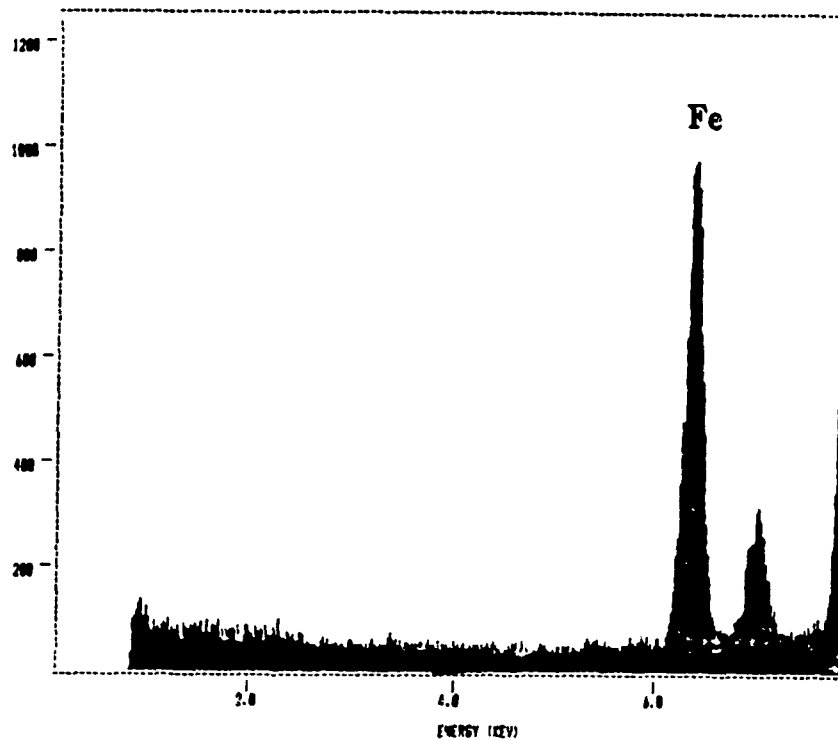
#### V.1.2.2 Nature and Distribution of the Small Precipitates

This part only concerned the Nb+B and Nb steels, because similar intracrystalline Nb-rich precipitates were found in both steels. This group is composed of (Ti, Nb)-rich precipitates, 25-30 nm in diameter, and Nb-rich particles 5-30 nm in diameter. In Fig.V.2, micrographs of such complex (Ti,Nb) and Nb-containing precipitates are presented, along with their EDX spectra. These figures pertain to a Nb+B steel specimen after stress relaxation at 850°C (25% deformation) for 15 and 1800 s, respectively. It should also be pointed out that large precipitates were found at the grain boundaries in both steels. Microanalysis revealed that, shortly after deformation, they are rich in Ti. As the holding time is increased, they become more and more rich in Nb, such that at the end the Ti is swamped and only a Nb peak is found in the EDX spectra.

It was mentioned in the literature review part (II.7.2), almost all the carbides and nitrides of Ti and Nb have the NaCl (B1) crystal structure, with metallic atoms in the fcc positions and C and/or N in the interstitial sites. Consequently, the morphologies of the (Ti,Nb) rich precipitates and those of the Nb-



a)



b)

Fig.V.1 Carbon extraction replicas showing iron containing precipitates along with their EDX spectra, observed in the B steel after 1800 s of holding at 850°C.

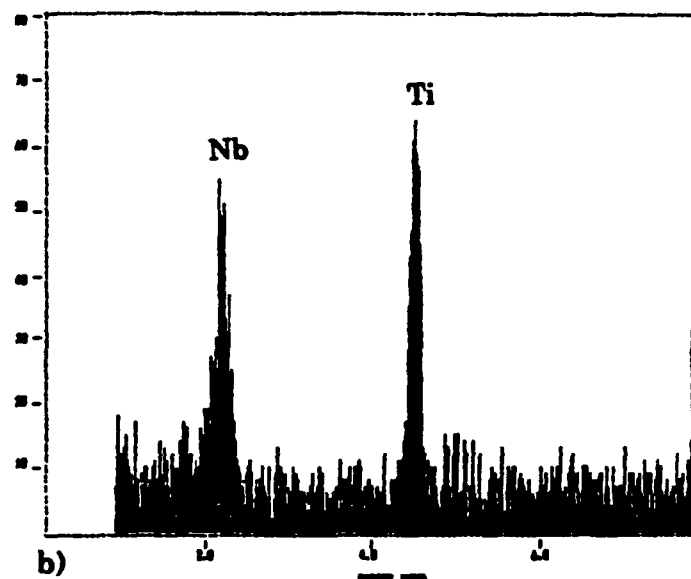
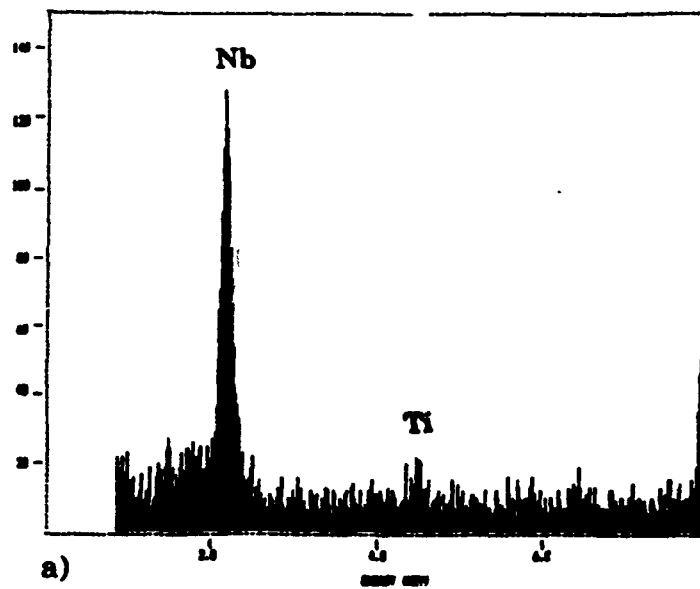
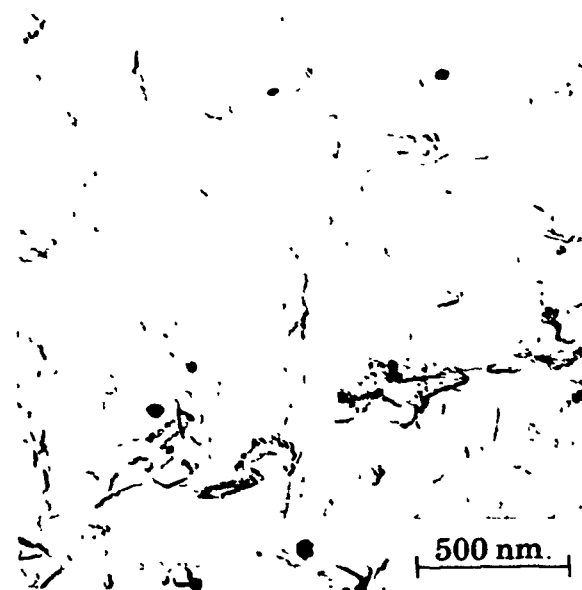
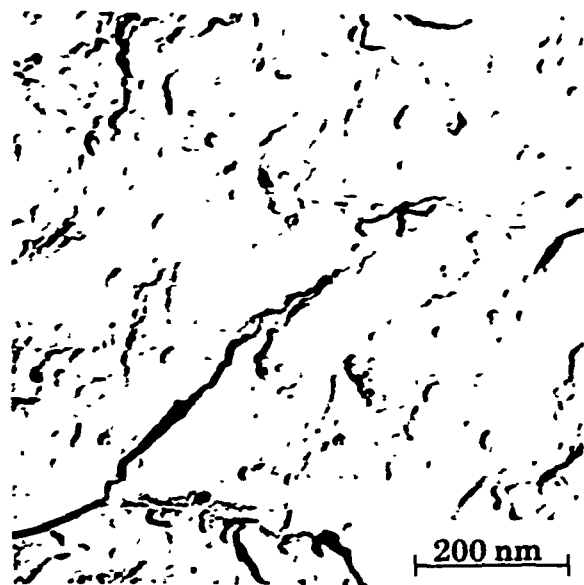


Fig.V.2 Carbon extraction replicas and the EDX spectra of : a) a Nb rich precipitate, and b) a complex (Ti, Nb) precipitate.

rich ones are similar. This similarity makes difficult the distinction between precipitates of similar size but of different chemical composition. This problem arises mainly after long holding times, where the sizes of the strain-induced precipitates (i.e. the Nb-rich ones) are close to those of the undissolved (Ti,Nb) particles. It is important to mention that, because of their sizes, the (Ti,Nb) precipitates do not affect the process of stress relaxation and only the Nb-rich precipitates, which nucleate after deformation, influence the relaxation.

In view of the TEM observations described above, it can be said that five kinds of precipitate were detected in the investigated materials. These are MnS,  $M_{23}(C,B)_6$ , Ti-rich, (Ti,Nb)-rich and Nb-rich particles. Only the first three exist in the boron steel, while all of them were found in the Nb + B and Nb steels. The undissolved MnS and Ti-rich precipitates and the iron borocarbides were much larger than the two other types. Finally, the composition of the complex (Ti, Nb) precipitates was not constant and an evolution was observed. This situation is illustrated in Fig.V.3, where the change in the Ti/Nb ratio with increasing holding time is depicted for the Nb + B steel tested at 850°C and deformed 25%. It should be added that the same kind of behaviour occurred in the Nb steel.

### V.1.3 Identification of the Interstitial Elements by EELS

#### V.1.3.1 Introduction

Although EDX spectra give valuable information regarding the composition of the precipitates, they cannot provide data regarding the nature of the interstitials present in the particles. Carbon, N and B can combine with the precipitate forming elements leading to the formation of complex compounds. The existence of mixed carbonitrides with general formulae of  $Nb(C_x, N_{1-x})$ ,  $Ti(C_x, N_{1-x})$  and  $(Ti_y, Nb_{1-y})(C_x, N_{1-x})$  has been solidly established and numerous investigations have been carried out on different aspects of this kind of precipitate. However, although there is general agreement that boron can enter into the structure of the carbonitrides, to our knowledge, no data have been published regarding the presence of boron in strain-induced (Ti, Nb) or Nb carbonitrides.

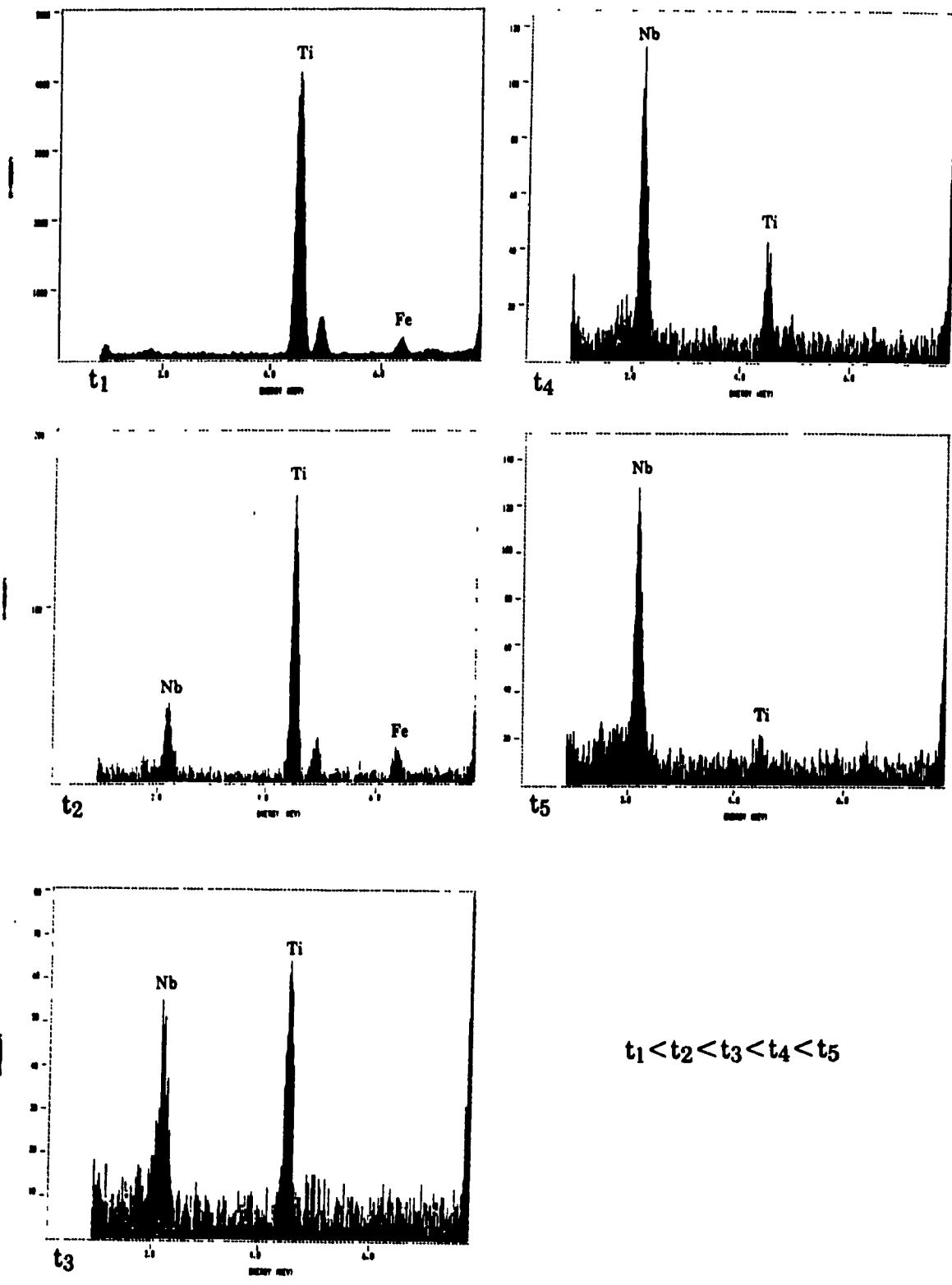


Fig.V.3 EDX spectra showing the evolution in precipitate composition during stress relaxation in both Nb + B and Nb steels.

In order to obtain some information about the nature of the interstitial elements present in the different kinds of precipitate found in our steels, the EELS technique was employed. Although EELS is able to detect light elements such as B, C and N, it was found [152] that boron detection is more difficult than that of carbon and nitrogen. The detection limit for boron was estimated to be between 3 to 5% of the boron atoms present in the precipitates.

The investigation was carried out on carbon extraction replicas. Consequently, the interpretation of the results regarding the presence of carbon in the particles was difficult. However, based on the data in the literature, it can be concluded that carbon is present in all the strain induced precipitates. The study was limited to the case of the Nb + B steel due to the fact that the precipitates present in this steel are similar to those found in the Nb steel. For the case of the boron steel, as the presence of boron in the iron rich precipitates has been clearly established, no EELS investigation was attempted.

#### V.1.3.2 The Analysis

The analysis of the large Ti-rich precipitates indicated the presence of N confirming that they are TiN particles. A carbon peak was also observed, which was believed to originate from the carbon film. Even if some carbon is present within the precipitate, its concentration is expected to be small. This kind of reasoning is only valid for the large precipitates which were formed at high temperatures and consequently should mostly contain N as the interstitial element. No sign of boron was found in any of the large TiN precipitates analyzed.

The presence of boron was detected, however, in the (Ti, Nb) and Nb-rich precipitates. Fig.V.4 illustrates an electron micrograph of a Nb + B steel specimen deformed 25% at 850°C and quenched after 1800 s of stress relaxation. As can be seen, there is a clustering of the precipitates. In Figs.V.5 to 7, the EELS spectra corresponding to the areas labelled 1, 2 and 3, respectively, in Fig.V.4 are reproduced. The presence of boron in the Nb carbonitride precipitate presented in area 1 of the Fig.V.4 is clearly verified. The boron signals recorded on the other precipitates are weaker; this is believed to be related to the difficulty of detecting small amounts of this element by EELS.

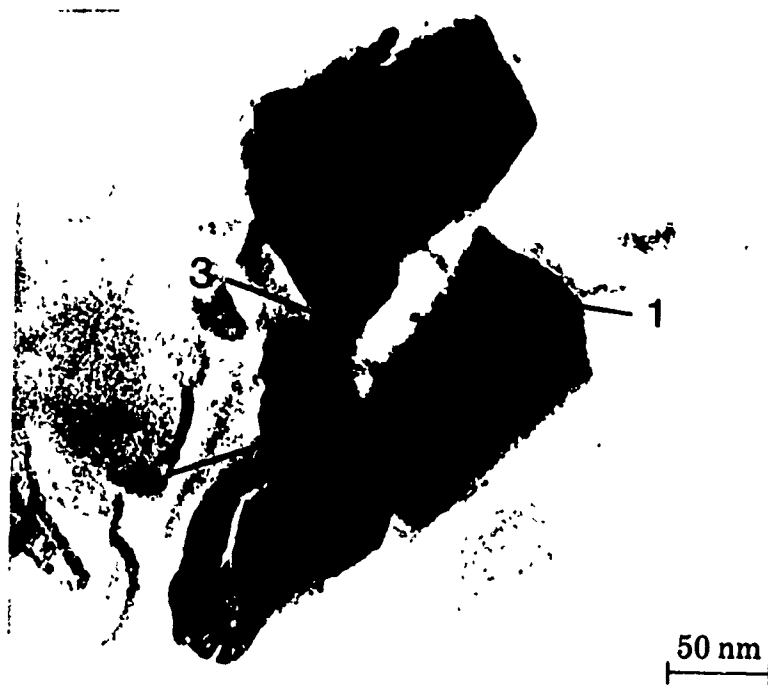


Fig.V.4 Cluster of B-containing precipitates.

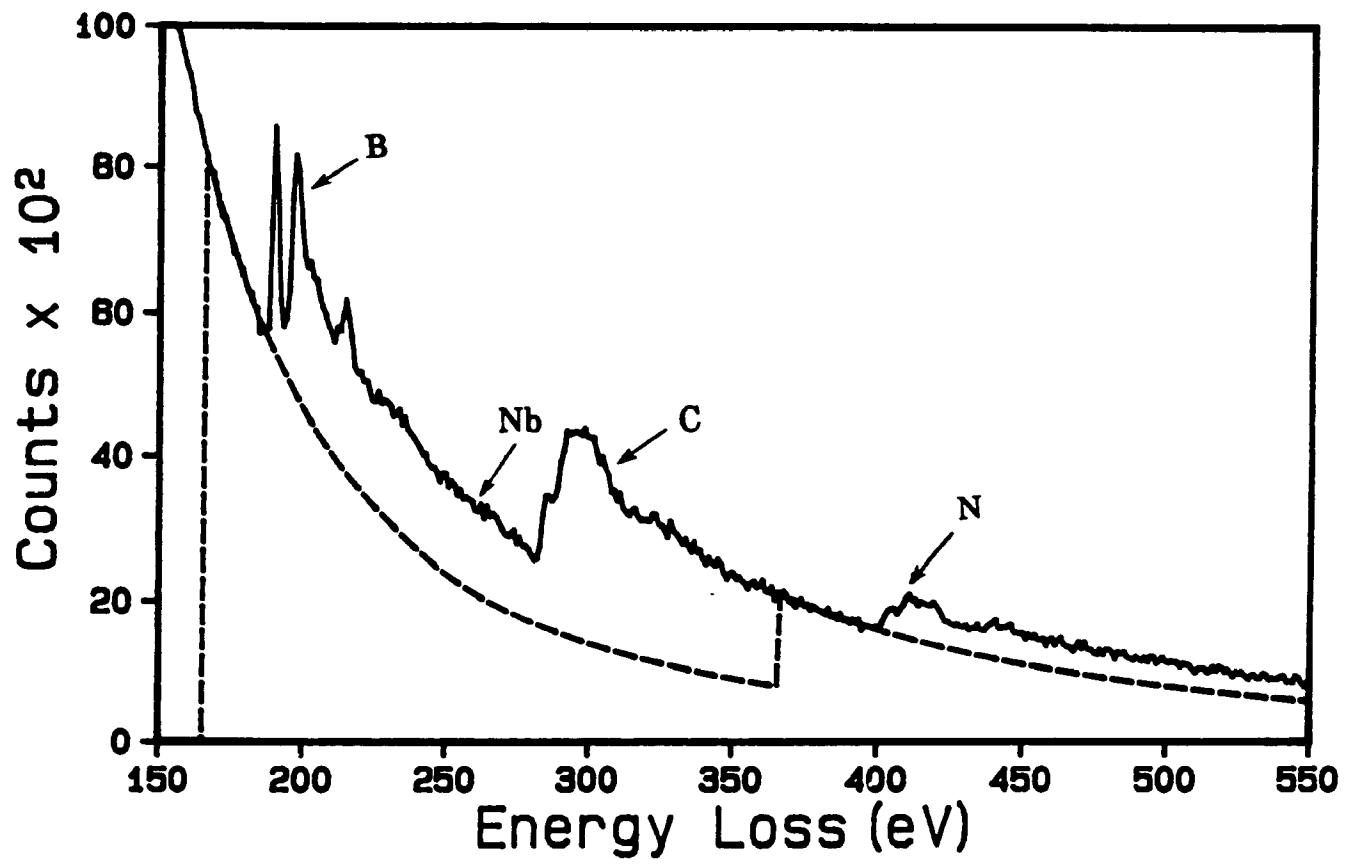


Fig.V.5 EELS spectra showing area 1 in Fig. V.4.

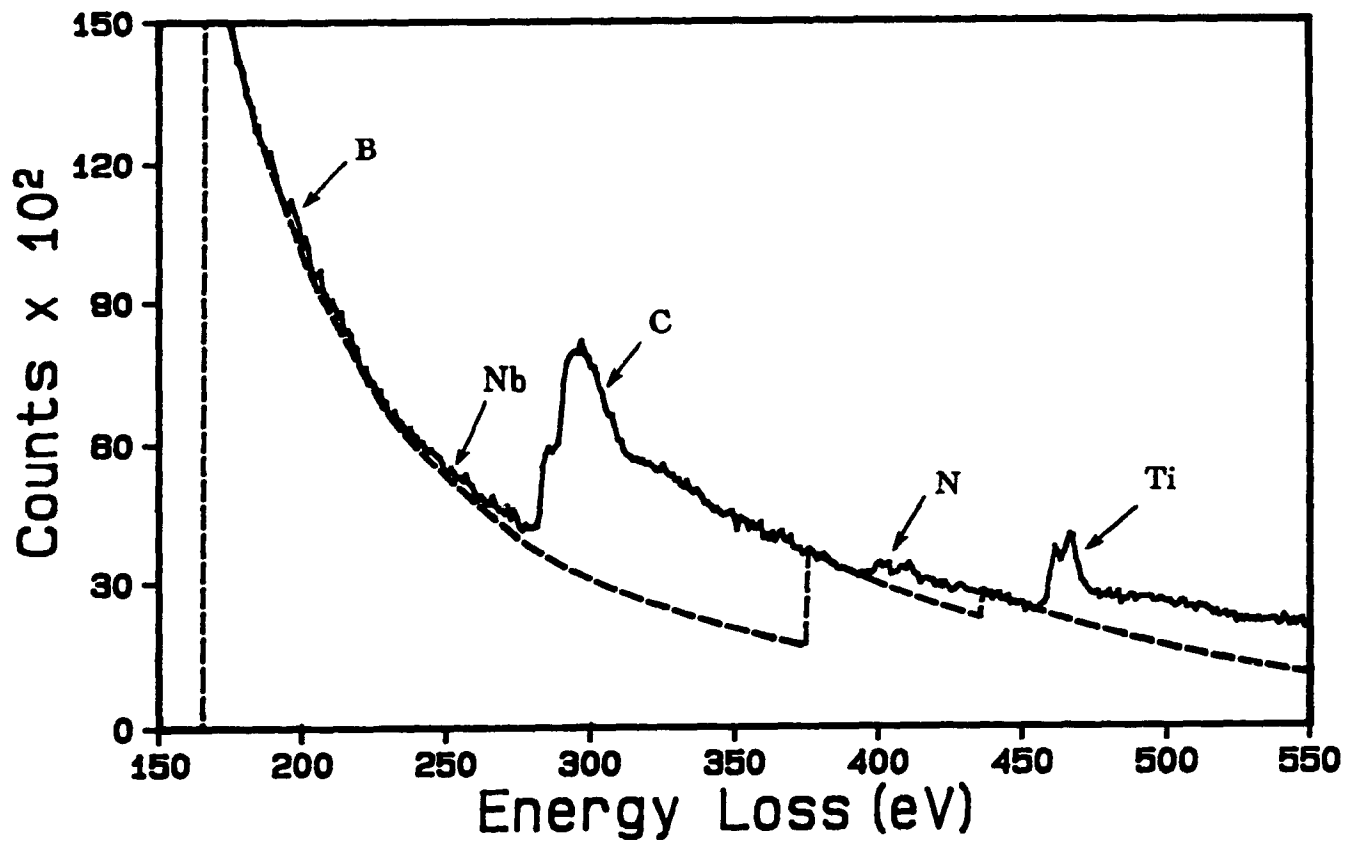


Fig.V.6 EELS spectra showing area 2 in Fig. V.4.

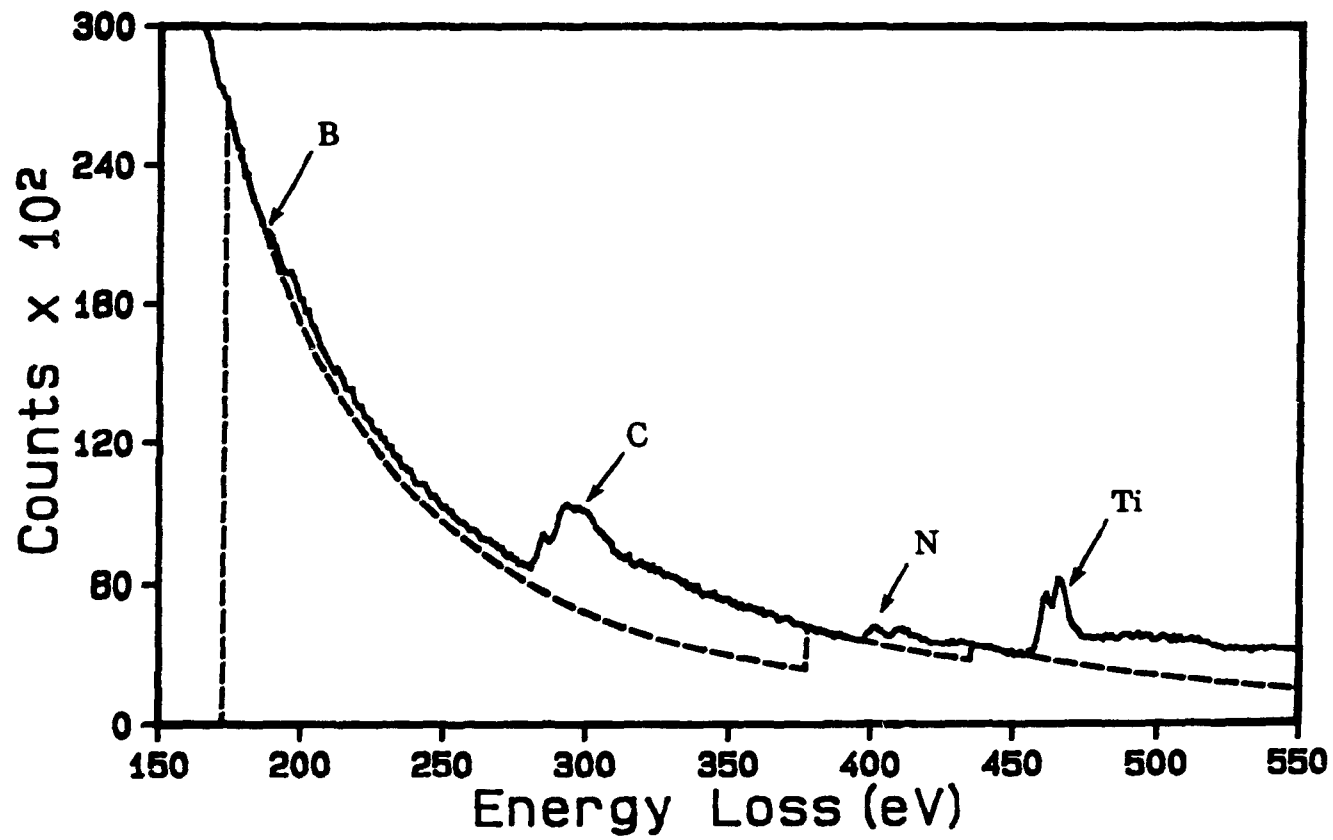


Fig.V.7 EELS spectra showing area 3 in Fig. V.4.

Finally, it should be pointed out that the presence of boron was not detected in all the analyzed precipitates. This was attributed to the lack of sensitivity of the technique rather than to the absence of boron. Consequently, it will be assumed here that some boron is present in both the (Ti,Nb) and Nb carbonitrides. Additional proof regarding the presence of boron in the inclusions and precipitates will be presented in the second part of this chapter.

#### **V.1.4 Evolution of the Precipitation Process During Stress Relaxation**

The thermomechanical histories of the specimens investigated by TEM were displayed in Table V.1. As described above, carbon extraction replicas were prepared from the quenched samples and several micrographs were taken in each case. However, only some of the results are presented here for the sake of brevity.

##### **V.1.4.1 After 25% Deformation at 850°C**

Examples are given in Figs.V.8 and V.9 of the precipitates present in the Nb + B and Nb steels, respectively. A few seconds after deformation, some small precipitates ranging from 3 to 5 nm in diameter are present in the two steels (Figs.V.8a and V.9a). As the relaxation time is increased from less than 10 s to 50 and then 300 s, the density and mean particle diameter both increase. The observations indicate that the density of precipitates is higher in the Nb + B than in the Nb steel. The diameters of the particles on the other hand, seem to be consistently smaller in the Nb + B steel specimens. As shown in Figs.V.8c and d and V.9c and d, the rate of size increase diminished after 300 s. The mean diameters of the precipitates increase only a few nm when the relaxation time is extended from 300 to 1800 seconds.

##### **V.1.4.2 After 5% Deformation at 850°C**

The electron micrographs displayed in Fig.V.10 pertain to the Nb + B steel. The influence of holding time on precipitate density is similar to the previous case. However, the observations indicate that after 5% deformation, the precipitates are larger and have lower densities than when the samples are deformed 25% and held for the same time. For example, the mean diameter of

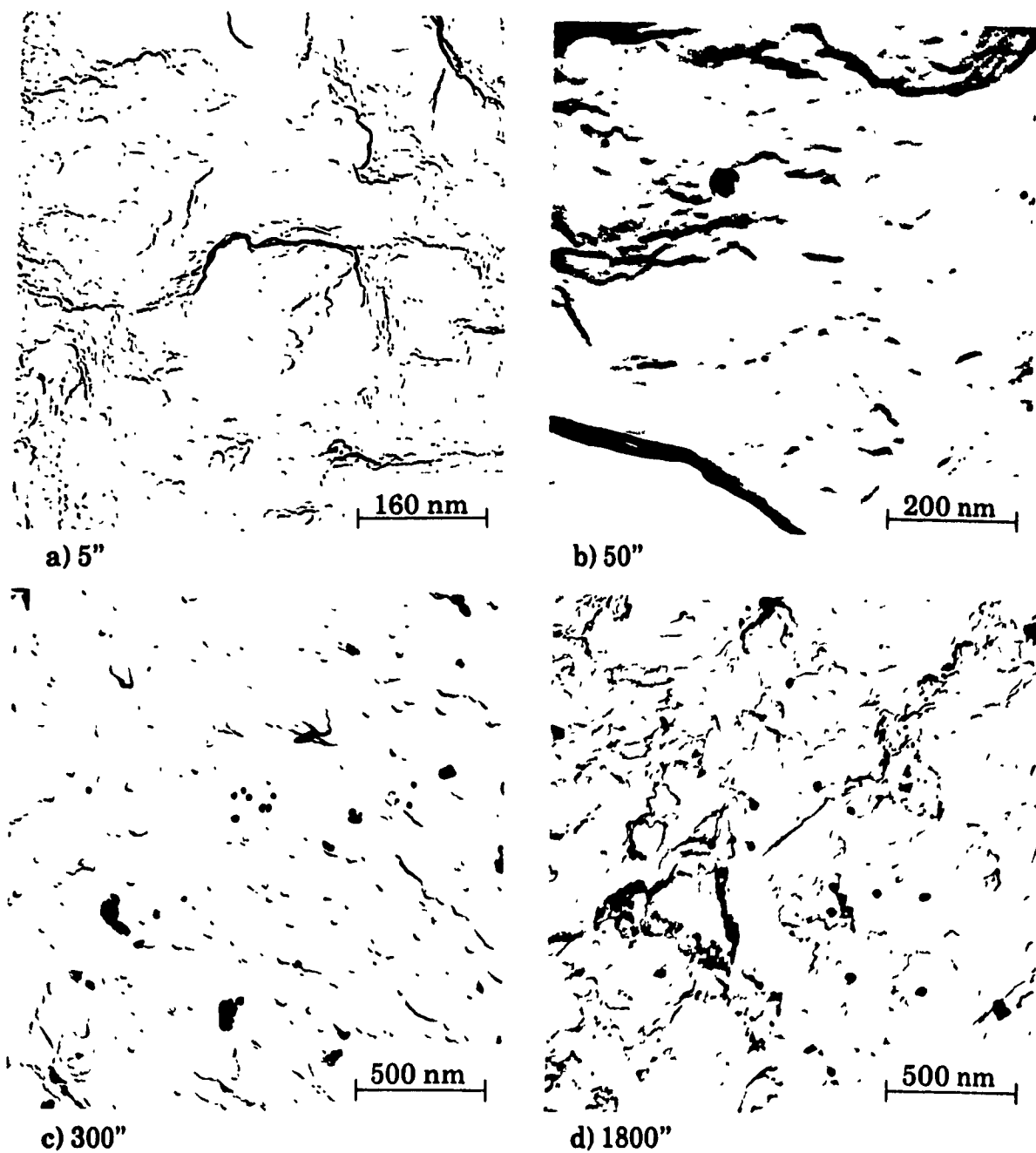


**Fig.V.8** Carbon extraction replicas showing the progress of precipitation in the Nb + B steel after 25% deformation at 850°C and different relaxation times.

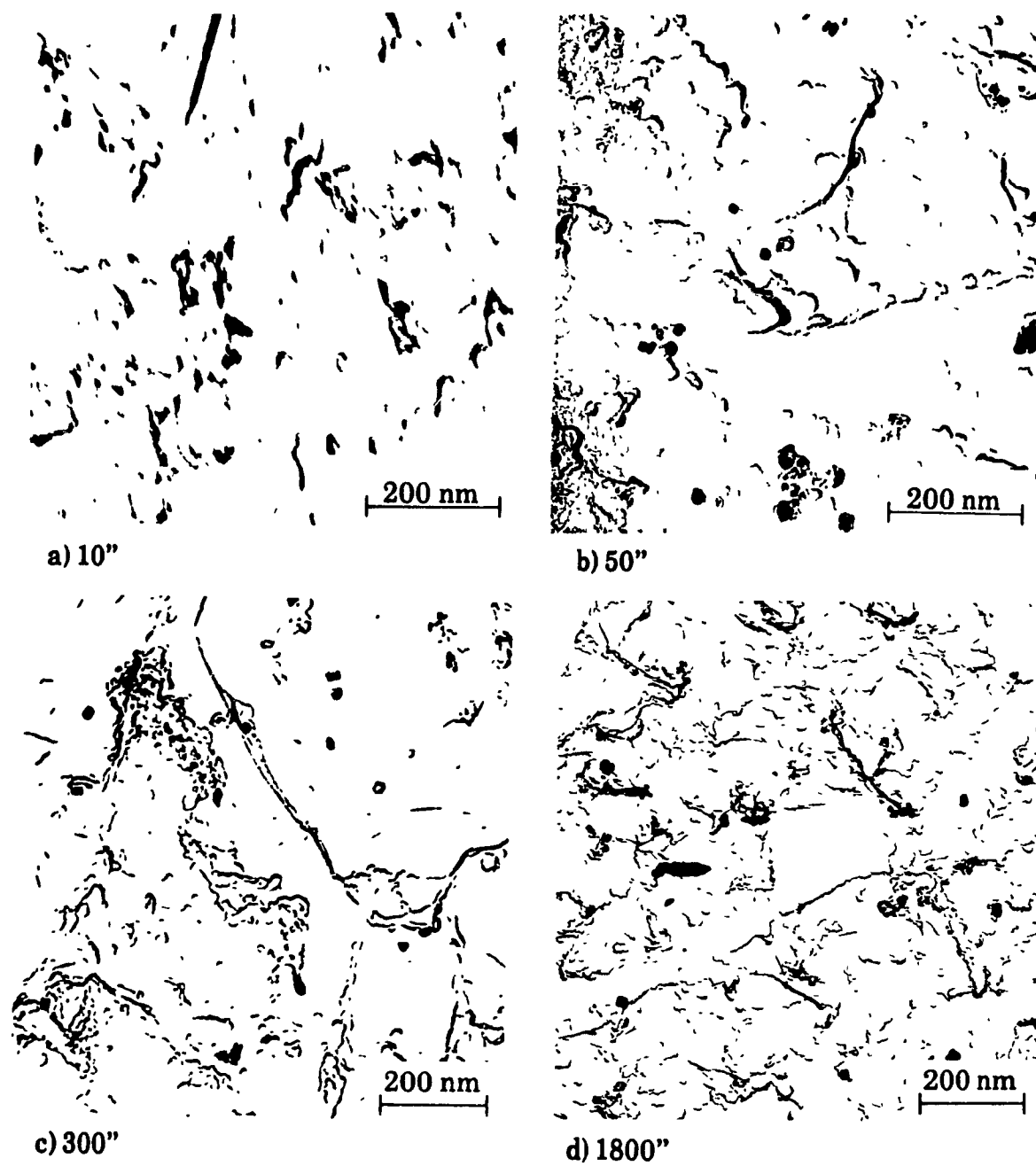


**Fig.V.9** Carbon extraction replicas showing the progress of precipitation in the Nb steel after 25% deformation at 850°C and different relaxation times.

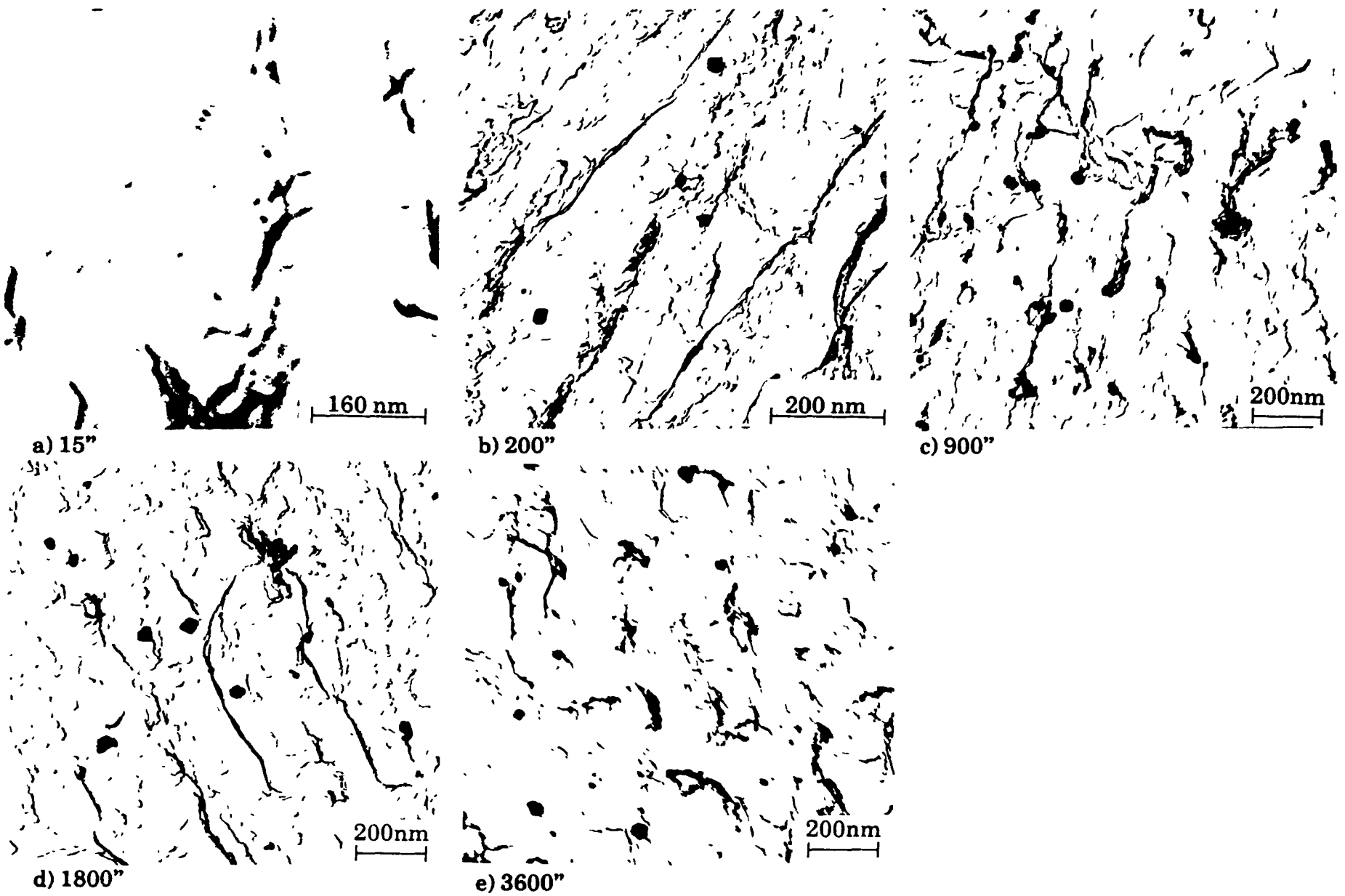


Fig.V.16 Carbon extraction replicas showing the progress of precipitation in the Nb + B steel after 5% deformation at 850°C and different relaxation times.

the particles after 1800 s in the sample deformed 25% is about 23 nm (Fig.V.8d), while it is more than 31 nm after the 5% prestrain, as is evident from Fig.V.10d.

#### V.1.4.3 In the Absence of Deformation at 850°C

In this case, only 3 samples of the Nb + B steel were quenched after 600, 1800 and 3600 seconds. The micrographs are presented in Fig.V.11. The density of the precipitates is much lower than in the two previous cases (i.e. 5% and 25% deformation). Note that here, in order to have a better idea of the precipitate morphology, the photographs were taken in regions where several particles were agglomerated; thus the micrographs are not representative of the true particle distribution.

#### V.1.4.4 After 25% Deformation at 900 and 950°C

Figs.V.12 and V.13 illustrate the results obtained at 900 and 950°C, respectively. Comparison between the results indicates that, as the test temperature is increased, the density of precipitates decreases while their mean size increases. For example, after 500 s of relaxation at 900°C, the precipitates have a mean diameter of about 30 nm, while only 300 s after deformation at 950°C, they have reached a mean size of 35 nm. Here again, the micrographs do not represent the real densities of precipitation.

### V.1.5 Composition and Morphology Changes in the Precipitates

#### V.1.5.1 Composition Changes

As described earlier, both (Ti,Nb) and Nb-rich precipitates were observed in the Nb + B and Nb steels. However, it was found that the compositions of the complex (Ti,Nb) particles are not constant but change as the relaxation time is increased. In fact, in the samples quenched a short time after deformation, the EDX spectra of the complex precipitates show a strong Ti peak and a somewhat smaller Nb one. However, as the holding time is increased, the ratio of the Ti to Nb peak height decreases and becomes less than unity after a long period of time. It was also observed that, for the same holding time, the Nb content of the complex (Ti,Nb) precipitates changes with testing temperature. Although no

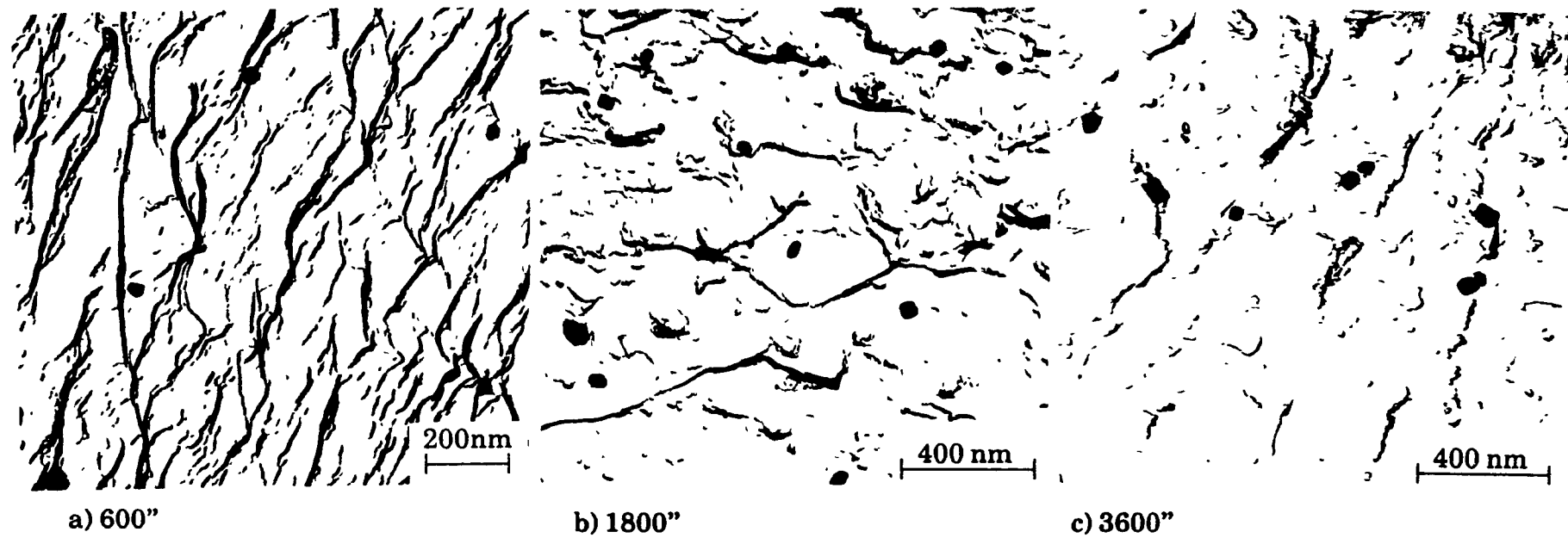


**Fig.V.11 Carbon extraction replicas showing the progress of precipitation in an undeformed Nb + B steel sample at 850°C and different holding times.**

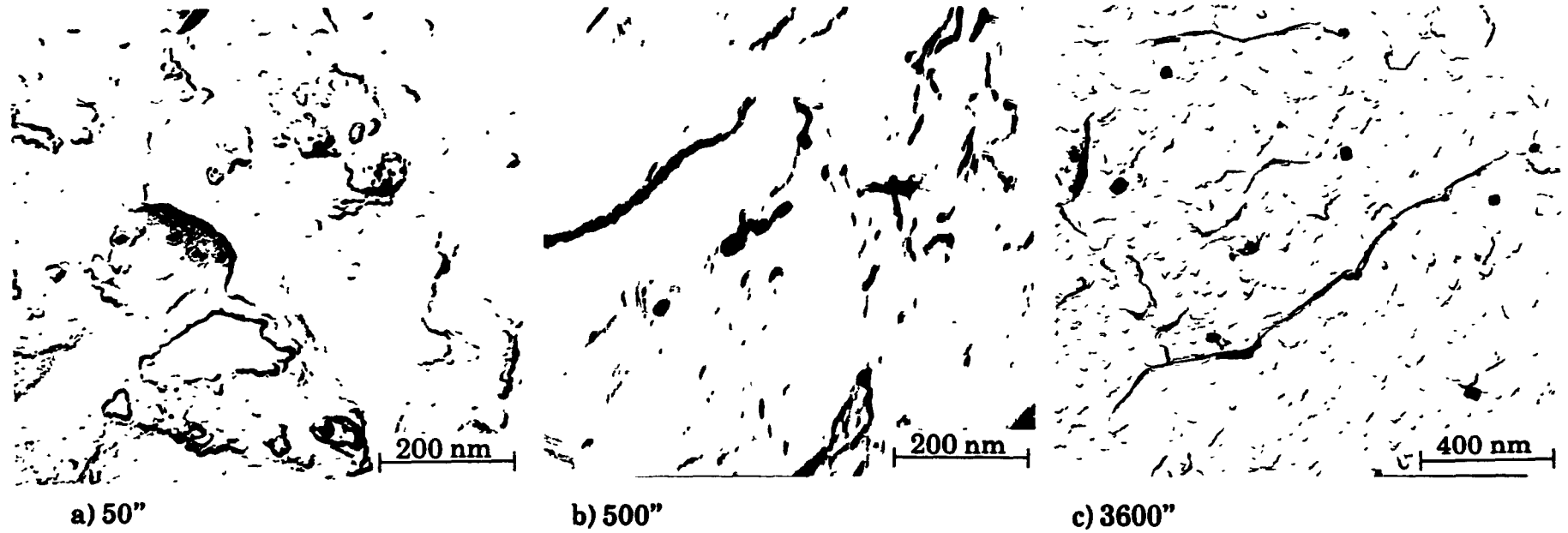


**Fig.V.12 Carbon extraction replicas showing the progress of precipitation in the Nb + B steel after 25% deformation at 900°C and different relaxation times.**

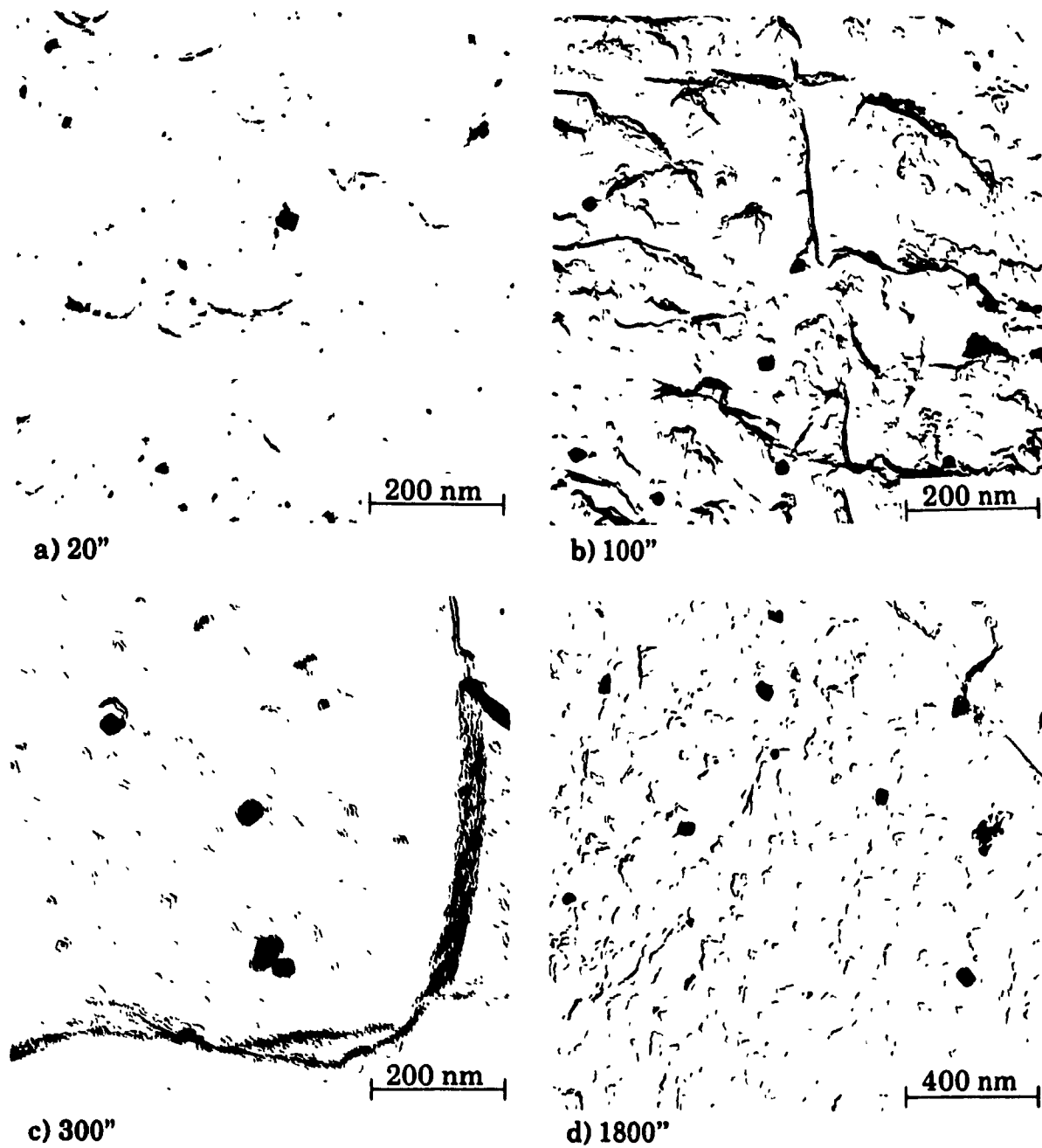


**Fig.V.13** Carbon extraction replicas showing the progress of precipitation in the Nb + B steel after 25% deformation at 950°C and different relaxation times.

quantitative analysis regarding the Nb/(Ti + Nb) weight ratios was carried out, comparison between the Ti and Nb peak heights clearly indicates that the Nb content of the precipitates increases as the holding time after deformation is increased. It should also be pointed out that these changes in particle composition were observed on both the Nb + B and Nb steels, and under all the experimental conditions used in this investigation.

#### V.1.5.2 Morphology of the Precipitates

It has been widely reported in the literature (see chapter II) that a specific orientation relationship exists between the cuboid shaped Nb(C,N) precipitates and the parent austenite. Furthermore, the interface between the particles and the matrix is believed to be coherent or semi-coherent and the orientation relationship between them is of the form:

$$\begin{aligned} \{111\}_{\text{ppt}} \parallel \{111\}_{\gamma\text{-Fe}} \\ \langle 110 \rangle_{\text{ppt}} \parallel \langle 110 \rangle_{\gamma\text{-Fe}} \end{aligned}$$

As illustrated in Figs.V.8 to V.13, the (Ti,Nb) and Nb-rich precipitates have cuboidal shapes in the present steels. These observations suggest that the above orientation relationship can also be valid for these particles. However, the latter do not always have precise cubic shapes and in some cases a protuberance is observed close to one edge of a given precipitate (see for example Fig.V.13a).

As the relaxation time was increased, it was found that the edges of the precipitates became rounded and less and less clear. Such a modification in morphology can be associated with the changes observed in the chemical compositions of the particles. In fact, when analyzed by EDX, the protuberances exhibit high concentrations of Nb, while the remainders of the precipitates contain mostly Ti.

### V.1.6 Particle Size Distribution

The following procedure was employed to determine the particle size distribution. Each micrograph was enlarged to a magnification of at least 100,000; the diameters of the precipitates were then measured with the aid of a 7 power monocular which provides a precision of  $\pm 0.1$   $\mu\text{m}$ . Depending on the thermomechanical history of the specimen, between 100 to 450 precipitates were taken into account. An important point here is that the undissolved complex (Ti,Nb) precipitates present in the specimens after solutionizing ( $d=25$  to 30 nm) do not affect the stress relaxation process. Consequently, the size distributions shown here concern only the Nb-rich particles which are responsible for the relaxation arrest. However, as the distinction between these two types of precipitate is practically impossible, some size overlap occurs after long holding times. This has the effect of moving the mean particle size to the right, exaggerating the real size of the precipitates in this way.

The influence of temperature, deformation and steel composition on the precipitate size distribution is illustrated in Figs.V.14 to V.16, respectively. The mean particle diameters calculated from each distribution are also displayed in these figures. Examination of Fig.V.14 reveals that, as the testing temperature is increased, the mean particle size increases and the size distribution tends to become wider.

The influence of deformation on precipitate size can be seen from the results presented in Fig.V.15. It is clear that as the amount of prestrain is increased, the precipitates tend to become smaller. The influence of composition (i.e. the presence of boron) on the particle size distribution does not seem to be very important (Fig.V.16). Although the mean diameters of the precipitates in the Nb steel are somewhat larger than those located in the Nb+B grade, the differences fall within the error bars associated with the measurements.

Deformation and composition affect not only the size distribution, but also the density of the precipitates (i.e. the number of precipitates per unit area). The dependence of the precipitate density,  $N_p$ , on time when the prestrain and/or composition are changed is displayed in Table V.2.

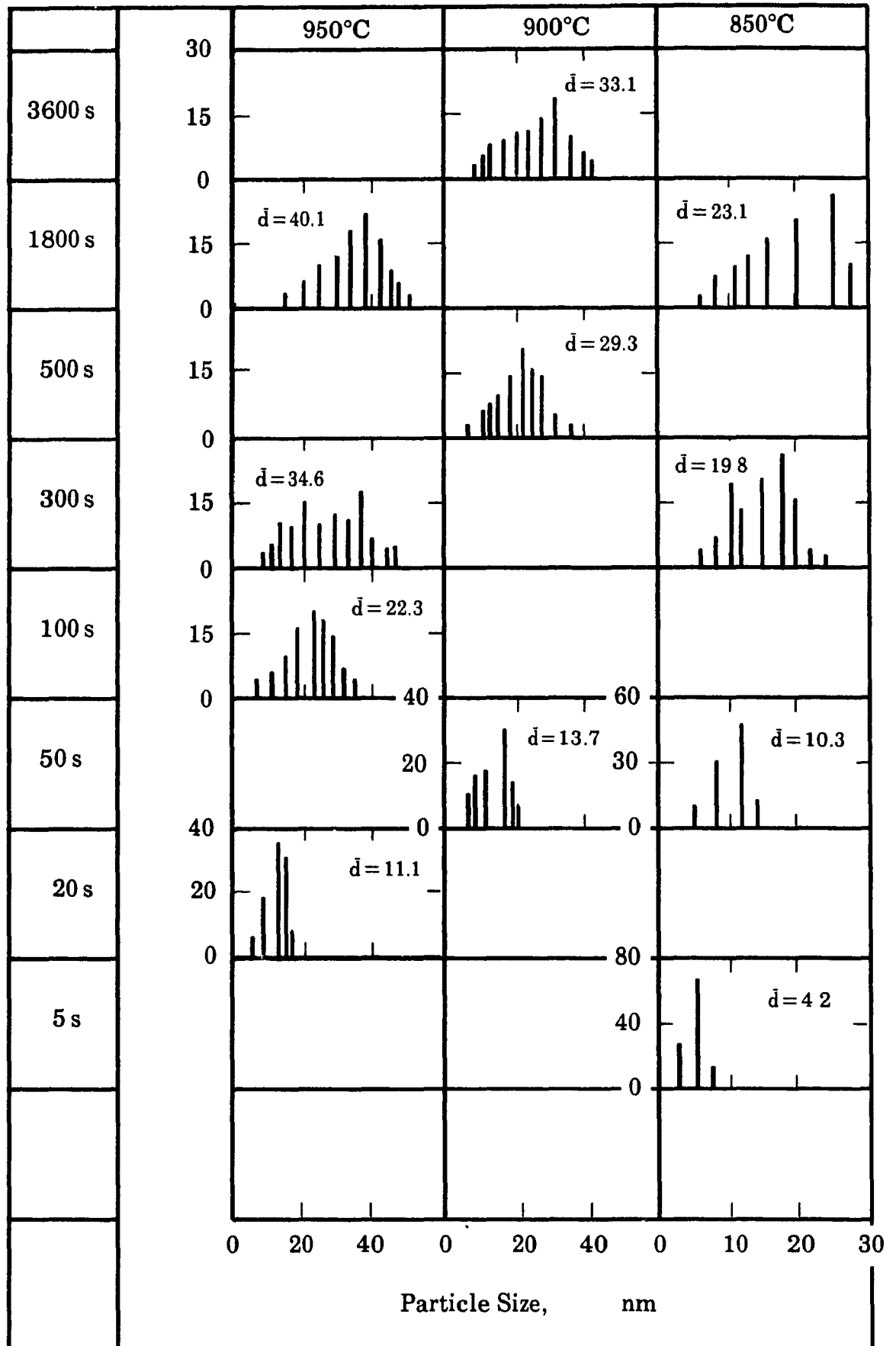


Fig.V.14 Effect of temperature and relaxation time on the particle size distribution in the Nb + B steel after 25% deformation.

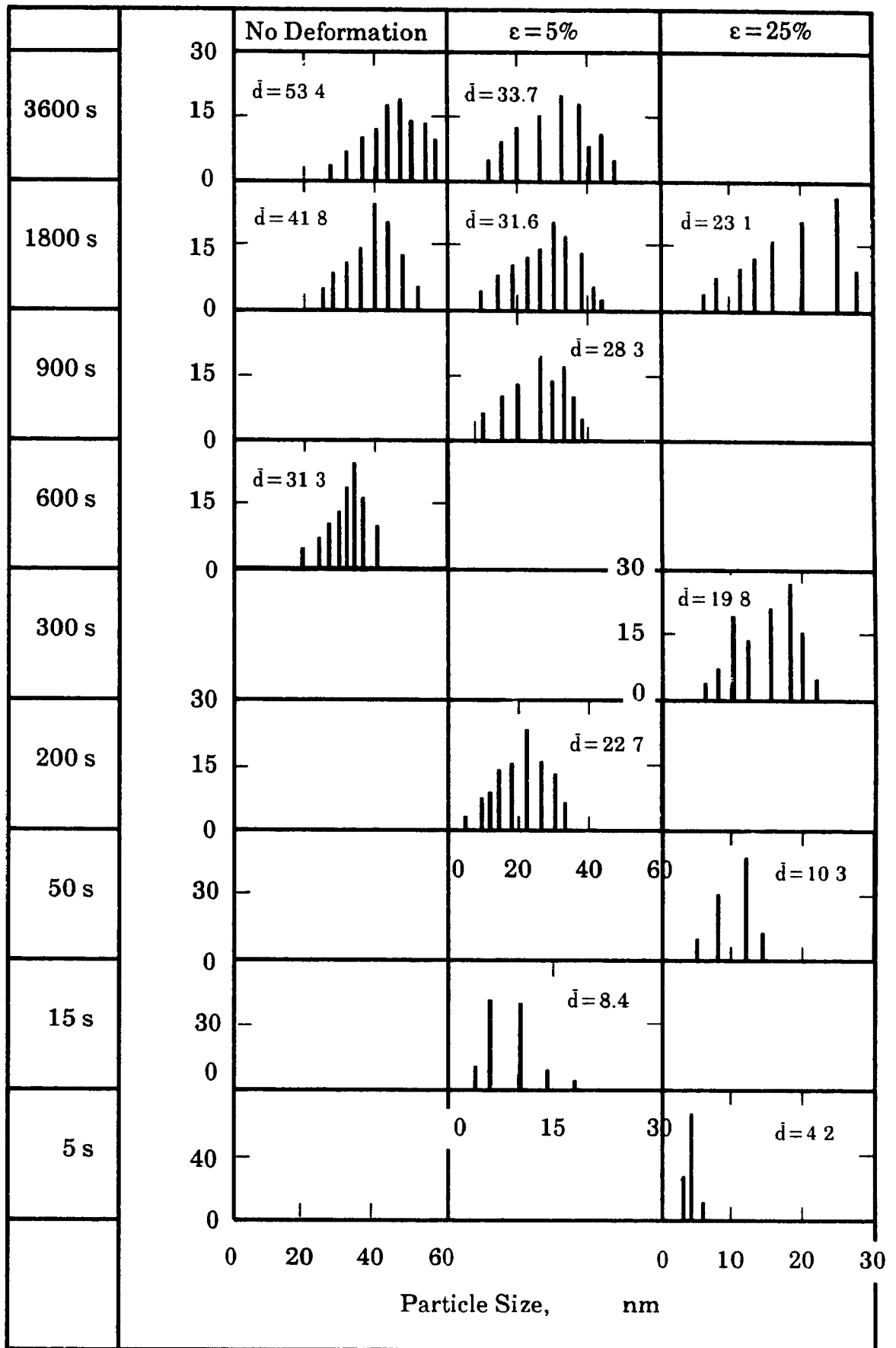


Fig.V.15 Effect of deformation and relaxation time on the particle size distribution in the Nb + B steel at 850°C.

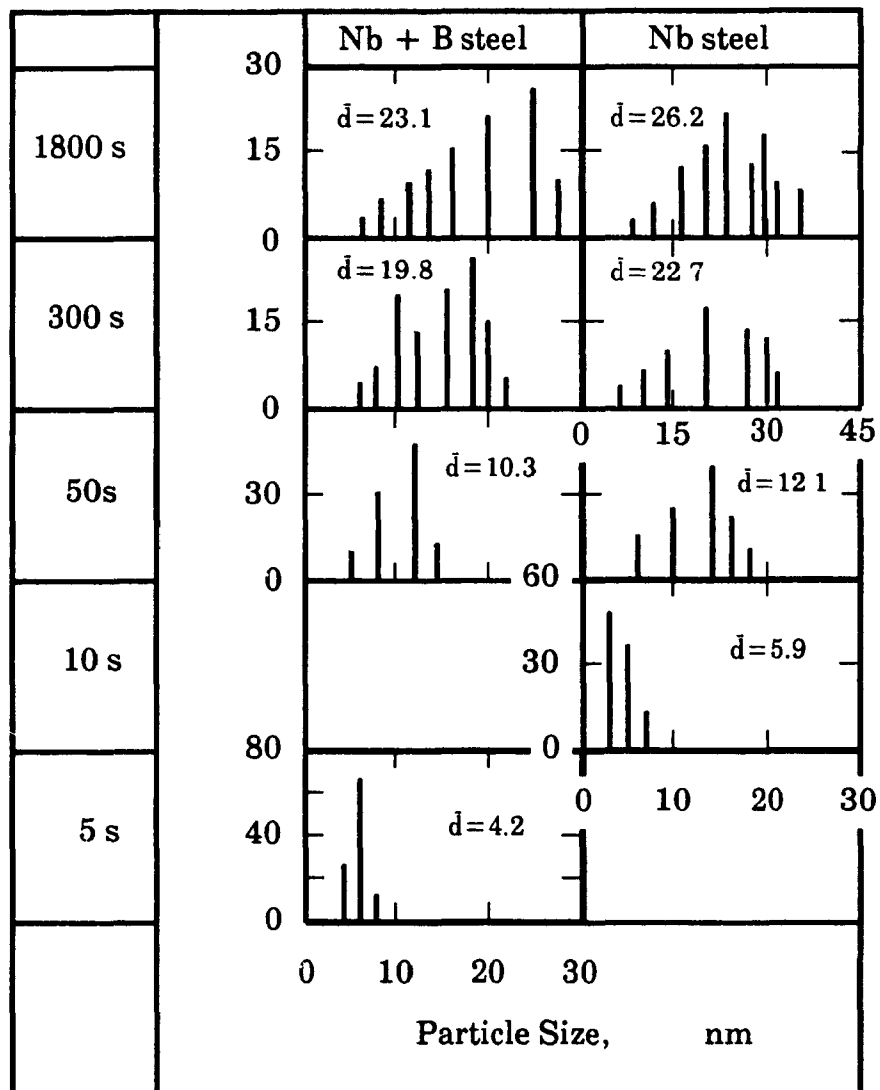


Fig.V.16 Effect of composition and relaxation time on the particle size distribution after 25% deformation at 850°C.

**Table V.2.**  
**Influence of Composition, Deformation and Time on the Particle**  
**Density at 850 °C**

Steel	Prestrain %	Time sec.	$N_p/\mu\text{m}^2$	S.D.
Nb+B	25	50	0.57	0.19
		300	1.17	0.26
		1800	1.74	0.32
Nb+B	5	200	0.31	0.09
		900	0.69	0.17
		1800	0.92	0.21
		3600	0.98	0.26
Nb+B	0	50	0.13	0.06
		300	0.22	0.11
		1800	0.68	0.23
Nb	25	50	0.46	0.11
		300	1.03	0.21
		1800	1.56	0.30

These results reveal that:

- 1) the presence of boron leads to higher densities of precipitates, and
- 2) the density of the precipitates decreases as the amount of deformation is decreased.

The mean particle diameters and the corresponding standard deviations were measured on replicas and are therefore surface quantities. The volume mean particle sizes and standard deviations were obtained using the equations developed by Ashby and Ebeling [153]:

$$\bar{d}_v = \frac{\bar{d}_s}{1 + \left(\frac{S.D._{(s)}}{\bar{d}_s}\right)^2} \quad (V.1)$$

$$S.D._{(v)} = \frac{S.D._{(s)}}{1 + \left(\frac{S.D._{(s)}}{\bar{d}_s}\right)^2} \quad (V.2)$$

Here,  $d$  and S.D. refer to the mean particle diameter and standard deviation, and the subscripts  $s$  and  $v$  refer to surface and volume, respectively. The values of  $d_s$ ,  $S.D._{(s)}$ ,  $d_v$ , and  $S.D._{(v)}$  corresponding to the precipitates observed in the Nb + B and Nb steels are listed in Tables V.3 and V.4, respectively.

It is clear from these tables that temperature, deformation and steel composition influence the evolution of particle size. The effects are shown more explicitly in Figs.V.17 to V.19, where  $\log(\bar{d}_v)$  is plotted versus relaxation time for the different experimental conditions. It can be seen that the curves have two parts: in the first, they are linear and their slopes are close to 0.5 (from 0.48 to 0.52), indicating that the theory of diffusion controlled particle growth can be applied in these cases. In the second part, the curves depart from their linear trends and level out. Finally, it is of interest to note that the transition times observed are close to the precipitation finish times determined in the stress relaxation experiments.

**Table V.3.**  
**Influence of Composition, Deformation and Time on the Mean**  
**Particle Size for the Nb + B Steel**

$\epsilon$	Temp.	Time	Surface quantities		Volume quantities	
			$\bar{d}_s$ nm	S.D.(s)	$\bar{d}_v$ nm	S.D.(v)
%	°C	sec.				
25	850	5	4.2	1.7	3.6	1.4
		50	10.3	3.9	9.5	3.4
		300	19.8	5.1	18.7	4.8
		1800	23.1	6.8	21.7	6.2
25	900	50	13.7	3.9	12.7	3.6
		500	29.3	5.3	28.4	5.1
		3600	33.1	7.3	31.6	6.9
25	950	20	11.1	3.2	10.3	2.9
		100	22.3	5.8	21.1	5.4
		300	34.6	6.9	33.5	6.6
		1800	40.1	8.3	39.1	7.9
5	830	20	6.1	2.4	5.3	2.1
		200	20.8	4.1	20	3.9
		900	25.3	6.2	23.4	5.8
5	850	15	8.4	3.5	7.6	2.9
		200	22.7	5.1	21.6	4.8
		900	28.3	5.6	27.2	5.3
		1800	31.6	7.2	30	6.8
		3600	33.7	7.8	32.3	7.4
5	900	10	5.7	2.1	5.1	1.8
		200	27.2	4.9	26.3	4.7
		500	32.1	6.4	30.1	6.1
		3600	39.6	8.5	37.8	8.1
0	850	600	31.3	5.8	30.2	5.6
		1800	41.8	8.2	40.2	7.8
		3600	53.4	10.9	51.3	10.4

**Table V.4.**  
**Influence of Composition, Deformation and Time on the Mean**  
**Particle Size for the Nb Steel**

$\varepsilon$ %	Temp. °C	Time sec.	Surface quantities		Volume quantities	
			$\bar{d}_s$ nm	S.D. <sub>(s)</sub>	$\bar{d}_v$ nm	S.D. <sub>(v)</sub>
25	850	10	5.9	2.1	5.2	1.8
		50	12.1	4.6	11.1	4.1
		300	22.7	6.1	21.3	5.6
		1800	26.2	6.8	24.8	6.3
5	830	10	5.7	3.1	4.4	2.4
		100	14.1	4.5	12.8	4.1
		600	24.2	7.1	22.3	6.5
		1800	27.8	7.8	25.8	7.2
5	850	20	6.9	2.8	5.92	2.4
		100	13.7	4.3	12.5	3.9
		300	24.5	6.7	22.8	6.2
		600	28.4	7.2	26.7	6.8
		1800	32.8	7.6	31.1	7.2
		3600	35.4	8.1	33.6	7.7
5	900	30	6.7	2.9	5.6	2.4
		100	17.3	4.9	16	4.5
		300	30.4	6.7	28.9	6.4
		1800	36.5	7.3	35.1	7.1

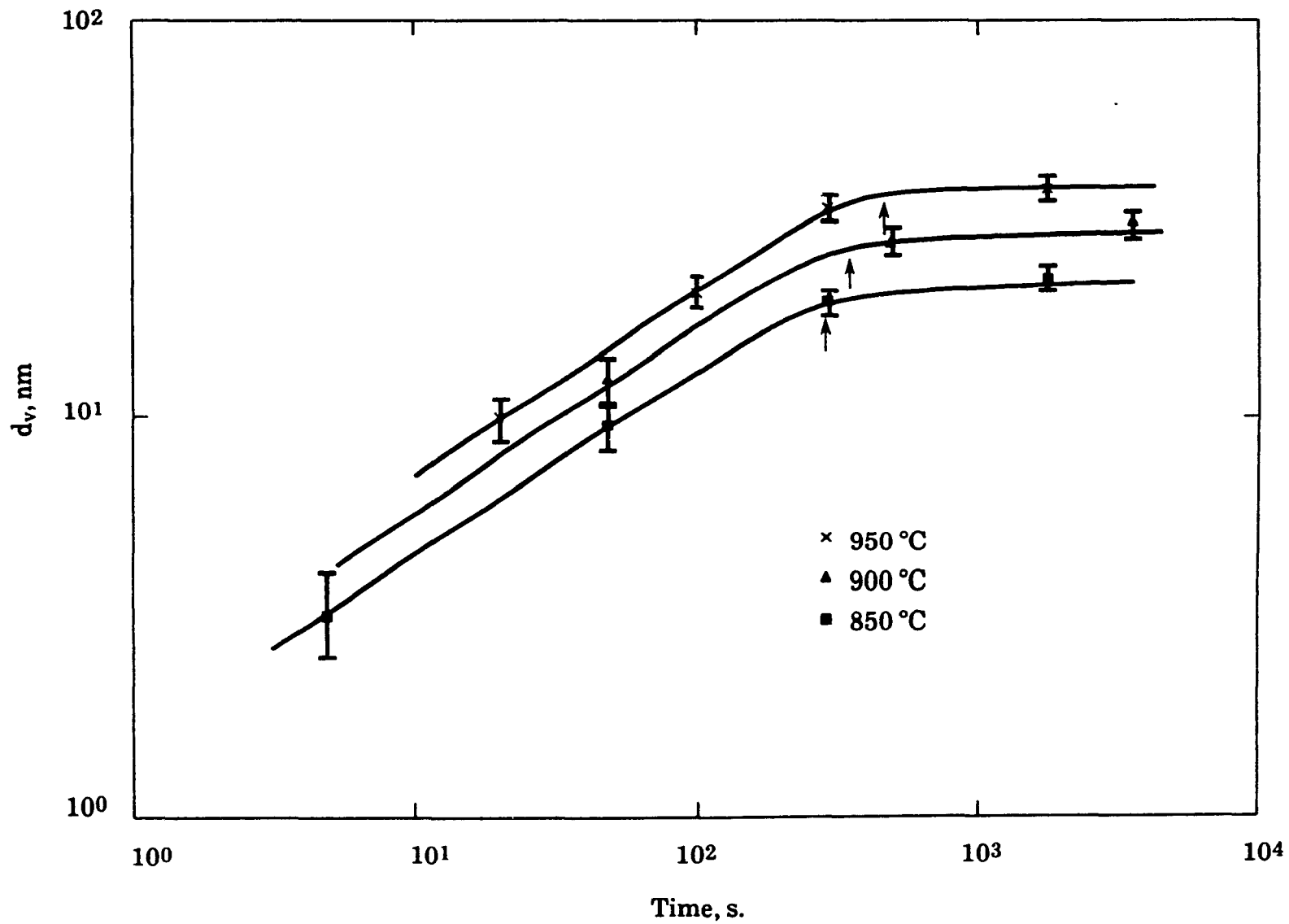


Fig.V. 17 Effect of test temperature on the mean particle size ( $d_v$ ) in the Nb + B steel after 25% deformation.

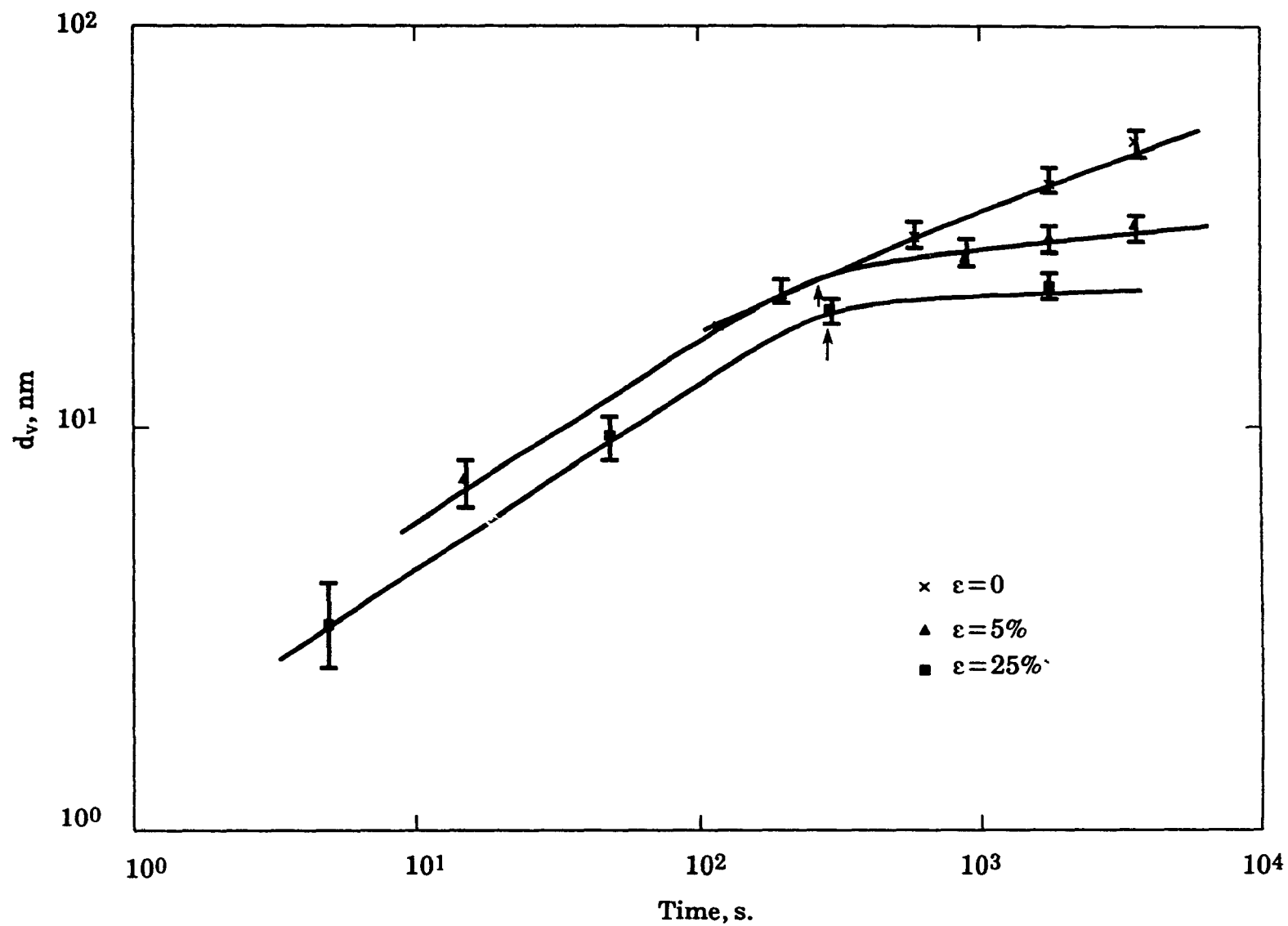


Fig.V. 18 Effect of deformation and relaxation time on the mean particle size ( $d_v$ ) in the Nb + B steel at 850°C.

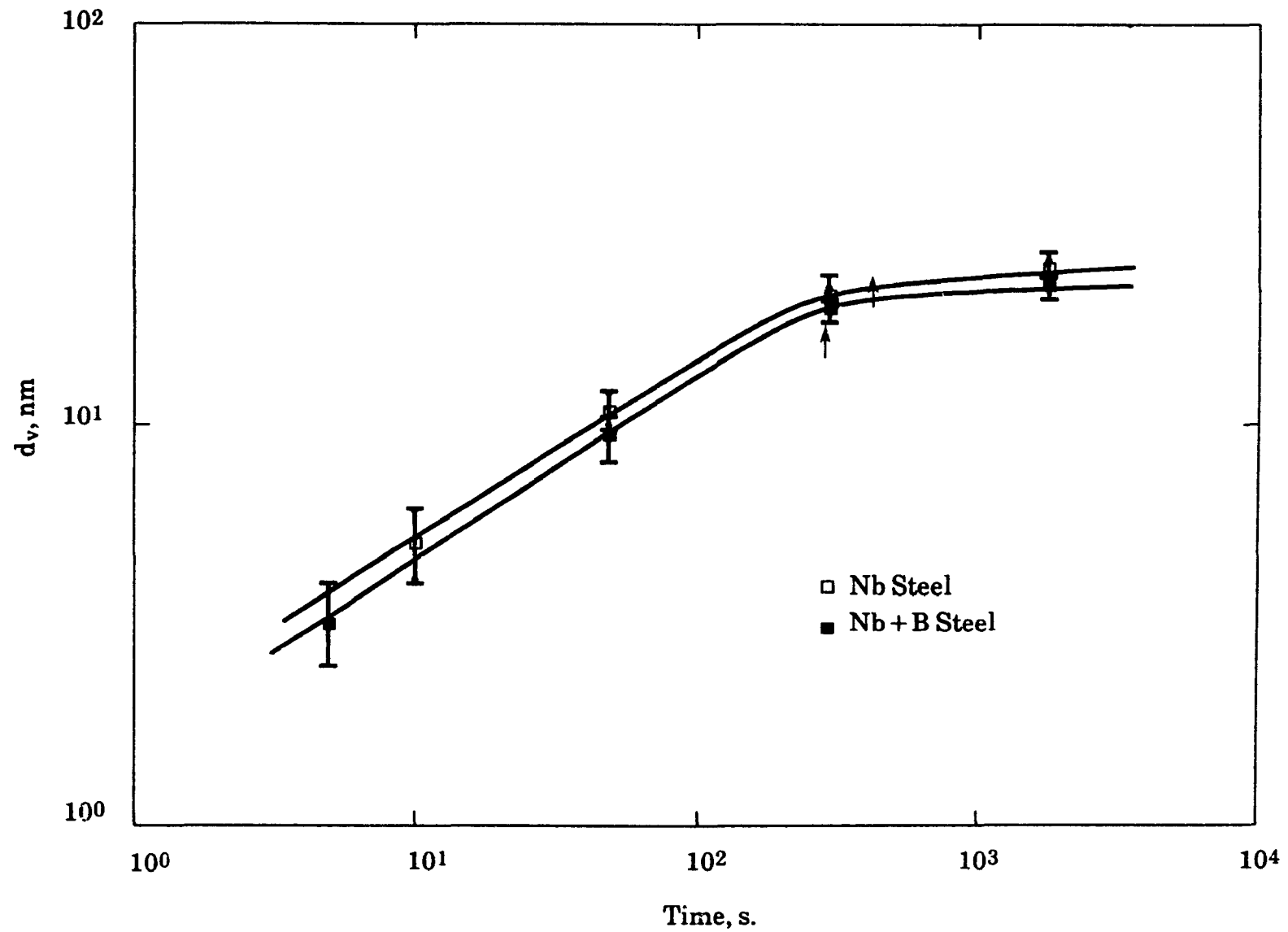


Fig.V. 19 Effect of composition on the mean particle size ( $d_v$ ) during stress relaxation at 850 °C.

## CHAPTER V

### PART 2: PTA AND SIMS RESULTS

As discussed above, some knowledge of the distribution of boron is important for an understanding of the boron effect. In this context, the PTA and SIMS techniques occupy an important place, the first identifying the location of boron and boron compounds with precision, while the second provides information regarding the simultaneous presence of boron and of other elements in the material.

In this investigation, the influence was studied of deformation (0, 5 and 25%), cooling rate (quenching or controlled cooling), holding time (3 to 10,800 s) and temperature (800 to 1200°C) on the distribution of boron in austenite. More than 200 samples were prepared and analyzed in this way. However, for brevity, only some of the results will be presented. Tables V.5 and V.6, respectively, for the Nb+B and B steels, show the quenching schedules of the samples for which PTA and SIMS results will be included here.

#### V.2.1. The Segregation of Boron During Quenching

In these tests, after solutionizing, the specimen was cooled at 0.5°C/s to the test temperature (850, 900, 950, 1000, 1100 or 1200°C), held for ten minutes and subsequently water or oil quenched. As the distribution of boron is better revealed when the cooling rate is slower, the results of the oil quenched (cooling rate = 20°C/s) samples will be shown here.

##### V 2.1.1. Case of the Nb + B Steel

Fig.V.20 illustrates the evolution of the boron distribution as a function of holding temperature. It can be seen that, when quenched from 1200°C, strong segregation is produced at the prior austenite grain boundaries (Fig.V.20a). A white zone can also be distinguished along the boundaries. This indicates the absence of boron in these areas; it is known as the boron depleted zone.

**Table V.5.**  
**Quenching Schedule Used for PTA and SIMS analysis in the**  
**Nb + B Steel**

Test Temp. °C	Prestrain %	Quenching Medium	Holding Time sec
1200	0	Oil	600
1100	0	Oil	600
1000	0	Oil	600
	25	Oil	3, 60, 600
	25	Ice Brine	before deformation, 3, 10, 60, 100, 150, 600
950	0	Oil	600
	25	He	20, 170, 1000
900	0	Oil	600
	25	C.C.*	10, 50, 500, 3600
850	0	Oil	600
	5	He	15, 200, 900
	25	He	3, 50, 300, 1800

\* C.C. : Control Cooled, cooling rate = 13 to 17 °C/sec.

**Table V.6.**  
**Quenching Schedule Used for PTA and SIMS analysis in the B**  
**Steel**

Test Temp. °C	Prestrain %	Quenching Medium	Holding Time sec
1200	0	Oil	600
1100	0	Oil	600
1000	0	Oil	600
	25	Oil	3, 60, 600
	25	Ice Brine	before deformation, 3, 5, 10, 60, 150
950	0	Oil	600
	25	He	20, 200, 700
900	0	Oil	600
	25	He	3, 5, 50, 100
	25	C.C.*	5, 30, 100, 600
850	0	Oil	600
	5	He	40, 100, 300, 600
	25	He	20, 70, 100, 300

\* C.C. : Control cooled, cooling rate = 13 to 17 °C/sec.

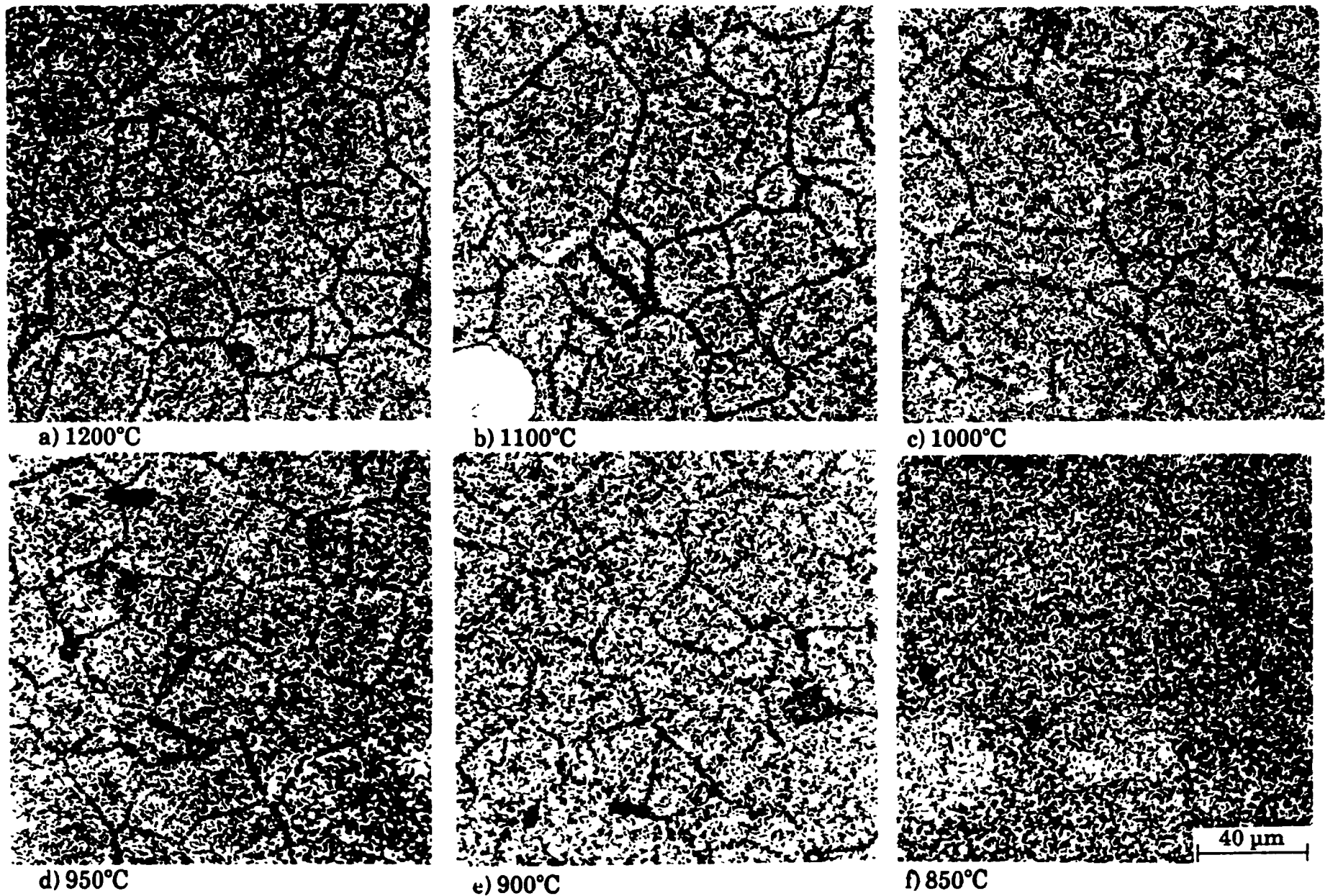


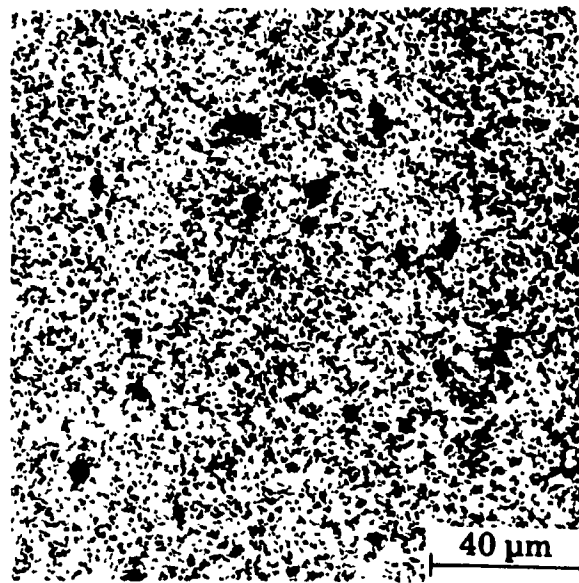
**Fig. V.20** The boron distributions revealed by PTA in the Nb + B steel as a function of quench temperature. Oil quenched after 600 s of isothermal holding.

The results at 1100 and 1000°C (Figs.V.20b and c) are similar to those obtained at 1200°C. However, at the same magnification, the boron depleted zone is less clear in the sample tested at 1100°C and can no longer be seen at 1000°C. This indicates that, as the quenching temperature is decreased, the width of the boron depleted zone decreases, which means that the amplitude of segregation decreases with decreasing quenching temperature. This effect can be clearly seen if the results obtained at 950, 900 and 850°C are considered. As the quenching temperature is decreased in this range, the segregation becomes less and less noticeable, so that quenching from 850°C produces very little segregation (Fig.V.20f).

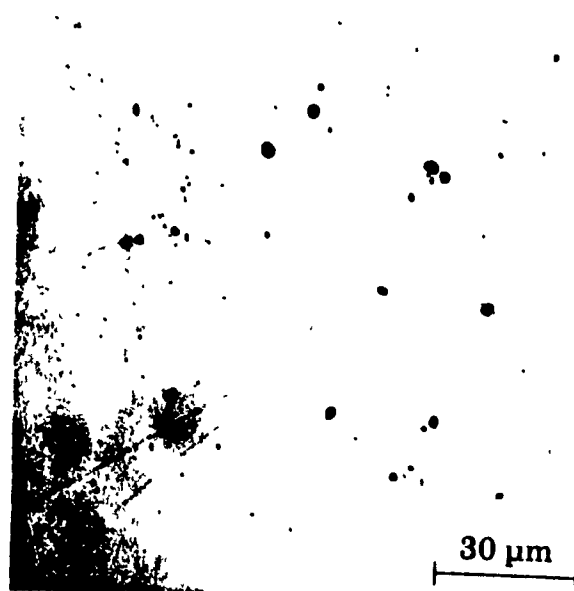
The presence of agglomerated etch pits and/or black spots in a PTA micrograph is indicative of the existence of boron-containing precipitates in the specimen. Such a situation was not observed in the samples quenched from 1200, 1100 and 1000°C. By contrast, a few precipitates were observed in the specimen quenched from 950°C. This tendency is accelerated when the quenching temperature is decreased to 900 and 850°C. Comparison of Figs. V.20d to f, shows that, when the test temperature is decreased, the number of precipitates increases. These trends are associated with an increase in the size of the precipitates. The precipitates first appear at austenite grain boundaries; intragranular particles were also found in the sample quenched from 850°C. The nature of these precipitates has been discussed in V.1.2.1; they are believed to be  $M_{23}(C, B)_6$  borocarbides.

It should be pointed out that the size of a spot observed on a PTA micrograph is not exactly that of the associated precipitate. This is because the mean free path of the alpha particles emitted from the boron atoms of the precipitate is approximately 1  $\mu\text{m}$ , the error introduced in this way consequently being about 2  $\mu\text{m}$  ( $\pm 1$ ). An approximate idea of the size of the precipitates can then be obtained by subtracting 2  $\mu\text{m}$  from the size of the spot on the PTA micrograph.

Because of their large sizes,  $M_{23}(C, B)_6$  precipitates are observable with an optical micrograph. PTA and optical micrographs of a Nb + B steel specimen held for 30 min at 850°C are presented in Fig.V.21. It can be seen that the



a) PTA



b) Optical

**Fig.V.21 Comparison between PTA and optical micrographs of a Nb + B steel specimen held isothermally for 30 min at 850°C.**

particle distribution is similar in both micrographs, so it can be concluded that the precipitates observed on the surfaces of the samples are largely the iron borocarbides found in the PTA micrographs.

Finally, a SIMS analysis was also performed on all the samples. In preparation for the SIMS investigation, the surfaces were mechanically polished and carefully cleaned. The Cameca IMS4f instrument using 12.5 keV  $O_2^+$  as primary ions was employed. The strongest B channel for analysis of the B distribution is the  $^{11}B^{16}O_2^-$  signal at mass 43.

This channel was used and it was verified that no interference occurred between the B signal and that of Al as  $^{27}Al^{16}O^-$ , which also has a mass of 43. Fig.V.22 gives examples of ion micrographs of the samples quenched from 1100, 900 and 850°C. As is readily evident, the segregation and precipitation behaviour of boron and the boron compounds follows the same pattern as that observed on the PTA micrographs. The agreement between the SIMS and PTA results confirms the validity of our results concerning the state of distribution of the boron in the material.

#### V.2.1.2. Case of the Boron Steel

The evolution of the boron distribution as a function of holding temperature prior to quenching from 1200, 1100 and 1000°C is presented in Fig.V.23. It can be seen that oil quenching from 1200°C induces the strong segregation of boron to prior austenite grain boundaries. The same behaviour is observed at 1100 and 1000°C; however, in the case of the Nb + B steel, the degree of segregation decreases as the holding temperature is decreased. Figs.V.23 d-f illustrate the results at 950, 900 and 850°C. In the sample quenched from 850°C, there is clearly less segregation than at 1200°C, and along the grain boundaries, the etch pit bands are much less dense and continue as observed at higher temperatures. Also, after quenching from 950°C, several precipitates are present at the austenite grain boundaries and their size and density increase as the holding temperature is decreased.

The results obtained for the Nb + B and B steels show that the amplitude of segregation in the B steel is somewhat greater than in the Nb + B grade. This

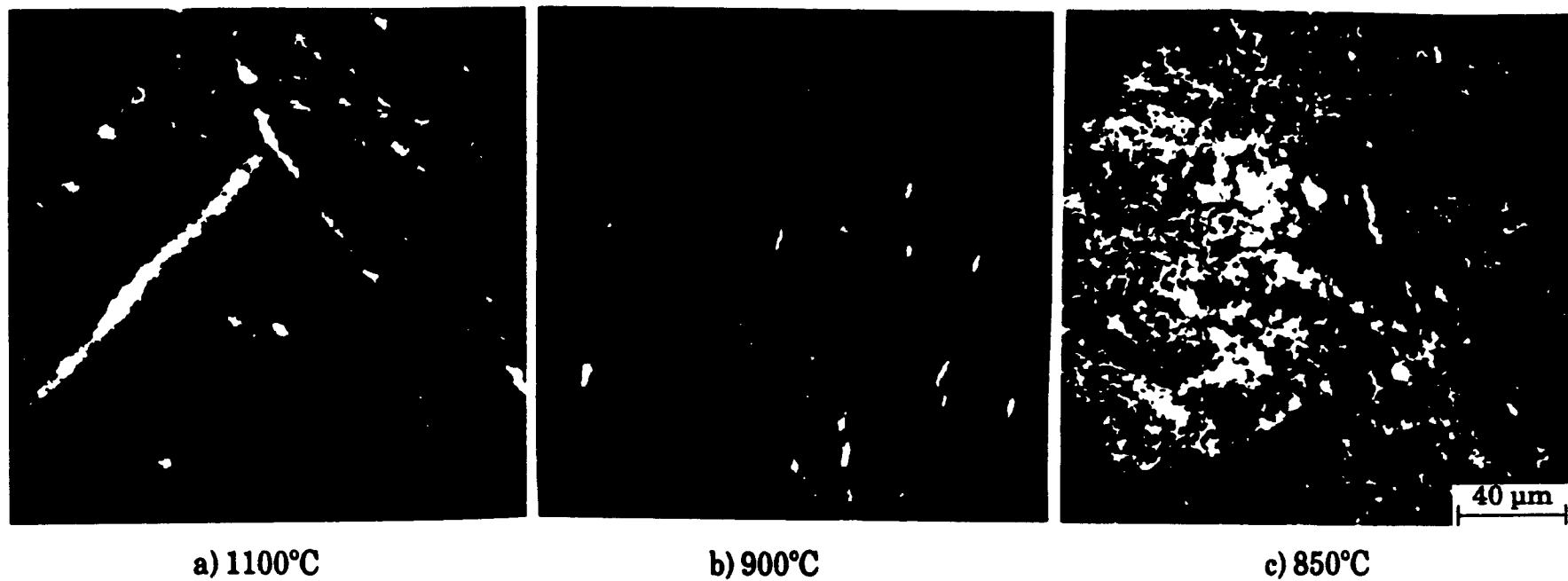


**Fig.V.22** Ion micrographs showing the distribution of boron in the Nb + B steel after quenching from different temperatures.  $O_2^+$  was used as the primary ion and  $BO_2^-$  as the secondary ion.

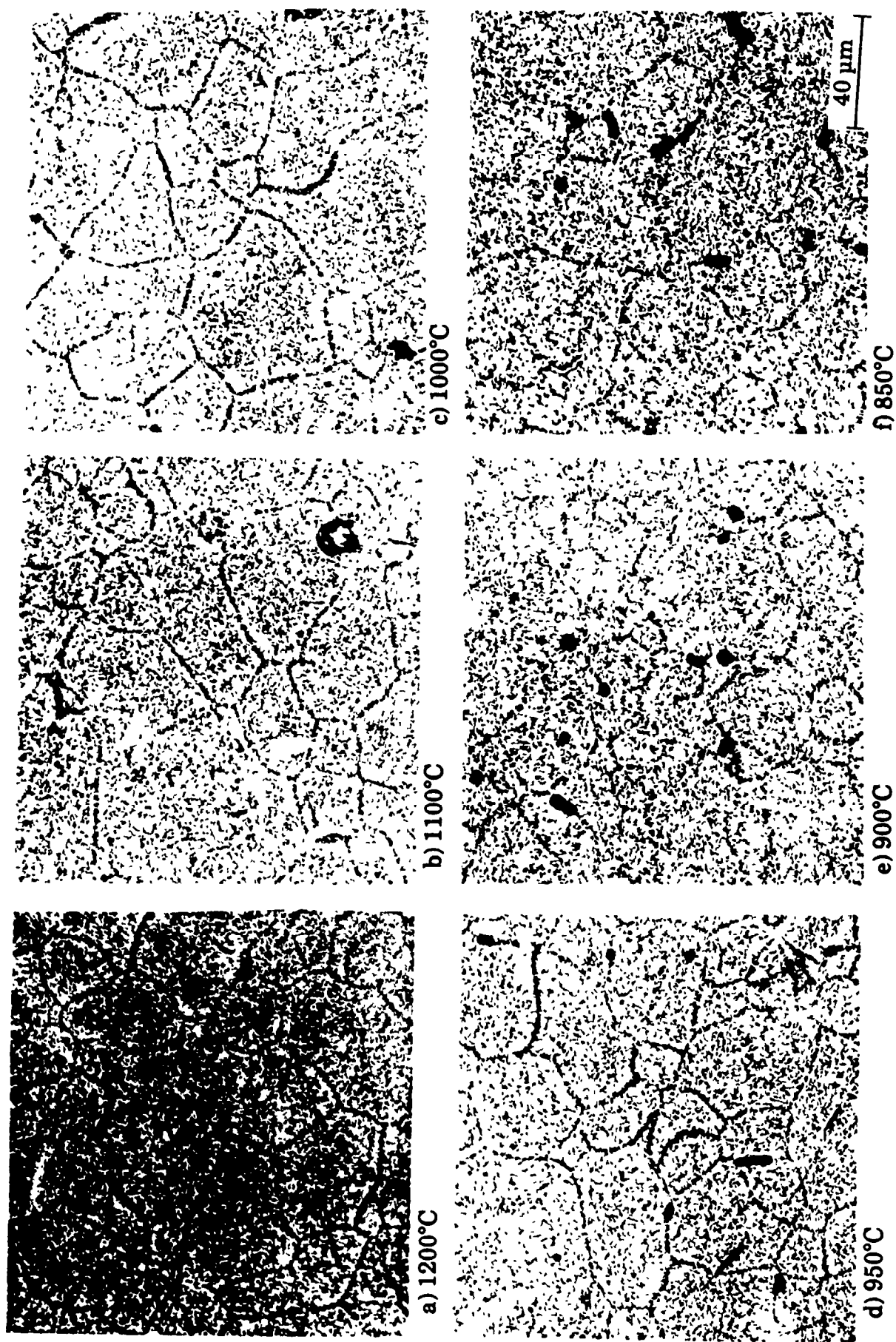


Fig. V.23 The boron distributions revealed by PTA in the B steel as a function of quench temperature. Oil quenched after 600 s of isothermal holding.

phenomenon is particularly well illustrated at 850°C, where clear segregation is still present in the B steel (Fig.V.23f), while it is weak in the Nb+B material (Fig.V.20f). Although in both cases the first precipitates were observed at 950°C, their numbers and sizes are larger in the B than in the Nb+B steel.

## V.2.2. Boron Segregation After High Temperature Deformation

Deformation markedly influences the kinetics of recrystallization and precipitation. When studying the effect of boron on these phenomena, it becomes important to know how deformation affects the boron distribution. After austenitization, samples of the Nb+B and B steels were cooled to the test temperature (850-1000°C), and then hot compressed (5 or 25%). After deformation, the specimens were held at temperature for increasing times, then quenched or control cooled (13 to 17°C/sec). In the sections that follow, the boron distribution results in the two steels are presented after 25% deformation.

### V.2.2.1. Results Pertaining to the Nb+B Steel

The boron distributions after deformation at 1000°C are shown in Figs. V.24a-f. It can be seen that slight segregation is observed around the prior austenite boundaries 3 s after straining. As the holding time is increased to 10 and then to 60 s, the number of boundaries that display boron segregation increases, and the degree of segregation intensifies. Also, in the sample quenched 10 s after deformation, a little segregation is observed around the newly formed austenite grains and this tendency accelerates with holding time (i.e. there is more and more segregation on new boundaries with increasing holding time).

The amplitude of segregation attains a maximum at about 100 s, at which point clear and continuous segregation is present around the recrystallized grains (Fig.V.24d). When the holding time is further increased to 150 and 600 s, the density of segregation decreases gradually and almost disappears after 600 s of isothermal holding (Fig.V.24e and f).

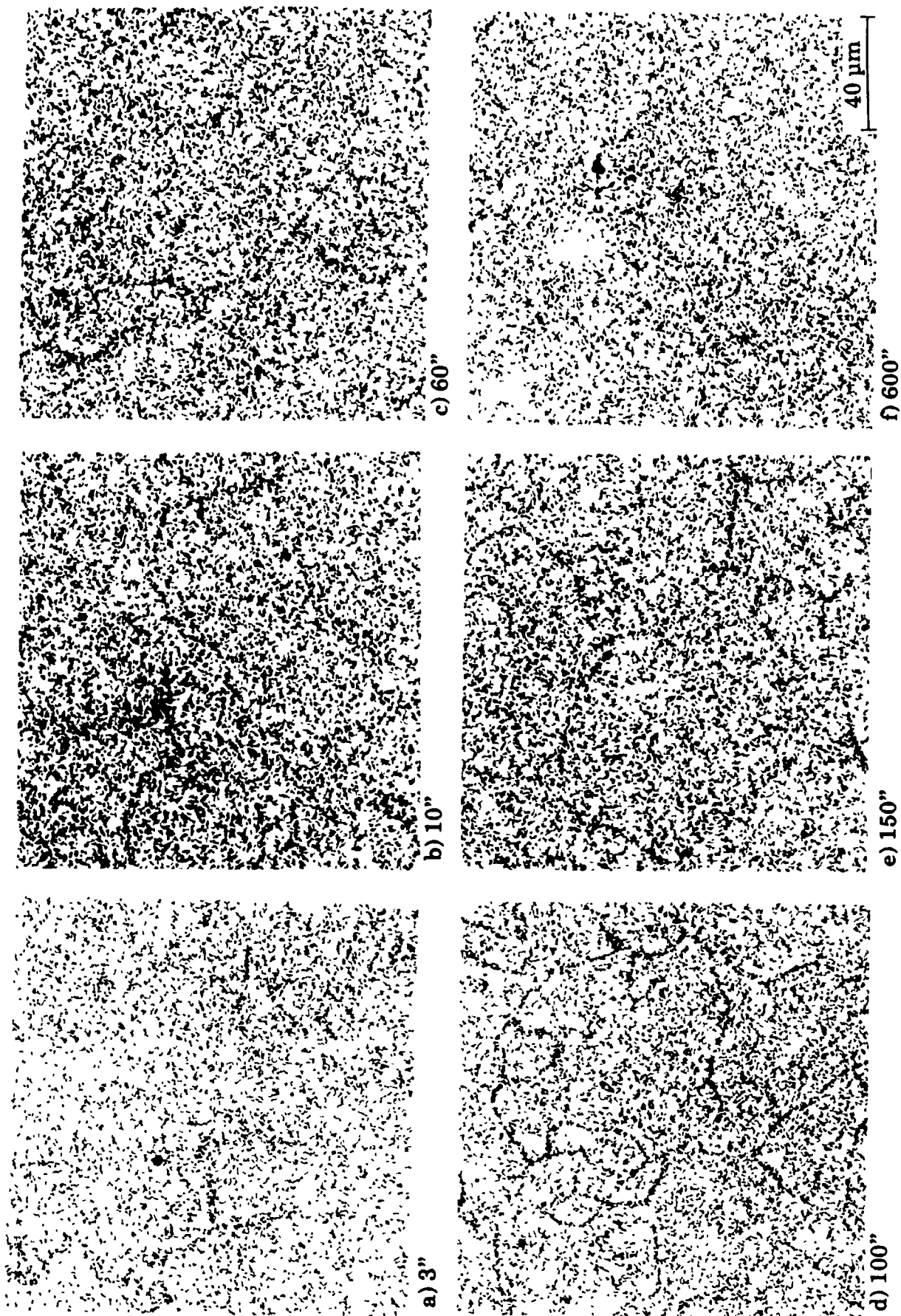


Fig. V.24 The boron distributions revealed by PTA in the Nb + B steel after 25% deformation at 1000°C and different holding times (ice brine quenching).

It is of interest to note here that the presence of recrystallized austenite grains 10 s after deformation confirms that the change observed in the stress relaxation curve of Fig. IV.9 was related to the occurrence of recrystallization.

The evolution of the boron distribution after deformation was also studied by SIMS. In this experiment,  $O^{2+}$  primary ions with an energy of 12.5 keV were again employed, and the B distribution was obtained by recording the  $^{11}B^{16}O_2^+$  signal at mass 43. The ion probe had a diameter of 100  $\mu m$  for normal operating conditions or 62  $\mu m$  by 62  $\mu m$  for high resolution studies.

Fig.V.25 shows the ion micrographs obtained on the samples deformed 25% at 1000°C and quenched in ice brine after increasing holding times. The evolution of the boron distribution is the same as that revealed by the PTA technique. It can be seen that some very slight segregation occurs a few seconds after straining (Fig.V.25a). The degree of segregation increases with holding time, and the SIMS results confirm that the optimum segregation is attained at about 100 s. As can be seen in Fig.V.25d, all the new boundaries display clear segregation to them. Finally, 600 s after deformation (Fig.V.25f), the back diffusion of boron atoms has extensively reduced the intensity of the segregation and a situation similar to the original one can be seen.

Tests were also carried out at 950, 900 and 850°C. The evolution of the boron distribution in these tests is somewhat different from the previous case. After deformation at 950°C, the boron atoms start to segregate to the boundaries of the deformed grains. The degree of segregation increases with holding time and attains its maximum at about 170 s, and then declines, but does not disappear completely. In the sample quenched 1000 s after deformation, some segregation and few precipitates can be observed around the grain boundaries, which are in fact the newly formed austenite grains. The evolution of the boron distribution 20, 170 and 1000 seconds after deformation is shown in Fig.V.26.

Isothermal holding at 900°C leads to similar patterns of segregation. However, the maximum concentration of boron atoms at the boundaries is at about 1000 s after deformation. It should also be mentioned that several precipitates are also found at the boundaries at this stage. As the holding time

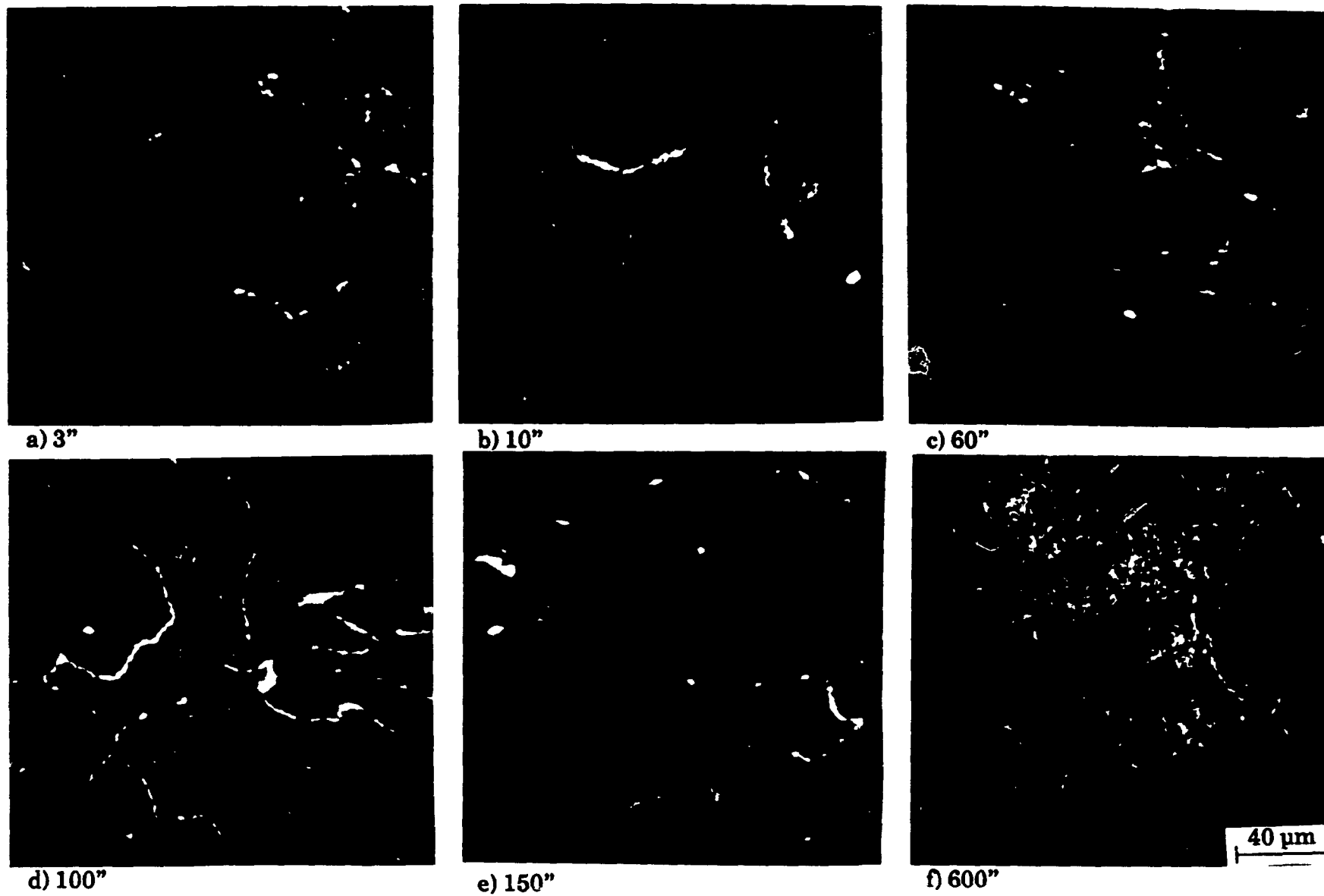


**Fig.V.25** The boron distributions revealed by SIMS in the Nb + B steel after 25% deformation at 1000°C and different holding times (ice brine quenching).

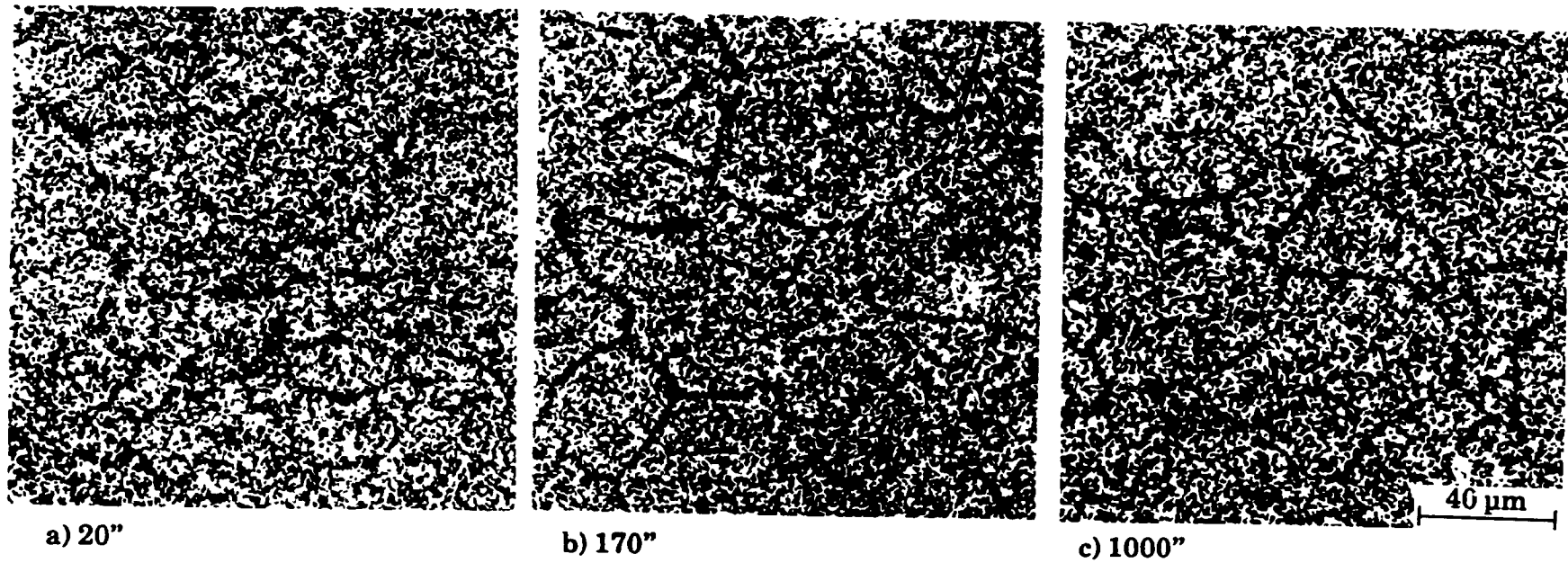


**Fig.V.26** The boron distributions revealed by PTA in the Nb + B steel after 25% deformation at 950°C and different holding times (helium quenching).

is increased to one, two and three hours, the level of segregation continuously decreases and the number of grain boundary precipitates clearly increases.

Comparison with the 950 or 1000°C results indicates that, as the deformation temperature is decreased, the maximum segregation is found after longer times, but the segregation amplitude (height of the peak) is higher.

The state of the boron distribution after testing at 850°C is somewhat different compared to the previous cases. In fact, in the sample quenched a few seconds ( $\approx 3$ ) after deformation, some slight segregation accompanied by several precipitates is observed. 50 s after straining, the degree of segregation increases a little, but the number and size of the precipitates becomes larger. As the holding time is further increased, the slight segregation tends to disappear completely. It then seems that the appearance of the precipitates strongly affects the segregation of boron to the austenite grain boundaries. The micrograph shown in Fig.V.27 illustrates the evolution of the boron distribution at 850°C after different holding times. It is of interest that, in the sample quenched 50 s after deformation, several intracrystalline boron-containing precipitates can be seen.

#### V.2.2.2 Results Pertaining to the Boron Steel

The boron distribution revealed by PTA after 25% deformation at 1000°C is depicted in Fig.V.28. Here again it can be seen that, prior to deformation, the distribution is nearly homogenous (Fig.V.28a). A little segregation can be observed along the original boundaries 3 s after straining (Fig.V.28b). However, a few short curved boundaries, delineating newly formed austenite grains, are outlined by bands of continuous etch pits. As the holding time is increased, more and more segregation occurs, and in the sample quenched 5 s after deformation, almost all of the boundaries have boron atoms segregated on them (Fig.V.28c). This point corresponds to the segregation maximum, because after 10 s, the degree of segregation is slightly lower and the boundary fraction displaying continuous etch pits is diminished (Fig.V.28d). As the holding time is further prolonged, the degree of segregation is decreased still more, and finally, in the sample quenched 150 s after straining, the state of the boron distribution is similar to the one before deformation (Fig.V.28e and f).

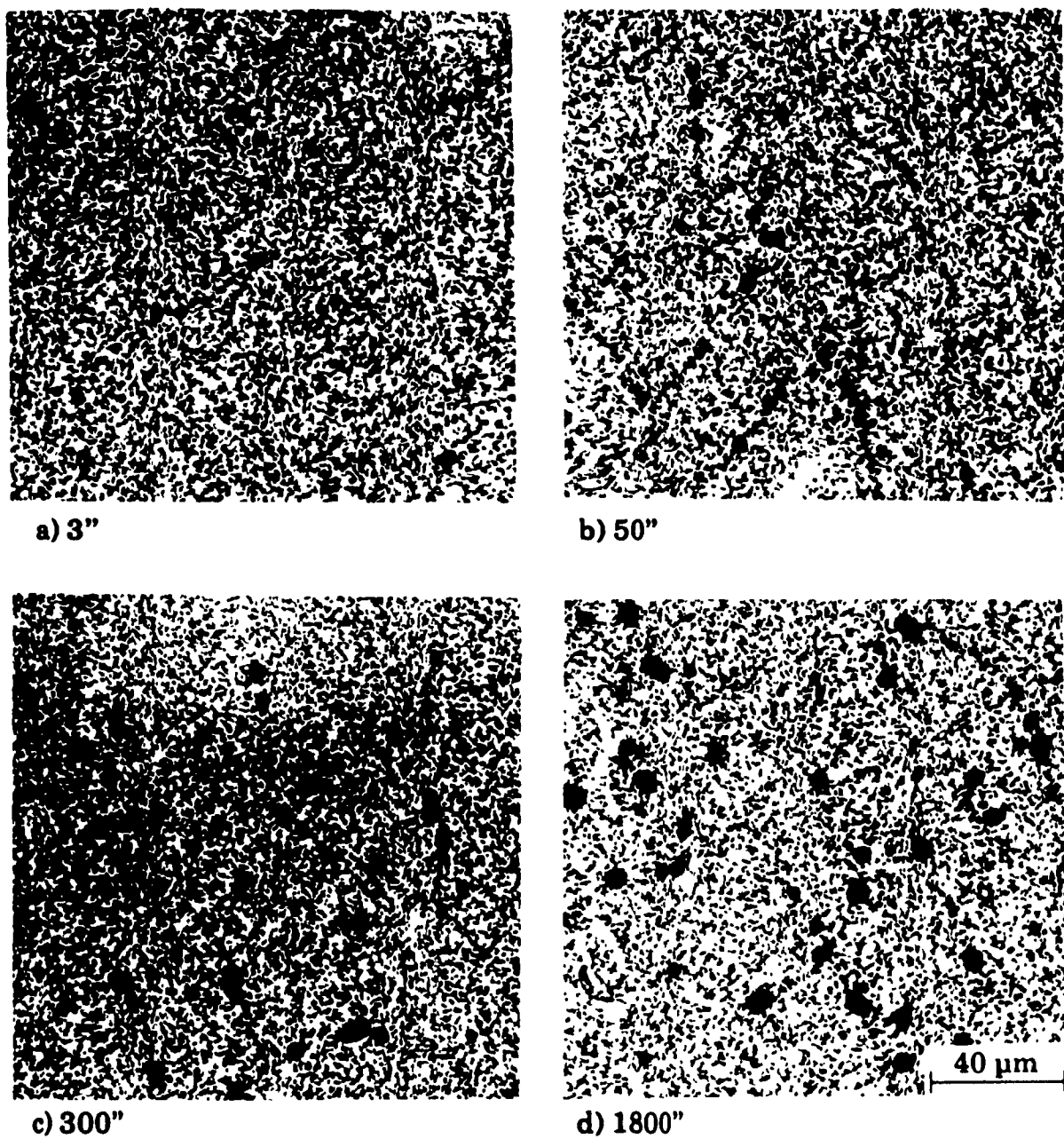


**Fig. V.27** The boron distribution revealed by PTA in the Nb+B steel after 25% deformation at 850°C and different holding times (helium quenching).

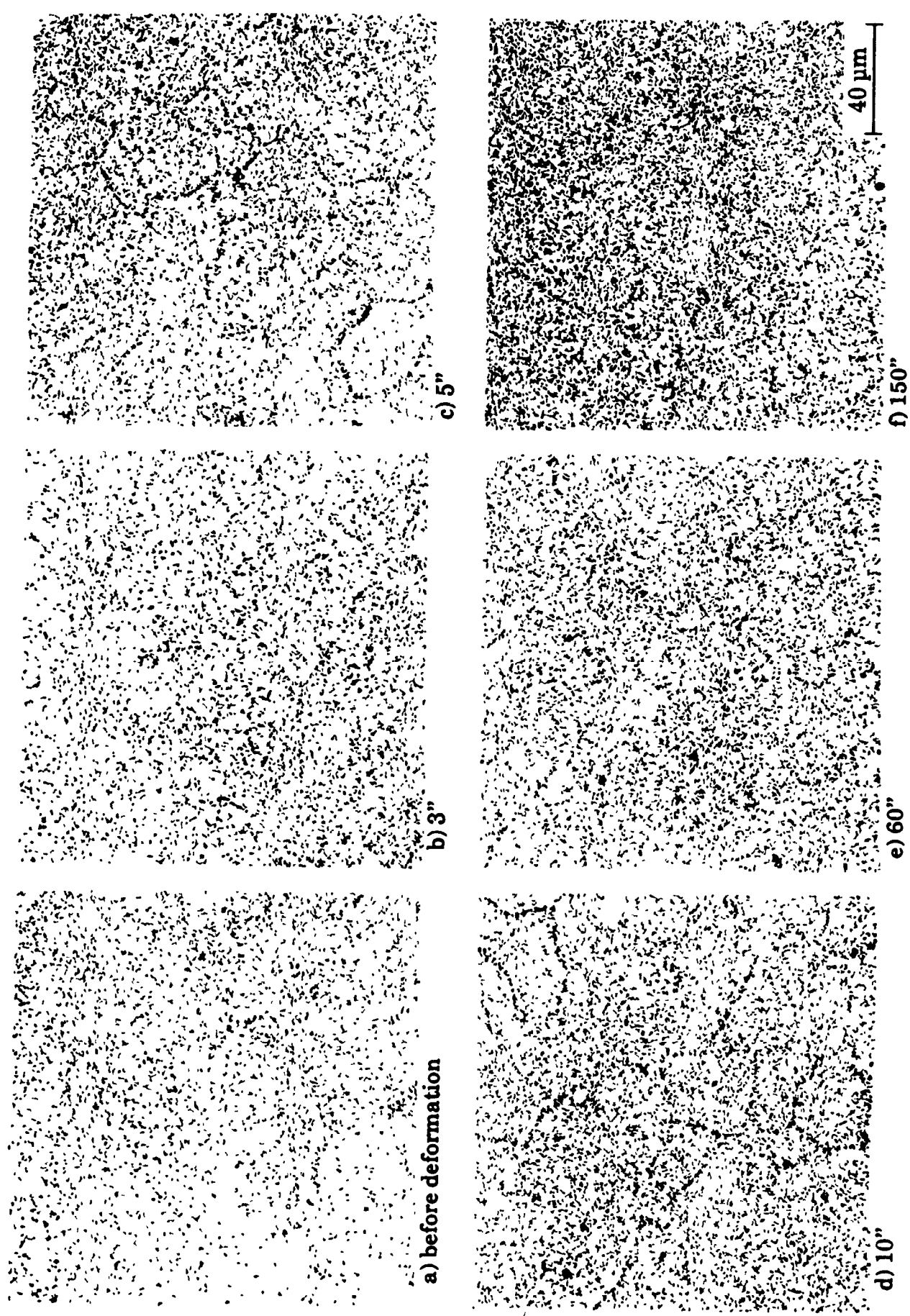


Fig. V.28 The boron distribution revealed by PTA in the B steel after 25% deformation at 1000°C and different holding times (ice brine quenching).

The changes in boron distribution after deformation at 950, 900 and 850°C were also studied. The general features of the development and elimination of grain boundary segregation and the progress of precipitation are similar to those obtained for the Nb+B steel. To illustrate the different situations, selected PTA micrographs of the specimen tested at 900°C are shown in Fig.V.29. In the sample quenched 3 s after deformation, some slight segregation is developed around the original grain boundaries. After 5 s, clear segregation can be observed both on the original and newly formed boundaries (Fig.V.29b). As the holding time is increased, the degree of segregation increases to reach a maximum at about 30 s; after this stage, the segregation decreases continuously with holding time and the number of boundaries outlined by continuous etch pits diminishes (Figs.V.29c and V.29d). It should also be pointed out that some precipitates were observed in the sample quenched 30 s after deformation. The number of these boron rich particles increases with the holding time.

### V.2.3 The Characteristics of Grain Boundary Segregation

The results obtained for the Nb+B and B steels indicate that segregation occurs on two kinds of boundaries. The first concerns the original boundaries, on which the segregation develops because of deformation. This type of segregation is similar to that observed during cooling, as described in V.2.2. The driving force for such segregation is related to the vacancy supersaturation created by the deformation, as will be discussed in detail in chapter VII. The second type of segregation appeared at the boundaries of the newly formed austenite grains. This kind of segregation is also non-equilibrium in nature and disappears as the holding time is increased.

The degree of segregation was observed to evolve in all cases. Generally, the amplitude of segregation starts to increase after deformation and reaches a maximum after a certain time, which is dependent on the test temperature and the composition of the steel. After this point, the number of boundaries depicting continuous etch pits starts to diminish and finally the boron distribution becomes almost homogeneous after still longer holding times.

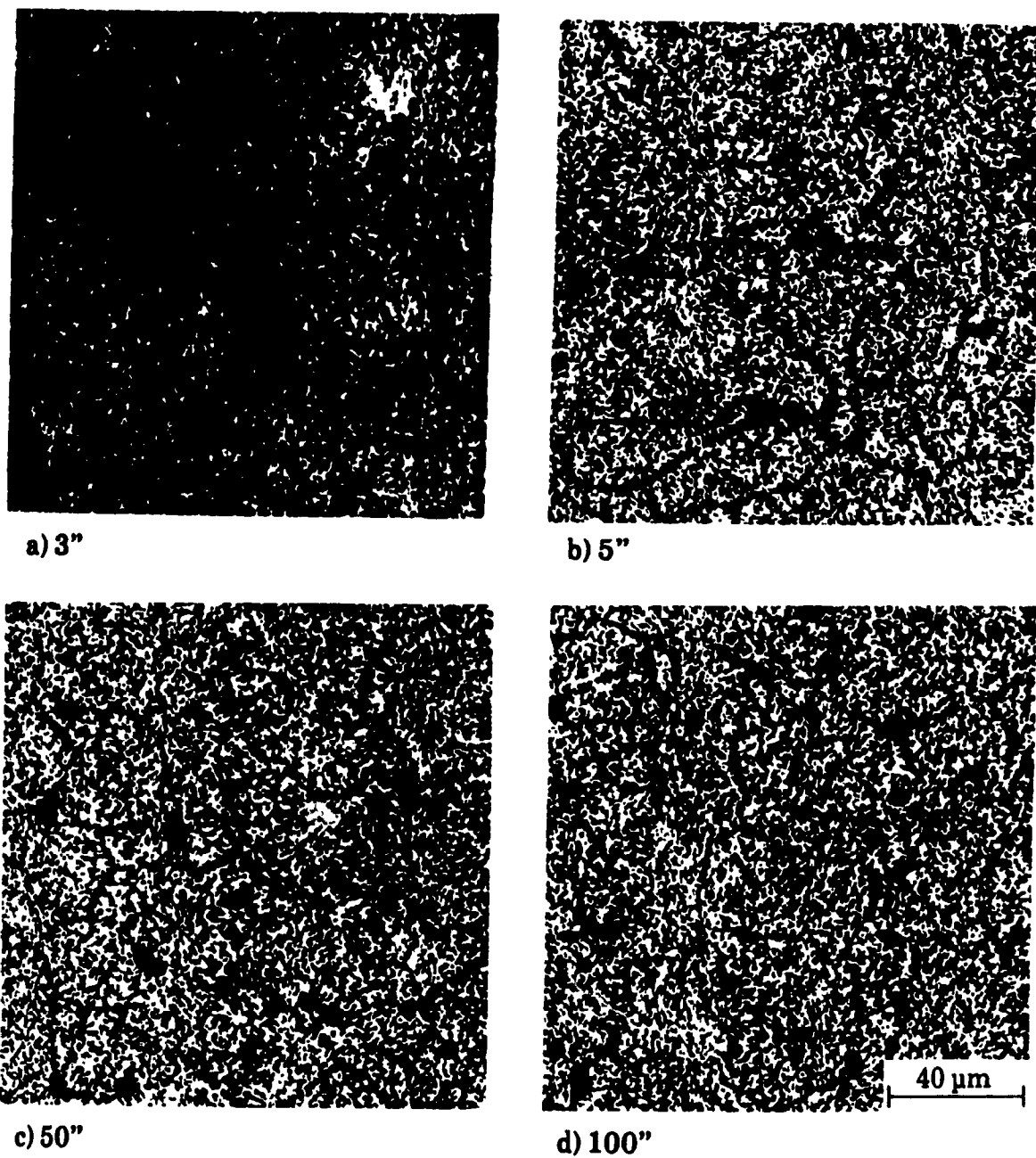


**Fig. V.29** The boron distribution revealed by PTA in the B steel after 25% deformation at 900°C and different holding times (helium quenching).

The variations in the level of grain boundary segregation can be described by measuring the length of grain boundary segregation (i.e. the length of continuous etch pits) as a function of holding time. For this purpose, the parameter  $A = L_S / L_{S_{max}}$  is introduced, where  $L_{S_{max}}$  corresponds to the sample which presents the maximum length of segregation per unit area and  $L_S$  represents the other states of boron distribution at the temperature considered. For a given sample,  $L_S$  (or  $L_{S_{max}}$ ) is obtained by measuring the total length per unit area of continuous etch pitting (i.e. boron segregation) revealed on the PTA film of the specimen.

The values of  $L_S$  and  $L_{S_{max}}$  were measured directly on the PTA micrographs using a Zeiss IBAS image analysis system. Micrographs were prepared at 500 magnification and more than 4000 mm of austenite grain boundaries were measured. In this way, the error associated with the length measurement of continuous etch pitting was less than 10%.

The measurements were carried out only on the samples tested at 1000°C, because the occurrence of precipitation at all lower temperatures was believed to affect the results. Fig.V.30 shows the evolution of the boron segregation during isothermal holding at 1000°C for the Nb + B and B steels. It can be seen that in the B steel, the segregation develops faster and also declines faster than in the Nb + B grade. Although it was not possible to perform a quantitative analysis of the absolute amounts of maximum segregation, metallographic observations showed that more boron atoms segregate in the Nb + B than in the B steel.

#### V.2.4. Influence of Cooling Rate on Boron Distribution

Depending on the experimental conditions, samples of the Nb + B and B steels were ice brine, water or oil quenched. They were also control cooled (cooling rate of 13 to 17°C/sec) to room temperature. The most important reason for changing the cooling rate was the need for precise knowledge of the state of the microstructure. This information is required to produce a better understanding of the behaviour of boron.

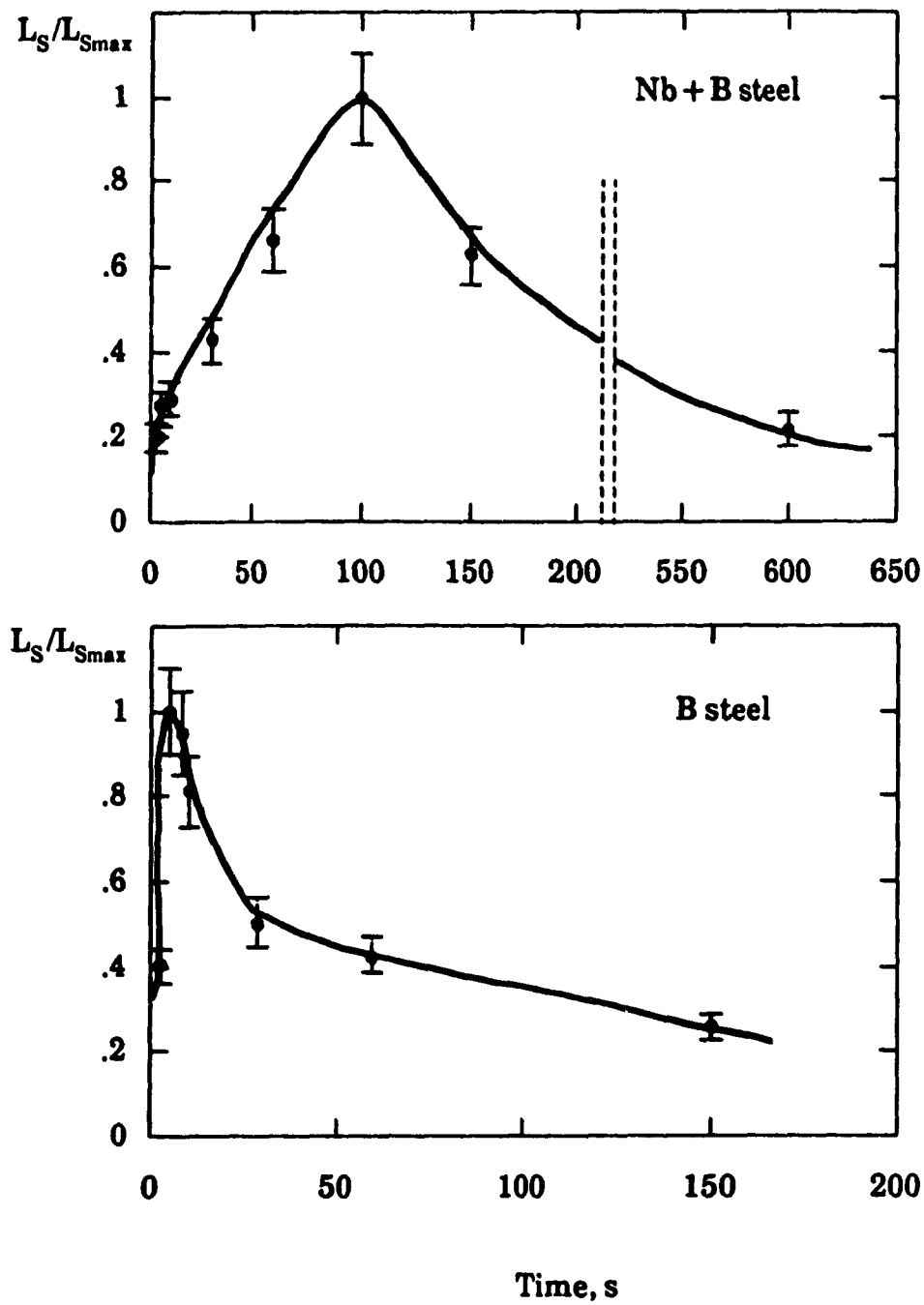


Fig.V.30 Evolution of the amplitude of segregation with isothermal holding time after 25% deformation at 1000°C.

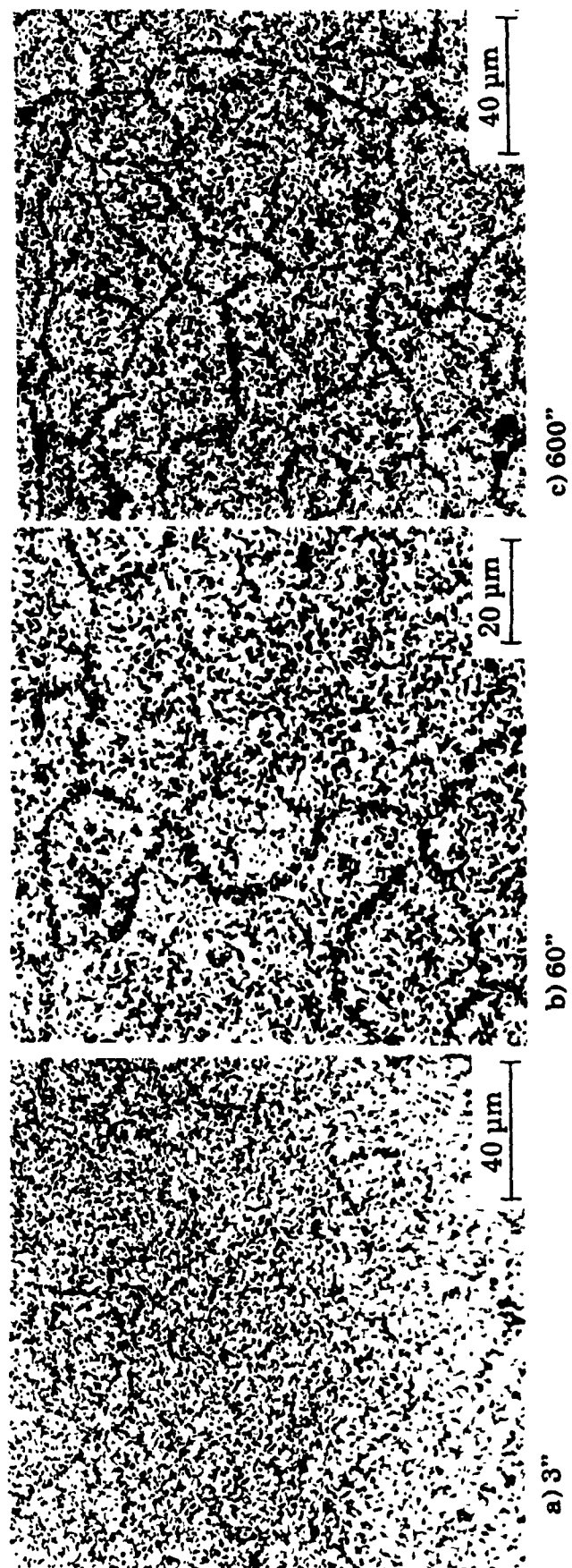


Fig. V.31 The boron distribution revealed by PTA in the Nb + B steel after 25% deformation at 1000°C and different holding times (oil quenching).

This behaviour is illustrated in Fig.V.31, where PTA micrographs of Nb + B steel specimens, deformed 25% at 1000°C and oil quenched after different holding times, are presented. When these micrographs are compared to those obtained after ice brine quenching (Fig. V.24), it can be seen that the state of the microstructure is much more clear in the oil quenched case than in the ice brine one.

Three seconds after deformation, in the ice brine quenched sample, only slight segregation can be observed around the original grain boundaries (Fig.V.24a). By contrast, on the same sample quenched in oil, not only can strong segregation be observed at the original boundaries, but clear segregation is also observed at newly formed grains (Fig.V.31a). This indicates that already 3 s after deformation at 1000°C, nucleation of the new grains has begun in the Nb + B steel. It is interesting to note that this information could not be obtained when the sample was rapidly quenched.

Another important point is revealed when the results obtained after 60 s of holding are compared (Figs.V.24c and V.31b). Boron segregation was found only around the newly formed grains in the ice brine quenched sample, while in the oil quenched one, clear segregation around the original grain boundaries can be observed. This result indicates two things: i) that although recrystallization is taking place, it has not gone to completion; and ii) that the boron atoms which segregated to the original boundaries after deformation have almost diffused back into the matrix 60 s later.

Finally, the results obtained with the oil quenched sample after 600 s of holding show that recrystallization is now complete and grain coarsening has already occurred. It is interesting to note that at this stage in the rapidly quenched sample almost no segregation can be observed. It should also be mentioned that the results obtained after water quenching are similar to those obtained after quenching in ice brine. Consequently these results will not be shown here.

Similar tests were carried out at 950, 900 and 850°C. However, for these tests, the samples were not oil quenched but control cooled to room temperature.

The evolution of the boron distribution at 900°C for the Nb+B steel is illustrated in Fig.V.32. The slow cooling rate (as compared to quenching) induces boron segregation, revealing the elongated austenite grains after deformation in this way. The observations show that recrystallization has not yet begun after 10 s (Fig.V.32a), 50 s (Fig.V.32b) or 300 s (not shown here). However, 500 s after deformation, recrystallization seems to have started (Fig. V.32c). As the holding time is increased to one hour, recrystallization progresses significantly (Fig.V.32d), and after 3 hours, grain coarsening has already occurred (not shown here).

The situation for the boron steel under the same experimental conditions is almost identical, with the exception that the recrystallization phenomenon occurs more quickly. Only 5 s after deformation, several recrystallized grains can be observed, indicating that recrystallization occurs rapidly at this temperature in the boron steel. As the time is increased to 30 and 100 s, the number of recrystallized grains grows very quickly, and in fact, it seems to be complete about 100 s after prestraining. Finally, grain coarsening is observed in the specimen quenched 600 s after deformation.

### **V.2.5 State of the Boron Distribution in the Samples Examined by TEM**

Most of the specimens investigated by TEM were those tested at 850°C, because there is appreciable precipitation at this temperature. The aim was to determine the state of boron segregation and precipitation during testing at 850°C. For this purpose, samples of the Nb+B steel were quenched before deformation or at different stages of stress relaxation after prestraining.

Isothermal holding after 5% deformation shows that, 15 s after straining, segregated boron atoms and boron containing precipitates are present at the austenite grain boundaries. The segregation is not very strong and generally only part of the boundary is outlined by continuous etch pitting. The degree of segregation becomes much weaker after 200 s and it disappears almost completely after 900 s. By contrast, as the holding time is increased, more and more precipitates appear at the grain boundaries and their mean size increases.

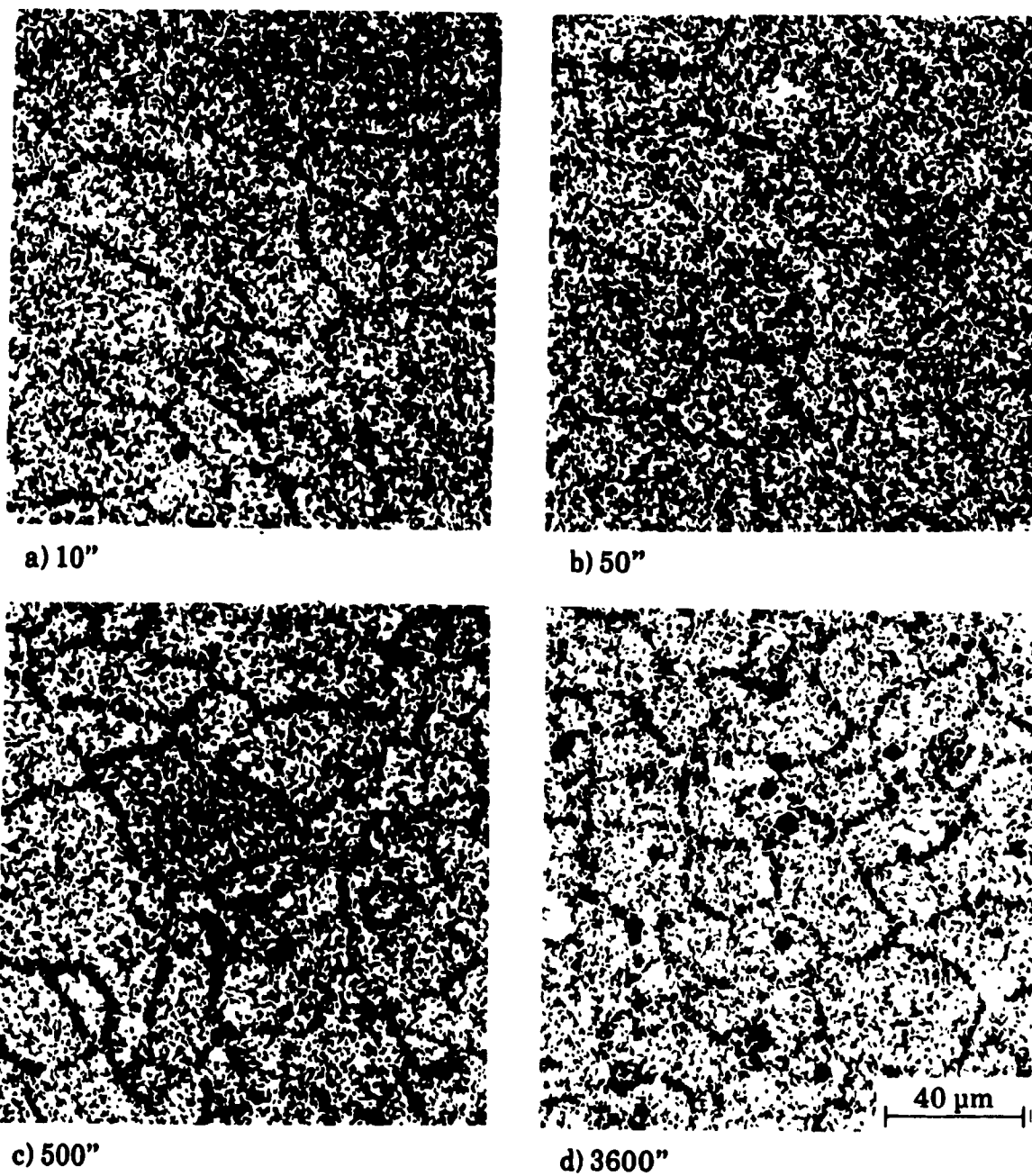


**Fig.V.32** The boron distribution revealed by PTA in the Nb + B steel after 25% deformation at 900°C after different holding times (cooling rate 13 to 17 °C/sec).

The situation after 25% deformation is similar to that of the previous case, and has already been described in V.2.2.1. The results were presented in Fig.V.27 and it is evident that segregation occurs more quickly when the amount of deformation is increased from 5 to 25%.

### V.2.6 Evolution From Segregation to Precipitation

It is apparent from the experimental results presented in the previous sections that boron can either be present as atomic boron in segregated form or combined with other elements in the form of precipitates. However, these two conditions are not independent, but strongly related to each other, the segregation being necessary prior to precipitation. At the test temperatures where precipitation can take place (950, 900 and 850°C), it was found that there was a clear evolution from segregation to precipitation as the holding time was increased.

A good example is illustrated in Fig.V.33, where the influence of holding time is shown on the boron distribution in the B steel at 850°C. In these tests, the sample was cooled to the test temperature at 2 °C/sec; this was done in order to produce significant segregation around the grain boundaries. Already forty seconds after deformation, marked segregation is observed around the prior austenite grain boundaries and numerous precipitates have also been formed at the boundaries. As the holding time is increased to 100s, the segregation is already much weaker and instead, some more precipitates have appeared (Fig.V.33b). After 300 s of holding, Fig.V.33c, less segregation is apparent, and the precipitates have grown in size. Finally, 600 s after deformation, almost no segregation is observed and the precipitates are now more uniformly distributed around the specimen.

It should be mentioned that, although the boron segregation at this temperature is of the non-equilibrium type, the rate of boron back diffusion is small. The low testing temperature also implies that recrystallization cannot take place during the test. Consequently, the weakening of the segregation level in the specimen is not due to recrystallization or boron back diffusion but rather to evolution from a segregated to a precipitated state. Finally, it is worth

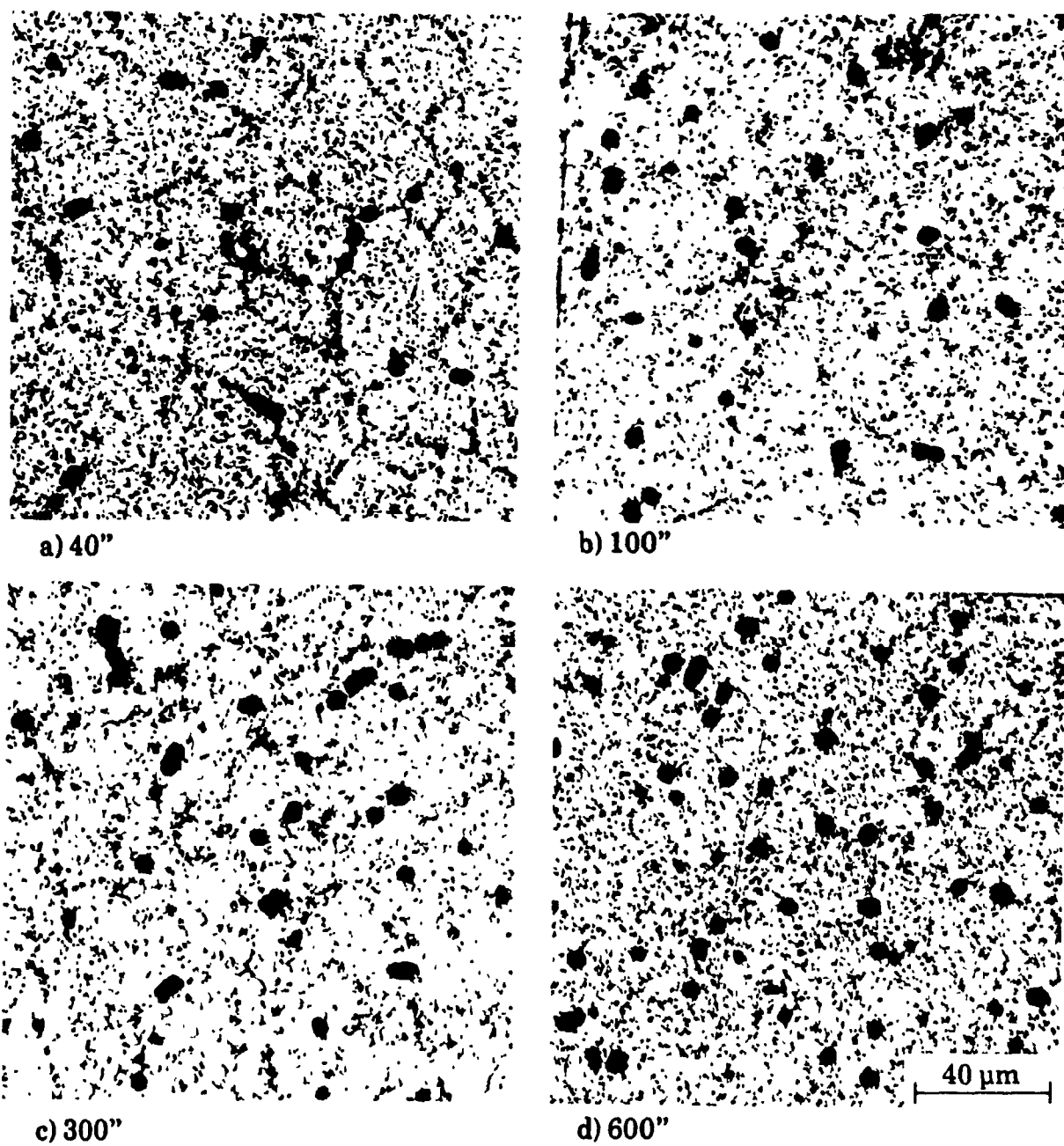


**Fig.V.33** Evolution from segregation to precipitation in the B steel after deformation at 850°C.

while noting that the same phenomenon was observed in the Nb + B steel, and also at higher temperatures (see for example Fig.V.32).

## V.2.7. Presence of Boron in Inclusions and Precipitates

### V.2.7.1 Inclusions

During steelmaking, boron is added at the last stage in order to reduce its opportunities for combining with nitrogen and other alloying elements. Nevertheless, SIMS analysis revealed that it is present in large inclusions. A set of ion micrographs of a Nb + B steel specimen, deformed 25% at 1000°C and quenched 100 s later, is presented in Fig. V.34. For this investigation, 12.5 keV  $O^{2+}$  ions were used as the primary beam and the secondary positive ions were collected and imaged. These inclusions were not dissolved during solution treatment, and in addition to boron, they usually contained Mn, Al, Ti and Nb.

The presence of boron in aluminum oxide inclusions [92] as well as in undissolved  $V_4C_3$  carbides [31] has already been reported. However, this is the first time that the presence of boron in Mn, Al, Ti and Nb containing inclusions has been demonstrated. It should be pointed out that, in several of the inclusions listed above, only some of the elements were present. It is clear from the results obtained that the amount of boron dissolved in the matrix is less than the total boron content of the material since the more stable boron-containing inclusions are not easily dissolved during normal solution treatments.

### V.2.7.2 Precipitates

The presence of boron in the large  $M_{23}I_6$  (M=metal, I=interstitial) particles was revealed by both PTA and optical microscopy, as illustrated several times in the previous sections. Also, when the PTA films are inspected at higher magnifications, agglomerations of etch pits, composed of groups of 3 to 5 pits, are found within the grains. Each agglomeration indicates a higher concentration of boron at that particular site in the matrix. Furthermore, evidence was presented in the first part of this chapter that, after solutionizing, Ti or (Ti, Nb)-rich particles remain undissolved in the material. Following

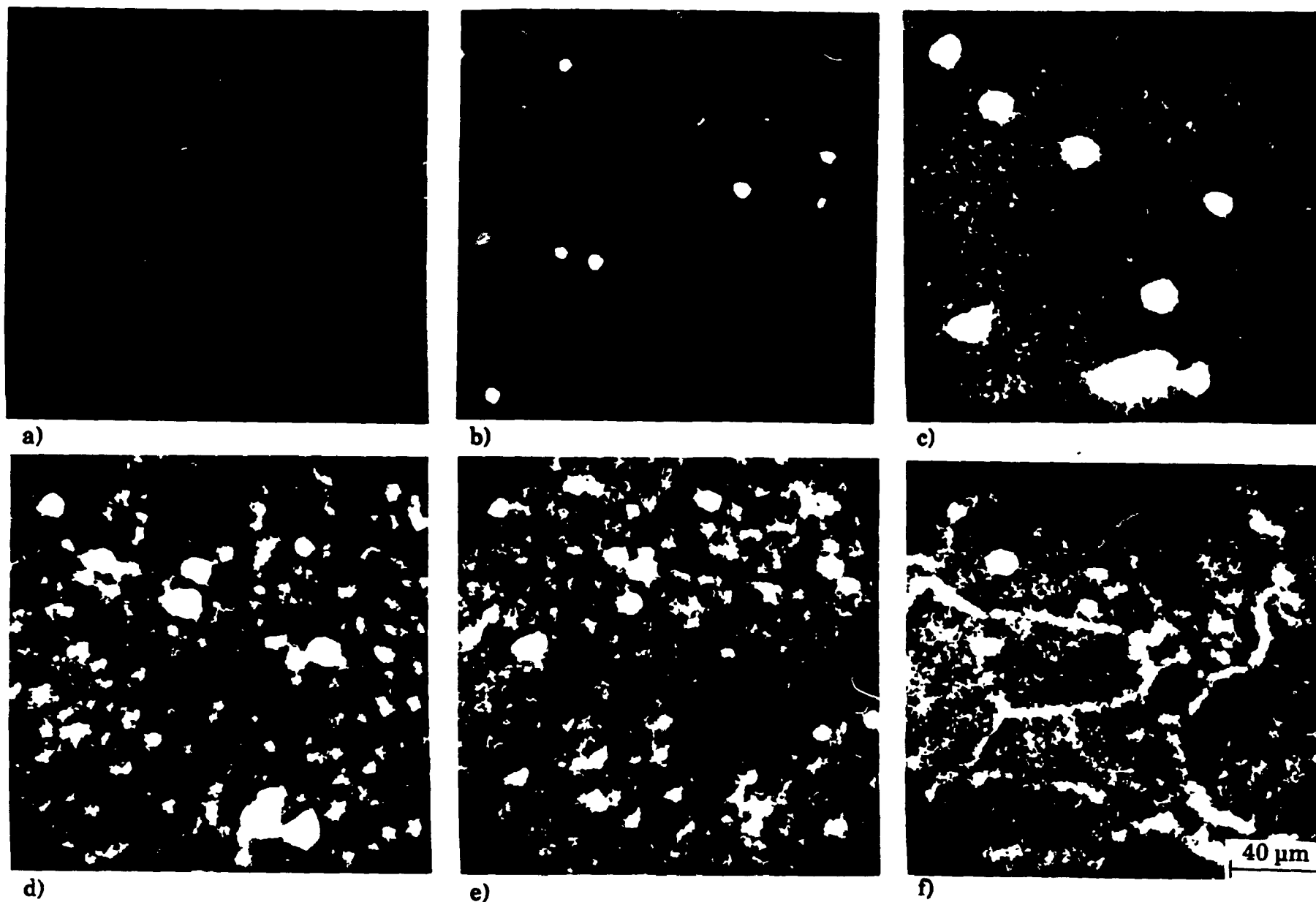


**Fig.V.34 Ion micrographs showing the distribution of boron and other alloying elements in undissolved inclusions in the Nb + B steel.  $O_2^+$  was used as the primary ion and  $BO_2^-$  as the secondary ion. a)  $Fe^+$ , b)  $Mn^+$ , c)  $Al^+$ , d)  $Ti^+$ , e)  $Nb^+$ , f)  $B^+$ .**

stress relaxation, Nb-rich precipitates are formed in addition to the undissolved particles.

In view of these observations, it can reasonably be assumed that the agglomerated etch pits are undissolved (Ti, Nb) or Nb-rich precipitates. However, in order to check the validity of the above assumption, i.e. in order to remove the possible interference between the alpha particles emitted from the precipitates and those coming from the matrix (more precisely from the boron atoms in solution), the following experiment was performed.

Carbon extraction replicas were first prepared from the samples that had undergone stress relaxation at 850°C for 50, 200, 500, and 1800 s. Following this step, a cellulose acetate film was slipped over the replica, and the samples were irradiated with a neutron flux of  $1.02 \times 10^{16}$  n/cm<sup>2</sup>. This high neutron dose was used in order to have the highest response possible as the amount of boron present in the precipitates was much less than the total amount of boron in the bulk material.

The results are presented in Fig.V.35, where it can be seen clearly that boron is present in the small undissolved as well as in the strain-induced precipitates. It should be emphasized that the trace of a precipitate on the PTA film is much larger than its real size, as discussed in V.2.1.1.

Finally, although boron-containing precipitates were detected during the EELS experiments, the results of the PTA investigation indicate that boron is contained in both types of precipitate. Consequently, the assumption made regarding the existence of boron in strain-induced precipitates seems to be a reasonable one. Moreover, the present SIMS and PTA results confirm that boron is contained in both inclusions and large grain boundary precipitates.

## **V.2.8 Influence of Boron on Recrystallization at 950°C**

The stress relaxation curves for the Nb+B and Nb steels after 25% deformation at 950°C were found to be different (Figs.IV.10 and IV.12). The relaxation rate for the Nb steel changed suddenly after about 10 seconds, before the appearance of a plateau at about 80 s. By contrast, no change in rate was

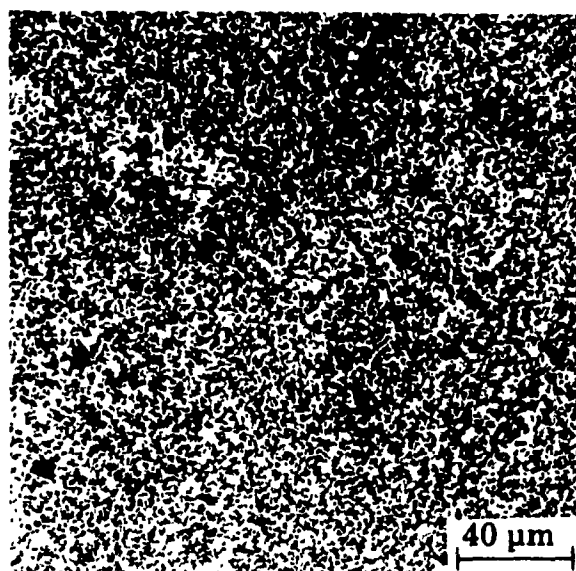
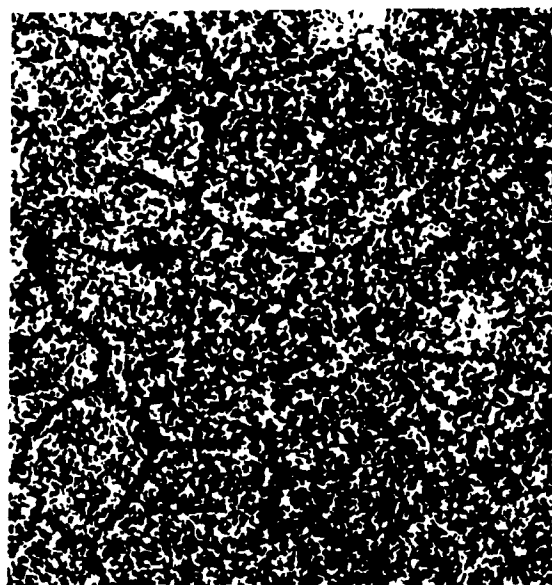


**Fig.V.35** PTA micrograph of carbon extraction replicas showing the presence of boron in the precipitates; Nb + B steel deformed 5% at 850°C.

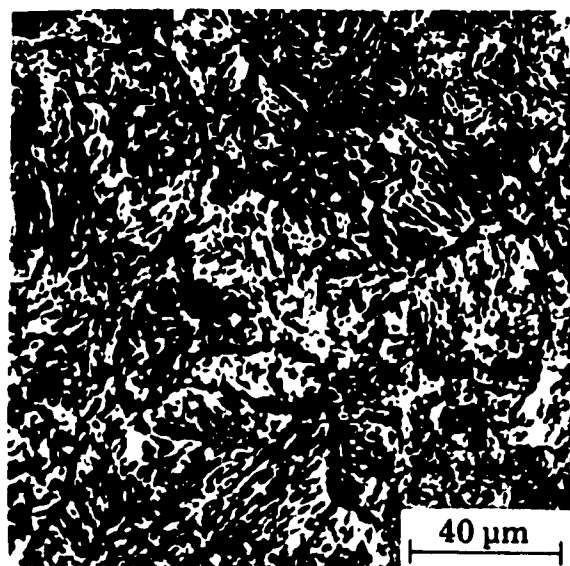
observed on the relaxation curve of the Nb+B steel except for the one corresponding to the occurrence of precipitation.

The change in slope of the Nb steel curve was associated with the beginning of recrystallization in this material. To confirm this hypothesis, a Nb steel specimen was quenched about 65 s after deformation; a Nb + B steel sample quenched 100 s after straining was used for comparison purposes. Hot picric acid was employed to reveal the austenite grain boundaries in the Nb steel and the PTA technique was applied to the other sample.

The results are illustrated in Fig.V.36. It can be seen that new grains are present in the Nb steel specimen. On the other hand, no sign of recrystallization was detected in the Nb+B steel, and only elongated grains were found, as shown in Fig.V.36a. Finally, these results indicate that partial recrystallization occurs at 950°C after 25% deformation in the Nb steel. The presence of boron delays recrystallization long enough for precipitation to be initiated before the former can begin.



a)



b)

**Fig.V.36** State of the microstructure in the Nb + B and Nb steels after 25% deformation at 950°C. a) PTA micrograph of the Nb + B steel held for 100 s, and b) optical micrograph of the Nb steel after etching with hot picric acid after 65 s of holding.

## CHAPTER VI

### DISCUSSION

#### PART 1: MICROSTRUCTURAL EVOLUTION DURING STRESS RELAXATION

The mechanical testing results of chapter IV and the microscopy observations presented in chapter V showed clearly that the stress relaxation technique is able to detect the occurrence of both recrystallization and precipitation in hot worked austenite. In this chapter, the theory of thermally activated dislocation movement and that of particle-dislocation interaction will be used to interpret the experimental results.

##### VI.1.1 Stress Relaxation After Deformation

It should be pointed out that other mechanisms for high temperature deformation, such as the stress directed diffusion of vacancies (Nabarro-Herring diffusion creep) and grain boundary sliding, were rejected in this analysis. The reason is that, as reported by Herring [154], Dorn [155] and Langdon [156], diffusion creep makes appreciable contributions only at very high temperatures (close to  $T_m$ ), very low stresses (i.e. at extremely slow strain rates) and finally when the grain size is small. Similar considerations apply to grain boundary sliding, but the stress levels are somewhat higher. Consequently, only the theory of the thermally activated motion of dislocations will be adopted.

##### VI.1.1.1 Formulation of the Problem

When a polycrystal is deformed, various mechanisms of deformation can operate at different temperatures. We consider the following here :

- 1) intersection of dislocations
- 2) cross slip
- 3) motion of jogged screw dislocations
- 4) climb of dislocations

The activation energies for the first two processes are so small [155] that, at high testing temperatures (such those used in this investigation), dislocation intersection and cross slip are expected to occur so frequently that they no longer serve as barriers to the motion of dislocations.

By contrast, at these temperatures, the mobility and concentration of vacancies is high enough for dislocation climb to become important. As shown by Mott [157] and others [158, 159], this mechanism leads to a power law of stress dependence. However, equation IV.1 obtained from the stress relaxation data reveals an exponential dependence of the stress. Consequently, the mechanism of edge dislocation climb will be excluded and only the theory based on the motion of jogged screw dislocations will be considered here. As will be shown later, this process leads to an exponential dependence of the strain rate on stress.

#### VI.1.1.2 Dislocation Dynamics During Stress Relaxation

A jog is an offset in a dislocation line which has a component normal to the glide plane. When produced in edge dislocations, they do not restrain movement as they have the same slip directions. The situation for a jogged screw dislocation is somewhat different. In this case, the jog itself has an edge component in its glide plane and is sessile. Thus, when the screw dislocation is forced to move, these jogs must climb from one slip plane to the next by non-conservative motion.

Jogs can form by a number of mechanisms during deformation [155]. For example, when a screw dislocation intersects a forest screw dislocation, unit jogs are produced. Also, when a screw dislocation cross slips from plane P1 to some other slip plane P2 and then back to P3, which is parallel to P1, super jogs many planes in height are formed by the segment left in plane P1.

The thermally activated motion of jogged screw dislocations was first analyzed by Mott [157], and later treated by several other workers [155, 160, 161]. The analysis presented here is based on that of Hirsch and Warrington [161].

Let us consider some sessile jogs (i.e. jogs which are dissociated and cannot glide conservatively along the dislocation) which are restraining a screw dislocation. When the dislocation is forced to move, two situations can arise depending on the temperature :

- 1) at low temperatures, the screw dislocation can only advance by leaving a line of point defects or a dislocation dipole. This gives rise to a flow stress which is temperature independent.
- 2) Above a sufficiently high temperature corresponding to a given rate of strain, thermal activation becomes rate determining. In this process, for the dislocation to move, a point defect is created and moved away from the jog in the same jump.

At high temperatures, in view of the high energy required to create interstitials [155], the point defects created by the non-conservative motion of jogs are vacancies. Also, in fcc crystals, if the jogs are small, only vacancy-producing jogs are sessile [161]. Consequently, the operative process must depend primarily on the vacancy mechanism.

Consider sessile jogs with Burgers vectors  $b$ , spaced at a mean distance  $l$ , along the dislocations. The energy that must be supplied by a thermal fluctuation in order to form a vacancy is [161]:

$$E = U_0 - \frac{\tau_e A^* b}{h} \quad (\text{VI.1})$$

Here  $U_0$  is the free energy of formation and motion of a vacancy,  $\tau_e$  is the effective shear stress defined as the difference between the applied stress,  $\tau$ , and the internal stress,  $\tau_i$ , and  $A^*$  is the area swept by the dislocation during its movement (known as the activation area). The value of  $A^*$  is not constant and depends on the deformation mechanism, as will be shown in detail in the next section.

The net frequency for the forward motion of a vacancy-forming jog can then be described as:

$$v_f = \frac{vN}{h} \exp\left(\frac{-U_o}{kT}\right) \left\{ \exp\left(\frac{\tau_e A^* b}{hkT}\right) - 1 \right\} \quad (\text{VI.2})$$

where  $v$  is a factor slightly less than the Debye factor,  $N$  is the coordination number,  $k$  is Boltzmann's constant and  $T$  is the absolute temperature.

The average velocity of jogged screw dislocations then becomes equal to

$$\bar{v} = \frac{bvN}{h} \exp\left(\frac{-U_o}{kT}\right) \left\{ \exp\left(\frac{\tau_e A^* b}{hkT}\right) - 1 \right\} \quad (\text{VI.3})$$

The left side of the above equation is related to the plastic strain rate by the Orowan equation [162]

$$\dot{\epsilon} = \frac{1}{M} b \rho_m \bar{v} \quad (\text{VI.4})$$

In this equation,  $M$  is the mean Taylor factor and  $\rho_m$  the mobile dislocation density.

The substitution of equation VI.3 in VI.4 leads to

$$\dot{\epsilon} = \frac{b^2 \rho_m vN}{Mh} \exp\left(\frac{-U_o}{kT}\right) \left\{ \exp\left(\frac{\tau_e A^* b}{hkT}\right) - 1 \right\} \quad (\text{VI.5})$$

For high effective stresses, equation VI.5 can be approximated as

$$\dot{\epsilon} = \frac{b^2 \rho_m vN}{Mh} \exp\left(\frac{-U_o}{kT}\right) \exp\left(\frac{\tau_e A^* b}{hkT}\right) \quad (\text{VI.6})$$

On the other hand, it was shown in chapter IV that the stress relaxation before precipitation can be described by equation IV.1

$$\sigma = \sigma_0 - a \ln(1 + \beta t) \quad (\text{IV.1})$$

But

$$\sigma - \sigma_0 = -E \varepsilon \quad (\text{VI.7})$$

So

$$\varepsilon = \frac{a}{E} \ln(1 + \beta t) \quad (\text{VI.8})$$

and finally

$$\dot{\varepsilon} = \frac{a\beta}{E} \exp\left(-\frac{\sigma}{a}\right) \exp\left(\frac{\sigma}{a}\right) \quad (\text{VI.9})$$

Comparison of equations VI.6 and VI.9 shows clearly that the interpretation based on the motion of jogged screw dislocations leads to the same type of stress dependence for the plastic strain rate (i.e. an exponential stress dependence).

The possible chronology of the "events" from the dislocation dynamics point of view may be the following. During deformation, as a result of dislocation intersections and cross slips, jogs are created and the density of both dislocations and jogs increases as the plastic strain is increased. Following the prestrain, the dislocations move continuously in the direction of the effective stress. This stress is in fact the thermal component of the developed stress and can be associated with the short range resistance to dislocation motion from jog dragging. The jog dragging is overcome by thermal fluctuations leading to the conversion of the elastic strain of the sample into plastic strain. Because of jog dragging, the mobility of jogged screw dislocations is lower than that of edge dislocations; this effect appears to be confirmed by the observations of Chen and Pond [163]. Consequently, a possible rate controlling mechanism during stress relaxation following deformation is the motion of jogged screw dislocations leading to the exponential stress dependence of the stress relaxation data obtained in this investigation.

Experimental support for the operation of this mechanism was provided by Hirsch and Warrington [161], who measured the high temperature flow stress of single crystals of Al and polycrystalline Al and Cu. Also, the creep and

stress relaxation data obtained on polycrystalline Mg by Gibbs [164] were interpreted in terms of the jogged dislocation mechanism.

### VI.1.1.3 Application of the Model

In this section, the stress relaxation data will be used in the framework of the suggested model. For this purpose, the values of the activation area,  $A^*$ , will be calculated for the different experimental conditions.

#### a) The Activation Area, $A^*$

A precise definition of the activation area was given by Li [165], who defined it as the area swept out by a dislocation segment during thermal activation in the presence of an effective stress.

$A^*$  is not constant and varies over a wide range depending on the deformation mechanism. For example, for dislocation climb  $A^*$  (in  $b^2$  units) is equal to unity; it is between 10 to 100 when the deformation process is controlled by cross slip, and finally it ranges from 100 to 10,000 when the non-conservative motion of dislocations is rate controlling [166]. These variations are directly dependent on the geometry of the Helmholtz free energy barrier or the force-distance profile. In the case of a vacancy-emitting jog, a rectangular force-distance profile was assumed by Seeger [167], which was supported as a reasonable approximation by Gibbs [166]. Under these conditions, the activation area is almost independent of the effective stress and is equal to  $l_j b$ , where  $l_j$  is the mean distance between jogs.

#### b) The Internal Stress, $\tau_i$

For the purpose of calculating  $A^*$ , it is important to know how the internal stress varies during stress relaxation. Without carrying out any calculations, it can be assumed that the internal stress in a specimen is constant during relaxation. This arises from the fact that the plastic strain taking place during a test is so small ( $\approx 2 \times 10^{-4}$  at  $850^\circ\text{C}$ ), that only negligible microstructural changes are likely to occur during stress relaxation.

### c) Calculation of $A^*$

Comparing equations VI.6 and VI.9, taking into account the previous assumption regarding the internal stress, and finally using the relation  $\sigma = M\tau$ , the following relationship is obtained for the activation area:

$$A^* = M \frac{hkT}{ab} \quad (\text{VI.10})$$

Now we know that  $A^* = l_j b$ ; thus

$$l_j = M \frac{hkT}{ab^2} \quad (\text{VI.11})$$

It can be seen from equations VI.10 and VI.11 that both the activation area and the average distance between jogs are constant during an individual stress relaxation test.

From the stress relaxation results presented in Figs. IV.3 to IV.12, the values of  $\alpha$  and  $\beta$  were obtained. The different  $A^*$ 's were then estimated using equation VI.10. The following values were used in the calculation and the results are displayed in Tables VI.1 and VI.2.

$$M = 3.06$$

$$k = 1.38 \cdot 10^{-23} \text{ J/}^\circ\text{K}$$

$$h = 1$$

It is interesting to note that in the two steels and under the different experimental conditions,  $A^*$  fell in the interval 100-1600  $b^2$ . This range of  $A^*$  values is typical for the non-conservative motion of jogs and indicates that the glide of jogged screw dislocations could be the rate controlling mechanism for stress relaxation prior to precipitation. It can also be seen from the results that increasing the deformation leads to higher values of  $\alpha$  and consequently lower activation areas. This is associated with the fact that higher prestrains produce higher dislocation densities (see Appendix 2) and consequently the area which can be swept by each dislocation becomes smaller.

**Table VI.1.**  
**Values of  $\alpha$ ,  $\beta$  and  $A^*$  Determined from the**  
**Stress Relaxation Data for the Nb Steel**

Solutionizing Temperature °C	Prestrain %	Test Temp. °C	$\alpha$ MPa	$\beta$ s <sup>-1</sup>	$A^*$ b <sup>2</sup>
1100	5	800	2.11	39.69	1334
		830	2.06	44.41	1405
		850	1.95	55.87	1511
		870	1.87	59.11	1604
		900	1.78	63.82	1777
1100	25	800	7.86	112.53	335
		850	7.40	158.11	373
		900	7.73	176.73	376
		950	7.69	181.56	391
		1000	7.71	179.12	405
1200	5	800	3.28	37.60	916
		830	2.07	44.21	1363
		850	1.93	46.87	1397
		870	1.86	52.64	1558
		900	1.74	53.37	1569
		950	1.69	72.11	1779
1200	25	800	8.36	164.86	396
		850	8.29	134.09	437
		900	6.66	231.43	347
		950	6.31	273.78	359

**Table VI.2.**  
**Values of  $\alpha$ ,  $\beta$  and  $A^*$  Determined from the**  
**Stress Relaxation Data for the Nb + B Steel**

Solutionizing Temperature °C	Prestrain %	Test Temp. °C	$\alpha$ MPa	$\beta$ s <sup>-1</sup>	$A^*$ b <sup>2</sup>
1100	5	800	2.61	24.32	1078
		830	2.53	31.86	1144
		850	2.46	42.52	1197
		870	2.29	48.31	1309
		900	2.10	53.19	1465
1100	25	800	7.81	167.23	337
		850	7.63	189.56	361
		900	7.78	208.38	370
		950	7.42	239.89	405
		1000	7.16	416.82	437
1200	5	800	2.41	28.03	1094
		830	2.36	43.31	1149
		850	2.17	57.70	1272
		870	2.06	68.25	1364
		900	2.38	66.79	1211
		950	1.95	82.29	1542
1200	25	800	7.96	183.62	331
		850	7.71	197.11	358
		900	7.48	216.54	385
		950	7.36	244.19	408

## VI.1.2 Effect of Precipitation on Stress Relaxation

The stress relaxation results of Chapter IV showed clearly that, under the experimental conditions where carbonitride precipitation is expected, a plateau appears on the stress versus log(time) curves. Furthermore, the electron microscopy results presented in chapter V demonstrated that the observed stress plateau can be attributed to the occurrence of Nb(C,N) or Nb(C,N,B) precipitation. As the relaxation process is controlled by a dislocation mechanism, its arrest may be related to an interaction between dislocations and precipitates.

### VI.1.2.1 Dislocation-Particle Interactions at High Temperatures

When a glide dislocation encounters an array of obstacles (Fig.VI.1), it must be bent to some angle  $\phi$  before it can move on. In the most general case, where the character of the dislocation is ignored, the obstacle will exert a force on the dislocation equal to

$$F = 2E \cos\left(\frac{\phi}{2}\right) \quad (\text{VI.12})$$

Here  $E$  is the line tension of the dislocation.

Under these conditions, a local shear stress,  $\tau_l$  (due to the reaction force acting on the particle) exists at the particle-matrix interface tending to shear the particle of diameter  $d$ . Considering that  $E = G_M b^2/2$ ,  $\tau_l$  is given by [168]

$$\tau_l = \frac{F}{bd} = \frac{G_M b}{d} \cos\left(\frac{\phi}{2}\right) \quad (\text{VI.13})$$

where  $G_M$  is the shear modulus of the matrix.

#### a) Cutting or Bowing?

According to equation VI.13, if the local shear stress  $\tau_l$  exceeds the strength of the particle  $\tau_{ic}$ , the latter will be cut by the gliding dislocation. On

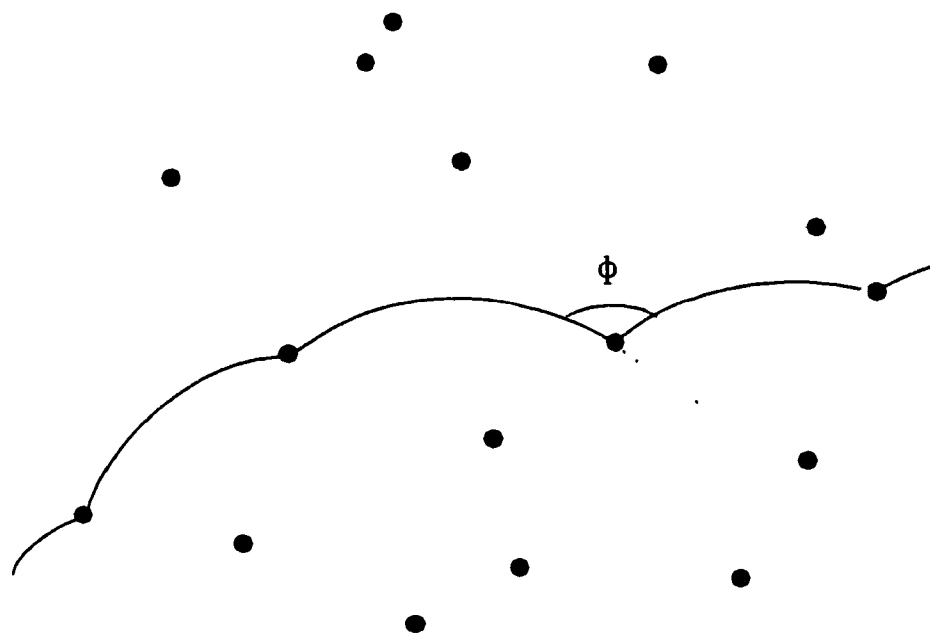


Fig.VI.1 Dislocation held up at a random array of particles.

the other hand, if  $\tau_{ic} > G_M b/d$ , the particle will be bypassed by the Orowan mechanism (in this case  $\phi = 0$ ) and will not be cut. However, the transition from cutting to bowing does not depend only on the strength of the precipitate and, as reported by Humphreys [168], depending on its size, even the strongest particle can be sheared. The question then arises, what will the diameter of the Nb(C,N) precipitates be for the transition from cutting to bowing?. To answer this question, the mechanisms which involve particle strengthening will now be considered.

The strength originates from a number of short range interactions between dislocations and particles [169]. However, only two of them seem to be important in our case and are considered here:

- i) coherency hardening, in which the misfitting particle is associated with elastic stresses which interact with the dislocations;
- ii) elastic modulus hardening, in which the energy of the dislocation is proportional to the shear modulus of the lattice, and differences in modulus between particle and matrix give rise to the interactive force.

The stress associated with the coherency hardening mechanism is equal to [170]:

$$\tau_c = 3 G_M \varepsilon^{3/2} \left( \frac{df_v}{2b} \right)^{1/2} \quad (\text{VI.14})$$

where  $\varepsilon$  is the misfit parameter and is given by

$$\varepsilon = \frac{2}{3} \frac{a_p - a_M}{a_M} \quad (\text{VI.15})$$

$d$  is the diameter of the particle and  $f_v$  its volume fraction,  $G_M$  the shear modulus of the matrix and  $b$  has its usual meaning. Finally  $a_p$  and  $a_M$  are the lattice parameters of the precipitate and matrix, respectively.

According to Knowles and Kelly [171], the stress associated with the elastic modulus mechanism is given by:

$$\tau_G = \frac{\Delta G}{4\pi^2} \left( \frac{3\Delta G}{G_M b} \right)^{1/2} \{0.8 - 0.13 \ln(\frac{d}{2b})\}^{1/2} \left( \frac{df_v}{2} \right)^{1/2} \quad (\text{VI.16})$$

Here  $\Delta G$  is the difference between the shear modulus of the matrix and the precipitates.

On the other hand, the Orowan stress can be written approximately as [162]

$$\tau_0 = 0.8 \frac{Gb}{\lambda} \quad (\text{VI.17})$$

where  $\lambda$  is the particle spacing and is given by [153]

$$\lambda = 0.5 \left[ \frac{\pi}{6 f_v} \right] \quad (\text{VI.18})$$

The dependences of  $\tau_c$ ,  $\tau_G$  and  $\tau_0$  on particle diameter were calculated and the results are presented in Fig. VI.2. It can be seen that both  $\tau_c$  and  $\tau_G$  increase with particle diameter, while the situation is the reverse for the Orowan stress. The intersections occur at 8 and 17 Å, respectively. These sizes are extremely small and are in fact of the order of the nucleus diameter [101].

It can be concluded from these results that the Nb(C,N) and (Ti, Nb) (C,N) precipitates are non-deformable, i.e. are not sheared, at all particle sizes.

The following numerical values were employed in the calculations:

$$T = 1123 \text{ }^\circ\text{K}$$

$$G_M = 8.1[1 - 0.91(T - 300)/1810] \times 10^4 \quad \text{MPa} \quad [172]$$

$$G_p = 1.34[1 - 0.18(T - 300)/3613] \times 10^5 \quad \text{MPa} \quad [\text{see Appendix 2}]$$

$$a_{\text{Nb(C,N)}} = 4.49 \text{ \AA} \quad [173]$$

$$a_M = 2.58 \text{ \AA}$$

$$f_v = 1 \times 10^{-6}$$

It should be pointed out that in the absence of data concerning the effect of boron, the calculations were limited to the case of the Nb(C,N) precipitates.

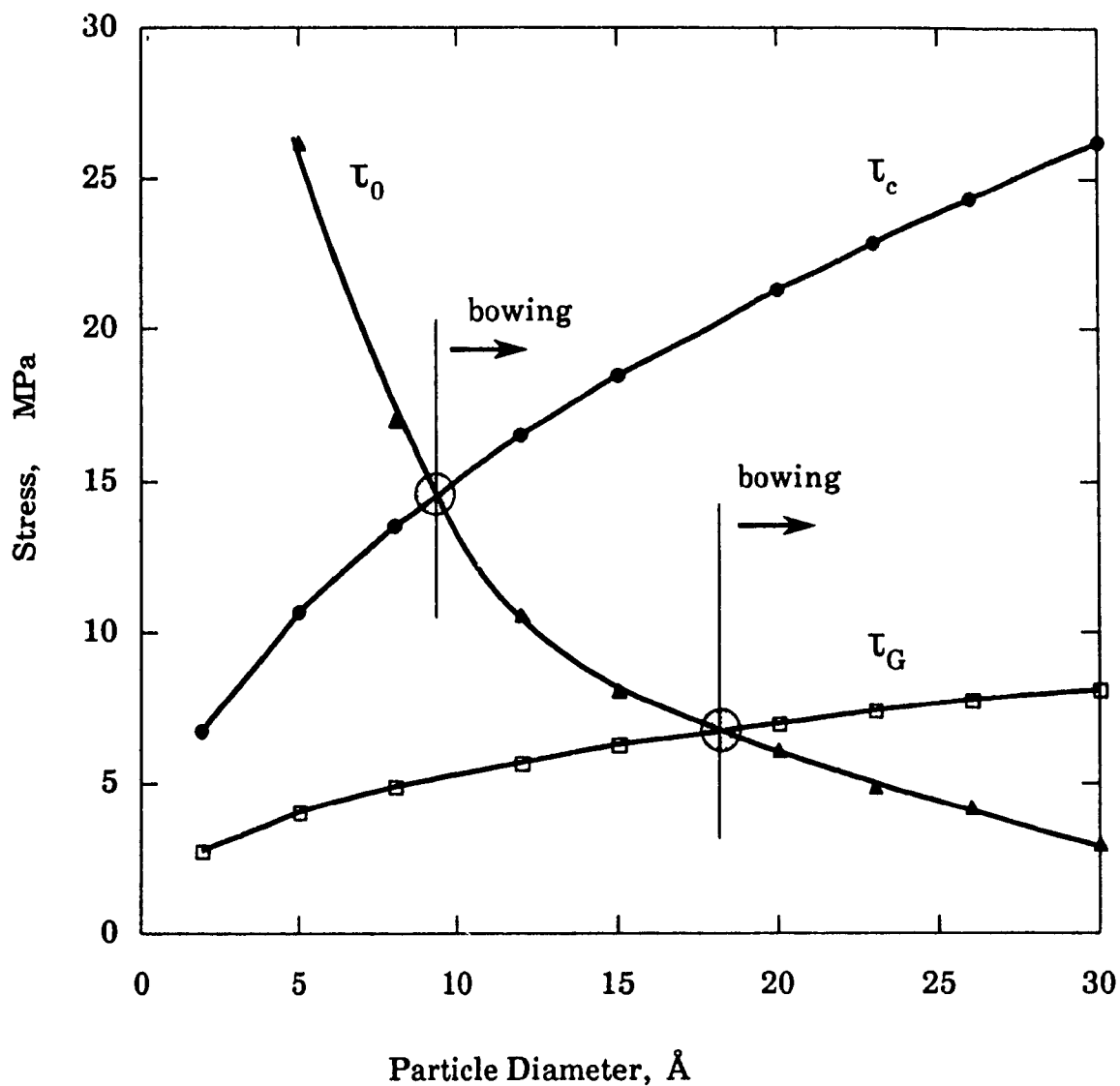


Fig.VI.2 Interaction between coherency hardening, shear modulus hardening and the Orowan stress showing the transition from cutting to bowing.

However, the same conclusions probably apply to the case of the Nb(C,N,B) particles.

#### b) Elastic Dislocation-Particle Interactions

Two other types of interaction are also present between a moving dislocation and a precipitate [174]. If the shear modulus of the particle,  $G_p$ , is lower than that of the matrix,  $G_M$ , the dislocation is attracted and will become pinned by the particle. On the other hand, if  $G_p > G_M$ , the particle will exert a repulsive force on the dislocation and if the applied stress is lower than the Orowan stress, the dislocation may bypass the particle by local climb [168]. In the above two situations, it is assumed that the particle-matrix interface cannot be sheared.

The interface between the precipitates observed in the present investigation and the austenite matrix is incoherent or at most semi-coherent. The shear modulus of the particles is also much higher than that of the parent austenite. Consequently, it can be reasonably assumed that the edge dislocations are free to climb over the particles.

The climb of edge dislocations has been considered to be the rate controlling mechanism for the high temperature creep of dispersion strengthened alloys. The first model was developed by Ansell and Weertman in 1959 [145] and since then, several refinements to the original model have been proposed [174-177].

In order to check whether the stress relaxation results obtained in this investigation can be interpreted in terms of these models or not, the creep equation for edge dislocation climb over particles developed by Hausselt and Nix [177] was employed. In their analysis, they do not include a threshold stress for the climb process and they consider that the rate of climb is limited by vacancy diffusion to (or from) the dislocations. On the basis of the previous assumptions, the following creep equation was proposed:

$$\dot{\epsilon} = \frac{(1+\nu)^{2/3}}{2(2\pi)^{1/2}} \rho_m D C \phi^2 \frac{\lambda^{8/3} b^{7/3} E^{1/3} \tau_e}{h^2 k t} \frac{1}{1 - (1+\nu)^{4/3} (\lambda/b)^{4/3} (\tau_e/E)^{4/3}} \quad (\text{VI.19})$$

Here,  $E$  is the Young's modulus of the austenite,  $\nu$  the Poisson's ratio,  $D$  the self diffusion coefficient,  $\rho_m$  the mobile dislocation density,  $\phi$  the angle of the particle-matrix interface when a dislocation strikes the particle half way between the mid plane and the top of the particle,  $\lambda$  the planar spacing between particles,  $h$  the passing height for a dislocation to climb over a particle,  $\tau_e$  is the effective shear stress and finally  $b$ ,  $k$  and  $T$  have their usual meanings.

The details of this calculation are presented in Appendix 3 and the experimental and calculated strain rates for the case of the Nb steel deformed 5% at 850°C are compared in Fig. VI.3. It can be seen clearly that the two curves diverge. At a time close to  $P_s$ , the experimental strain rate decreases suddenly and becomes almost stable until about  $P_f$ . After this time, the strain rate drop takes on a steeper log-log slope than during the first 20 s. By contrast, the strain rates predicted by the Hausselt and Nix model drop continuously with increasing time and possess higher values than the measured ones. However, close to  $P_f$ , they seem to agree with each other. Consequently, it appears that the climb of edge dislocations over particles is not the rate controlling mechanism during the first two stages of stress relaxation (i.e. after deformation until  $P_s$  and in the interval  $P_s - P_f$ ), while it may be operative during the third stage (between  $P_f$  and the end of the test) which, as will be shown later, corresponds to particle coarsening. It should be mentioned that similar calculations were made for the case of the Nb + B steel. The same type of behaviour was found; consequently, for purposes of brevity, only the above results are presented.

The inapplicability of these models can be related to the basic assumptions employed to derive them. In fact, all of them assume that the volume fraction and size distribution of the particles remain constant during deformation. By contrast, in the present stress relaxation tests, it was clearly observed that both the volume fraction and distribution of the precipitates continuously change, influencing the dislocation-particle interactions in this way.

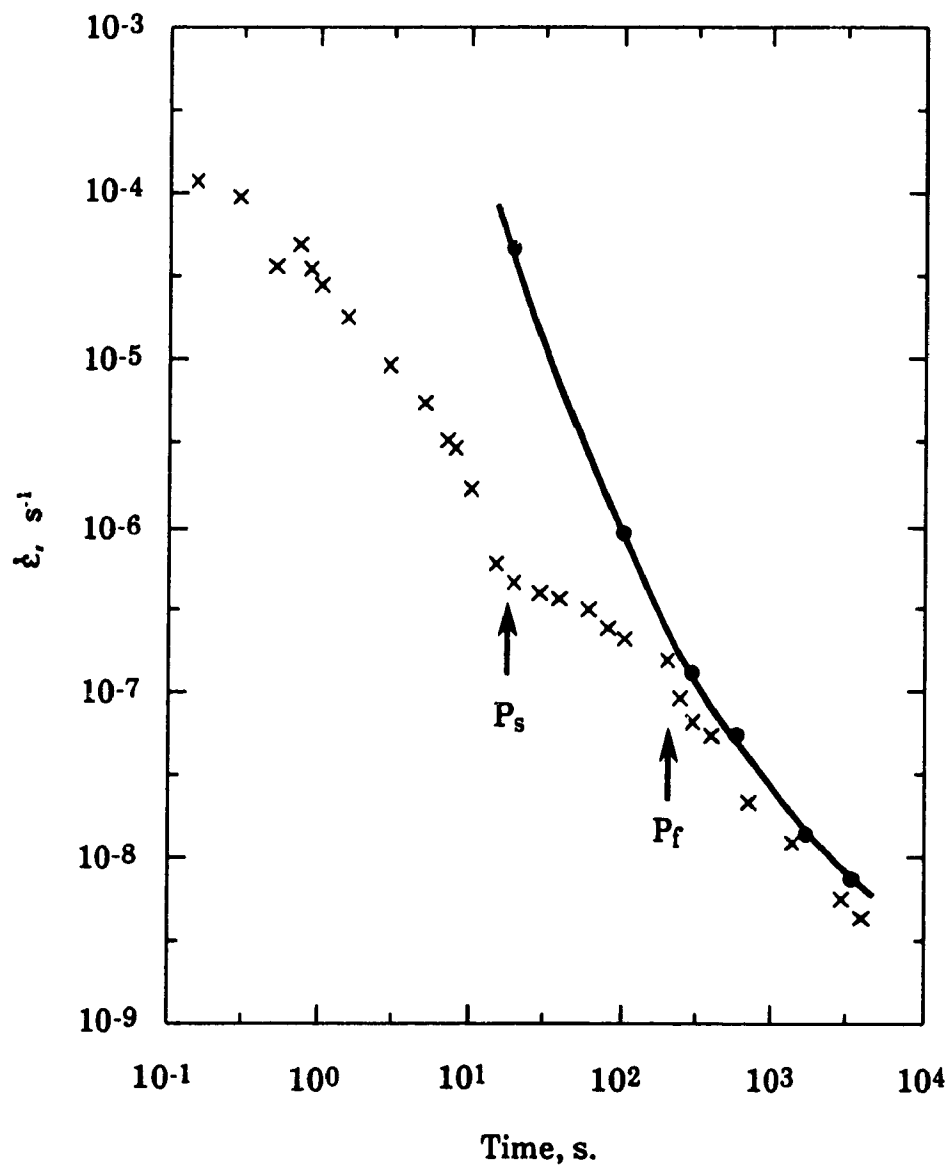


Fig.VI.3 Evolution of the plastic strain rate with time for the Nb steel deformed 5% at 850°C. (x) experimental, (●) Hausselt and Nix model.

### VI.1.2.3 A Possible Explanation

The observations described above about the continuous change in the volume fraction and distribution of the precipitates during stress relaxation suggests that the dynamic character of the precipitation process is the key factor affecting the dislocation-particle interaction. The dynamic precipitation of carbonitrides in deformed austenite has been discussed by several authors [135, 178]. But these studies did not concern themselves with the mechanism of the dislocation-particle interaction. In what follows, a possible mechanism for the pinning and unpinning of the dislocations will be proposed.

#### a) Nucleation of Precipitates on Mobile Dislocations

As a result of the large difference in lattice parameter with respect to the parent austenite, the transition metal carbonitrides are generally considered to nucleate on lattice defects. Such precipitation occurs mainly on the dislocation substructure formed during deformation and the precipitates are then distributed in a chain-like manner. This is in fact what we observed in our TEM investigation.

If a precipitate is nucleated on a segment of a mobile dislocation, this portion becomes pinned as it is incorporated into the new precipitate-matrix interface. At high temperatures on the other hand, the semi-coherent particle-matrix interface is a very good sink for dislocations. As a result, dislocations are attracted to the interface and once there become pinned by the relaxation of their cores into the interface [174]. The dislocations can also become locked at the particle-matrix interface because of local climb. In fact, the vacancies required by a growing particle can be provided by an edge dislocation present in the neighborhood. The climb of this dislocation will lead it to the interface, where it becomes part of the interface dislocation and is consequently pinned. As a result of the operation of the above three mechanisms, the great majority of mobile dislocations is stopped, leading to the stress plateau observed in the stress relaxation tests.

### b) The Unpinning Stress

It is evident that if a sufficiently high stress is applied to the sample, either the pinned dislocation will be liberated, or a new dislocation segment will be created to replace the one relaxed at the interface. Srolovitz et al. [174] reported that the critical stress  $\sigma_c$  for the operation of these two mechanisms is almost the same and proposed the following equation:

$$\sigma_c = \frac{Gb}{2\pi(1-\nu)\lambda} [2 + \ln(r_0/r_1)] \quad (\text{VI.20})$$

Here,  $r_0$  is the particle radius and  $r_1$  the inner cut-off radius.

They and other workers [179] stated that this stress is approximately equal to the Orowan stress, which is given by

$$\tau_0 = 0.8 \frac{Gb}{\lambda} \quad (\text{VI.17})$$

Because of its simplicity, equation VI.17 will be used instead of VI.20.  $\lambda$  was evaluated by the procedures described in Appendix 4.

The Orowan stresses were calculated for the different testing conditions and some of the results are presented in Figs. VI.4 and VI.5 along with the respective stress relaxation curves. It can be clearly seen that the Orowan stresses are low at the beginning of precipitation; they increase monotonically until about  $P_f$ , and then begin to drop.

Based on the above findings, it is apparent that when particles are present in the material, they exert a local back stress on the pinned dislocations, the maximum value of which is equal to the Orowan stress. In terms of the rate equation, it can be said that:

- |                                  |   |
|----------------------------------|---|
| i) with no precipitation         | $\dot{\epsilon} \propto \exp \tau_e$            |
| ii) in the presence of particles | $\dot{\epsilon} \propto \exp (\tau_e - \tau_0)$ |

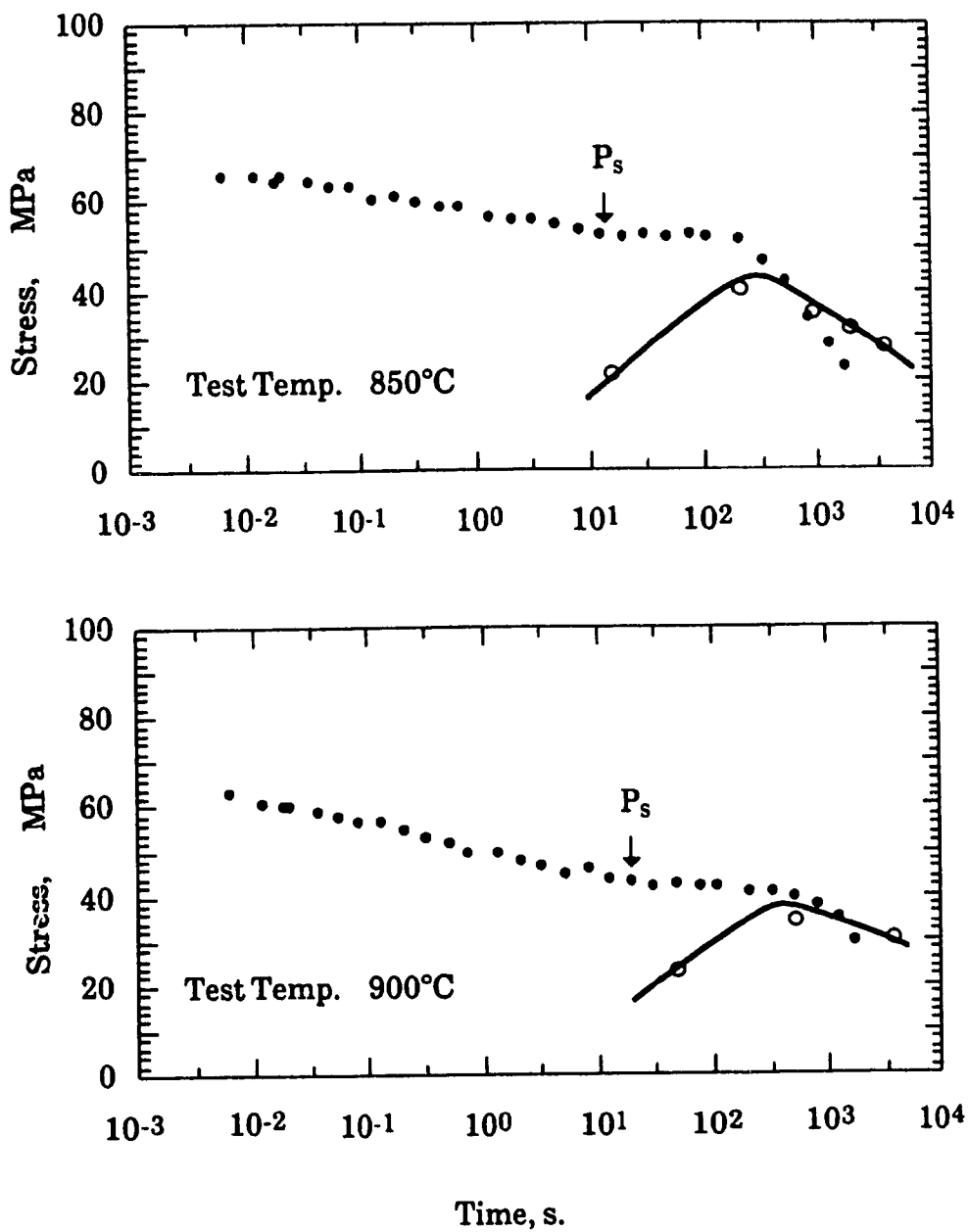


Fig.VI.4 Variation of the Orowan stress during stress relaxation of the Nb + B steel after 5% deformation at different temperatures.

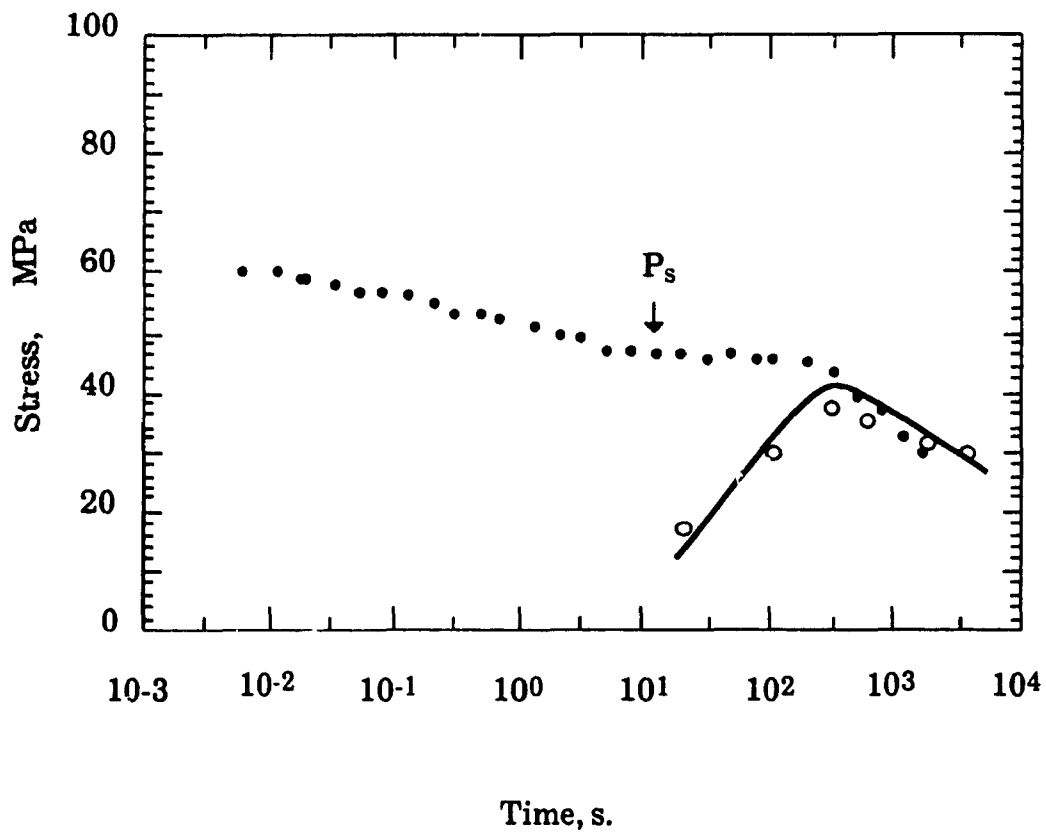


Fig.VI.5 Variation of the Orowan stress during stress relaxation of the Nb steel after 5% deformation at 850°C .

It is interesting to note here that the calculated Orowan stresses exceed the experimental stresses after  $P_f$ . This suggests that the strain rate should become zero as  $\tau_0$  becomes equal to or greater than  $\tau_e$ . However, this is not observed experimentally and, as shown in Fig.VI.3, the reverse situation (i.e. an acceleration of the strain rate drop) is observed. This is related to the interaction between the dislocations and the coarsening particles, which will be the subject of the next section.

### VI.1.3 Stress Relaxation During Particle Coarsening

It is of importance to know which mechanisms intervene in the relaxation process once precipitation is complete. Comparison of the stress relaxation results presented in Chapter IV indicates that the slopes of the stress versus log(time) curves are different before  $P_s$  and after  $P_f$ . To check whether stress relaxation during particle coarsening is controlled by the glide of jogged screw dislocations, the following analysis was carried out for the case of a Nb + B steel specimen deformed 5% at 850°C. Different points were chosen on the straight line representing the behaviour of the stress relaxation curve when the relaxation is controlled by the glide of jogged screw dislocations. To the abscissa of each point, a value equal to the time difference between  $P_s$  and  $P_f$  was added. Under these conditions, the relaxation curve is much steeper than the observed one, as can be seen in Fig.VI.6. Consequently, it appears that the glide of jogged screw dislocations is not the sole mechanism influencing the rate of relaxation during particle coarsening. Other parameters also affect the relaxation rate, leading to the gentler slope obtained experimentally. The gradual unpinning of dislocations, described below, is believed to be the key parameter that modifies the relaxation behaviour.

Ostwald ripening takes place at the end of precipitation, when the volume fraction of the precipitates becomes constant. It is well known that during this process, small particles are dissolved for the benefit of the larger ones. The dissolution of the small particles and the coarsening of the larger ones influence the dislocation-particle interactions in several ways: i) the dislocations pinned by the small particles are freed following the dissolution of the latter; ii) the spacing between the particles is increased as a result of the dissolution, consequently the stress required for dislocation movement (by the

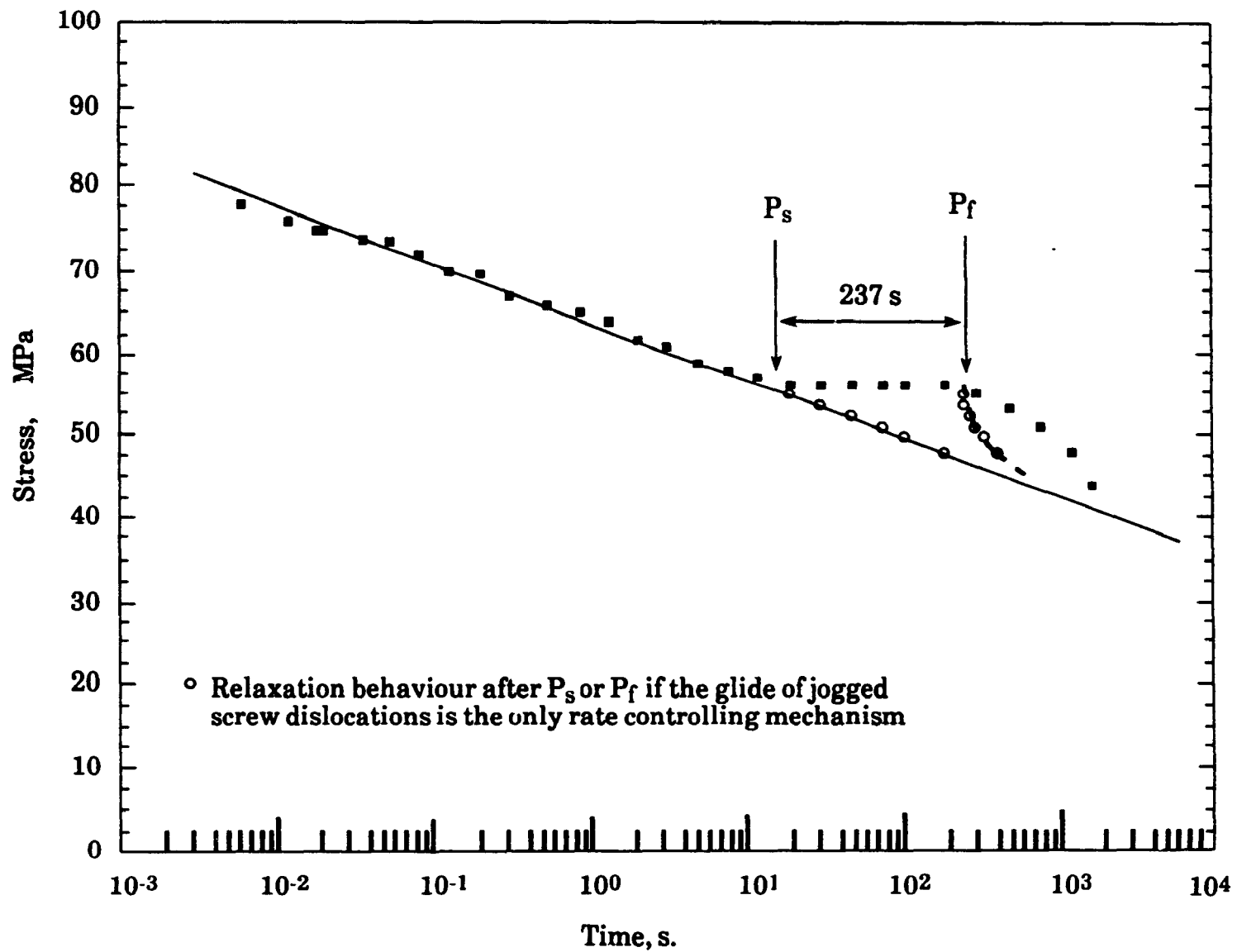


Fig.VI.6 Influence of particle coarsening on relaxation behaviour for the Nb + B steel deformed 5% at 850 °C.

Orowan mechanism or climb) is lowered; iii) as the particles coarsen, the nature of their interfaces with the matrix is transformed from semi-coherent to completely incoherent; this leads to much lower stress fields surrounding the particles, so less interface dislocations are required; iv) as the mean diameter of the dissolving particles shrinks, the climb of dislocation over them becomes easier and easier. Because of the activation of the above mechanisms, the mobility of dislocations increases when particle coarsening starts and this tendency is accelerated as coarsening progresses.

In summary, the mechanisms which probably intervene during stress relaxation are:

- a) region 1: after deformation, before  $P_s$   
relaxation rate controlled by the glide of jogged screw dislocations
- b) region 2: between  $P_s$  and  $P_f$   
dynamic precipitation on mobile dislocations, pinning of the dislocations by the particles and at the particle-matrix interface
- c) region 3: between  $P_f$  and the end of the test  
glide of jogged screw dislocations + particle coarsening and dislocation unpinning by total dissolution of the precipitate, climb or the Orowan mechanism.

#### **VI.1.4 Influence of Composition and Testing Conditions on Dislocation Density**

The discussion of the previous section has revealed clearly the importance of determining the dislocation density. Moreover, knowledge of the dislocation density will be useful when studying the nucleation kinetics of the precipitates, which will be presented in the second part of this chapter.

Using equation VI.5, the dislocation density can be derived. The influences of composition and deformation at different temperatures were determined in this way. The details of the calculations are presented in Appendix 2 and the results in Table VI.3 and Figs.VI.7 and VI.8. Under the same testing conditions, as the testing temperature is increased, the dislocation density is reduced. For example, in the case of the Nb steel samples deformed 25%, it decreases by 77% when the testing temperature is increased from 800 to 1000°C.

**Table VI.3.**  
**Effects of Composition, Deformation and Temperature**  
**on Dislocation Density**

Steel	$\epsilon$ %	Temp. °C	$\rho_0 \times 10^{-12}$ m <sup>-2</sup>
Nb	5	800	5.9
		830	5.1
		850	4.6
		870	3.9
		900	3.1
Nb	25	800	342
		850	251
		900	120
		950	92
		1000	78
Nb + B	5	800	16
		830	11
		850	8
		870	8
		900	6

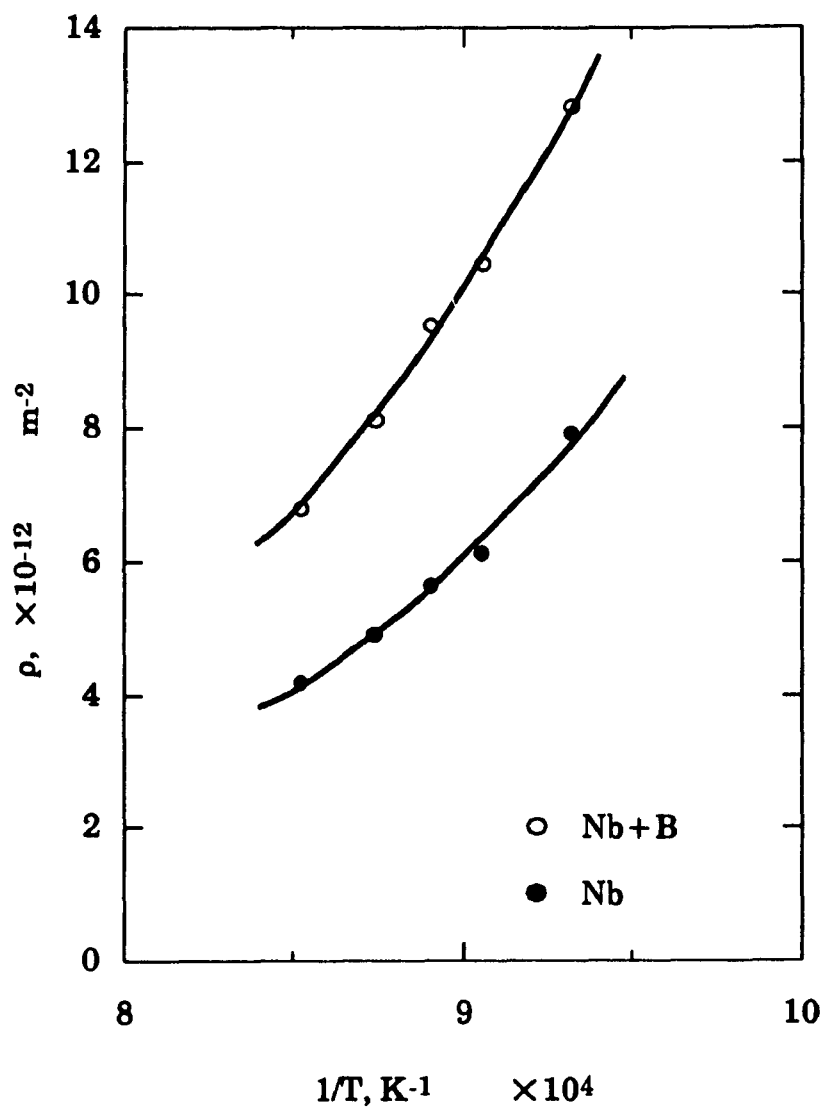


Fig.VI.8 Influence of temperature and composition on dislocation density.

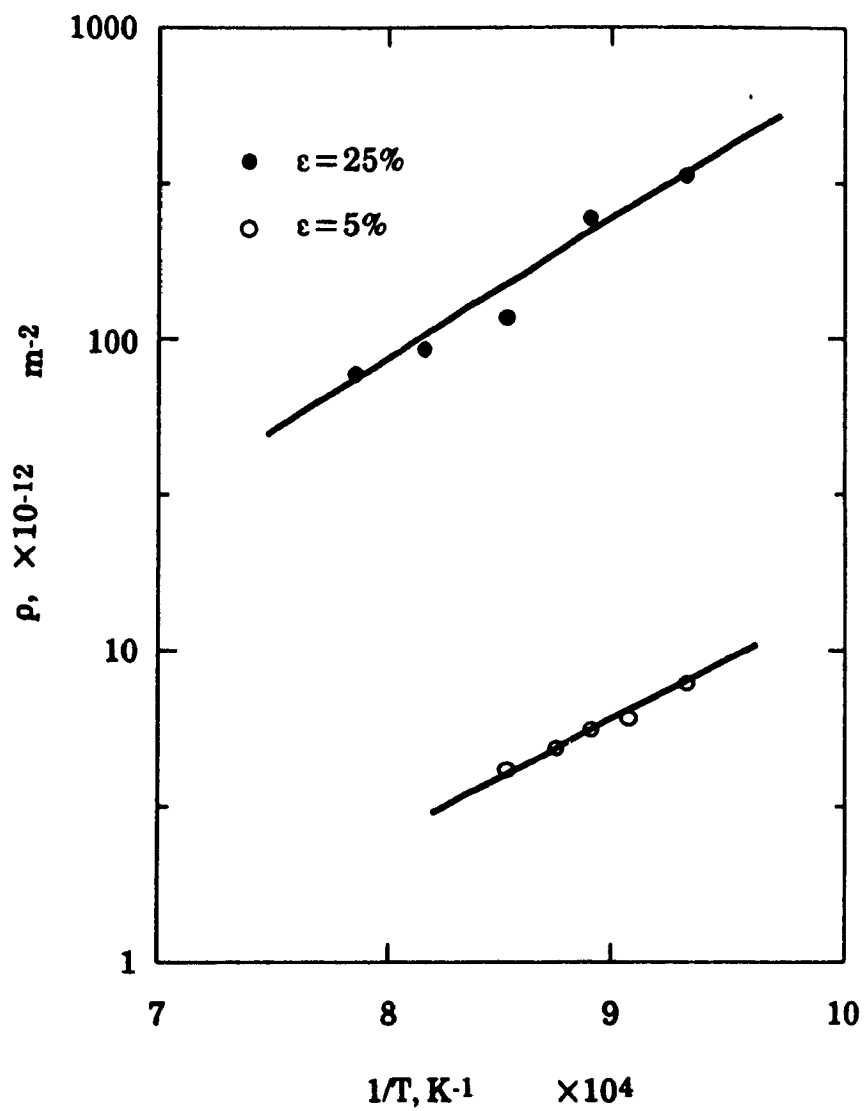


Fig.VI.9 Influence of temperature and deformation on dislocation density for the Nb steel.

## CHAPTER VI

### PART 2: NUCLEATION, GROWTH AND COARSENING OF THE PRECIPITATES

In relation to the kinetics of precipitation, the following observations described in Chapters IV and V are summarized here:

- i) The PTT curves are all of C-shape, indicating that the transformation is diffusion controlled.
- ii) The distribution of the particles was not homogeneous and they were arranged in a chain-like manner. This type of precipitation is characteristic of that occurring on dislocations or on dislocation networks.
- iii) The mean diameter of the precipitates varied as  $t^{1/2}$ , where  $t$  is the relaxation time. This behavior is no longer followed beyond the precipitation finish time  $P_f$ , i.e. once coarsening or ripening begins.

In this part, these points will be studied in relation to the theories of nucleation on dislocations and of diffusion-controlled growth. The experimental results will be compared with the predictions of these theories and the differences will be discussed. The parameters which govern the nucleation of precipitates will be evaluated; in this way, the differences between our results and those of other workers will become evident.

#### VI.2.1 Nucleation

The thermodynamics of the precipitation of second phases on dislocations were first derived by J.W.Cahn [180]. The Gibbs free energy change,  $\Delta G$ , accompanying precipitate formation may be written as

$$\Delta G = V_0 (\Delta G_c + \Delta G_s) + S_0 \gamma + W \quad (\text{VI.21})$$

where

$V_0, S_0$  = volume and surface area of the nucleus, respectively,

$\Delta G_c$  = chemical free energy change (also chemical driving force) due to nucleation,

$\Delta G_s$  = total elastic strain energy per unit volume of precipitate when precipitation occurs in the absence of a dislocation,

$\gamma$  = unit interfacial free energy of the nucleus-matrix interface, and

$W$  = the elastic interaction energy, i.e. the additional elastic energy change when the precipitate forms in the presence of a dislocation.

Because the interaction between a nucleus and a dislocation is rather complicated, it was assumed [142] that the energy contribution made by a dislocation to nucleation,  $W$ , is equivalent to a reduction in the interfacial energy. Following this assumption, equation VI.21 becomes

$$\Delta G = V_0 (\Delta G_c + \Delta G_s) + S_0 \eta \gamma \quad (\text{VI.22})$$

where  $\eta$  is a constant between 0 and 1.

According to the classical theory of diffusion controlled nucleation, the steady state nucleation rate  $J$  per unit volume (nuclei  $\text{cm}^{-3} \text{sec}^{-1}$ ) is given by

$$J = N \frac{D_0 X}{a^2} \exp\left(-\frac{Q}{RT}\right) \exp\left(-\frac{\Delta G^*}{kT}\right) \quad (\text{VI.23})$$

Here  $N$  = number of nucleation sites per unit volume,

$X$  = effective concentration of the rate controlling element,

$D_0$  = pre-exponential diffusion constant,

$a$  = lattice parameter of the austenite,

$Q$  = activation energy for the diffusion of Nb in austenite,

$\Delta G^*$  = critical free energy for a particle of critical diameter,  $d^*$ , to form, and

$k$ ,  $R$  and  $T$  have their usual meanings.

In the case of nucleation on dislocations,  $N$  is given by [181]

$$N = \frac{\rho}{a} \quad (\text{VI.24})$$

with  $\rho$  being the dislocation density.

Under these conditions, the nucleation rate equation becomes

$$J = \frac{D_0 X}{a^3} \rho \exp\left(-\frac{Q}{RT}\right) \exp\left(-\frac{\Delta G^*}{kT}\right) \quad (\text{VI.25})$$

It should be noted here that, since the diffusivities of the interstitials (C, N and B) in austenite are much faster than those of the substitutional atoms, the diffusivities of the latter are rate controlling with regard to particle nucleation [142].

#### VI.2.1.1 Critical Free Energy for Nucleation, $\Delta G^*$

Most of the variables in equation VI.25 can be determined in a straightforward manner except for  $\Delta G^*$ , which is one of the most important quantities influencing the nucleation rate. This parameter can be defined as the free energy barrier which the nucleation process must overcome with the aid of thermal activation.

By differentiating the  $\Delta G$  of equation VI.22 with respect to  $d$  and setting the resulting expression equal to zero, the critical diameter,  $d^*$ , of a nucleus can be found, from which we obtain

$$\Delta G^* = \frac{16\pi\eta^3\gamma^3}{3(\Delta G_c + \Delta G_s)^2} \quad (\text{VI.26})$$

The determination of  $\Delta G^*$  depends on that of  $\gamma$ ,  $\Delta G_c$  and  $\Delta G_s$ . This was done and the details of the calculation are presented in Appendix 5. Table VI.4 illustrates the dependence of  $\gamma$ ,  $\Delta G_c$  and  $\Delta G_s$  on temperature.

**Table VI.4.**  
**Dependence of the Surface and Volume Free Energies**  
**on Temperature**

Temp. °C	800	830	850	870	900	950
Y Jm <sup>-2</sup>	0.611	0.595	0.582	0.576	0.565	0.557
ΔG <sub>s</sub> Jm <sup>-3</sup> ×10 <sup>-9</sup>	6.32	6.19	6.11	6.03	5.91	5.71
ΔG <sub>c</sub> Jm <sup>-3</sup> ×10 <sup>-9</sup>	-2.06	-1.83	-1.68	-1.53	-1.31	-1.28

The changes are not very significant, due to the fact that the above three parameters depend on temperature only through the shear modulus.

#### VI.2.1.2 Precipitation Start Time, P<sub>s</sub>

In the most general case, the number of nuclei per unit volume formed during a time interval, t, may be written as

$$N = \int_0^t J dt \quad (\text{VI.27})$$

Considering that a number N\* of nuclei per unit volume must be formed in a time t = P<sub>s</sub> for nucleation to be detected (about 5% precipitation), then

$$P_s = \frac{N^*}{J} \quad (\text{VI.28})$$

The combination of equations VI.25 and VI.28 leads to

$$P_s = K \frac{1}{\rho X} \exp\left(\frac{Q}{RT}\right) \exp\left(\frac{\Delta G^*}{kT}\right) \quad (\text{VI.29})$$

where

$$K = \frac{N^* a_{\gamma-Fe}^3}{D_0} \quad (\text{VI.30})$$

A least squares method was applied to equation VI.29 and the constants  $K$ , and  $\eta$  were determined for different testing conditions. In the calculations, the measured values of  $P_s$  presented in Tables IV.2 and IV.3, those of Table VI.3 for the dislocation densities and the calculated ones for  $\Delta G^*$  from Table VI.4 were employed. Finally, for the diffusion coefficient of Nb in austenite, the influence of steel composition was neglected and the values  $D_0 = 1.4 \cdot 10^{-4} \text{ m}^2\text{s}^{-1}$  and  $Q = 270 \text{ kJmol}^{-1}$  given by Kurokawa et al. [182] were used.

The effects of steel composition and amount of deformation on the values of  $K$  and  $\eta$  are illustrated in Table VI.5.

**Table VI.5.**  
**Effect of Testing Conditions on the Values of  $K$  and  $\eta$**

Steel	Prestrain %	$K$ $\text{sm}^{-2}$	$\eta$
Nb	5	$3.57 \times 10^{-3}$	0.43
Nb	25	$3.81 \times 10^{-2}$	0.42
Nb + B	5	$3.61 \times 10^{-3}$	0.42

It is interesting to note that the constant  $\eta$  is practically independent of steel composition or the amount of deformation. This seems reasonable if we consider that  $\eta$  is a measure of the interaction energy between a nucleus and a dislocation. Consequently  $\eta$  should remain independent of steel composition.

Dutta and Sellars analyzed [142] the kinetics of Nb(C,N) precipitation in terms of classical nucleation theory. They fitted the  $P_s$  times obtained by different investigators and various experimental techniques with an equation similar to VI.29. Reasonably good agreement was obtained between their calculated values and the literature ones. The average value of  $\eta$  determined in this investigation is close to that (0.41) reported by these authors.

Recently, Liu and Jonas [183] analyzed the precipitation of Ti(C, N) using a kinetic model, which considers that the composition of the Ti(C, N) nucleus is not the same as that of the bulk precipitate at equilibrium at the holding temperature, but is considerably richer in N. They obtained a  $\eta$  value (0.39) close to that determined by Dutta and Sellars and in this investigation. The fact that the value of the constant  $\eta$  is almost identical for both Nb(C,N) and Ti(C,N) precipitation in deformed austenite indicates that the nucleation sites are the same (in this case the dislocations) for the two types of precipitate. The constants  $K$  and  $\eta$  were substituted in equation VI.29 and the  $P_s$  values predicted by the theory were determined. Table VI.6 and Figs.VI.9 and VI.10 show the comparisons between the observed  $P_s$  times and the calculated ones.

### VI.2.2 Growth

As illustrated in Figs.V.17 to V.19, the mean diameter of the particles was found to be approximately proportional to  $t^{1/2}$ . This type of relationship is characteristic of the diffusion controlled growth of precipitates. The theory was originally proposed by Zener [184] and, according to his treatment of the problem, the dependence of particle diameter on time can be described by

$$d = a (Dt)^{1/2} \quad (\text{VI.31})$$

where  $D$  is the diffusion coefficient of the element which controls the growth rate, and  $a$  is the growth coefficient given by [184]

$$a = 2 \left\{ \frac{2(X_{Nb}^0 - X_{Nb}^V)}{(X_{Nb}^P - X_{Nb}^V)} \right\}^{1/2} \quad (\text{VI.32})$$

Here  $X_{Nb}^0$  is the concentration of Nb dissolved in the austenite,  $X_{Nb}^V$  is its equilibrium concentration, which is also assumed to be the concentration of Nb at the particle-matrix interface. Finally,  $X_{Nb}^P$  is the concentration of Nb in the precipitate. taken equal to 0.5.

**Table VI.6.**  
**Comparison Between the Observed and Calculated  $P_s$  Values**

Steel	$\epsilon$ %	Temp. °C	$P_s$ observed sec.	$P_s$ calculated sec.
Nb + B	5	800	17	15
		830	14	12
		850	13	10
		870	15	13
		900	22	25
		950	47	50
Nb + B	25	800	9	11
		850	6	7
		900	10	9
		950	35	33
Nb	5	800	22	19
		830	18	23
		850	20	18
		870	27	29
		900	35	31
		950	79	81
Nb	25	800	15	17
		850	19	20
		900	33	35
		950	80	76

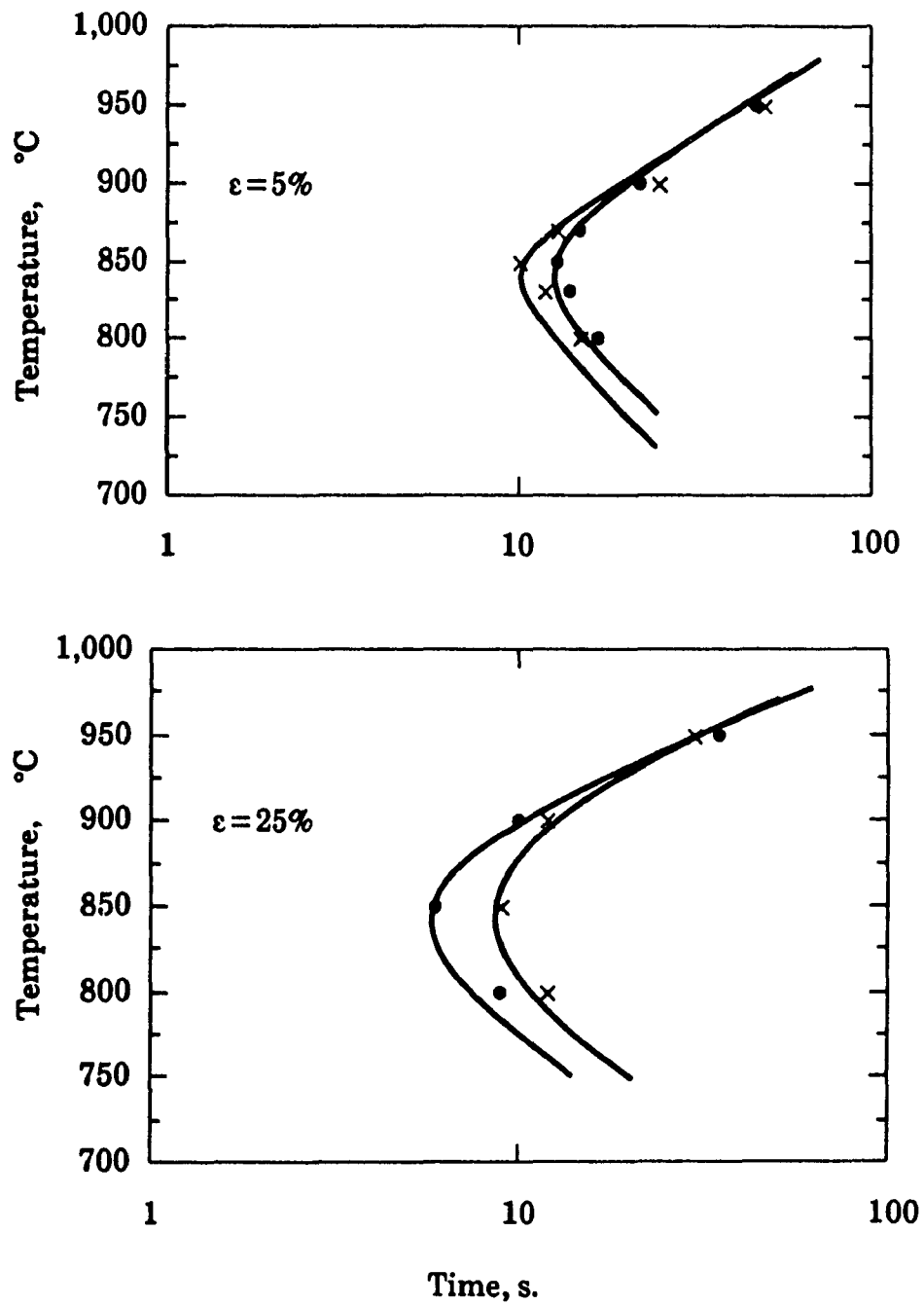


Fig. VI.9 Comparison between the observed (●) and calculated (×)  $P_s$  values for the Nb + B steel.

### VI.2.2.1 Determination of the Diffusion Coefficients

It is apparent from equation VI.31 that, once  $d$ ,  $a$  and  $t$  are known, the diffusion coefficient of the growth rate controlling element (Nb in this case) can be determined from the slope of the  $d^2/a^2$  versus time curve. This was done for the Nb and Nb + B steels tested at different temperatures after 5% deformation and the results are displayed in Figs. VI.11 and VI.12.

All the curves presented in the above figures show rapid growth for the first few hundred seconds and then a break to a lower slope. The change in behaviour is associated with the occurrence of particle *coarsening* which will be considered in the next section. It is interesting to note here that the point of deviation is close to the  $P_f$  time determined by the stress relaxation technique. Also, if a finer scale is used to represent the dependence of  $d^2/a^2$  on time for the early stages of precipitation, it can be seen (c.f. Fig. VI.13) that there is an incubation or delay time prior to growth. Only after  $P_s$  does the curve behave linearly. This is because nucleation does not occur at the same time everywhere in the material. As a result, when the first nucleus has already reached some degree of growth, a certain number of prospective nucleation sites remain inactive. Consequently, the beginning of the straight line corresponds to the time at which all the nucleation sites have been activated and a nucleus is present at each site. The fact that the transition from the first to the second (i.e. linear) region is not identical with the measured  $P_s$  time, but is somewhat larger, means that the plateau in the stress relaxation test is not associated with the exhaustion of nucleation sites but with the pinning of a sufficient number of dislocations. Finally, the growth kinetics are then represented by the second part (or the linear part) of the particle diameter-relaxation time curve.

The values of the diffusion coefficient at different temperatures were determined from the above data. The Arrhenius equation was fitted to the experimental results and the following values were obtained for the frequency factor ( $D_0$ ) and activation energy for diffusion :

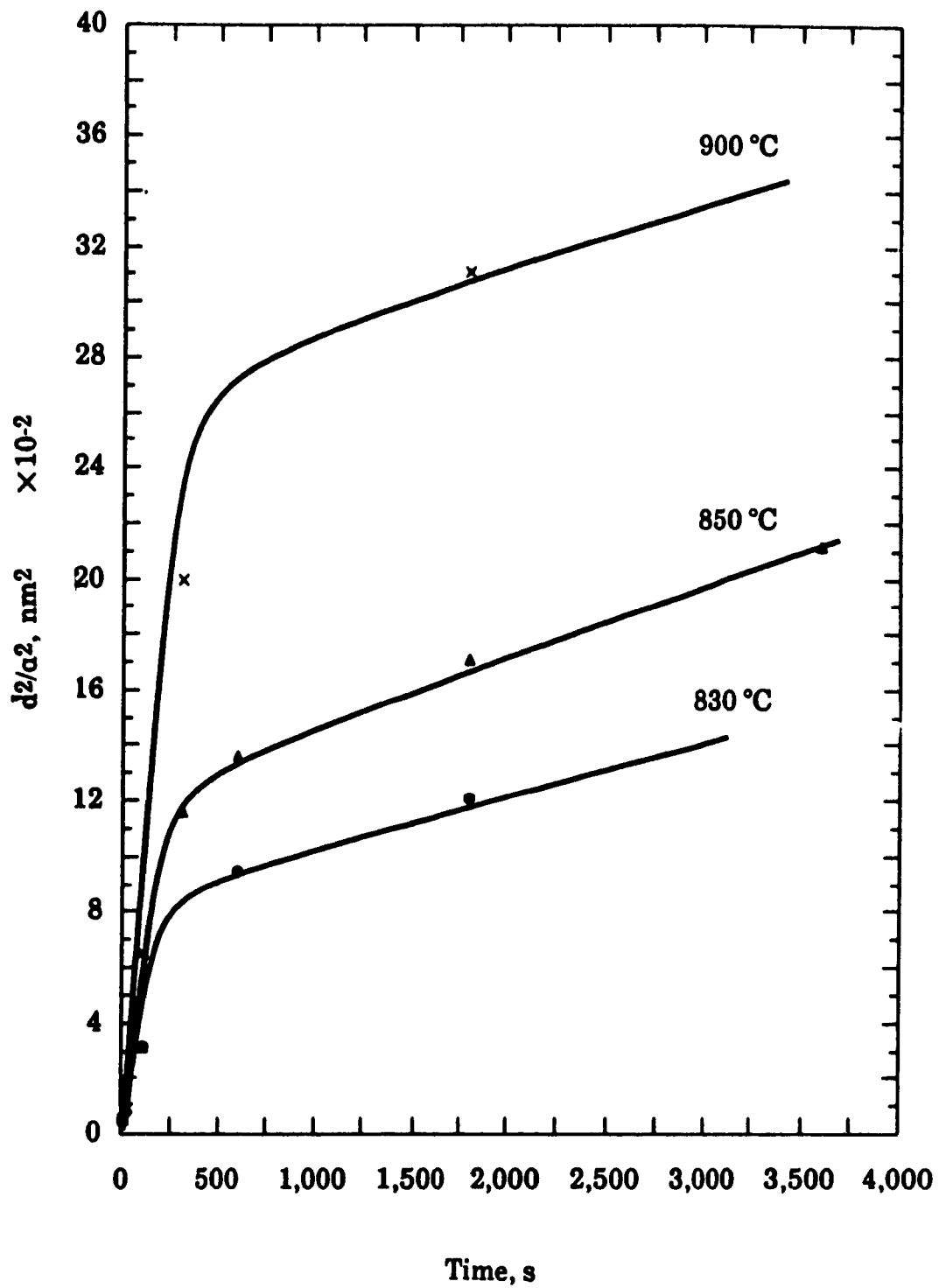


Fig.VI.11 Dependence of  $d^2/\alpha^2$  on relaxation time in the Nb steel after 5% deformation.

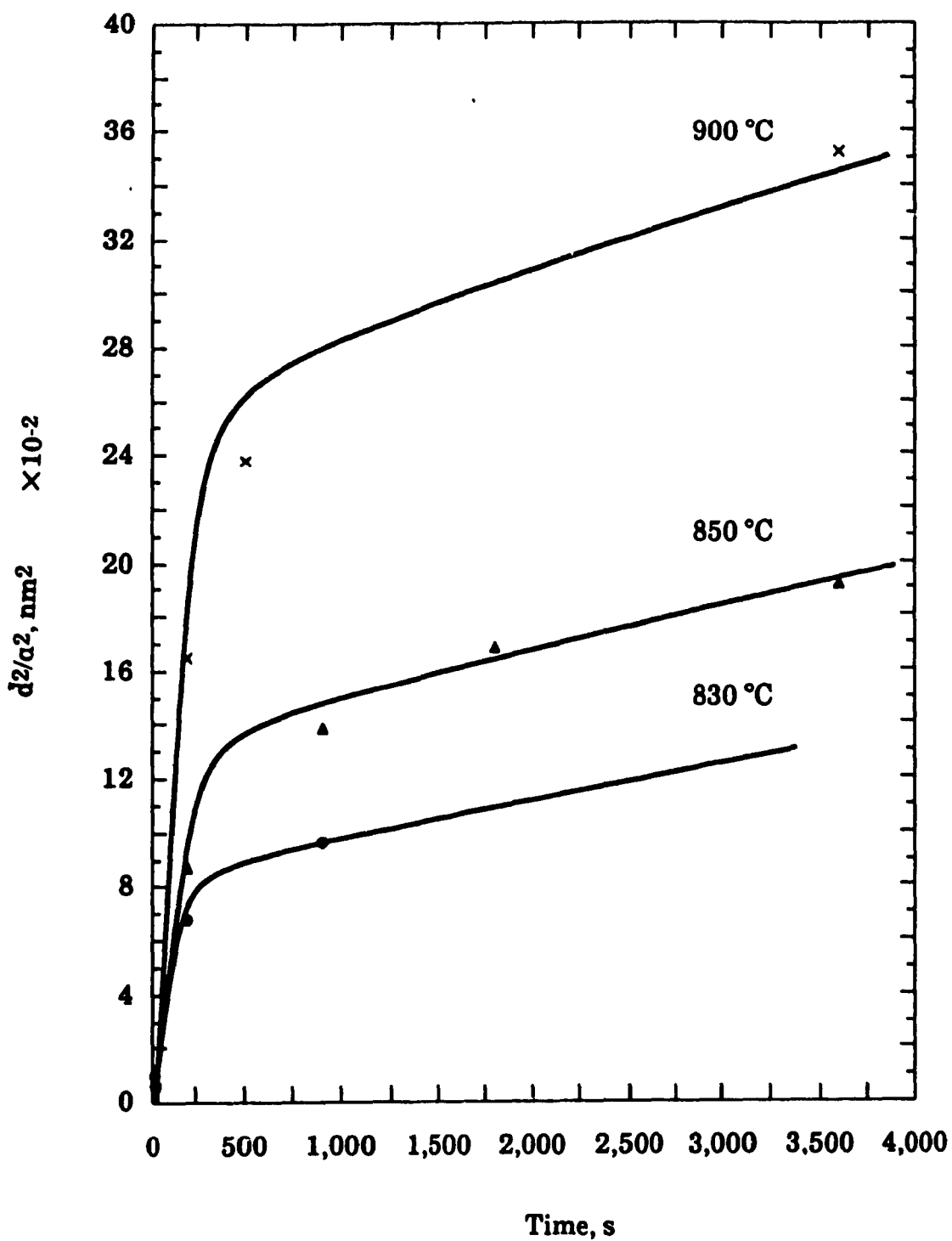


Fig.VI.12 Dependence of  $d^2/a^2$  on relaxation time in the Nb + B steel after 5% deformation.

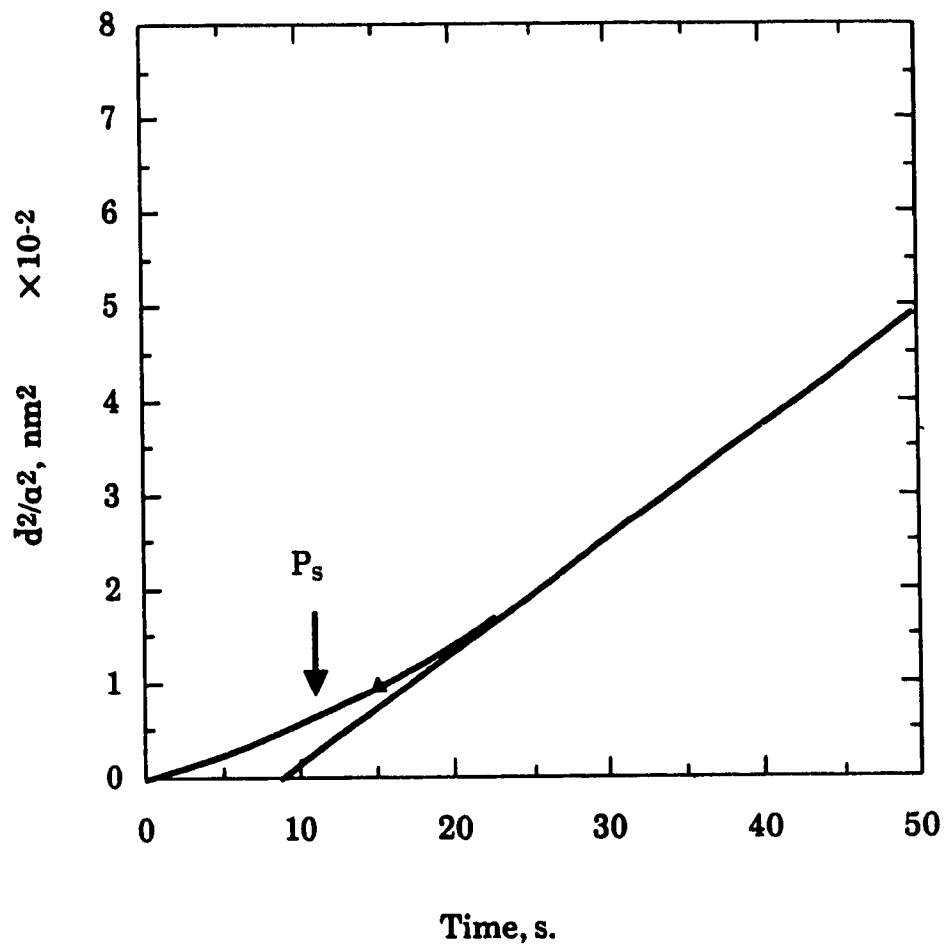


Fig.VI.13 Dependence of  $d^2/a^2$  on time during the early stages of stress relaxation for the Nb + B steel after 5% deformation at 850°C.

$$D_{Nb+B} = 2.26 \exp\left(-\frac{289,000}{RT}\right) \cdot 10^{-4} \text{ m}^2 \text{ sec}^{-1}$$

$$D_{Nb} = 1.12 \exp\left(-\frac{283,000}{RT}\right) \cdot 10^{-4} \text{ m}^2 \text{ sec}^{-1}$$

The differences between the diffusion coefficients for the two steels are illustrated in Fig.VI.14. Although the ratio  $D_{Nb+B}/D_{Nb}$  varies between 1.03 and 1.09, the values remain approximate as the errors associated with the TEM investigation fall in the interval 10-20%.

### VI.2.3 Coarsening

It is of interest to note from Figs.VI.11 and VI.12 that the deviation from linear behaviour corresponds approximately to the  $P_f$  times determined in the stress relaxation tests. Following the completion of precipitation, coarsening starts to take place. Weiss and Jonas [118] and other workers [185-187] have reported that the Lifshitz-Wagner [188, 189] formalism for particle coarsening can be applied to the case of carbonitride precipitation in austenite. According to this theory, if diffusion is the rate controlling mechanism, the mean particle diameters at coarsening times  $t$  and  $t=0$  are given by

$$\left[\frac{\bar{d}}{2}\right]^3 - \left[\frac{d_0}{2}\right]^3 = Kt \quad (\text{VI.33})$$

where  $K$  is the rate constant.

For the coarsening of the Nb(C,N) or Nb(C,N,B) precipitates after the end of precipitation, the above equation becomes:

$$\left[\frac{\bar{d}}{2}\right]^3 - \left[\frac{d_f}{2}\right]^3 = K(t - P_f) \quad (\text{VI.34})$$

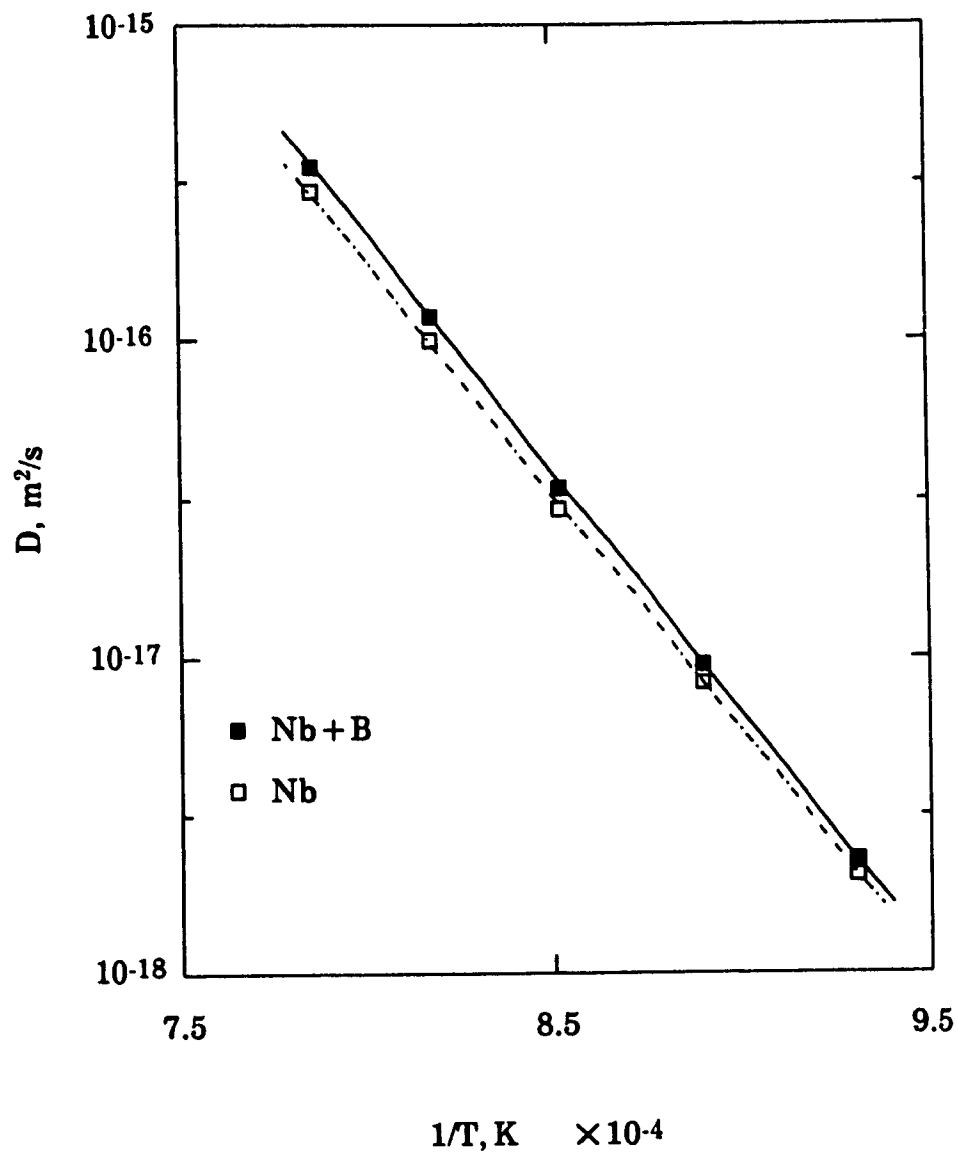


Fig.VI.14 Influence of boron on the diffusion coefficient of Nb.

where  $d_f$  is the mean diameter of the particles at the end of precipitation. On the other hand, it was reported that  $K$  is a function of temperature and the diffusion coefficient of the rate controlling element and is given by [190]

$$K = \frac{\zeta}{T} D_0 \exp\left(-\frac{Q}{RT}\right) \quad (\text{VI.35})$$

where  $\zeta$  is a temperature independent factor.

The combination of equations VI.34 and VI.35 leads to

$$\frac{\left[\frac{\bar{d}}{2}\right]^3 - \left[\frac{d_f}{2}\right]^3}{(t - P_f)} T = \zeta D_0 \exp\left(-\frac{Q}{RT}\right) \quad (\text{VI.36})$$

A linear regression analysis was applied to equation VI.36 and the activation energy for the diffusion of Nb in austenite was found to be equal to 288 KJmol<sup>-1</sup>. As displayed in Table VI.7, the values for the activation energy obtained in this investigation are in good agreement with those reported in the literature.

**Table VI.7.**  
**Comparison of Observed Activation Energies for**  
**the Diffusion of Nb**

Activation Energy KJmol <sup>-1</sup>	Reference
270	Kurokawa et al.[182]
286	[210]
288	Present investigation
283	Present investigation

## CHAPTER VII

### THE MECHANISMS ASSOCIATED WITH THE EFFECT OF BORON

A comparison between the results obtained for the Nb + B, B and Nb steels leads to the following observations:

- 1) Under similar testing conditions, the precipitation start time is shorter in the Nb+B steel than in the Nb grade. Moreover, precipitation starts at higher temperatures in the Nb + B steel specimens.
- 2) The PTT curves for the Nb and Nb+B steels are of C-shape, indicating that the presence of boron does not influence the nature of the precipitation process.
- 3) The number of particles per unit area is lower in the Nb than in the Nb + B steel.
- 4) The presence of boron suppresses the partial recrystallization of austenite observed in the Nb steel deformed 25% at 950°C.
- 5) The non-equilibrium segregation of boron is produced on the original austenite grain boundaries after cooling and/or deformation. It also occurs on moving grain boundaries during recrystallization.
- 6) The kinetics of segregation and desegregation are much slower in the Nb + B than in the boron steel.

These observations clearly indicate that the presence of boron influences the kinetics of both precipitation and recrystallization. Moreover, it seems that boron in the presence of Nb behaves differently than when it is alone. The

distribution of boron in the material and its interaction with the other entities (such as alloying elements or vacancies) appear to be the key factors in controlling the above mentioned kinetics. In this chapter, the ways in which boron affects the precipitation of Nb(C,N) and the recrystallization of austenite will be discussed. Attention will be paid to the synergistic effect of Nb on these processes. The different origins of the non-equilibrium segregation of boron will be presented and two new causes of boron segregation will be introduced. Finally, some mechanisms which may be responsible for such segregation will be proposed.

### VII.1 The Influence of Boron on the Precipitation Kinetics

The stress relaxation curves obtained at 850°C in the Nb + B and Nb steels are compared in Fig.VII.1. The samples were solutionized at 1100°C, cooled, and then deformed 25%. It is clear that the stress plateau appears about 20 seconds sooner in the boron-containing steel than in the other one. As indicated by the PTT curves (Figs. IV.13 to IV.16), this accelerating effect of boron exists under all the testing conditions.

By contrast, comparison of the results presented in Tables V.3 and V.4 shows that, under identical testing conditions, the mean diameter of the precipitates in the Nb + B steel is generally smaller than that determined in the Nb grade. Similarly, the area density of the particles is larger (by 11 to 17%) in the Nb + B than in the Nb steel (see Table V.2).

Although to our knowledge no quantitative data are available on the effect of boron on carbonitride precipitation in HSLA steels, the present results are in agreement with those obtained on stainless steels [35, 44, 57]. Consequently, based on the experimental findings of this investigation as well as those reported in the literature, it can be said that boron plays its most important role in the *nucleation* stage of precipitation. Because of the nature of the precipitates (i.e. incoherent or at most semi-coherent), the role of boron is then to be sought in its possible effects on the various factors controlling the nucleation of precipitates on dislocations.

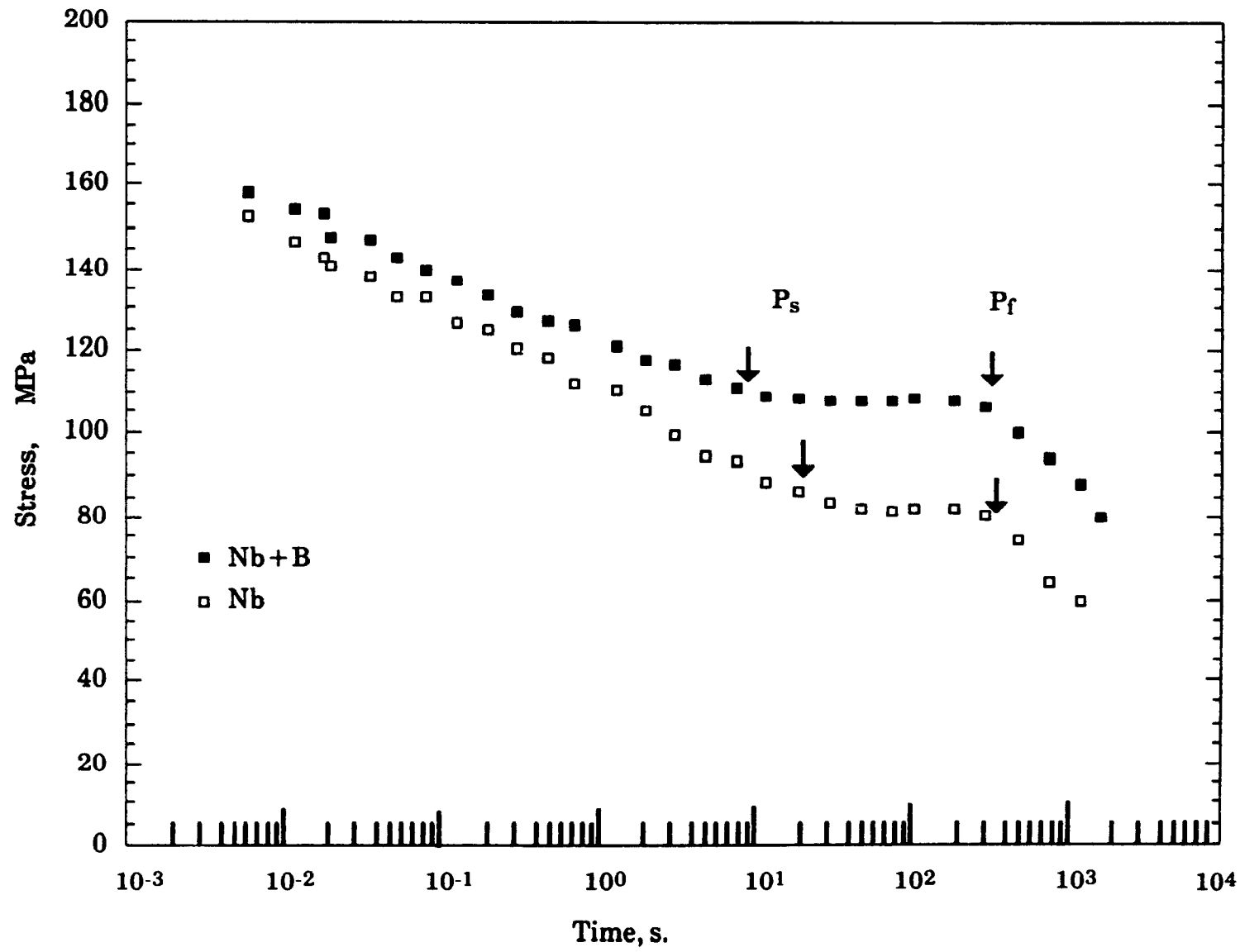


Fig.VII.1 Comparison between the stress relaxation curves for the Nb + B and Nb steels after 25% deformation at 850°C.

As mentioned in the previous chapter, the free energy for nucleation is a function of the surface energy, chemical free energy and strain energy :

$$\Delta G = f(\gamma, \Delta G_c, \Delta G_s) \quad (\text{VII.1})$$

Davidson et al. [60] suggested that the presence of boron increases the activity of carbon in the matrix, lowering in this way the chemical free energy term in the nucleation activation energy. However, no evaluation of the order of magnitude of this effect has been attempted. A lack of information also exists regarding the influence of boron on the surface energy term. The absence of thermodynamic data on the interaction of boron with other elements means that there is no precise knowledge regarding the composition of the nucleus when boron is present. As a result, quantification of the effect of boron on the interfacial energy is very difficult. However, it has been reported [70, 170] that boron reduces the grain boundary energy by a few percent. It therefore seems unlikely that the interfacial energy is reduced significantly by the addition of boron.

Based on the above remarks, boron does not seem to affect the different factors in the free energy term for nucleation *directly*. The boron effect may be manifested instead through its interaction with vacancies and the precipitate forming elements (in this case Nb) and also through the non-equilibrium segregation to dislocations of boron and boron-vacancy complexes or the formation of Nb-B complexes at these sites. These points will be taken up in the sections that follow so that the accelerating effect of boron on precipitation can be interpreted.

### VII.1.1 Influence of Boron Segregation on Precipitate Nucleation

The large size differences between C, Nb, B and the matrix atoms result in the equilibrium segregation of these elements to dislocations. The magnitude of the segregation is given by McLean's equation [28]

$$C_g = \frac{C_0 \exp(E/kT)}{1 + C_0 \exp(E/kT)} \quad (\text{VII.2})$$

where  $C_g$  is the concentration of boron at the dislocations,  $C_0$  is its concentration in the matrix and  $E$  is the binding energy.

The PTA and SIMS results indicated clearly that the non-equilibrium segregation of boron is produced at vacancy sinks. Although we have shown boron segregation at austenite grain boundaries, it appears that it also occurs at dislocations. Furthermore, our results on carbonitride precipitation and austenite recrystallization suggest strongly that there is a synergistic effect between Nb and B atoms. This latter effect has been associated with the formation of Nb-B complexes at dislocations (see later in this chapter).

The combination of the above three mechanisms leads to higher concentrations of interstitials (by the non-equilibrium segregation of B to dislocations) and of precipitate forming substitutional elements (in this case Nb), increasing in this way the concentration product of the precipitating species, finally leading to easier nucleation.

For example, the presence of boron in steel increases the concentration of the interstitial elements from 0.12 atomic percent in the B-free steel to 0.14 atomic percent in the Nb + B grade. The presence of nitrogen is neglected here, as most of it is expected to have combined with Ti during solidification and subsequent cooling. This increases the concentration product of the precipitating species by about 14%. If we now consider that segregation on dislocations increases the boron (or Nb) concentration substantially at these sites, the accelerating effect of boron on precipitate nucleation becomes clear.

Another aspect of the influence of boron on precipitation is related to the interaction which exists between boron atoms and the vacancies present in the matrix. In fact, the specific volume (i.e. the ratio between the volume of the unit cell and the number of metallic atoms in it) of Ti or Nb carbonitrides and  $M_{23}(C,B)_6$  precipitates is greater than that of austenite (see Table VII.1). The supply of vacancies to the nucleus then becomes a primordial factor in the process of nucleating these precipitates.

It is generally accepted [41, 42, 142] that boron atoms combine with vacancies to form complexes. The precipitate nucleus needs boron atoms for its

**Table VII.1**  
**Specific Volumes of Selected Precipitates and Austenite (Å)**

$\gamma$ -Fe	$\text{Fe}_{23}(\text{C},\text{B})_6$	Nb(C,N)	Ti(C,N)
11.5	12.9	22.1	20.1

growth, and the latter bring the vacancies which are attached to them during their movement to the nucleus. Once at the nucleus surface, the boron atoms are incorporated into it and the vacancies reduce the strain energy created by the nucleus by their presence. In this way, the nucleus becomes more stable and reaches its critical size faster.

Finally, as shown in chapter VI, the addition of boron to the Nb steel increases the dislocation density by almost one order of magnitude. The existence of a greater number of dislocations in the material leads to more interaction and dislocation entanglement. Precipitate nucleation is then favored at these sites by reduction of the strain energy term (due to the strain field of the dislocations) in the activation energy for nucleation.

In summary, the accelerating effect of boron on precipitate nucleation can be clarified on the basis of the above mechanisms. The latter are not independent and intervene simultaneously with regard to the nucleation process. Although it does not seem possible to quantify the individual effects, the non-equilibrium segregation of boron probably plays the most important role.

### VII.1.2 Effect of Boron on Particle Growth

As mentioned in chapter VI, the growth of the precipitates is diffusion controlled. Consequently, the influence of boron on the growth rate of the particles is manifested through its effects on the diffusion coefficient of the Nb atoms. Although our calculations show that the diffusion coefficient for Nb in the presence of boron is somewhat higher than in its absence, the difference falls in the error range associated with the particle size measurements.

## VII.2 Influence of Boron on the Recrystallization Process

In this part of the thesis, the discussion will be limited to the results obtained at 1000 and 950°C, although recrystallization can even occur at 900°C after long holding times.

The stress relaxation results obtained for the Nb and Nb+B steels deformed 25% at 1000 and 950°C are compared in Figs.VII.2 and VII.3, respectively. It is clear that the presence of boron retards the recrystallization start time at both temperatures. The question arises here whether the presence of boron alone would have the same retarding effect on austenite recrystallization or not? To answer this question, samples of the Nb+B and B steels were oil quenched 10 s after deformation at 1000°C and the state of the microstructure was revealed by the PTA technique, as shown in Fig.VII.4.

It is clear that recrystallization has progressed extensively in the boron steel, while in the Nb+B grade, only a few new grains are observed. This indicates that recrystallization starts much sooner in the boron than in the Nb+B steel and consequently boron alone does not have a strong effect on retarding recrystallization.

In another study, the recrystallization kinetics of the four steels used in this investigation were studied by interrupted compression testing [191] and some of the results obtained are displayed in Fig.VII.5. It can be seen that, after deformation at 1000°C, the retarding effect of boron on recrystallization is small, leading to the statement made above, that boron alone does not influence the recrystallization kinetics. Based on the data of Fig.VII.5, the times for 20% softening (recrystallization start time,  $R_s$ ) and for 70% softening ( $\approx$  50% recrystallization,  $R_{0.5}$ ) were calculated for the four steels and are illustrated in Table VII.2. It is of interest to note that the presence of Nb alone retards recrystallization significantly at 1000°C and that, in combination with boron, the retarding influence of Nb is greater than the sum of their individual effects.

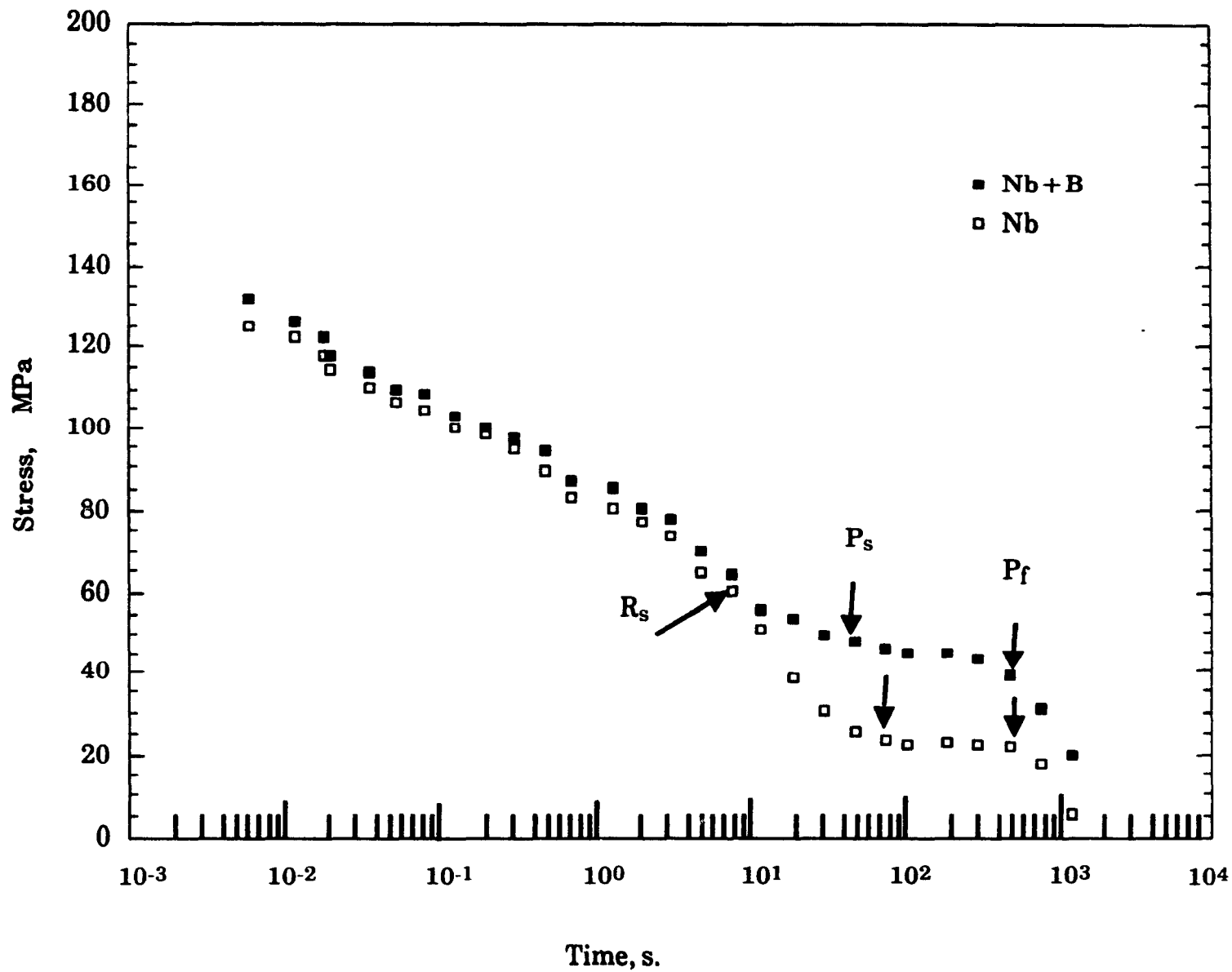


Fig.VII.2 Comparison between the stress relaxation curves for the Nb + B and Nb steels after 25% deformation at 950 °C.

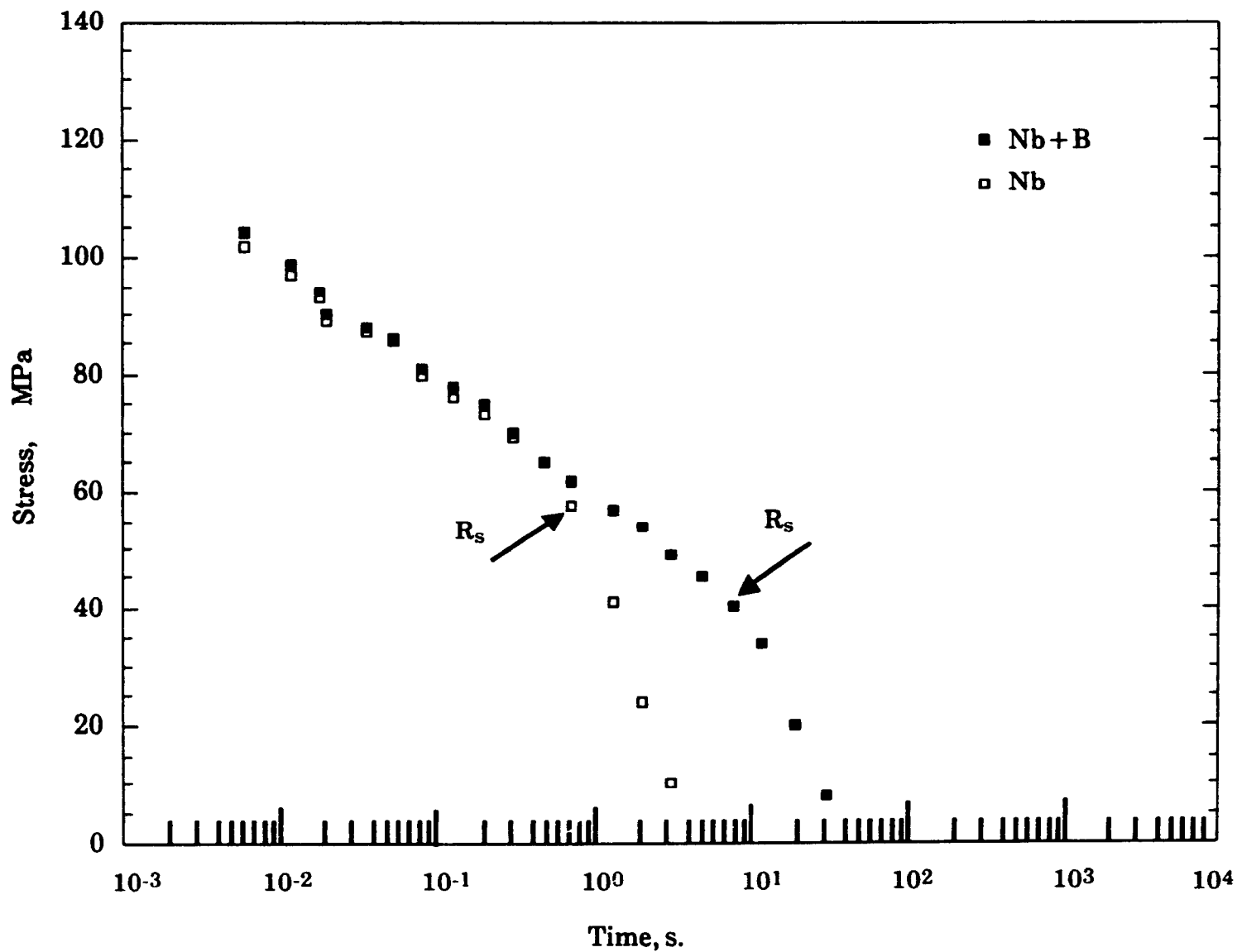
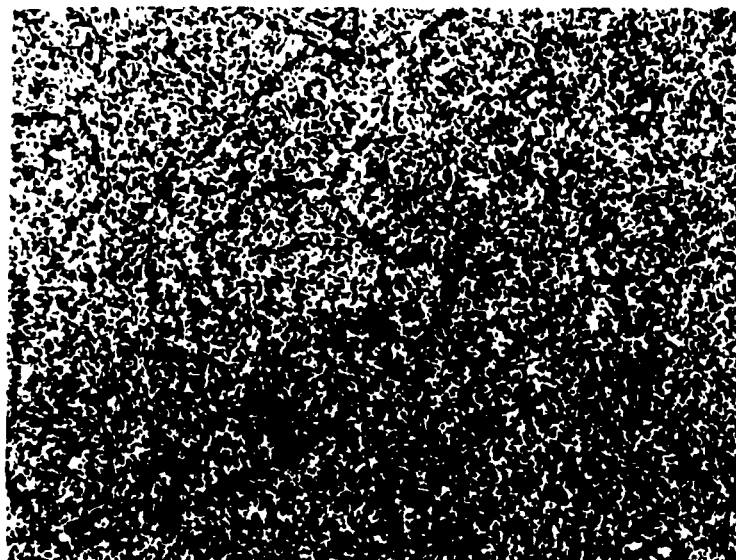
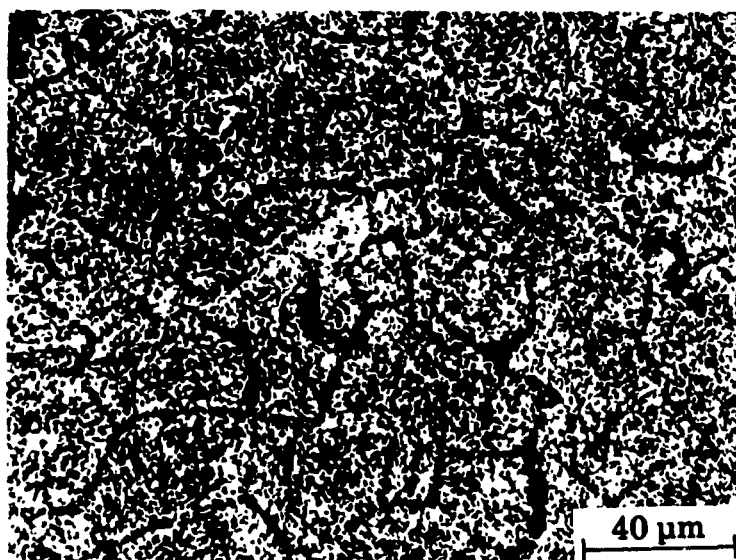


Fig.VII.3. Comparison between the stress relaxation curves for the Nb + B and Nb steels after 25% deformation at 1000°C.

**Nb + B****B**

**Fig. VII.4** Influence of the simultaneous presence of Nb and boron on the recrystallization process. PTA micrographs of the Nb + B and B steels deformed 25% at 1000°C and quenched after 10 s.

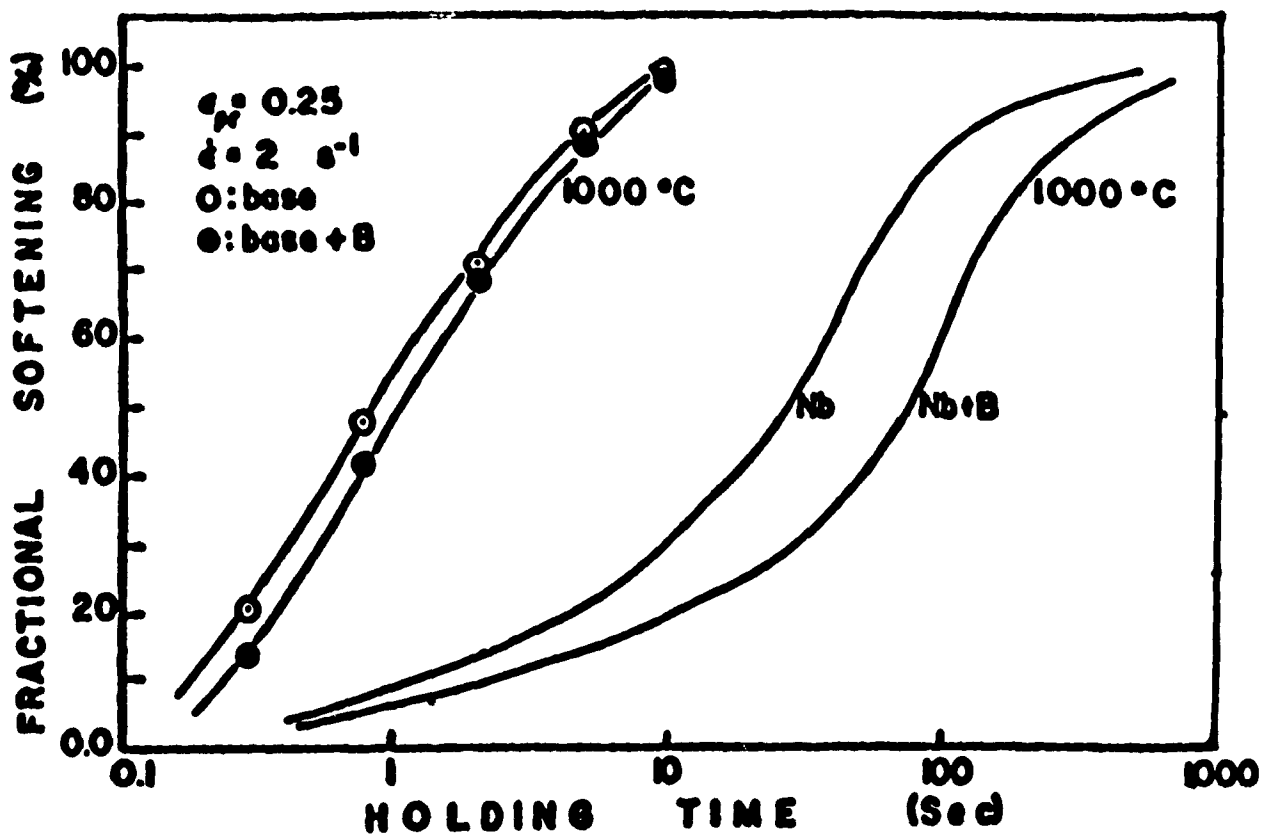


Fig. VII.5 The softening behaviours of the four steels deformed 25% at 1000°C.

**Table VII.2**  
**Times for the Beginning( $t_0$ ) and the Half**  
**Completion of Recrystallization( $t_{0.5}$ ).**

Steel	$t_0$ sec	$t_{0.5}$ sec
Base	0.35	1.32
B	0.42	1.65
Nb	5	38
Nb + B	12	98

The retardation of austenite recrystallization caused by Nb can be interpreted in terms of the solute drag theory [135, 141, 192, 193] or by the pinning effect of the grain boundaries by strain induced precipitates [103, 139, 194, 195]. The stress relaxation results and TEM observations of the samples tested at 1000°C showed clearly that no precipitates were present at this temperature. Consequently, a solute drag effect is probably responsible for delaying austenite recrystallization at 1000°C. However, as shown in Figs. VII.4 and VII.5, boron alone has a weak drag effect, significant retardations being produced only when it is present with Nb.

The role played by boron may then be interpreted in terms of how: i) its presence increases the solute drag effect of Nb, resulting in slower grain boundary migration; and ii) the simultaneous presence of Nb and B atoms produces a synergistic effect, which in fact may be responsible for retarding austenite recrystallization.

### VII.2.1 Influence of Boron on the Solute Drag Effect of Nb

According to the solute drag theory [196, 197], the drag exerted on a moving boundary by the atmosphere of solute atoms trailing it is not a linear function of its velocity. Instead, the drag first increases with the velocity, reaches a maximum, and then decreases. When the velocity of the grain boundary is relatively high, the solute atoms can no longer follow the boundary.

Based on the Hillert and Sundman treatment [197], the drag force increases as the ratio of  $D_{I,gb}/D_{I,m}$  decreases, where  $D_{I,gb}$  and  $D_{I,m}$  are the impurity grain boundary and matrix diffusivities, respectively. Consequently, the greater retardation of recrystallization observed when boron is added to the Nb steel indicates that this element decreases the grain boundary diffusivity of Nb ( $D_{Nb,gb}$ ).

The PTA results of chapter V showed that boron segregation is produced at the moving grain boundaries. As mentioned in VII.1, microalloying elements such as Ti and Nb, because of their large size differences with respect to austenite, have the tendency to segregate to the grain boundaries. Furthermore, it has been reported [198] that the presence of even small amounts of interstitials (e.g. 20-40 ppm by wt) can seriously reduce the grain boundary diffusivity of the substitutional solutes which are present there. Consequently, the presence of boron at the grain boundaries will tend to decrease the grain boundary diffusivity of Nb.

According to the above discussion of the results, it seems reasonable to conclude that, in the framework of the Hillert and Sundman theory, the presence of boron leads to lower values of the ratio  $D_{Nb,gb}/D_{Nb,m}$ . This reduction will produce larger drag forces on the grain boundaries.

## VII.2.2 The Synergistic Effect of Nb and Boron

The strong tendency of boron to segregate to austenite grain boundaries (original and new ones) was clearly demonstrated in this investigation. Also, as discussed earlier in this chapter, Nb can segregate to grain boundaries as well. In fact, some recent reports in the literature [199] suggest that Nb can segregate to the new boundaries during recrystallization and consequently delay the nucleation and development of new grains.

The fact that the simultaneous presence of boron and Nb slows down the recrystallization kinetics by more than the sum of their individual effects suggests that interactions exist between the Nb and boron atoms. In fact, the Nb-B phase diagram shows that these elements can form several compounds.

Furthermore, the atomic radii of Nb, B and Fe are 1.468, 0.97 and 1.274 Å, respectively, so that

$$2R_{\text{Fe}} \approx R_{\text{Nb}} + R_{\text{B}}$$

The above discussion explains why Nb and boron have a strong tendency to form complexes; this combination is able to reduce the lattice distortion energy. Now, as mentioned in the previous section, the retardation produced by a given element is dependent on the ratio  $D_{\text{I,gb}}/D_{\text{I,m}}$ . If we assume that the Nb-B complexes have higher diffusivities than the Nb atoms, then  $D_{\text{Nb,m}}$  is increased and finally greater recrystallization delays are obtained. The addition of these two effects leads to the greater retardation observed in the case of the Nb + B steel.

The operation of the above mechanism relies on the assumption that the Nb-B complexes diffuse faster than Nb atoms. This seems reasonable if we take into account the dual nature of the boron atoms in the austenite lattice. In fact, as mentioned in chapter II, depending on their environment, boron atoms can occupy either substitutional or interstitial sites. When it possesses sufficient energy, a boron atom can make the transition from its substitutional position to an interstitial one. Under these conditions, the adjacent Nb atom can fill the vacant site left by the latter and diffuse in this way. Once the Nb atom diffuses away, the interstitial boron atom can recombine with a conveniently located vacancy and again take on its substitutional guise. In this case, the presence of boron leads to an effective increase in the vacancy concentration in the vicinity of Nb atoms, and therefore in the rate of Nb diffusion. It is important to note here that it is not necessary for the same boron and Nb atoms to diffuse together and if favorable thermodynamic conditions are present, the Nb atom can continue on its way with another boron atom.

In summary, it can be said that the simultaneous presence of Nb and B leads to the formation of Nb-B complexes. The existence of the latter in the matrix effectively retards austenite recrystallization by increasing  $D_{\text{Nb,m}}$ ; their presence at the grain boundaries acts by decreasing  $D_{\text{Nb,gb}}$ . The above concept can be employed to interpret the differences observed in the relaxation

behaviours of the Nb + B and Nb steels at 950°C. In fact, after deformation at this temperature, the effect of Nb addition alone is not enough to prevent the occurrence of recrystallization, which starts about 5 s after deformation and is arrested about 75 s later by carbonitride precipitation. By contrast, in the Nb+B steel, the presence of Nb-B complexes at dislocations and grain boundaries has two effects:

i) at dislocations, it increases the concentration of the precipitating elements, accelerating the precipitation process in this way.

ii) at the grain boundaries, Nb-B complexes exert their retarding effect on recrystallization.

The superposition of these two effects results in the occurrence of precipitation before recrystallization, as observed in the stress versus log (time) curve.

### VII.3 Origins of the Non-equilibrium Segregation of Boron

The primordial role of boron segregation in precipitation and recrystallization was discussed in the above two sections of this chapter. Our experimental observations have revealed that the non-equilibrium segregation of boron can not only be produced during cooling after isothermal holding (as is generally accepted), but it can also occur after deformation and during recrystallization. In what follows, each of these types of segregation will be discussed in turn and an attempt will be made to distinguish semi-quantitatively between the segregation produced after deformation at original austenite boundaries and the one observed on new boundaries.

#### VII.3.1 Cooling Induced Segregation of Boron

The present experimental results have demonstrated that the non-equilibrium segregation of boron occurs during cooling (i.e. quenching or continuous cooling) and that the amplitude of the segregation increases with the difference between the solution and quench temperatures. These results are in good agreement with those reported in the literature [37, 38, 42, 53]. In chapter II, the model first proposed by Williams et al. [42] for the mechanism of boron segregation was described. In what follows, the mechanisms of segregation suggested by the experimental results obtained in this

investigation will be interpreted and compared with those reported in the literature.

The mechanism for the non-equilibrium segregation of boron proposed by Williams et al. is based on the existence of mobile boron-vacancy (B-V) complexes. The driving force for segregation is the change in equilibrium vacancy concentration produced during cooling. At thermal equilibrium, the concentrations of vacancies and complexes are given by

$$C_V = K_V \exp\left(-\frac{E_V^F}{kT}\right) \quad (\text{VII.3})$$

$$C_{B-V} = K_{B-V} C_B C_V \exp\left(-\frac{E_{B-V}^b}{kT}\right) \quad (\text{VII.4})$$

where  $E_V^F = 1.4$  eV is the vacancy formation energy,  $E_{B-V}^b = 0.5$  eV is the binding energy of the complexes, and  $K_V = 4$  and  $K_{B-V} = 12$  are constants containing various geometric and entropy terms. Using the above numerical values [42], the vacancy and B-V complex equilibrium concentrations were evaluated for a nominal boron content of 156 at ppm; these are presented in Table VII.3.

**Table VII.3**  
**Influence of Solutionizing Temperature on the**  
**Vacancy( $C_V$ ), Complex( $C_C$ ) and Boron ( $C_B$ )**  
**Concentrations.**

Temp. °C	$C_V$ 10 <sup>6</sup>	$C_C$ 10 <sup>6</sup>	$C_B$ 10 <sup>6</sup>
900	3.9	1.1	154.9
950	6.8	1.5	154.5
1000	11.6	2.1	153.9
1100	29.3	3.8	152.2
1200	64.7	6.2	149.8

During cooling, the strong supersaturation of vacancies that is produced leads to higher concentrations of complexes. The latter are annihilated at vacancy sinks (i.e. grain boundaries, dislocations...) and deposit their boron atoms at these sites. As a result, the concentration of complexes decreases and that of the isolated boron atoms increases. In the Williams et al. analysis [42], it is assumed that the complexes diffuse from the centers of the grains towards the grain boundaries and maintain a high concentration of boron atoms at the boundaries in this way. For this mechanism to be operative during cooling, the mobility of the complexes must be higher than that of either individual vacancies or boron atoms. Several estimates were made of the diffusivities of boron atoms, vacancies and B-V complexes. The diffusivity values proposed by Williams et al. [42] and Karlsson [47] are compared in Fig. VII.6 as a function of inverse temperature. The equations used to plot the data are reported in Table VII.4.

**Table VII.4**  
**Diffusivity Equations for Vacancies, Complexes and Boron Atoms.**

Diffusion Equation cm <sup>2</sup> /sec	Reference
$D_V = 1.4 \cdot 10^{-5} \exp\{-1.4 \text{ eV}/kT\}$ $D_{B-V} = 2 \cdot 10^{-6} \exp\{-1.15 \text{ eV}/kT\}$ $D_B = 2 \cdot 10^{-7} \exp\{-1.15 \text{ eV}/kT\}$	Karlsson [47]
$D_V = 1.4 \cdot 10^{-5} \exp\{-1.4 \text{ eV}/kT\}$ $D_{B-V} = 1.4 \cdot 10^{-5} \exp\{-0.91 \text{ eV}/kT\}$ $D_B = 2 \cdot 10^{-7} \exp\{-0.91 \text{ eV}/kT\}$	Williams et al. [42]

Two comments can be made regarding the above model:

i) The present experimental results and several reports in the literature [33, 36, 43, 46] indicate that a boron depleted zone exists adjacent to the two sides of the boundaries, the width of which increases with the quenching temperature difference. Moreover, semi-quantitative analyses [200, 201] and computer simulations [46, 47, 200] have indicated that the boron concentration

reaches that of the matrix at a short distance beyond the depleted zone. These observations indicate that boron segregation during cooling is the result of complex diffusion from the depleted zone to the boundary. Consequently, it appears that the effect of quenching temperature difference on the intensity of segregation would be better quantified by the width of the boron depleted zone. The grain size criterion (as proposed by Williams et al.,[42]) should have only relative importance; i.e. the degree of segregation should be independent of grain size as long as the grain diameter is more than double the width of the depleted zone.

ii) The second comment concerns the choice of the diffusion coefficient for B-V complexes made by Williams et al. [42] and Karlsson [47]. It is of interest to note that (see Fig.VII.6), in both models, the complex diffusivity is much higher than that of individual vacancies or boron atoms. For example, Karlsson considers that, at 1000°C, the complexes diffuse 10 times faster than individual boron atoms, while for Williams et al., they diffuse about 70 times more rapidly. Although the choice of a higher diffusion coefficient for complexes is fundamental to the occurrence of segregation, it is not clear why the complexes should diffuse faster than even the fastest diffusing element.

Another potential mechanism for the non-equilibrium segregation of boron may be that proposed by Aust et al. [202]. They suggested that groups of solute complexes can form near grain boundaries, provided that strong interactions exist between solute atoms and vacancies. This concept was originally applied to the case of zone refined metals (Pb, Sn and Zn) doped with various solutes. It may be applied to our case as strong interactions exist between boron atoms and vacancies. The clustering of the boron atoms retains them for longer times at the boundaries, leading to higher boron concentrations. It is interesting to note that, in this analysis, no prior assumption is made regarding complex diffusivity.

An additional factor which can contribute to keeping the boron concentration high at the boundaries is that, during cooling, a continuous flux of vacancies and complexes moves to the boundaries, which brings boron atoms with it. After a certain time, when the boron concentration gradient is

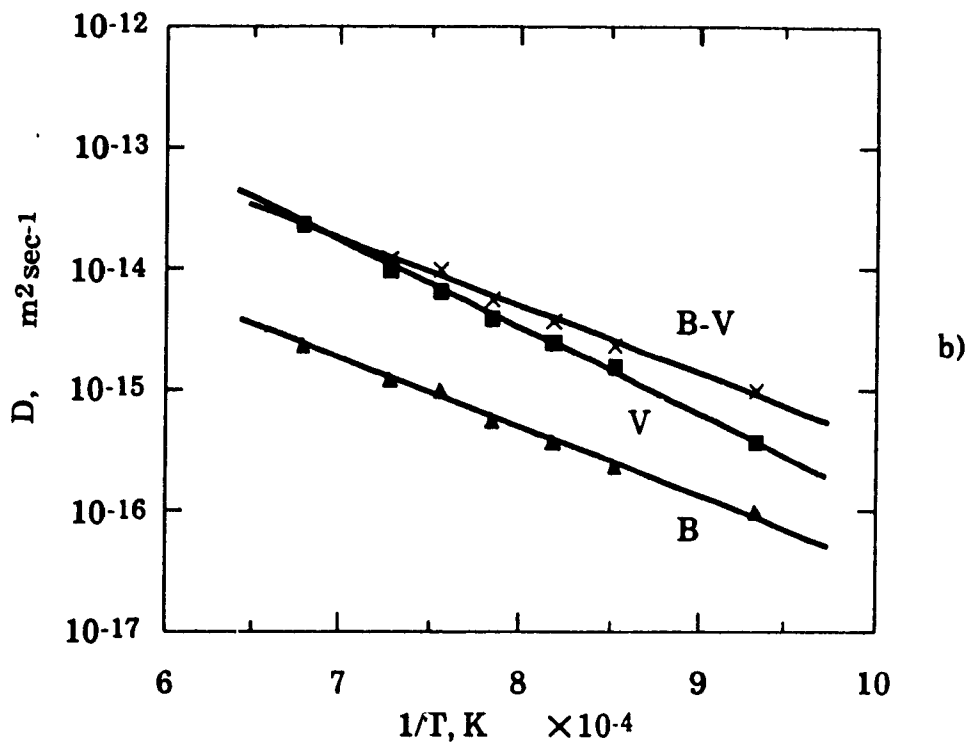
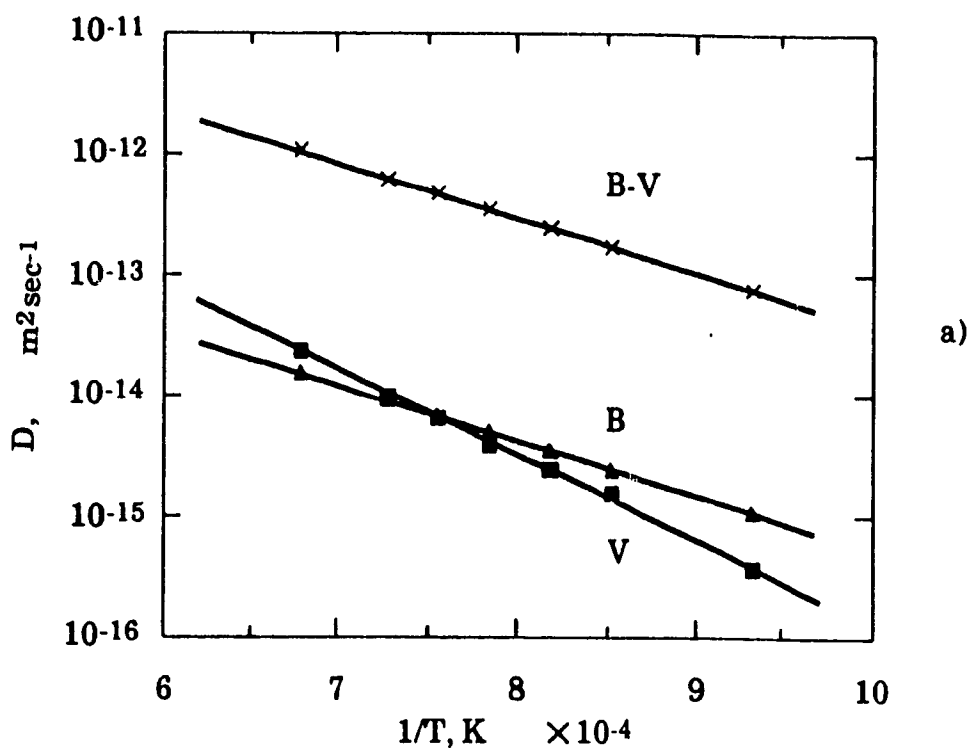


Fig.VII.6 Comparison the diffusivities of between B-V complexes, vacancies and boron atoms according to the Williams (a) and Karlsson (b) models.

established, a reverse flow of boron atoms takes place from the grain boundaries towards the interiors of the grains. These "returning" boron atoms encounter individual vacancies moving in the opposite direction. Because of their strong interaction, some of the vacancies combine with the boron atoms and bring them back to the boundaries, keeping the boron concentration at a high level.

### VII.3.2 Boron Segregation after High Temperature Deformation

The PTA and SIMS results of chapter V indicated that boron segregation is produced at prior austenite grain boundaries after deformation followed by isothermal holding. This segregation is also of the non-equilibrium type and disappears after a certain time. Such segregation has also been reported recently [191, 203]. To interpret the above results, a concept similar to that used in the previous section may be employed. In fact, like quenching, deformation increases the vacancy concentration significantly. The deformation  $\epsilon$  is related to the increase in vacancy concentration  $\rho_v$  by [204]:

$$\rho_v \approx 10^{-4} \epsilon$$

As for the case of quenching, the vacancies form complexes with the boron atoms and move with them to the original boundaries before being annihilated there. This non-equilibrium segregation persists until the boron atoms move away by back diffusion or the boundaries are eliminated by recrystallization. Moreover, He et al. [201] have reported that deformation does not change the width of the boron depleted zones; however, they remarked that the degree of boron depletion is more severe after deformation. These results seem to indicate that either deformation does not affect the complex diffusivity or its influence is very small.

### VII.3.3 The Non-equilibrium Segregation of Boron during Recrystallization

The third type of boron segregation observed during this investigation is the one produced on moving grain boundaries. PTA micrographs and SIMS ion micrographs illustrating this effect were presented in chapter V (see for example Figs.V.24 and V.25). Boron segregation also occurs after

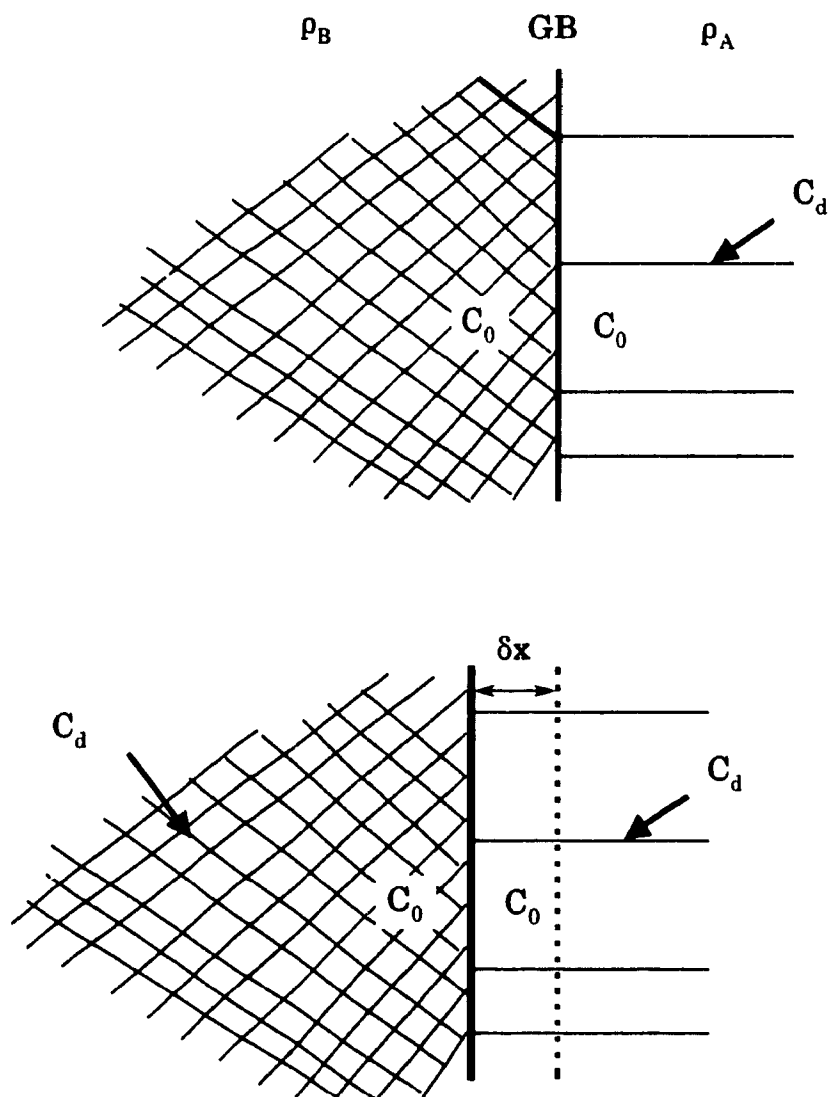
deformation, the latter providing the driving force for migration of the newly formed grain boundaries. Consequently, under appropriate conditions of temperature and deformation (here  $T=1000^{\circ}\text{C}$ ,  $\epsilon=25\%$ ), segregation can be observed both at the original and at newly formed grain boundaries. Two questions arise at this point: i) by what mechanism is the segregation produced at the new boundaries? and ii) is it possible to separate the two types of segregation, either quantitatively or at least semi-quantitatively?

### VII.3.3.1. The Mechanism of Segregation

It is widely accepted that the equilibrium segregation of boron takes place at grain boundaries and dislocations. After deformation, the density of dislocations increases substantially; these are subsequently affected by the equilibrium segregation of boron atoms. Moreover, because of the excess vacancies produced by the deformation, non-equilibrium segregation is also produced on the dislocations. However, this latter segregation does not persist and soon vanishes.

Under favorable conditions, recrystallization takes place. The newly formed nuclei grow into the deformed material by the migration of their boundaries. The driving force for migration is provided by the difference in dislocation density between the interior of a nucleus and the surrounding worked metal. The annihilation of the dislocations at the moving boundaries leads to the deposition of the boron atoms and consequently to an increase in boron concentration at the boundaries. Fig. VII.7 illustrates schematically the process of grain boundary enrichment by boron atoms when the boundary moves from position  $x$  to  $x + \delta x$ .

As recrystallization progresses, the level of segregation increases until a concentration gradient of boron atoms is established. Subsequently, the back diffusion of boron atoms starts. However, segregation continues to increase at the boundary until a steady state is reached, where the numbers of boron atoms added to the boundary during its movement are approximately equal to those leaving it. The intensity of segregation decreases when the boundaries of the new grains impinge on each other (i.e. the movement of the new boundary is stopped), while back diffusion continues to take place. Finally, it



legend

$\rho_A$ : dislocation density in region A  
 $\rho_B$ : dislocation density in region B  
 $C_0$ : boron concentration in the matrix  
 $C_d$ : boron concentration on dislocations

Fig. VII.7 Grain boundary enrichment by boron atoms when the boundary moves from  $x$  to  $x + \delta x$ .

should be mentioned that the above suggested mechanism is qualitative and theoretical calculations are underway.

The application of deformation leads to the occurrence of temporary segregation, both at the original and the moving grain boundaries. As a quantitative evaluation is impossible, the following, which is a semi-quantitative estimation of the segregation levels, is presented. The calculations were performed only on the Nb + B steel specimens deformed 25% at 1000°C and held for different times. However, similar conclusions are expected for the boron grade.

#### VII.4. Semi-Quantitative Analysis of Segregation

In order to proceed with the analysis, two important sets of variables are required : i) evaluation of the total length of the boundaries (original + recrystallized), and ii) the variations in the level of grain boundary segregation. The latter have already been measured and the results were displayed in Fig.V.30. The total length of austenite grain boundary after different holding times can be obtained from the PTA micrographs of the oil quenched samples (see Fig.V.31). In fact, during oil quenching, strong boron segregation is produced at all austenite grain boundaries; in this way, we are able to have a precise idea of the total length of the boundary. The method of measurement was the same as the one used to obtain Fig.V.31. The data obtained are presented in Fig.VII.8a along with a reproduction of Fig.V.31a for comparison purposes (Fig.VII.8b). Comparison of the two curves shows that  $L_{S_{max}}$  is not equal to  $L_{max}$  and is given instead by  $L_{S_{max}} = 0.95 L_{max}$ . This means that, even when the segregation maximum is attained during holding, some boundaries still remain without evident segregation. In this figure, the different parameters are defined as follows:

- L = total length of grain boundary per unit area measured on the oil quenched samples,
- $L_{max}$  = the maximum value of L attained during isothermal holding,
- $L_S$  = total length of continuous etch pits (i.e. of boron segregation) per unit area measured on the ice brine quenched samples (using ice brine

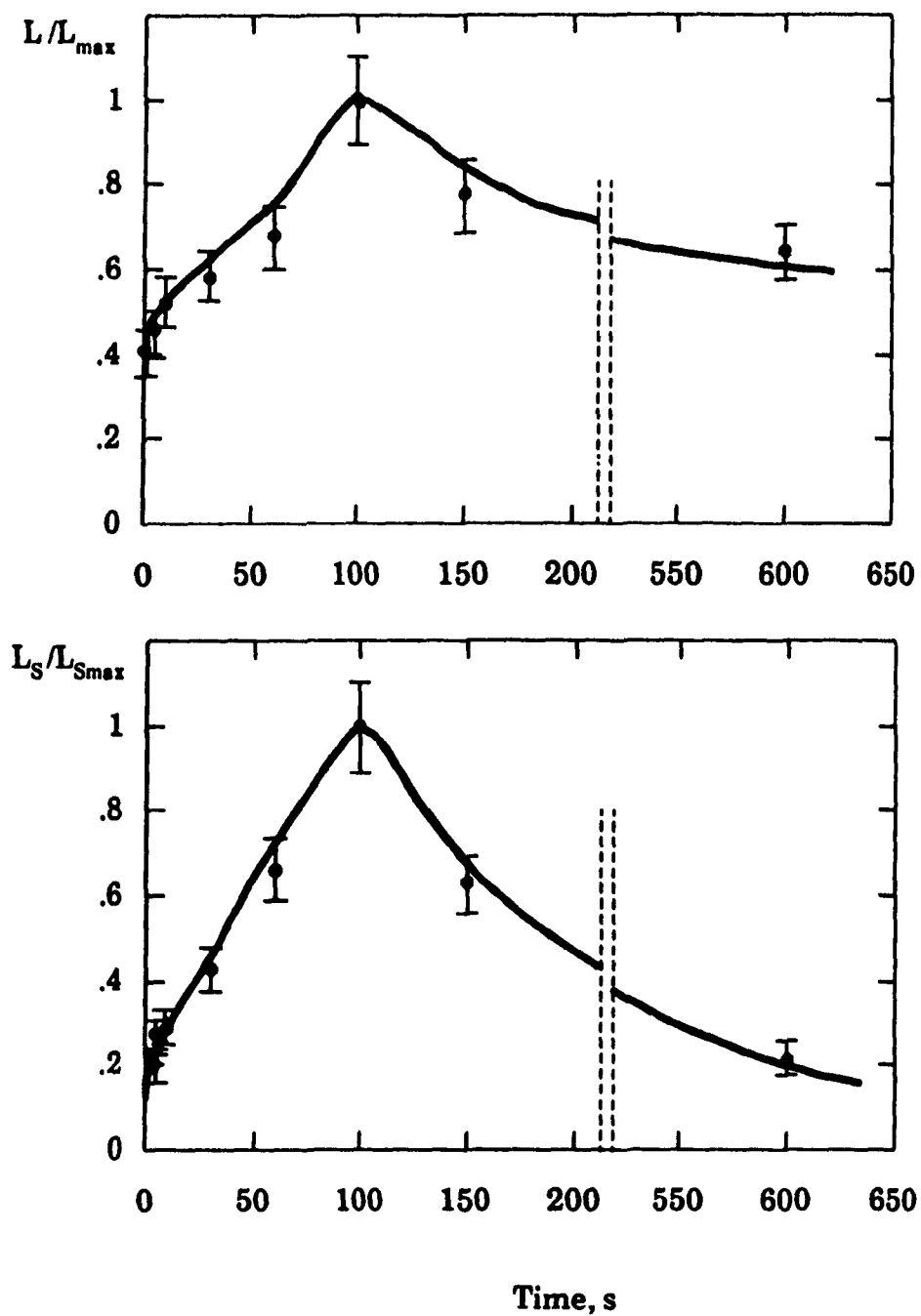


Fig.VII.8 Dependence of  $L/L_{max}$  and  $L_S/L_{Smax}$  on isothermal holding time in the Nb+B steel after 25% deformation at 1000°C.

quenching, only the segregation due to deformation and recrystallization are revealed), and

$L_{S_{max}}$  = the maximum value of  $L_S$  attained during isothermal holding.

The PTA results and the data of Fig.VII.8 indicate that:

- 1) The nucleation of new grains occurs at the original austenite grain boundaries. The former grow until impingement occurs.
- 2) The original boundaries are gradually replaced by the nucleation and growth of new grains. The total length of boundary in the sample increases continuously until impingement occurs. After this stage, grain coarsening begins and leads to a decrease in the total length of boundary.

#### VII.4.1. Assumptions and Analysis

Based on the above remarks, the following assumptions can now be made in this analysis:

- i) the original austenite grains have cross sections which are regular hexagons, and
- ii) the nuclei are all of spherical shape and their growth rate is linear and constant until impingement.

Fig.VII.9 illustrates schematically the progress of recrystallization from nucleation until the meeting of the new boundaries.

Let  $L_0$  be the total length per unit area of original grain boundary before recrystallization. If  $L_T$  is the total length of boundary at any time, before recrystallization (i.e. at  $t = 0$ ), we have

$$L_{T0} = L_0 \quad (\text{VII.5})$$

Once recrystallization begins, new grains, of radius  $r$ , are formed at the triple points. Their total length,  $L_N$ , is given by

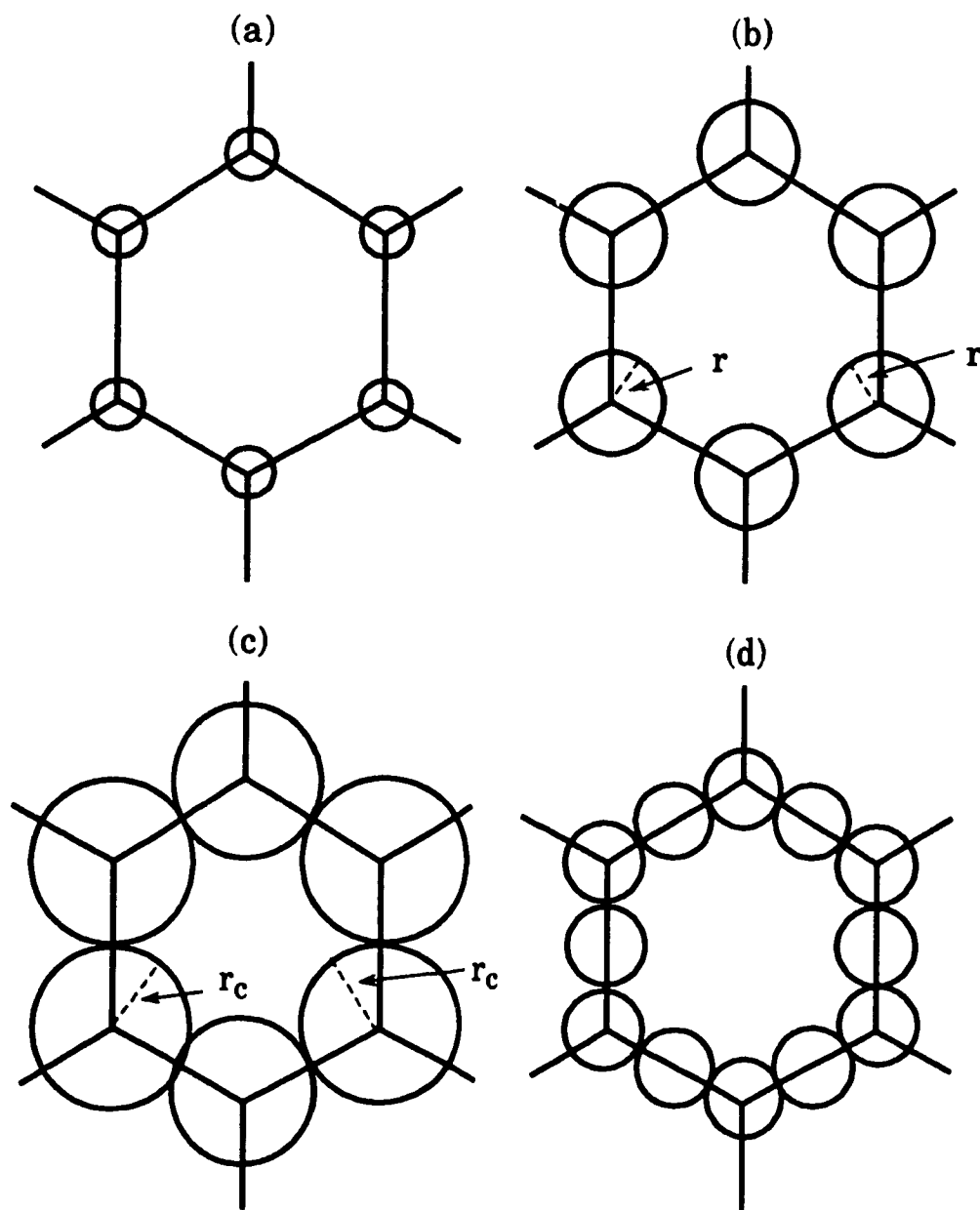


Fig.VII.9 Schematic illustration of the formation of new boundaries and the annihilation of old ones.

$$L_N = n \times 2\pi r \quad (\text{VII.6})$$

where  $n$  is the total number of newly formed grains. At any time  $t$ , the length of original boundaries eliminated because of the progress of recrystallization (Fig. VII.9b) is equal to

$$L_E = n \times 3r \quad (\text{VII.7})$$

under these conditions, the total length of boundary at any time  $t$ ,  $L_{Tt}$ , is

$$L_{Tt} = (L_0 - n \times 3r) + 2\pi r \quad (\text{VII.8})$$

This relation is valid as long as the new boundaries continue to move. When impingement occurs (Fig. VII.9c),  $r = r_c$  and

$$L_0 - n \times 3r_c = 0 \quad (\text{VII.9})$$

Also, at this time,  $L_N$  reaches its maximum value and is given by

$$L_N = L_{Nmax} = n \times 2\pi r_c \quad (\text{VII.10})$$

This leads to

$$L_{Tt} = L_{Tmax} = n \times 2\pi r_c \quad (\text{VII.11})$$

In the above equations,  $r_c$  is the radius of the new grain at impingement.

Relations VII.5 and VII.9 to VII.11 indicate that, during recrystallization, the total length of the original boundary ( $L_0 - n \times 3r$ ) decreases linearly from  $L_0$  to zero between the nucleation and impingement stages. By contrast, the length of new boundaries evolves from zero to a maximum value of  $L_{Nmax} = n \times 2\pi r_c$ . Finally, the total length of boundary (original and new) increases from  $L_{T0} = L_0$  to  $L_{Tmax} = n \times 2\pi r_c$ .

At the point of impingement,  $L_{Tmax}/L_{T0}$  can be calculated and is given by

$$\frac{L_{Tmax}}{L_{T0}} = \frac{n \times 2\pi r_c}{n \times 3r_c} = 2.1 \quad (\text{VII.12})$$

Moreover, at this point, the area fraction of new grains is equal to

$$R = \frac{6 \times \frac{1}{3} \pi r_c^2}{6 \times 3^{1/2} r_c^2} = 0.6 \quad (\text{VII.13})$$

The volume fraction of new grains was also calculated and is approximately equal to 0.48.

#### VII.4.2 Comparison of the Results

It is of interest to note that, according to the data of Fig.VII.5, in the case of the Nb + B steel, the time for 50% recrystallization (i.e. the time when the total length of boundary reaches its maximum value) is 100 s. This value is in very good agreement with the one determined in this investigation (see Fig. VII.8a).

It is clear that, after impingement, when grain coarsening starts, the total length of boundary,  $L_T$ , will decrease. The expected dependences of  $L_N/L_{max}$ ,  $L_T/L_{max}$  and  $L_O/L_{max}$  on holding time are presented in Fig.VII.10. As a comparison, the experimental results for  $L/L_{max}$  are also displayed. It can be seen that the behaviours of  $L_T/L_{max}$  and  $L/L_{max}$  are similar in the interval 0-100 s. In order to distinguish between the two types of segregation, the dependence of  $L_S/L_{max}$  on holding time was evaluated and is presented in Fig. VII.11.

The following observations can be made about this figure:

- 1) The  $L_T/L_{max}$  and  $L_S/L_{max}$  curves do not coincide with each other. This indicates that, at any time during isothermal holding, the totality of the grain boundaries cannot attain a degree of segregation that can be revealed by PTA as continuous etch pits.

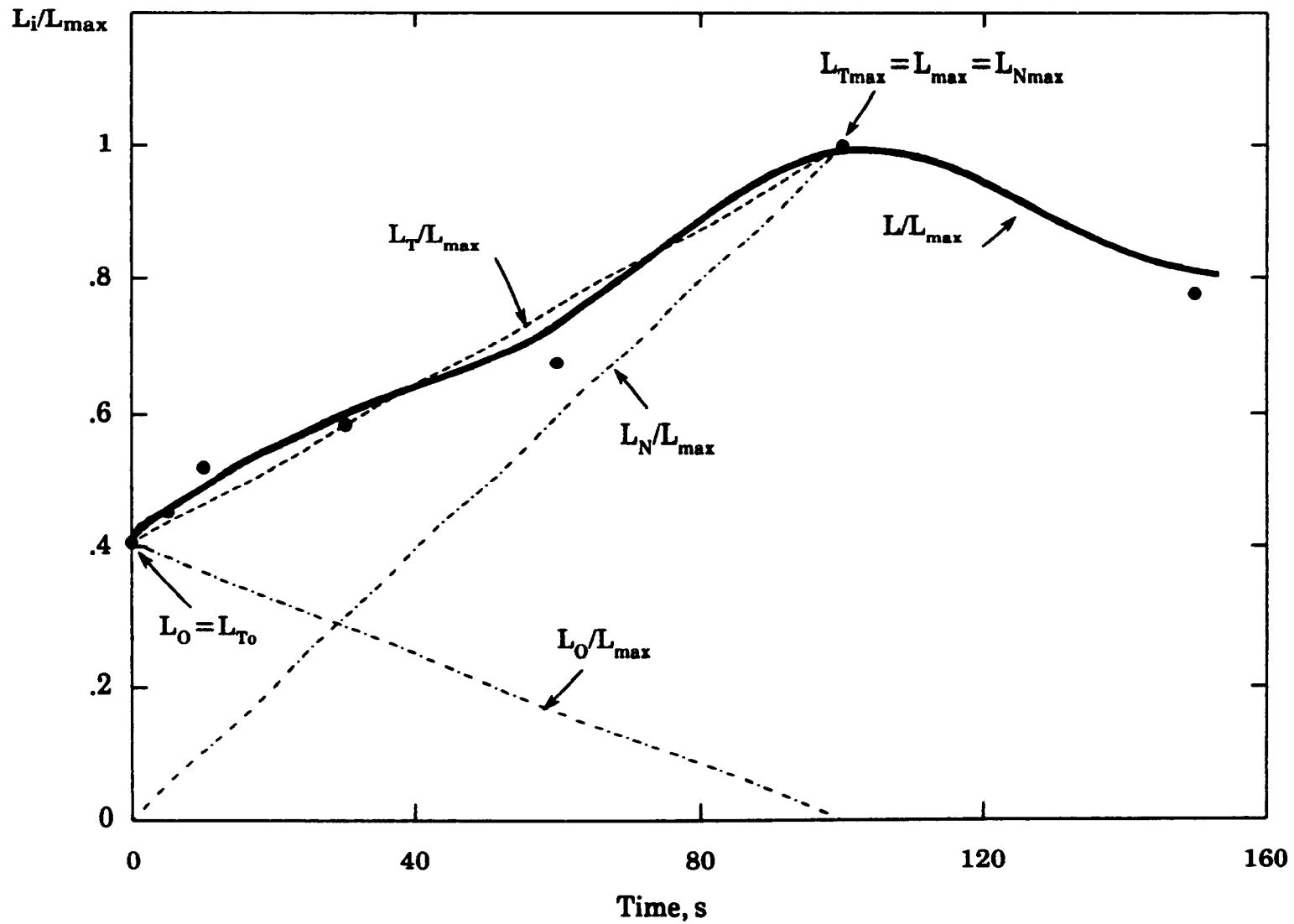


Fig.VII.10 Dependences of  $L_T/L_{max}$ ,  $L_N/L_{max}$ ,  $L_O/L_{max}$  and  $L/L_{max}$  on holding time for the Nb + B steel deformed 25% at 1000°C.

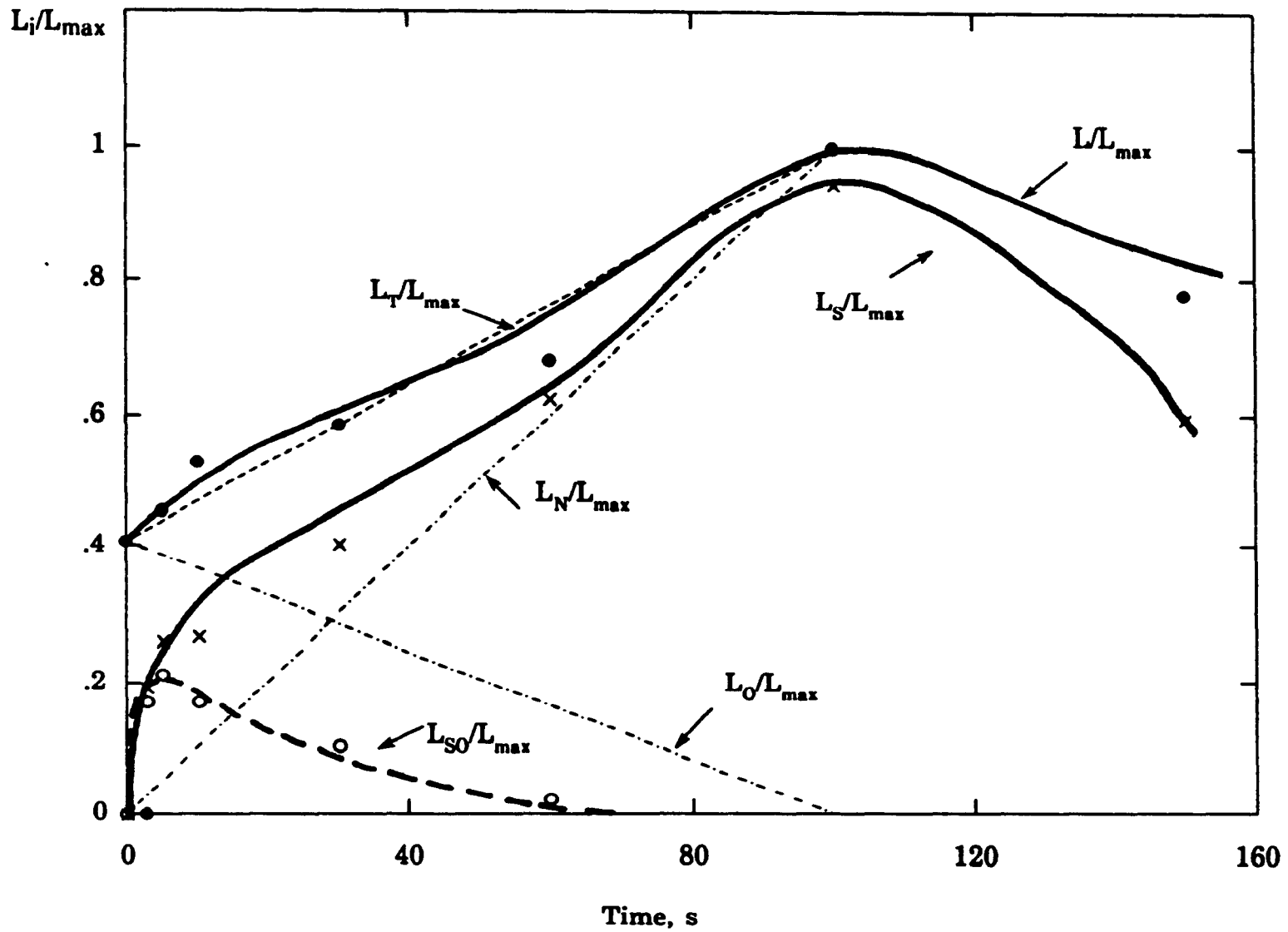


Fig.VII.11 Distinction between the segregation produced at original and newly formed boundaries.

- 2) The severity of segregation on new boundaries increases continuously from the nucleation stage until impingement occurs. By contrast, the segregation level on original boundaries first increases to a maximum and then drops monotonously.
  
- 3)  $L_S$  represents the sum of segregation at both the original and new grain boundaries. If it is assumed that, after about 100 s of holding, all the new boundaries contain observable boron segregation, then the difference between the  $L_S/L_{\max}$  and  $L_N/L_{\max}$  curves indicates the variations in segregation level on the original grain boundaries during isothermal holding. This situation is illustrated on the  $L_{S0}/L_{\max}$  curve, where  $L_{S0}$  is given by  $L_{S0} = L_S - L_N$ . As can be seen, the segregation induced by deformation on the original boundaries is, as described previously, of the non-equilibrium type. It reaches its maximum 5-10 s after deformation and then decreases continuously such that almost no segregation is found 60 s later. By contrast, the segregation produced at the new boundaries increases until impingement occurs. After this step, a portion of the boundary moves towards the center of the distorted grain (and in this case the segregation persists). The other parts of the boundary come into contact with the boundaries of other grains and as a consequence the segregation level decreases as the boundary advances.

Finally, it should be mentioned that it was assumed in the above model that all the new grains nucleate at triple points. Another assumption could be that nucleation can also occur at the centers of the old boundaries, as shown in Fig. VII.9.d. Similar calculations were carried out and a value of 2.6 for the ratio  $L_{T\max}/L_{T0}$  was obtained (as compared to 2.1 when nucleation occurs only at triple points). On the other hand, measurements on the PTA micrographs led to the ratio  $L_m/L_0 = 2.4$ . Here  $L_0$  and  $L_m$  are the values of  $L$  measured on the samples quenched before recrystallization and 100 s after deformation, respectively. It therefore seems reasonable to conclude that the contribution of the grains nucleated at the boundaries is small and that the most important nucleation sites are the triple points.

## VII.5. Comparison with the Precipitation Results of Other Workers

As mentioned in chapters IV and V, no quantitative data regarding the influence of boron on the kinetics of carbonitride precipitation in microalloyed austenite were found. Nevertheless, our results are in good agreement with those of several workers [14, 60-62, 74] who observed that boron accelerates the precipitation process. As a result, comparisons can only be made for the Nb steel.

The PTT curves for the present Nb steel are presented together with the results from several other investigations in Fig. VII.12. The C, N and Nb contents of the steels used in these studies are reported in Table VII.5 along with the experimental conditions. As can be seen from this table, the product of the Nb, N and C concentrations in our steel is lower than that of all the other researchers. This is the reason for the downward shift of the nose of the PTT curve. The presence of Ti in our steel also contributes to the above process; in fact, the TEM examination showed that Nb atoms diffuse towards the undissolved TiN particles, decreasing the Nb supersaturation in the matrix in this way. Furthermore, as reported by Watanabe et al. [132], the simultaneous presence of other precipitate forming elements in addition to Nb shifts the nose of the PTT curve to lower temperatures. For example, the above workers reported that the addition of Mo to a Nb microalloyed steel lowers the maximum precipitation temperature by about 40°C.

Comparison with the data reported in the literature regarding the size and distribution of the precipitates shows very good agreement. As was found in this study, several investigators [60-62] have reported the precipitate refining effect of boron (case of the Nb + B steel). In addition, in the Nb and Nb + B steels, the particles were distributed in a chain-like manner, which is characteristic of strain induced precipitation and has already been reported in the literature [112].

Table VII.5.

Comparison Between the PTT Curves Obtained by Different  
Investigators.

C wt%	N wt%	Nb wt%	Hot Deformation	Method	Reference
0.05	0.005	.035	$\epsilon = 5\%$ Compression	flow curve	[135]
0.06	0.0062	0.084	$\epsilon = 5\%$ Rolling	chem. ext.	[132]
0.06	0.0061	0.084	$\epsilon = 5\%$ Rolling	chem. ext.	[132]
0.05	0.0060	0.035	$\epsilon = 5\%$ Compression	flow curve	[138]
0.026	0.0063	0.055	$\epsilon = 5\%$ Compression	stress relaxation	present work

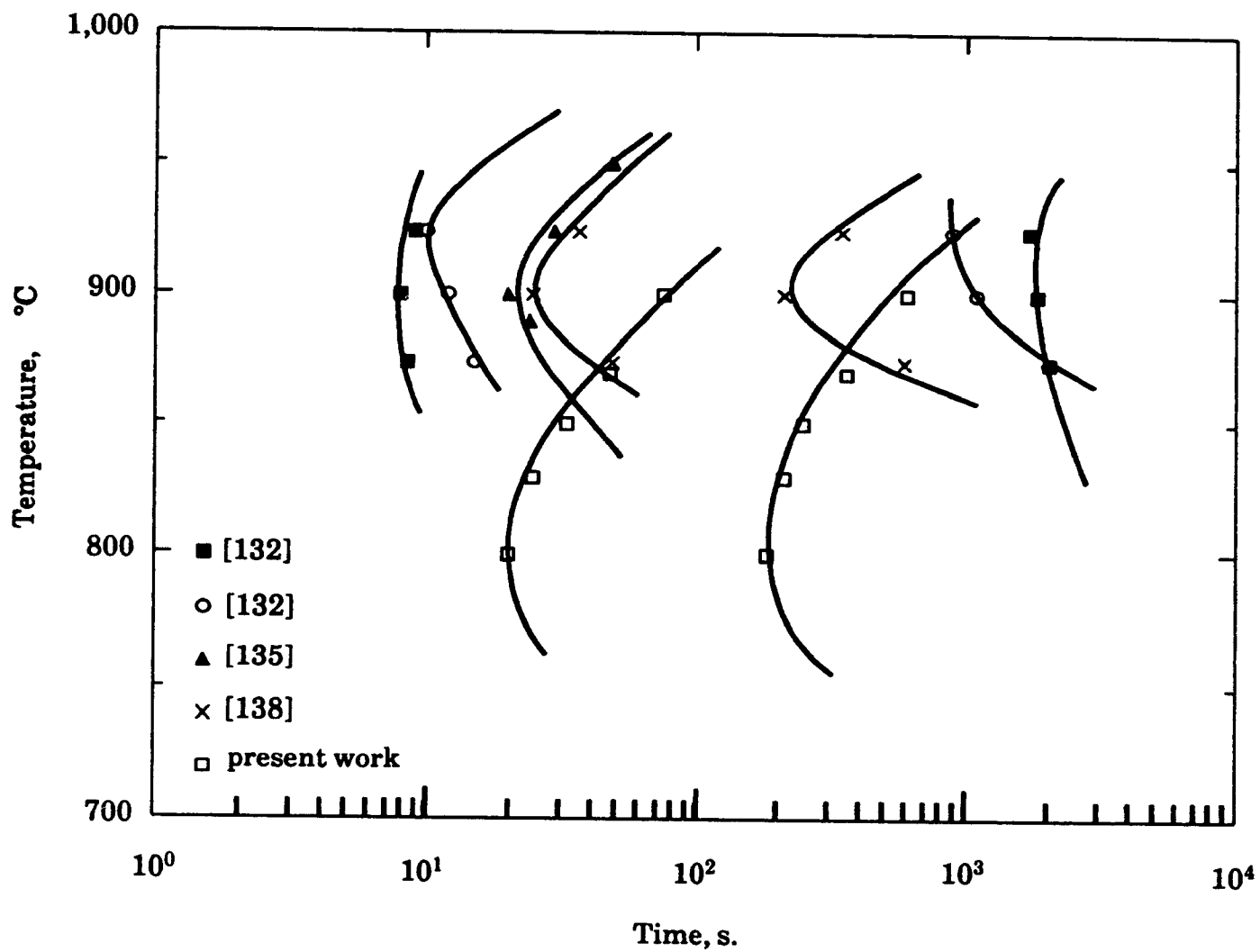


Fig.VII.12 Comparison between the PTT curves determined in this investigation and those of some other workers.

## CHAPTER VIII

### CONCLUSIONS

In the present investigation, the influence of boron distribution was studied on recrystallization and precipitation in hot worked austenite. A stress relaxation technique was employed for the first time to detect the occurrence of both recrystallization and precipitation and to study the interaction between these two processes. After austenitization at 1200 and 1100°C, the samples were cooled to the test temperature and then deformed 5 or 25% and held for different periods of time. Using this method, PTT diagrams were determined for the Nb + B and Nb steels between 800 and 1000°C. The recrystallization start times at 1000 and 950°C were obtained for these two materials by the above mechanical tests. Furthermore, the progress of recrystallization and precipitation was followed in the B steel by the PTA, SIMS and TEM techniques.

Samples were quenched after different holding times and the influence of composition, deformation and time on the boron distribution and on recrystallization and precipitation was studied by means of the TEM, SIMS and PTA techniques. In addition, the effect of different cooling rates on the boron distribution was evaluated and the results were employed to interpret the influence of boron on recrystallization. The experimental results obtained in the current research were analyzed in terms of the diffusion controlled nucleation and growth theories. Finally, based on the PTA observations, the non-equilibrium segregation of boron produced at the original and newly formed austenite grain boundaries was separated in a semi-quantitative manner. As a result of this study, the following conclusions can be drawn:

- 1) In the absence of precipitation, the stress versus log(time) curve is a straight line under all conditions of deformation and temperature. However, the occurrence of precipitation leads to the appearance of a stress plateau. Relaxation resumes after precipitation is complete.

2) The glide of jogged screw dislocations is probably the rate controlling mechanism during the early stages of stress relaxation (i.e. before  $P_s$ ). On the other hand, a model based on dislocation-particle interactions can account for the existence of the stress plateau in the stress versus  $\log(\text{time})$  curve. According to this model, the dislocations are stopped in their movement by the sequential occurrence of the following events : i) nucleation of a precipitate on a segment of a dislocation, ii) the attraction of dislocations to the particle-matrix interface as the latter is a good sink for dislocations, and iii) the locking of dislocations at the particle-matrix interface by localized climb. Such pinning is effective until the end of the precipitation process. Following this stage, Ostwald ripening starts, which influences dislocation-particle interactions in several ways: i) the dislocations pinned by the small particles are freed after the dissolution of the latter; ii) the spacing between the precipitates is increased as a result of the dissolution, decreasing the stress required for dislocation movement; iii) the coarsening transforms the particle-matrix interface from semi-coherent to completely incoherent: this leads to a lower stress field surrounding the precipitates, so less interface dislocations are required; and iv) as the mean diameter of the disappearing particles shrinks, the climb of dislocations over them becomes easier and easier.

3) The PTT diagrams determined in this investigation are of C-shape for both the Nb + B and Nb steels after 5 or 25% deformation. The presence of boron does not influence the nature of the precipitation process. By contrast, under similar testing conditions, the precipitation start time is shorter in the Nb + B steel than in the Nb grade. In addition, precipitation starts at higher temperatures in the Nb + B steel specimens.

4) TEM examination of the carbon extraction replicas of the quenched samples indicates that the plateau region in the stress relaxation curve corresponds to the occurrence of precipitation. The undissolved Ti and (Ti,Nb) rich particles are of cuboid shape, indicating that a specific orientation relationship exists between the particles and the matrix. Similar remarks apply to many of the strain induced Nb rich particles. The presence of boron in the Ti and (Ti,Nb) rich precipitates of the Nb + B steel was revealed in this investigation by means of the EELS and PTA techniques applied to the carbon extraction replicas. Consequently, the precipitates observed in the Nb + B steel

are believed to be Nb(C,N,B) and (Ti,Nb)(C,N,B). The mean diameters of the particles are similar in the two steels, but the area density of the precipitates is greater in the Nb + B steel than in the Nb grade. The observed particles were heterogeneously distributed in either a chain like or a cell like manner. This indicates that the precipitates are nucleated on dislocations or on dislocation substructures.

5) The mean diameter of the particles increases with the square root of the time, indicating that their growth is diffusion controlled. This behaviour begins to be disobeyed at around the precipitation finish time. The interpretation of the results based on the diffusion controlled growth theory indicates that nucleation is not complete at the  $P_s$  time determined by the stress relaxation method; rather, the nucleation sites are saturated some time after the beginning of precipitation. Once the nucleation process is completed, particle growth alone takes place, leading to linear growth behaviour. Finally, Ostwald ripening occurs at the end of precipitation, where the curve begins to deviate from its linear trend. The transition time from the nucleation to the growth stage is longer than the  $P_s$  time determined by the stress relaxation technique. This indicates that the appearance of the relaxation plateau depends on the number of pinned dislocations rather than on the saturation of the nucleation sites. However, the transition times from growth to coarsening are in good agreement with the  $P_f$  times shown on the stress plateaus.

6) The non-equilibrium segregation of boron is produced at austenite grain boundaries during continuous cooling. Its severity, as revealed by the PTA and SIMS techniques, increases with the difference between the solution and the quench temperatures. A boron depleted zone forms next to the segregated regions; its width (i.e. the intensity of the segregation) is sensitive to the cooling rate and quench temperature difference. The driving force for such segregation is believed to be the change in equilibrium vacancy concentration produced during cooling. The non-equilibrium segregation of boron is the result of the diffusion of B-V complexes through the boron depleted zones and their elimination at the grain boundaries. The existing models explaining the occurrence of such segregation were reviewed and it was concluded that the grain size has only a relative importance in the process of segregation.

7) The non-equilibrium segregation of boron is produced at original austenite grain boundaries after high temperature deformation. The mechanism for this type of segregation is similar to the one induced by cooling; deformation increases the concentration of vacancies and seems to increase that of the B-V complexes as well. A third type of non-equilibrium segregation occurs at the austenite grain boundaries during recrystallization. It develops quickly as a new boundary is formed and moves. As recrystallization progresses, the level of segregation increases until a concentration gradient of boron atoms is established. Subsequently, a boron back diffusion process begins; the segregation continues to develop until a steady state is reached, where the numbers of boron atoms added to a boundary during its movement are approximately equal to those leaving it. The intensity of segregation decreases when impingement takes place. The distinction between segregation at the original and newly formed boundaries was made by a semi-quantitative analysis. As a result of this study, it was found that the segregation induced by deformation is of the non-equilibrium type. On the other hand, the segregation produced at the new boundaries increases until impingement occurs because of continued sweeping.

8) After rapid cooling or deformation, a segregation peak is observed on the segregation-holding time curve. The existence of this peak is characteristic of the non-equilibrium nature of the segregation and is in agreement with the view that this phenomenon requires the formation of B-V complexes and the subsequent elimination of vacancies at grain boundaries. Furthermore, there is a clear evolution from segregation to precipitation. This transition is observed when the testing temperature is decreased or when slower cooling rates are applied to the specimens. By using appropriate cooling rates, it is possible to produce different distributions of boron atoms and to study the evolution of the microstructure during different stages of the test in this way.

9) The addition of boron to a Nb steel accelerates the precipitation of Nb(C,N) compared to that occurring in the boron free Nb containing steel. The most important role of boron seems to be its intervention in the nucleation stage of precipitation. The equilibrium and non-equilibrium segregation of boron and the presence of Nb-B complexes at the dislocations lead to higher concentrations

of the precipitating elements at these sites. In addition, the segregation of B-V complexes to dislocations not only increases the boron concentration but also supplies a flux of vacancies which is required to relieve the strain energy created by the nucleus.

10) The presence of boron in the Nb steel eliminates the partial recrystallization of austenite at 950°C after 25% deformation. This is due to the synergistic effect of Nb and boron, which retards recrystallization on the one hand and accelerates precipitation on the other. This synergistic effect can be attributed to the existence of Nb-B complexes. The formation of such constituents was proposed on the basis of their phase diagram and their favorable effect on reducing the lattice distortion energy. The presence of these complexes at dislocations and grain boundaries is believed to be responsible for the observed synergistic effect of Nb and boron on both recrystallization and precipitation in hot deformed austenite.

## STATEMENT OF ORIGINALITY AND CONTRIBUTION TO KNOWLEDGE

The present investigation led to the following original contributions:

1) Non-isothermal stress relaxation tests were employed for the first time to detect the occurrence of both recrystallization and precipitation in hot deformed austenite. In this way, it was possible to study the interaction between recrystallization and precipitation.

2) It was shown in a quantitative manner and for the first time that the presence of boron accelerates the precipitation of strain induced Nb(C,N). Under all conditions, precipitation begins after shorter times and at higher temperatures in the Nb+B than in the Nb steel. This effect is interpreted in terms of the segregation of boron and boron-vacancy complexes to nucleation sites followed by the formation of Nb-B complexes. Some role may also be played by the increase in the effective concentration of the precipitate forming interstitials.

3) A laboratory for carrying out particle tracking autoradiography was set up during the course of this investigation. The new technique employed here to prepare the samples (the double gluing method) increases the quality and resolution to a considerable extent. To the author's knowledge, no other university or research laboratory in Canada is capable, at present, of doing such experiments.

4) The PTA technique employed on carbon extraction replicas enabled the presence of boron to be demonstrated in the strain induced precipitates. This finding was confirmed by EELS analysis, which showed that the precipitates contained boron.

5) The non-equilibrium segregation of boron produced by deformation was revealed in this study by means of the PTA and SIMS techniques. The boron-vacancy interaction plays the same role here as in the case of continuous cooling. The mechanism proposed to account for the effect of deformation is

somewhat similar to that suggested to explain the effect of cooling on boron segregation. Deformation increases the vacancy concentration significantly, leading to a vacancy flux to grain boundaries, which deposits boron there through B-V complex formation in the grain interiors, followed by complex disintegration at the boundaries.

7) A new type of non-equilibrium segregation found in this investigation is that produced at newly formed austenite grain boundaries during recrystallization. In the suggested model, the segregation of boron is first produced at dislocations. The annihilation of dislocations at the moving boundaries leads to the deposition of the boron atoms and consequently to an increase in boron concentration at the boundaries. The intensity of the segregation decreases by back diffusion when the movement of the new boundaries is stopped.

8) In an original semi-quantitative analysis, the segregation produced at prior and at newly formed austenite grain boundaries was distinguished for the first time. In this way, it was shown that, during isothermal holding, the totality of the grain boundaries cannot attain a degree of segregation high enough to be revealed by PTA as continuous etch pits. Also, it was demonstrated that the severity of segregation on the new boundaries increases continuously from nucleation until impingement. By contrast, the segregation level on the original boundaries increases to a maximum and then drops monotonically.

9) It was revealed that the simultaneous presence of Nb and boron not only has an accelerating effect on precipitation but also retards recrystallization to a noticeable extent. Such synergism was found to be responsible for the elimination of partial recrystallization at 950°C in the Nb+B steel. A model based on the existence of Nb-B complexes was proposed to explain these effects.

10) The greater retardation of recrystallization, when Nb and boron are present simultaneously, was interpreted in terms of the solute drag theory. Also, on the basis of a physical model, it was concluded that Nb-B complexes have higher diffusivities than Nb atoms alone. The addition of these two effects leads to larger delays in austenite recrystallization. Regarding the synergistic

effect of Nb and boron on precipitation, it was suggested that the presence of Nb-B complexes at nucleation sites increases the concentration product of the precipitating elements, leading to easier nucleation.

11) The stress relaxation data were analyzed in terms of the theory of the thermally activated motion of dislocations. The pinning and unpinning effects of particles on dislocations were clarified in terms of a physical model in which precipitates are nucleated on mobile dislocations and are liberated later once precipitation is complete.

12) An analysis was performed on the basis of the theory of diffusion controlled nucleation. The predictions of precipitation start time made with this analysis are in good agreement with the present experimental results. The interaction energy between a precipitate nucleus and a dislocation, calculated in this investigation, was found to be consistent with those determined by other workers.

## REFERENCES

1. P.D. Deeley and K.J.A. Kundig, Shieldalloy Corporation, Newfield, New Jersey (1982).
2. R. Walter, British Patent 160, 792 (1921); U.S. Patent 1, 519, 388, Aug. 13 (1921).
3. M.A. Grossman, Trans. AIME, 150, p. 227 (1942).
4. G.F. Comstock, Trans. AIME, 150, p. 408 (1942).
5. R.A. Grange, "Boron in Iron and Steel", Boron, Calcium, Columbium and Zirconium in Iron and Steel Alloys of Iron, Research Monograph Series, John Wiley and Sons, Inc., N. Y., N. Y. p. 3 (1957).
6. G.D. Rahrer and C.D. Armstrong, Trans. ASM, 40, p. 1099 (1948).
7. B.M. Kapadia, R.M. Brown and W.J. Murphy, Trans. AIME, 242, p. 1689 (1968).
8. C.R. Simcoe, A.R. Elsea and G.K. Manning, Trans. AIME, 203, p. 193 (1955).
9. L.F. Porter, "Boron in Steel", Proc. Int. Symp. on Boron Steels, eds. S.K. Banerji and J.E. Morral, TMS/AIME, p. 199 (1980).
10. H. Nakasugui, H. Matsuda and H. Tamehiro, "Alloys for the Eighties", Proc. Int. Symp. on HSLA Steels, ed. R.Q. Barr, Climax Molybdenum Company, p. 213 (1980).
11. B. Serin, Y. Desalos, Ph. Maitrepierre and J. Rofes-Vernis, Mém. Sci. Rev. Mét. 75, p. 355 (1978).
12. K.-E. Thelning, "Boron in Steel", Proc. Int. Symp. on Boron Steels, eds. S.K. Banerji and J.E. Morral, TMS/AIME, p. 127 (1980).
13. K. Matsumoto, T. Taira, K. Ume, T. Hyodo, K. Tshhada and K. Arikata, Trans. ISIJ, 24, B92 (1984).
14. H. Tamehiro, M. Murata, R. Habu and M. Nagumo, Trans. ISIJ, 27, p. 120 (1987).
15. C.E. Birchenall, "Volume Diffusion- An Empirical Survey of Atom Movements", ASM, p. 112 (1951).
16. A. Brown, J.D. Garnish and R.W.K. Honeycombe, Met. Sci., 8, p. 317, (1974).
17. M. Deighton, J. Iron Steel Inst., 205, p. 355 (1967).

18. A. Brownrigg and G.G. Brown, *The Journal of the Australian Inst. of Metals*, 17, p. 192 (1972).
19. A.K. Shevelov, *Sov. Phys. Doklady*, 1, p. 453 (1958).
20. P.E. Busby, M.E. Warga and C. Wells, *Trans. AIME*, 197, p. 1463 (1953).
21. P.M. Strocchi, B.A. Melandri and A. Tamba, *Nuovo Cim.*, 51B, p. 1 (1967).
22. R.R. Hasiguti and G. Kamoshita, *J. Phys. Soc. Japan*, 9, p. 646 (1954).
23. Y. Hayashi and T. Sugeno, *Acta Metall.*, 18, p. 693 (1970).
24. M.E. Nicholson, *Trans. AIME*, 200, p. 185 (1954).
25. R.M. Goldhoff and J.W. Spretnak, *Trans. AIME*, 209, p. 1278 (1957).
26. A.K. Shevelov, *Sov. Phys. Doklady*, 3, p. 1254 (1958).
27. H.J. Goldschmidt, *J. Iron Steel Inst.*, 209, p. 900 (1971).
28. D. McLean, "Grain Boundaries in Metals", Oxford University Press (1957).
29. J.H. Westbrook, *Int. Metall. Rev.* 9, p. 415 (1964).
30. M. Djahazi, X.L. He, J.J. Jonas and G.E. Ruddle, "Processing, Microstructure and Properties of HSLA Steels", *Proc. Int. Conf. on HSLA Steels*, ed. A.J. DeArdo, ASM, p. 69 (1987).
31. S.R. Keown, *Scand. J. Metall.*, 2, p. 59 (1973).
32. M. Djahazi, X.L. He and J.J. Jonas, "THERMEC 88", *Proc. Int. Conf. on Phys. Metall. and Thermomechanical processing of Steels and Other Metals*, Iron and Steel Inst. of Japan, p. 246 (1988).
33. X. He, Y. Chu and T. Ko, *Acta Metall. Sin.*, 18, p. 11 (1982).
34. Ph. Maitrepierre, D. Thivellier and R. Tricot, *Metall. Trans.* 6A, p. 287 (1975).
35. L. Karlsson, H. Nordén and H. Odelius, *Acta Metall.*, 36, p. 1 (1988).
36. L. Karlsson and H. Nordén, *Acta Metall.*, 36, p. 13 (1988).
37. A.D. Marwick and R.C. Piller, *Radiat. Effects*, 33, p. 245 (1977).
38. G.C. Kuczynski, G. Matsumura and B.D. Cullity, *Acta Metall.*, 8, p. 209 (1960).
39. K.T. Aust, S.J. Armijo, E.F. Koch and J.A. Westbrook, *Trans. Amer. Soc. Metals.*, 60, p. 360 (1967).

40. T.R. Anthony, *Acta Metall.*, 17, p. 603 (1969).
41. S.J. Bercovici, C.E.L. Hunt and P. Niessen, *J. Mat. Sci.* 5, p. 326 (1970).
42. T.M. Williams, A.M. Stoneham and D.R. Harries, *Met. Sci.*, 1, p. 14 (1976).
43. X. He, Y. Youyi and J. Ke, *Acta Metall. Sin.*, 19, p. A459 (1983).
44. B.J. Thomas and G. Henry, "Boron in Steel", *Proc. Int. Symp. on Boron Steels*, eds. S.K. Banerji and J.E. Morral, TMS/AIME, p. 80 (1980).
45. Y. Chu and X. He, *Proc. Int. Conf. on HSLA Steels*, eds. D.P. Dunne and T. Chandra, ASM, p. 327 (1984).
46. X. He and Y. Chu, *J. Phys. D:Appl. Phys.*, 16, p.1145 (1983).
47. R.G. Faulkner, *J. Mater. Sci.*, 16, p.373 (1981).
48. M.A.V. Chapman and R.G. Faulkner, *Acta Metall.*, 31, p. 677 (1983).
49. L. Karlsson, *Acta Metall.*, 36, p. 25 (1988).
50. A. Taylor and B.J. Kagle, "Crystallographic Data on Metal and Alloy Structures", N.Y. Dover (1963).
51. H.J. Goldschmidt, "Interstitial Alloys", Butterworths & Co. Ltd., London (1967).
52. K.G. Carrol, *Nature*, 174, p. 978 (1954).
53. S. Watanabe, H. Ohtani and T. Kunitake, *Trans. ISIJ*, 23, p. 31 (1983).
54. J.R. Donati, D. Laurent and G. Zacharie, *Mém. Sci. Rev. Mét.*, 7, p. 355 (1978).
55. P. Rogl, J.C. Schuster and H. Nowotny, "Boron in Steel", *Proc. Int. Symp. on Boron Steels*, eds. S.K. Banerji and J.E. Morral, TMS/AIME, p. 33 (1980).
56. S.R. Keown and F.B. Pickering, *Met. Sci.*, 7, p. 225 (1977).
57. G. Henry, B. Thomas and R. Tixier, *Proc. 3rd Int. Conf. on Strength of Alloys*, Institute of Metals, London, p. 568 (1973).
58. Ph. Maitrepierre, J. Rofes-Vernis and D. Thivellier, "Boron in Steel", *Proc. Int. Symp. on Boron Steels*, eds. S.K. Banerji and J.E. Morral, TMS/AIME, p. 1 (1980).
59. G. Henry, Ph. Maitrepierre, B. Michaut and B. Thomas, *Journal de Physique c*, 36, p. 245 (1975).
60. J. Davidson, P. Balladon, Y. Honnorat and X. Waché, *Mém. Sci. Rev. Mét.*, 70, p. 543 (1973).

61. M. Aldén, S. Asplund and B. Aronsson, *J. Iron Steel Inst.*, 2, p. 235 (1969).
62. G. Henry and J. Philibert, *Mém. Sci. Rev. Mét.*, 67, p. 233 (1970).
63. T.M. Williams and M.G. Talks, *J. Iron Steel Inst.*, 210, p. 870 (1972).
64. J. Bourgeot, G. Henry, B. Michaut and B. Thomas, IRSID Report RE 334 (1975).
65. M. Djahazi, X.L. He and J.J. Jonas, 29th Mech. Working and Steel Processing Conf., Toronto, TMS/AIME, p. 403 (1987).
66. D.R. Harries and A.C. Roberts, A.S.T.M. Special Technical Publication 426, p. 21 (1967).
67. Ph. Maitrepierre, D. Thivellier, J. Rofes-Vernis, D. Rousseau and R. Tricot, "Hardenability Concepts with Applications to Steel", ed. D. Doane and J.S. Kirkaldy, AIME, p. 421 (1978).
68. B.M. Kapadia, *ibid.*, 448.
69. J.C. Fisher, *Trans. AIME*, 200, p.1146 (1954).
70. R.C. Sharma and G.R. Purdy, *Metall. Trans.* 4A, p. 2303 (1973).
71. J.E. Morral and T.B. Cameron, *Metall. Trans.* 8A, p. 1817 (1977).
72. V.V. Levitin, *Phys. Metals and Metallography*, 10, p. 130 (1960).
73. G.D. Brauch, A. Wickens and D.W.C. Baker, *Archiv Eisenhüttenwesen*, 43, p. 833 (1972).
74. G. Henry, A. Mercier, J. Plateau and J. Hochmann, *Rev. Mét.*, 60, p. 1221 (1963).
75. T.M. Williams, *Met. Sci.*, 6, p. 68 (1972).
76. Y.E. Gol'dshtein and A.L. Sarikova, *Metal Science and Heat Treatment*, Nos. 5-6, p. 250, May-June (1963).
77. A.T. Perlus, J.T. Griffiths and M. Coburn, U.S. Patent 4, 168, 181, Sept. 18 (1979).
78. A.G. Fuller and W.R. Middleton, *BCIRA Journal*, p. 167, March (1976).
79. W.F. Simmons, ASTM Data Series Publication No. DS9E.
80. D. Nathasingh and C.H. Smith, *Proc. Powercon 7*, San Diego, March 25-27 (1980).
81. K. Kawamura, T. Otsubo and T. Furukawa, *Trans. ISIJ*, 15, p. 538 (1976).

82. "Interfacial Segregation", eds. W.C. Johnson and J.M. Blakely, ASM (1979).
83. M.K. Miller, P.A. Beaven, R.J. Lewis and G.D.W. Smith, Surf. Sci., 70, p. 470 (1978).
84. A.P. Coldren, A. Joshi and D.F. Stein, Metall. Trans., 6A, p. 2304 (1975).
85. J.H. Thomas and J.M. Morabito, Surf. Sci., 41, p. 629 (1974).
86. G. Friedlander, J.W. Kennedy and J.M. Miller, Nuclear and Radiochemistry, 2nd ed., J. Wiley & Sons, Inc., N.Y., N.Y., p.53 (1964).
87. A.E. Barrington, R.F.D. Herzog and W.P. Poschenrieder, J. Vac. Sci. Technol., 3, p.239 (1966).
88. Y. Ohmori and K. Yamanaka, "Boron in Steel", Proc. Int. Symp. on Boron Steels, eds. S.K. Banerji and J.E. Morral, TMS/AIME, p. 44 (1980).
89. M. Hillert, Nature, 168, p. 39 (1951).
90. B.B. Thompson, Trans. AIME, 218, p. 228 (1960).
91. J.D.H. Hughes and G.T. Rogers, J. Inst. Met., 95, p. 299 (1967).
92. T.B. Cameron and J.E. Morral, "Boron in Steel", Proc. Int. Symp. on Boron Steels, eds. S.K. Banerji and J.E. Morral, TMS/AIME, p. 61 (1980).
93. J.D. Garnish and J.D.H. Hughes, J. Mat. Sci., 7, p. 7 (1972).
94. A. Joshi, in "Interfacial Segregation", eds. W.C. Johnson and J.M. Blakely, ASM, p.39 (1979).
95. E.D. Hondros and M.P. Seah, Internat. Met. Rev., 12, p. 262 (1977).
96. L.E. Toth, "Transition Metal Carbides and Nitrides", Academic Press, New York and London (1971).
97. R.C. Sharma, V.K. Lakshmanan and J.S. Kirkaldy, Metall. Trans., 15A, p.545 (1984).
98. N. Shams, J. Met., 5, p. 31, May (1986).
99. T. Shiraiwa, N. Fujino and J. Murayama, Trans. ISIJ, 10, p.406 (1970).
100. S. Suzuki, G.C. Weatherly and D.C. Houghton, Acta Metall., 35, p. 341 (1987).
101. W.J. Liu, Ph. D. Thesis, McGill University, Montreal (1987).
102. B. Loberg, R. Nordgren, J. Strid and K.E. Easterling, Metall. Trans., 15A, p. 33 (1984).

103. M.J. Crooks, A.J. Garrett-Reed, J.B. Vander Sand and W.S. Owen, *Metall. Trans.*, 12A, p. 1999 (1981).
104. A. Güth, L.Kaun, A. Kothe, D. Müller and J. Richter, *Scr. Metall.*, 21, p. 163 (1987).
105. T. Mori, M. Tokizane, Y. Nakazima and T. Suzuki, *Tetsu-to-Hagane*, 51, p. 2031 (1965).
106. H. Ohtani, T. Tanaka, M. Hasebe and T. Nishizawa, *Japan-Canada Seminar*, p. J-7, December (1985).
107. K. Narita, *J. Chem. Soc. Japan*, 77, p. 1536 (1956).
108. S. Koyoma, *Japan Inst. of Metals J.*, 35, p. 1090 (1972).
109. T. Sharaiwa, N. Fujino and J. Murayama, *Trans. ISIJ*, 10, p. 406 (1970).
110. K. Balasubramanian and J.S. Kirkaldy, *CALPHAD*, 10 No 2, p. 187 (1986).
111. F.H. Froes and D.H. Warrington, *Trans. AIME*, 245, p. 2009 (1969).
112. A.T. Davenport, R.E. Miner and R.A. Kot, "The Hot Deformation of Austenite", ed. J.B. Ballance, *AIME*, New York, N.Y., p. 186 (1977).
113. D.M. Haddad, R.N. Younge and R.G. Backer, *Acta Metall.*, 9, p. 982 (1961).
114. R.D. Naybour, *Acta Metall.*, 13, p. 1197 (1965).
115. J.M. Silcock, *J. Iron Steel Inst.*, 211, p. 792 (1973).
116. M.C. Chaturvedi, R.W.K. Honeycombe and D.H. Warrington, *J. Iron Steel Inst.*, 206, p. 1147 (1968).
117. G. Fitzsimons, K. Tiito, R. Fix and A.J. DeArdo, *Metall. Trans.*, 15A, p.241 (1983).
118. I. Weiss and J.J. Jonas, *Metall. Trans.*, 11A, p. 403 (1980).
119. J.M. Silcock and W.J. Tunstall, *Phil. Mag.*, 10, p. 361 (1964).
120. E. Nes, *Acta Metall.*, 22, p. 81 (1974).
121. W. Kesternich, *Phil. Mag.*, 52, p. 533 (1985).
122. J.S.T. Van Aswegen, R.W.K. Honeycombe and D.H. Warrington, *Acta Metall.*, 12, p. 1 (1964).
123. F.B. Pickering, "Symposium on Relation Between Structure and Mechanical Properties of Metals, NPL, p. 397 (1963).

124. F.H. Froes, Ph. D. Thesis, University of Sheffield (1967).
125. H. Hatwell and A. Berghezan, ISI Special Report, 64, p. 88 (1959).
126. M.K. Lewis and B. Hattersley, *Acta Metall.*, 13, p. 1159 (1965).
127. F.R. Beckitt and B.R. Clark, *Acta Metall.*, 15, p. 113 (1967).
128. L.K. Singhal and J.W. Martin, *Acta Metall.*, 16, p. 1169 (1968).
129. A.R. Jones, P.R. Howell and B. Ralph, *J. Mater. Sci.*, 11, p. 1593 (1976).
130. D.V. Edmonds and R.W.K. Honeycombe, "Precipitation Processes in Solids", eds. K.C. Russell and H.I. Aaronson, AIME, p.121 (1978).
131. T.M. Hoogendoorn and M.H. Spanraft, "Microalloying 75", ed. M.Korchynsky, Union Carbide Corp., New York, p. 75 (1977).
132. H. Watanabe, Y.E. Smith and R.D. Pehlke, "The Hot Deformation of Austenite", ed. J.B. Ballance, AIME, New York, N.Y., p. 140 (1977).
133. J. Bradford, *J. Iron Steel Inst.*, 204, p. 134 (1966).
134. S.J. Harris and N.R. Nag, *J. Mater. Sci.*, 11, p. 1320 (1976).
135. I. Weiss and J.J. Jonas, *Metall. Trans.*, 10A, p.831 (1979).
136. J.J. Jonas and I. Weiss, *Met. Sci.*, 3, p. 238 (1979).
137. S. Koyama, T. Ishii and K. Narita, *Jap. Inst. of Metal. J.*, 35, p. 698 (1971).
138. M.G. Akben and J.J. Jonas, *Acta Metall.*, 29, p. 111 (1981).
139. S.S. Hansen, J.B. Vander Sand and M. Cohen, *Metall. Trans.*, 11A, p.387 (1980).
140. A.LeBon, J. Rofes-Vernis and C. Rossard, *Mem. Sci. Rev. Met.*, 11A, p. 411 (1975).
141. S.Yamamoto, C. Ouchi and T. Osuka, "Thermomechanical Processing of Microalloyed Austenite", eds. A.J. DeArdo, G.A. Ratz and P.J. Wray, AIME, Warrendale, Pa., U.S.A., p. 613 (1982).
142. B. Dutta and C.M. Sellars, *Mater. Sci. Technol.*, 3, p. 197 (1987).
143. M.J. Luton, Ph.D. Thesis, McGill University, Montreal (1971).
144. R.A. Petkovic, Ph.D Thesis, McGill University, Montreal (1975).
145. G.S. Ansell and J. Weertman, *Trans. AIME*, 215, p. 835 (1959).

146. Ph. Maitrepierre, J. Rofes-Vernis, D. Thivellier and R. Tricot, "Heat Treatment 76", Conf. Proc., Stratford Upon Avon, G.B., May (1976).
147. K.J. Irvine, F.B. Pickering and T. Gladman, *J. Iron Steel Inst.*, 205, p. 171 (1967).
148. S.U.V. Idemark and E.R. Johansson, "Stress Relaxation Testing", ed. A. Fox, ASTM, Philadelphia, Pa. p. 61 (1979).
149. E.A. Davis, *J. Appl. Mech.*, 10, p. 101 (1943).
150. P.J. Wray and G.T. Horn, *Phil. Mag.*, 13, p. 899 (1966).
151. G.E. Melloy, P.R. Slimmon and P.P. Podgursky, *Metall. Trans.*, 4A, p.2279 (1973).
152. T. Malis, Private Communication, CANMET, Ottawa (1989).
153. M.F. Ashby and R. Ebeling, *Trans. AIME*, 236, p. 1396 (1966).
154. C. Herring, *J. Appl. Phys.*, 21, p. 437 (1950).
155. J.E. Dorn, "Energetics in Metallurgical Phenomena", 1, ed. W.M. Mueller, Gordon & Breach Science Publishers, p. 241 (1965).
156. T.G. Langdon, "Dislocations and Properties of Real Materials", Proc. Conf. to Celebrate the 50th Anniversary of the Concept of Dislocations in Crystals, The Institute of Metals, p. 221 (1984).
157. N.F. Mott, *Phil. Mag.*, 43, p. 1151 (1952).
158. J. Weertman, *J. Appl. Phys.*, 26, p. 1213 (1955).
159. A. Seeger, "Defects in Crystalline Solids", Conf. Proc., The Phys. Soc. London, p. 391 (1954).
160. A. Seeger, *Phil. Mag.*, 46, p. 1194 (1955).
161. P.B. Hirsch and D.H. Warrington, *Phil. Mag.*, 6, p. 735 (1961).
162. E. Orowan, *Proc. Roy. Soc. London*, 8, p. 52 (1940).
163. N.K. Chen and R.B. Pond, *J. Met.*, 4, p. 1085 (1952).
164. G.B. Gibbs, *Phil. Mag.*, 23, p. 317 (1966).
165. J.C.M. Li, "Dislocation Dynamics", McGraw-Hill, N.Y., p.87 (1968).
166. G.B. Gibbs, *Mater. Sci. Eng.*, 4, p. 313 (1969).
167. A. Seeger, "Dislocations and the Mechanical Properties of Materials", ed. J. Wiley&Sons, p. 234 (1956).

168. F.J. Humphreys, "Dislocations and Properties of Real Materials", Proc. Conf. to Celebrate the 50th Anniversary of the Concept of Dislocations in Crystals, The Institute of Metals, p. 175 (1984).
169. J.W. Martin, "Micromechanisms in Particle Hardened Alloys", Cambridge University Press (1980).
170. D.M. Barnett, *Scr. Metall.*, 5, p. 261 (1971).
171. G. Knowles and P.M. Kelly, Proc. ISI/BISRA Conf. at Scarborough, ISI, London (1971).
172. "Deformation-Mechanism Maps", ed. H.J. Frost and M.F. Ashby, Pergamon Press (1982).
173. R.O. Elliot and C.P. Kempter, *J. Phys. Chemistry*, 62, p. 630 (1958).
174. D.J. Srolovitz, R. Petkovic-Luton and M.J. Luton, *Acta Metall.*, 31, p. 2151 (1983).
175. D.J. Srolovitz, M.J. Luton, R. Petkovic-Luton, D.M. Barnett and W.D. Nix, *Acta Metall.*, 32, p. 1079 (1984).
176. R.S.W. Shewfelt and L.M. Brown, *Phil. Mag.*, 35, p. 845 (1977).
177. J.H. Hausselt and W.D. Nix, *Acta Metall.*, 25, p. 1491 (1977).
178. M.G. Akben, Ph. D. Thesis, McGill University, Montreal (1981).
179. R.W. Lund and W.D. Nix, *Scr. Metall.*, 10, p. 1007 (1976).
180. J.W. Cahn, *Acta Metall.*, 5, p. 169 (1957).
181. K.C. Russell, *Advances in Colloid and Interface Science*, 13, p. 205 (1980).
182. S. Kurokawa, J.E. Ruzzante, A.M. Hey and F. Dymont, *Met. Sci.*, 17, p. 433 (1983).
183. W.J. Liu and J.J. Jonas, *Metall. Trans.*, 20A, p. 689 (1989).
184. C. Zener, *J. Appl. Phys.*, 20, p. 950 (1949).
185. N.K. Balliger and R.W.K. Honeycombe, *Met. Sci.*, 14, p. 121 (1980).
186. T. Chandra, I. Weiss and J.J. Jonas, *Can. Metall. Quarterly*, 20, p. 421 (1981).
187. J. Strid and K.E. Easterling, *Acta Metall.*, 33, p. 2057 (1985).
188. I.M. Lifshitz and V.V. Slyozov, *J. Physics Chem. Solids*, 19, p. 35 (1961).
189. C. Wagner, *Z. Electrochemie*, 65, p. 581 (1961).

190. A.J. Ardell, *Acta Metall.*, 20, p. 601 (1972).
191. L.T. Mavropoulos and J.J. Jonas, *Can. Metall. Quarterly*, 28, p. 159 (1989).
192. J.J. Jonas and M.G. Akben, *Metals Forum*, 4, p. 92 (1981).
193. M.G. Akben, I. Weiss and J.J. Jonas, *Acta Metall.*, 29, p. 111 (1981).
194. M.G. Akben, B. Bacroix and J.J. Jonas, *Acta Metall.*, 31, p. 161 (1983).
195. M.J. White and W.S. Owen, *Metall. Trans.*, 11A, p. 597 (1980).
196. J.W. Cahn, *Acta Metall.*, 10, p. 789 (1962).
197. M. Hillert and B. Sundman, *Acta Metall.*, 24, p. 731 (1976).
198. C. Herzig, P. Neuhaus and J. Geise, "Solute-Defect Interaction Theory and Experiment", ed. S. Saimoto, G. Purdy and G. Kidson, Pergamon Press, p. 271 (1985).
199. G.J. Sojka, M.R. Krishnadev and S.K. Banerji, "Boron in Steel", *Proc. Int. Symp. on Boron Steels*, eds. S.K. Banerji and J.E. Morral, TMS/AIME, p. 165 (1980).
200. P. Doig and P.E.J. Flewitt, *Acta Metall.*, 29, p. 1831 (1981).
201. X.L. He, Y.Y. Chu and J.J. Jonas, *Acta Metall.*, 37, p. 147 (1989).
202. K.T. Aust, R.E. Hanneman, P. Niessen and J.H. Westbrook, *Acta Metall.*, 16, p. 291 (1968).
203. X.L. He, M. Djahazi and J.J. Jonas, Submitted to *Acta Metall.*
204. R.E. Smallman, "Modern Physical Metallurgy", 4th edn, Butterworths & Co. Ltd. London (1985).
205. J.H. Holbrook and W.D. Nix, *Metall. Trans.*, 5, p. 1033 (1974).
206. D. Turnbull, "Impurities and Imperfections", ASM, Cleveland, p. 121 (1955).
207. H. Brooks, "Metal Interfaces", ASM, Cleveland, (1952).
208. J.H. Van der Merwe, *J. Appl. Phys.*, 34, p. 117 (1963).
209. J.D. Eshelby, *Proc. Roy. Soc.*, A241, p. 376 (1957).
210. B.Sparke, D.W. James and G.M. Leak, *J. Iron Steel Inst.*, 203, p. 152 (1965).

**APPENDIX 1**

**LISTING OF THE COMPUTER PROGRAM FOR STRESS  
RELAXATION TESTING**

SET

MTS BASIC U01B-020

```
100 DIM A(150),B(150),B0(1000),B1(1000)
110 DIM X(101),H(18),X1(1000),X2(1000)
120 L$(0)="SAMPLE #"
130 L$(1)="AUST. TEMP."
140 L$(2)="TEST TEMP."
150 L$(3)="TRUE STRAIN"
160 L$(4)="TRUE STRAIN RATE (1/SEC)"
170 L$(5)="STROKE RANGE (MM)"
180 L$(6)="LOAD RANGE (KG)"
190 L$(7)="SPECIMEN HEIGHT (MM)"
200 L$(8)="SPECIMEN DIAM. (MM)"
205 L$(9)="RELAX TIME"
210 L$(10)="LCM #"
290 PRINT \PRINT L$(0);\INPUT N$
310 PRINT "DAY/MON./YEAR:";\INPUT H(17),H(11),H(12)\PRINT
320 PRINT "COM. OF C,NB,BORON,TI";\INPUT H(13),H(14),H(15),H(16)\PRINT
330 FOR I=1 TO 10
340 PRINT L$(I);\INPUT H(I)
350 PRINT \NEXT I
352 PRINT "HOW MANY PARTS TO FIT L-C";\INPUT N1
354 FOR I=1 TO N1
356 PRINT "STAR T, K, & N OF "I"-TH PART";
362 INPUT S0(I),S1(I),S2(I)\NEXT I
369 PRINT "L0=";\INPUT L0
400 T=H(3)/H(4)\A0=PI*H(8)^2/4
410 FOR I=0 TO 7
420 A4=I\I1=I*I+1
430 IF I<=3 THEN 440\I1=((I-4)^2+1)*10
440 R=INT(100/I1+.5)
450 N=INT(T*R)\IF N<100 THEN 460\N=100
460 Y(1)=2047/T*N/R
```

```

470 IF X(1)>50 THEN 530
480 NEXT I
490 PRINT "X(1)="X(1)", OK", \INPUT C$
500 IF H$="YES" THEN 530\STOP
530 MSW(2)
540 GOSUB 1050
555 D1=L0*(1-EXP(-S1(1)*S0(1)^S2(1)))
560 FOR I=2 TO N+1
580 H1=H(3)*(I-1)/N
600 X(I)=2047/H(5)*H(7)*(EXP(-H1)-1)
610 NEXT I
610 T0=S0(1)+T\FOR I=N+2 TO 101
615 T0=T0+T/N\D0=L0*(1-EXP(-S1(1)*T0^S2(1)))-D1
616 X(I)=X(N+1)-D0*204.7-.5
618 NEXT I
630 FOR I=1 TO 1000
641 T0=T0+100/1000
642 FOR J=1 TO N1-1
643 IF T0<S0(J+1) THEN 649
645 NEXT J
646 J=J+1
649 D0=L0*(1-EXP(-S1(J)*T0^S2(J)))-D1
650 X1(I)=X(N+1)-D0*204.7-.5
660 NEXT I
661 FOR I=1 TO 1000
662 T0=T0+(H(9)-100)/1000
663 FOR J=1 TO N1-1
664 IF T0<S0(J+1) THEN 668
666 NEXT J
667 J=J+1
668 D0=L0*(1-EXP(-S1(J)*T0^S2(J)))-D1
669 X2(I)=X(N+1)-D0*204.7-.5
670 NEXT I
672 X=101
674 U=100000/150*T/N

```

```

690 PRINT "CHECK DC ERR=0 --> R/L AT R --> SPAN 1 =0 --> STROKE CONTROL"
740 INPUT C$
780 EDMP
790 SDMP(1,A)\IF A=0 THEN 820
800 PRINT "DUMP CARD PROBLEM."
810 STOP
820 FG1(0)
830 PRINT "TURN ON HYDRAULICS --> SET 'SPAN 1' TO 10 --> ZERO LOAD"
860 INPUT C$
870 DACQ(0,Q1,0,0)
880 IF ABS(Q1)*5 THEN 930\GO TO 830
930 QUIT\GOSUB 2550
950 PRINT "PISTON AT"S/2047*HK5)"MM"
970 PRINT " TO POSITION AFTER A CERTAIN TIME";
980 INPUT C$\S0=S
990 FOR I=1 TO 500
1000 I2=S0-I
1010 FG1(I2)
1020 GOSUB 2550
1030 IF Q<=-15000/HK6) THEN 1060
1040 NEXT I
1050 PRINT "CHECK SAMPLE"\STOP
1060 PRINT "RETURN AS START COOLING DOWN";\INPUT C$
1065 T0=0
1070 GOSUB 2550
1080 IF Q<-1000/HK6) THEN 1090\GO TO 1100
1090 IF Q>-10000/HK6) THEN 1120\GO TO 1110
1100 I2=I2-1\GO TO 1130
1110 I2=I2+1\GO TO 1130
1120 I2=I2+0\GO TO 1130
1130 FG1(I2)
1140 T0=T0+.169\IF T0<S0(1) THEN 1070
1150 FOR I=2 TO 101\X(I)=X(I)+I2\NEXT I
1160 FOR I=1 TO 1000\X1(I)=X1(I)+I2\X2(I)=X2(I)+I2\NEXT I
1240 PRINT "***** TEST IS RUNNING *****"

```

```

1242 DACQ(3,8,0,0)~DACQ(5,A,2,2)
1244 FG1(X,1,7,A4)
1245 STAR
1246 BUF1(24)
1250 IF C4>=1 THEN 1248
1251 QUIT
1252 FOR I=1 TO 1000
1253 FOR J=1 TO 26
1254 L=3*J+1
1255 NEXT J
1256 Q2=X1(I)
1259 DACQ(0,Q2,0,0)~DACQ(0,S2,2,0)
1260 FG1(C2)
1262 X1(I)=S2~B0(I)=Q2
1265 NEXT I
1266 PRINT "2ND REGION TERMINATED"
1267 FOR I=1 TO 800
1268 FOR J=1 TO 350
1269 L=2*J+1
1270 NEXT J
1271 Q3=X2(I)
1274 DACQ(0,Q3,0,0)~DACQ(0,S3,2,0)
1275 FG1(C3)
1277 X2(I)=S3~B1(I)=Q3
1278 NEXT I
1279 PRINT "PART 1 OF 3RD REGION TERMINATED"
1280 FOR I=801 TO 1000
1281 FOR J=1 TO 900
1282 L=2*J+1
1283 NEXT J
1284 Q4=X2(I)
1287 DACQ(0,Q4,0,0)~DACQ(0,S4,2,0)
1288 FG1(C4)
1290 X2(I)=S4~B1(I)=Q4
1291 NEXT I

```

```

1370 GOTO 1370 A
1380 ***** TEST TERMINATED" \PRINT
1390 H=10000
1400 FOR I=1 TO H:18 (X(I)=A(I))-S \NEXT I
1410 FOR I=1 TO 1000: X(I)=X(I)-S \NEXT I
1420 PRINT "SAME DATA" \INPUT C$
1430 IF C$="YES" THEN 1800
1440 GOSUB 2020
1450 STOP
1460 ENTR(3)
1470 PRINT "STRESS RELAXATION TEST" \PRINT
1480 PRINT L$(0);N$
1490 PRINT "C-"H(13); "NB-"H(14); "BORON-"H(15); "TI-"H(16)
1500 PRINT "DAT /MON./YEAR: "H(17)"/"H(11)"/"H(12)
1510 PRINT
1520 FOR I=1 TO 10
1530 PRINT L$(I)" IS";H(I)
1540 PRINT \NEXT I
1550 FOR I=1 TO N1
1560 PRINT "STAR TIM. K. N OF" I"-TH PART" S0(I);S1(I);S2(I)
1570 NEXT I
1580 PRINT "L0=":L0
1590 PRINT \PRINT "X(1)="X(1); "LEVELS="N; "RANGE="R; "MOD #="A4
1600 RETURN
2020 X=36
2030 FOR I=1 TO 18
2040 X(I)=H(I); X(I+18)=0
2050 X1=X(I)-INT(X(I))+1.00000E-05)
2060 IF X1=0 THEN 2090
2070 X(I)=X(I)*10
2080 X(I+18)=X(I+18)-1 \GO TO 2050
2090 X(I)=INT(X(I)+.5)

```

```

2100 NEXT I
2105 X(37)=N\X(38)=N1
2110 OPEN "DX1:"&N$ FOR OUTPUT AS FILE #1
2120 AOUT(X,1,0,E1)
2130 AOUT(A,1,1,E2)
2140 AOUT(B,1,2,E3)
2142 AOUT(X1,1,3,E4)
2144 AOUT(B0,1,7,E5)
2145 AOUT(X2,1,11,E6)
2146 AOUT(B1,1,15,E7)
2150 CLOSE #1\RETURN
2550 REM
2570 Q=0\S=0
2580 FOR J=1 TO 20
2590 DACQ(0,Q1,0,0)\DACQ(0,S1,2,0)
2600 Q=Q+Q1\S=S+S1
2610 NEXT J
2620 Q=Q/20\S=S/20
2630 RETURN
3000 FOR I=1 TO 101\PRINT X(I);\NEXT I
3010 PRINT \FOR I=1 TO 1000\PRINT X1(I);\NEXT I
3020 PRINT \FOR I=1 TO 1000\PRINT X2(I);\NEXT I

```

READY

## APPENDIX 2

### DETERMINATION OF THE DISLOCATION DENSITY

The following method was employed for evaluating the dislocation density:

According to equation VI.5, we have

$$\dot{\epsilon} = \frac{b^2 \rho_m v N}{Mh} \exp\left(\frac{-U_0}{kT}\right) \left\{ \exp\left(\frac{\tau_e A^* b}{hkT}\right) - 1 \right\} \quad (\text{VI.5})$$

If we assume that the internal stress is caused only by dislocations, then [177]

$$\tau_i = \alpha G_M b (\rho_t)^{1/2} \quad (\text{A1.1})$$

where  $\rho_t$  is the dislocation density at stress relaxation time  $t$  and  $\alpha$  is a constant about equal to 0.5 [176].  $\rho_t$  is related to the total dislocation density (i.e. the dislocation density at  $t=0$ ),  $\rho_0$ , by

$$\rho_t = \rho_0 \exp(-wt) \quad (\text{A1.2})$$

where  $w$  is a temperature dependent constant given by :

$$w = w_0 \exp\left(-\frac{Q_d}{RT}\right) \quad (\text{A1.3})$$

$Q_d$  is the activation energy for the self diffusion of  $\gamma$ -Fe and  $w_0$  is a constant.

Furthermore, it can reasonably be assumed that  $U_0 = Q_d$ ; it should also be noted that

$$\rho_m = \delta \rho_t \quad (\text{A1.4})$$

where  $\delta$  is a constant smaller than unity. Under these conditions, Equation VI.5 becomes

$$\dot{\epsilon} = \frac{b^2 v N}{M h} \delta \rho_0 \exp(wt) \exp\left(-\frac{Q_d}{RT}\right) \left\{ \exp\left(\frac{\tau_e A^* b}{h k T}\right) - 1 \right\} \quad (\text{A1.5})$$

On the other hand, the strain rate can be calculated at any time from the stress relaxation data using the following equation:

$$\dot{\epsilon} = \frac{\alpha \beta}{E (1 + \beta t)} \quad (\text{A1.6})$$

The values of  $\rho_0$  and  $w_0$  were evaluated by combining the above equations and using a least squares method.  $w_0$  was found to be about  $1.38 \times 10^9$  and the influences of temperature, amount of prestrain and composition on the dislocation density are illustrated in Table VI.3 and Figures VI.7 and VI.7.

The following numerical values were employed for the calculations:

$$b = 2.58 \text{ \AA} \\ v = 10^{12} \text{ s}^{-1} \quad [181]$$

$$N = 12$$

$$M = 3.06$$

$$h = 1$$

$$Q_d = 291,000 \text{ J/mol}$$

$$R = 8.34 \text{ J mol}^{-1} \text{ } ^\circ\text{K}$$

$$k = 1.38 \cdot 10^{-23} \text{ J}^\circ\text{K}$$

$$G_M = 8.1(1 - 0.91(T - 300)/1810) \times 10^4 \text{ MPa} \quad [172]$$

$$\nu = 0.3$$

$$\delta = 1/2$$

Regarding the value chosen for  $\delta$ , it should be mentioned that, for the case of the glide of jogged screw dislocations, the density of the mobile dislocations can be considered equal to that of the screw ones [155]. If we assume that these make up about half of the total dislocations present at time  $t$  in the material, then  $\delta$  becomes equal to  $1/2$ .

### APPENDIX 3

#### CALCULATION OF THE STRAIN RATE USING A CREEP MODEL

The creep equation developed by Hausselt and Nix [177] and given in equation VI.18 can be rearranged and written as

$$\dot{\epsilon} = \frac{(2)^{1/2}}{M\pi} \rho_m D G_M C \cot^2 \phi \frac{\lambda^{8/3} b^{7/3}}{h^2 k t} \left( \frac{\tau_e}{G_M} \right)^{5/3} \frac{1}{1 - (\lambda \tau_e / b G_M)^{4/3}} \quad (\text{A2.1})$$

To calculate  $\dot{\epsilon}$ , the values of  $\tau_e$ ,  $\phi$ ,  $\lambda$ ,  $h$ , and  $\rho_m$  should be known (see section V.1.2. for the definition of these quantities).

According to the discussion presented in V.1.2, it can reasonably be assumed that  $\tau_i$  remains constant during an individual stress relaxation test. Consequently,  $\tau_e$  is given by

$$\tau_e = \tau_a - ct \quad (\text{A2.2})$$

Following the above authors,  $\phi$  was assumed to be  $60^\circ$ .  $\lambda$  is the planar spacing and can be calculated by using the formalism proposed by Ashby and Ebeling [153], where  $\lambda$  is given by

$$\lambda = 0.5 d \left( \frac{\pi}{6 f_v} \right)^{1/2} \quad (\text{A2.3})$$

Here,  $f_v$  is the equilibrium volume fraction of the precipitates, which is equal to

$$f_v = \frac{f a_p^3}{f a_p^3 + (2-f) a_M^3} \quad (\text{A2.4})$$

The change in mobile dislocation density during plastic deformation was calculated and is given by [177]

$$\rho_m = \rho \frac{1}{1-x} \exp\left(-\frac{x}{1-x}\right) \quad (\text{A2.5})$$

where  $x = \tau_i / \tau_a$

Finally,  $h$  was evaluated by a regression analysis of the numerical data obtained by Holbrook and Nix for the case of edge dislocation climb over non-deformable circular inclusions [205] (Figures 2 and 3 of the paper).

$$h = d/2(0.23\xi + 0.76)$$

$\xi$  was evaluated from the above literature data and was found to be equal to 1.03.

Using the above equations and the numerical values given below, the plastic strain rates pertaining to the Nb steel at 850°C after 25% deformation were calculated.

$$D = 2.85 \cdot 10^{-18} \text{ m}^2/\text{sec}$$

$$G_M = 8.1(1 - 0.91(T - 300)/1810) \times 10^4 \quad \text{MPa} \quad [172]$$

$$v_M = 0.3$$

$$v_P = 0.26 \quad [205]$$

$$\phi = 60^\circ$$

$$\rho_m = 4.6 \cdot 10^{12}$$

$$a_P = 4.49 \text{ \AA} \quad [173]$$

$$a_M = 3.54 \text{ \AA}$$

$$b = 2.58 \text{ \AA}$$

The results obtained are presented in Figure VI.3 along with the strain rates measured by means of stress relaxation.

## APPENDIX 4

DETERMINATION OF THE CRITICAL STRESS FOR  
DISLOCATION UNPINNING

As mentioned in the text, the magnitude of the critical stress is equal to that for operation of the Orowan mechanism. The Orowan stress is given by equation VI.17

$$\tau_0 = 0.8 \frac{Gb}{\lambda} \quad (\text{VI.17})$$

The interparticle spacing,  $\lambda$ , can be written as

$$\lambda = 0.5 \left( \frac{1}{dN_v} \right)^{1/2} \quad (\text{A3.1})$$

where  $N_v$  is the number of particles per unit volume.

It can reasonably be assumed that, after the early stages of precipitation, the nucleation sites are saturated. As a result, between this time and the time when particle coarsening starts (i.e. at the end of precipitation)  $N_v$  can be considered as a constant. Under these conditions,  $N_v$  is given by

$$N_v = \frac{6 f_v}{\pi d_f^3} \quad (\text{A3.2})$$

Here  $d_f$  is the particle diameter at the end of precipitation,  $f_v$  is the equilibrium volume fraction of precipitate and is related to the equilibrium mole fraction,  $f$ , by

$$f_v = \frac{f a_p^3}{f a_p^3 + (2-f) a_m^3} \quad (\text{A3.3})$$

$f$  was calculated from a thermodynamic model [183].

For the calculations, the following values were employed:

$$G_{\gamma\text{-Fe}} = 8.1(1 - 0.91(T - 300)/1810) \times 10^4 \quad \text{MPa} \quad [172]$$

$$b = 2.58 \text{ \AA}$$

$$a_{\text{Nb}(\text{C}, \text{N})} = 4.49 \text{ \AA} \quad [173]$$

$$a_{\gamma\text{-Fe}} = 3.54 \text{ \AA}$$

$$f_{850} = 9.16 \cdot 10^{-4}$$

$$f_{900} = 1.08 \cdot 10^{-3}$$

## APPENDIX 5

### DETERMINATION OF THE INTERFACIAL, STRAIN AND CHEMICAL FREE ENERGY FOR NUCLEATION

According to Equation VI.25, we have

$$\Delta G^* = \frac{16\pi\eta^3\gamma^3}{3(\Delta G_c + \Delta G_s)^2} \quad (\text{VI.25})$$

In order to determine  $\Delta G^*$ , the values of  $\gamma$ ,  $\Delta G_c$  and  $\Delta G_s$  should first be evaluated.

#### a) Determination of the interfacial energy, $\gamma$

The energy of an interface may consist of two parts [206]:

- i) a chemical interfacial energy,  $\gamma_c$ , due to bonding across the coherent interface between the particle and the matrix;
- ii) a structural interfacial energy,  $\gamma_{st}$ , which takes up any lack of coherency.

A characteristic feature of an interface is its disregistry, which is defined as

$$\delta = \frac{a_M - a_P}{a_M} \quad (\text{A4.1})$$

Here  $a_M$  and  $a_P$  are the lattice parameters of the matrix and the precipitate, respectively. According to Turnbull [206], for small values of the disregistry,  $\delta$ , the interfacial energy is approximately equal to the sum of the following two terms:

$$\gamma = \gamma_c + \gamma_{st} \quad (\text{A4.2})$$

Under these conditions,  $\gamma_c$  was evaluated [181, 206] and is given by

$$\gamma_c = \frac{N_s Z_s (X_M - X_P)^2 \Delta E^0}{N_0 Z_l} \quad (\text{A4.3})$$

where  $N_s$  = atoms/unit area of the interface,  
 $Z_s$  = bonds per atom across the interface,  
 $X_M, X_P$  = the concentration of precipitate forming elements in the matrix and the precipitate, respectively,  
 $\Delta E^0$  = heat of solution of the precipitate forming elements in a dilute solution (austenite),  
 $N_0$  = Avogadro's number,  
 $Z_l$  = lattice coordination number.

Calculations of the structural part of  $\gamma$  for planar interfaces have been presented by several authors [207, 208]. Assuming that the two phases have the same structure and orientation but different lattice spacings, the following expression for  $\gamma_{st}$  was obtained

$$\gamma_{st} = \frac{G^* a^*}{2 \pi^2} [1 + \beta - (1 + \beta^2)] \quad (\text{A4.4})$$

with

$$\beta = \frac{2\pi a^*}{\lambda(1 - \nu^*)} \quad (\text{A4.5})$$

$$\frac{1}{G^*} = \frac{1}{G_M} + \frac{1}{G_P} \quad [208] \quad (\text{A4.6})$$

$$\frac{2}{a^*} = \frac{1}{a_M} + \frac{1}{a_P} \quad [208] \quad (\text{A4.7})$$

Here  $\lambda$  is the spacing of the interfacial dislocations and can be determined from

$$\lambda = \frac{a^*}{\delta} \quad (\text{A4.8})$$

Finally,  $\nu^*$  is the interfacial poisson's ratio which, for the lack of other information, was assumed equal to the mean value of the poisson's ratios of Nb(C,N) and austenite.

b) Determination of the strain energy,  $\Delta G_s$

According to the Eshelby formalism, the strain energy created by the precipitate when the process is accompanied by a pure dilatation is given by [209]

$$\Delta G_s = \frac{2}{3} G_M \varepsilon^2 \frac{\alpha}{\alpha + (1-\alpha) \frac{K_M}{K_P}} \quad (\text{A4.9})$$

Here  $\varepsilon$  is the cubic dilatation associated with the transformation strain and has the following value

$$\varepsilon = \frac{a_P^3 - a_M^3}{a_P^3} \quad (\text{A4.10})$$

$\alpha$ ,  $K_M$  and  $K_P$  are related to the elastic constants by

$$\alpha = \frac{1}{3} \frac{1 + \nu_M}{1 - \nu_M} \quad (\text{A4.11})$$

$$K_M = G_M \left( 2 + \frac{3}{1 - \nu_M} \right) \quad (\text{A4.12})$$

$$K_P = G_P \left( 2 + \frac{3}{1 - \nu_P} \right) \quad (\text{A4.13})$$

It should be noted that Equation A4.9 is only valid for a spherical particle. This requirement is approximately fulfilled when the precipitates in question form in an fcc matrix. In this situation, the nucleus is likely to be an

octahedron separated from its parent phase by {111} atom planes for minimization of the interfacial energy. For the present purpose, such an octahedron may be considered to be represented approximately by a sphere.

c) Determination of the chemical free energy,  $\Delta G_c$

$\Delta G_c$  was defined as the driving force for nucleation of the precipitates. It can be related to the supersaturation ratio,  $k_s$ , by the following relation [142].

$$\Delta G_c = - \frac{RT}{V_m} \ln k_s \quad (\text{A4.14})$$

where  $V_m$  is the molar volume of Nb(C,N) and  $k_s$  is defined as

$$k_s = \frac{[\text{Nb}][\text{C} + \frac{12\text{N}}{14}]_{\text{sol}}}{10^{2.26 - 6770/T}} \quad (\text{A4.15})$$

The above relation was obtained from the solubility product equation for Nb(C,N) proposed by Irvine et al. [147].

Using the above equations and the numerical values given below, the unknowns  $\gamma$ ,  $\Delta G_c$  and  $\Delta G_s$  were evaluated and the results are presented in Table VI.5.

$a_p = 4.49 \text{ \AA}$		
$a_M = 3.54 \text{ \AA}$		
$N_s = [16/3]^{1/2} a_{\gamma\text{-Fe}}^2$	{111} interface	[96]
$Z_s = 3$	{111} interface	[96]
$(X_M - X_P)^2 = 0.25$		[101]
$\Delta E^0 = 129.457 \text{ kJ/mol}$		[96]
$N_0 = 1.06 \cdot 10^{23}$		
$Z_1 = 12$		
$G_M = 8.1[1 - 0.91(T - 300)/1810] \times 10^4 \text{ MPa}$		[172]

$$G_p = 1.34[1 - 0.18(T - 300)/3613] \times 10^5 \quad \text{MPa} \quad [172]$$

$$v_M = 0.3$$

$$v_p = 0.26$$

$$R = 8.314 \text{ Jmol}^{-1}\text{K}^{-1}$$

$$V_m = 1.28 \times 10^{-5} \quad \text{m}^3/\text{mol}$$